Habilitation Material

"Role of Gravitational-Wave Progenitors in the Universe"

Presented to **The Council of Scientific Excellence**

by

Dr. Dorottya Szécsi

Institute of Astronomy, Nicolaus Copernicus University in Toruń, Poland

Content

SUMMARY OF PROFESSIONAL ACCOMPLISHMENTS

SUMMARY OF PROFESSIONAL ACCOMPLISHMENTS

DOROTTYA SZÉCSI

1. Basic data

Name **Dr. rer. nat. Dorottya Szécsi** (iD) http://orcid.org/0000-0001-6473-7085

Address Institute of Astronomy, Nicolaus Copernicus University, Gagarina 11, 87-100 Toruń

Email dorottya@umk.pl

Website http://astro.umk.pl/~dorottya

Metrics ui.adsabs.harvard.edu-search-szecsi-dorottya-metrics

2. Diplomas and scientific degrees

04/07/2016 **PhD in Astrophysics**, *Argelander-Institut für Astronomie of the University Bonn (Germany)*, Thesis title: „The evolution of low-metallicity massive stars", Advisor: Prof. Norbert Langer.

22/06/2012 **Masters in Physics**, *Eötvös Loránd University, Budapest (Hungary)*, Thesis: „Direction Dependent Background Fitting Method for analysing the Fermi Gamma-ray Space Telescope's Data" (in Hungarian), Advisor: Dr. Zsolt Bagoly.

10/06/2010 **Bachelor in Physics with specialization in Astronomy**, *Eötvös Loránd University, Budapest (Hungary)*, Thesis: „Study of the Gamma-ray Bursts' Temporal Properties with the Fermi Satellite" (in Hungarian), Advisor: Dr. Zsolt Bagoly.

3. Education and employment history

10.2020 – ... **Assistant Professor & OPUS group leader**, *Institute of Astronomy – Faculty of Physics, Astronomy and Informatics – Nicolaus Copernicus University, Toruń, Poland.*

04.2019 – 09.2021 **Alexander von Humboldt Individual Research Fellow**, *University of Cologne, Germany.*

10.2017 – 03.2019 **Research assistant (PD)**, *Institute of Gravitational Wave Astronomy and School of Physics and Astronomy, University of Birmingham, UK.*

08.2016 – 09.2017 **Research assistant (PD)**, *Astronomical Institute of the Czech Academy of Sciences.*

04.2016 – 07.2016 **Post-doctoral Fellow**, *Argelander-Instutut für Astronomie of the University Bonn, Germany.*

09.2012 – 07.2016 **PhD Fellow**, *Argelander-Instutut für Astronomie of the University Bonn, Germany.*

01.2008 – 08.2012 **Research assistant**, *Konkoly Observatory of the Hungarian Academy of Sciences.*

09.2010 – 06.2012 **Master student**, *Eötvös Loránd University, Budapest, Hungary.*

10.2011 – 02.2012 **Erasmus exchange student**, *Scholarship at the Bergische Universität Wuppertal, Germany.*

01.2008 – 06.2012 **Intern**, *Non-paid research internship at the Hungarian research group OTKA-77795.*

09.2007 – 06.2010 **Bachelor student**, *Eötvös Loránd University, Budapest, Hungary.*

____

4. Habilitation achievement

Role of Gravitational-Wave Progenitors in the Universe

(Hab1) **Szécsi**, D., Agrawal, P., Wünsch, R., Langer, N.: *'Bonn' Optimized Stellar Tracks (BoOST). Simulated Populations of Massive and Very Massive Stars as Input for Astrophysical Applications*, A&A 658, A125 (2022). [LINK] [arXiv:2004.08203] [***Media Release***] – 22 pages.

(Hab2) Agrawal, P.; **Szécsi**, D.; Stevenson, S.; Hurley, J.: *Explaining the differences in massive star models from various simulations*, MNRAS Vol.512, Issue 4, pp.5717-5725 (2022). [LINK] [arXiv:2112.02800] – 9 pages.

(Hab3) **Szécsi**, D. and Wünsch, R.: *Role of supergiants in the formation of globular clusters*, ApJ 871, 20 (2019). [ADS] [arXiv:1809.01395] – 21 pages.

(Hab4) **Szécsi**, D., Mackey, J. and Langer, N.: *Supergiants and their shells in young globular clusters*, A&A 612, A55 (2018). [LINK] [arXiv:1711.04007] – 13 pages.

(Hab5) Kubátová, B.; **Szécsi**, D.; Sander, A. A. C.; Kubát, J.; Tramper, F.; Krtička, J.; Kehrig, C.; Hamann, W.-R.: *Low-metallicity massive single stars with rotation. II. Predicting spectra and spectral classes of chemically homogeneously evolving stars*, A&A, 623, A8 (2019). [LINK] [arXiv:1810.01267] – 33 pages.

I. INTRODUCTION

What do gravitational waves have in common with ancient starclusters? What links these to gamma-ray producing cosmic explosions, to the energetic radiation in star-forming galaxies and even to the dawn of our Universe? What they have in common, is that all these phenomena — and more — have been theorized to stem from **metal-poor massive stars**, in one way or another[1–7].
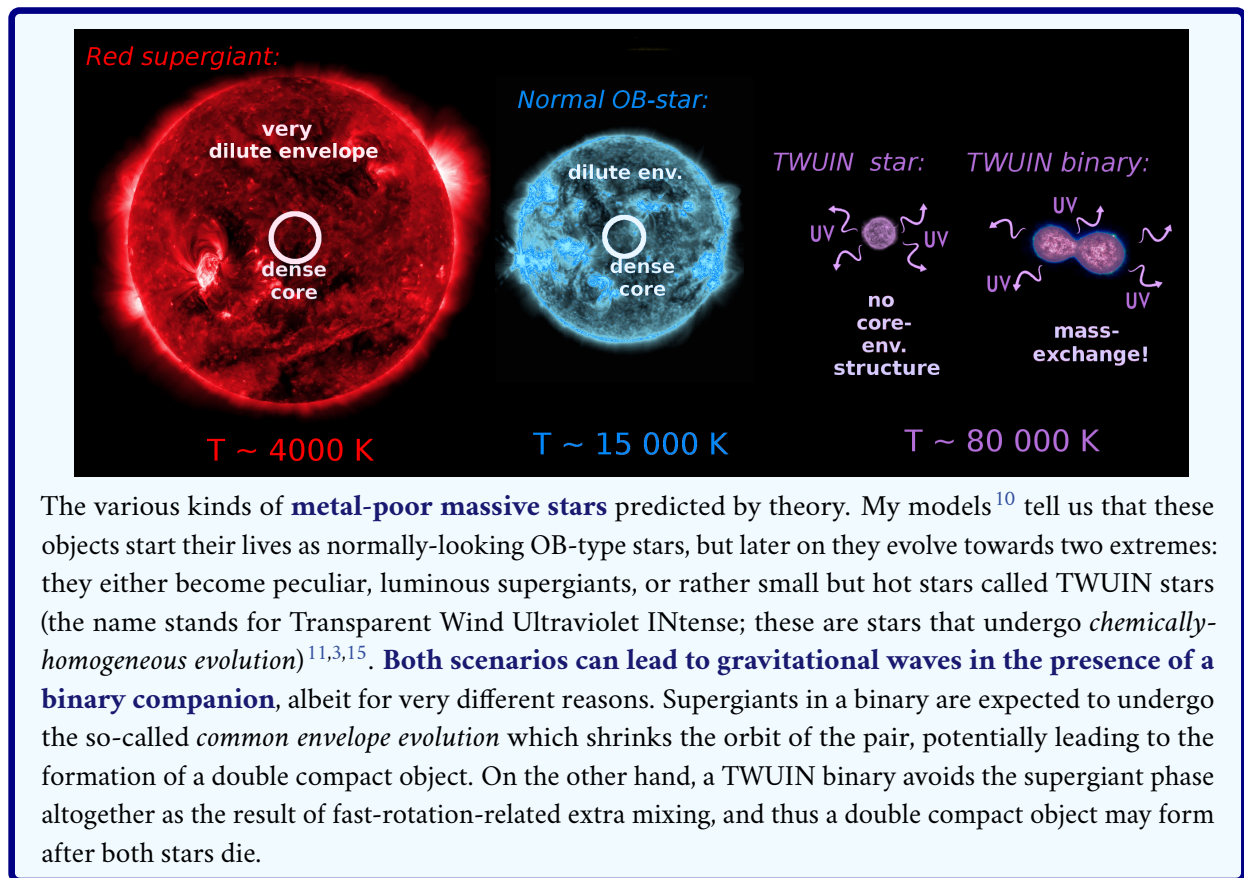
Yet, our knowledge of this type of star — more massive than 8 times our Sun, and containing only a tiny amount of heavy elements — is still quite poor. The evidence that exist for them is typically sporadic: after all, these stars are not only rarely born (all massive stars are rarely born[1]) but live far away from us, in other galaxies. Thus it is very difficult to carry out direct observations of them[8,9]. Most of the time we have to work with whatever *indirect* evidence we can get.

> I use the term 'metal-poor' to mean a metal content ('metallicity') lower than that of the Small Magellanic Cloud, i.e. $\lesssim 0.1\,Z_\odot$ but not yet completely metal-free.

We do know that these stars must be **massive** enough to form black holes or neutron stars (in short, massive compact objects) after they die. We also know that most of them must have **low metal content**. However, despite all the efforts of the last decade, the nature of these *metal-poor massive stars* still puzzles us[1,10,11,2] – for no one has ever *directly* observed a star which is, say, 100 times as massive while 100 time as metal-poor as the Sun. Our Milky Way – a rather old galaxy of high metal content – simply does not harbour such stars anymore.

From theory[10] it is predicted that metal-poor massive stars are able to behave in special ways (cf. the figure on page 3). For example, they can become **peculiar supergiant stars**[12,13] that are many orders of magnitude brighter than any supergiant observed so far. Or, under other circumstances, they may form **hot and fast-rotating stars**[14,15] which, upon exploding, produce some extremely energetic

phenomena (e.g. gamma-ray bursts [3,4]). In both cases, if such stars happen to be born in a binary star system, they may form double compact objects (albeit via different channels) which eventually merge and emit gravitational waves [16–20].

Red supergiant: very dilute envelope / dense core / T ~ 4000 K
Normal OB-star: dilute env. / dense core / T ~ 15 000 K
TWUIN star: UV / no core-env. structure
TWUIN binary: UV / mass-exchange! / T ~ 80 000 K

The various kinds of **metal-poor massive stars** predicted by theory. My models [10] tell us that these objects start their lives as normally-looking OB-type stars, but later on they evolve towards two extremes: they either become peculiar, luminous supergiants, or rather small but hot stars called TWUIN stars (the name stands for Transparent Wind Ultraviolet INtense; these are stars that undergo *chemically-homogeneous evolution*) [11,3,15]. **Both scenarios can lead to gravitational waves in the presence of a binary companion**, albeit for very different reasons. Supergiants in a binary are expected to undergo the so-called *common envelope evolution* which shrinks the orbit of the pair, potentially leading to the formation of a double compact object. On the other hand, a TWUIN binary avoids the supergiant phase altogether as the result of fast-rotation-related extra mixing, and thus a double compact object may form after both stars die.
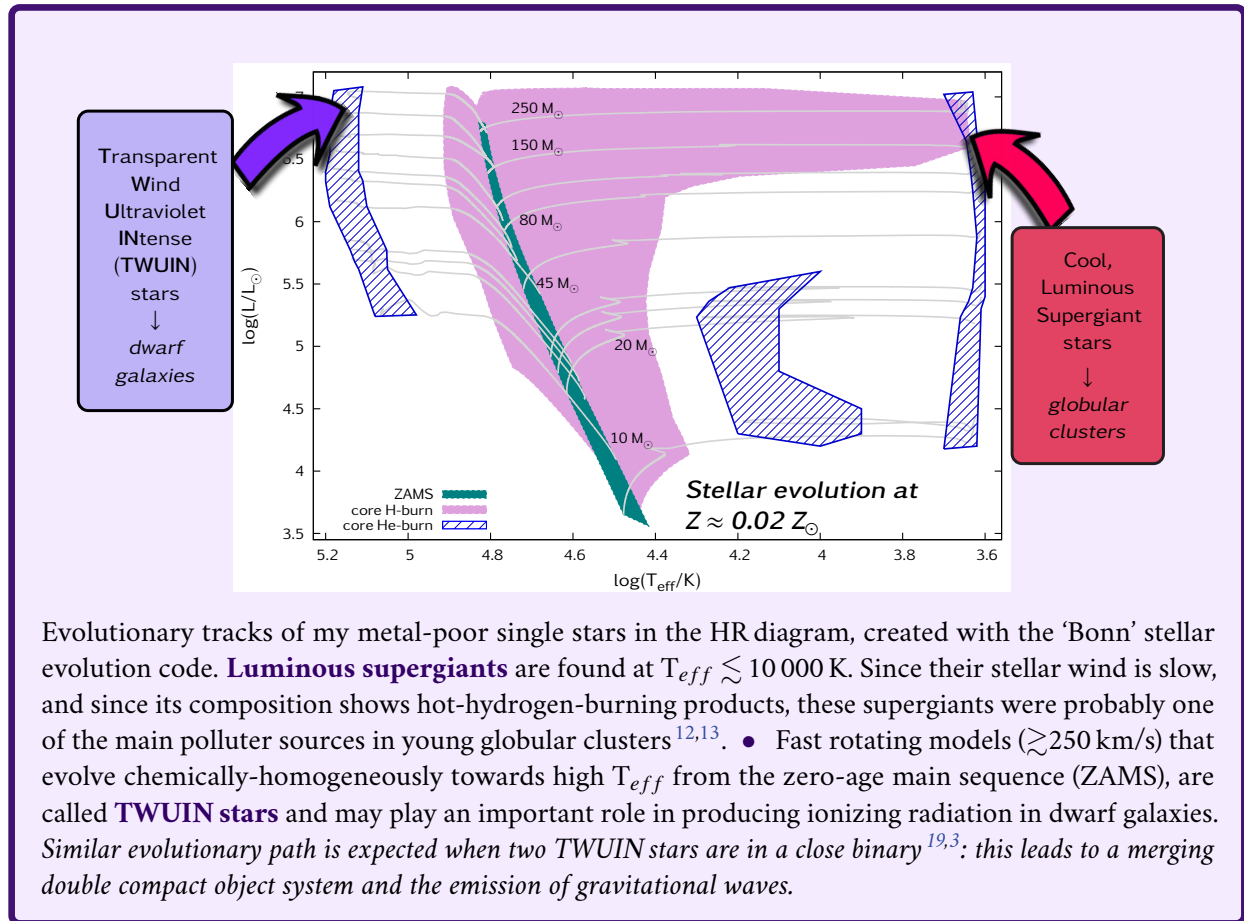
Although no *direct* detection is possible, some observational evidence for the existence and nature of these special stars has been collected – we may see their *traces*. The luminous, metal-poor supergiants may have played a role in the formation of ancient **globular clusters** [12,13]. As for the fast-rotating, so-called *chemically-homogeneously evolving* stars (or 'TWUIN stars', see the figure on page 3), these have been suggested as contributors to star-formation in dwarf galaxies [14] and account for **long-duration gamma ray bursts and certain supernovae** [4,21].

Amongst metal-poor massive stars, a special attention should be paid to those which are the **stellar parents (progenitors)** of gravitational-wave emitting compact object mergers. Although gravitational waves are being detected on a regular basis these days [22], open questions remain about their origin – especially when it comes to their stellar progenitors. This makes my research especially relevant and timely.

> **TWUIN** stands for: **T**ransparent **W**ind **U**ltraviolet **IN**tense. TWUIN stars are theoretically predicted stars that undergo *chemically-homogeneous evolution* [11,3,15] and are as hot as Wolf-Rayet stars. Yet they are *not* of type Wolf-Rayet because their wind is not optically thick. For details, see the figures on pages 3 and 4, as well as the research performed in **Hab5** [15].

During my post-PhD career as an individual researcher, I have **focused on proving, as well as disproving, theories about metal-poor massive stars**. The way I am doing this is completely unique, yet logical: I am combining the existing pieces of evidence, the various roles that these stars play in many areas of astrophysics, into a unified picture. As mentioned, whatever evidence we can have is typically indirect: and thus it comes from different fields such as e.g. gravitational-wave detections, supernova and gamma-ray burst research, stellar archaeology of ancient clusters and so on. Combining these various fields via the underlying contribution of metal-poor massive stars, is what I have achieved in **Hab1–5**.

While my PhD was about to generate the models themselves [11], I have embarked on a much more

Evolutionary tracks of my metal-poor single stars in the HR diagram, created with the 'Bonn' stellar evolution code. **Luminous supergiants** are found at $T_{eff} \lesssim 10\,000$ K. Since their stellar wind is slow, and since its composition shows hot-hydrogen-burning products, these supergiants were probably one of the main polluter sources in young globular clusters[12,13]. ● Fast rotating models ($\gtrsim 250$ km/s) that evolve chemically-homogeneously towards high T_{eff} from the zero-age main sequence (ZAMS), are called **TWUIN stars** and may play an important role in producing ionizing radiation in dwarf galaxies. *Similar evolutionary path is expected when two TWUIN stars are in a close binary[19,3]: this leads to a merging double compact object system and the emission of gravitational waves.*

comprehensive adventure since: I have applied the models in **various, independent research cases all around the Universe**. I have demonstrated key facts about these stars (such as their spectral types[15], **HAB5**), described some of their important properties (such as their wind material possibly forming new stars[12], **HAB4**), and connected different fields of astrophysics by applying these predictions (such as the field of massive stars with that of cluster formation[13], **HAB3**). Moreover, I have studied these stars' uncertain physics and their role in gravitational-wave research[23], **HAB2**, and provided an unprecedented – and widely used – set of publically available and well-maintained model sets for astrophysical applications[24], **HAB1**, crowning my achievements.

II. FROM STELLAR EVOLUTION TO GRAVITATIONAL WAVE RESEARCH: THE ELEMENTS OF STELLAR *VS.* POPULATION MODELLING

Stellar *evolutionary* modelling and stellar *population* modelling are often confused. While evolutionary codes compute stellar models from first principles (simulating the hydrodynamic structure of an isolated sphere of gas, that is, a 'star' or a 'stellar model'), **population synthesis codes typically rely on pre-computed stellar evolutionary models**, and estimate what the integrated properties of a *population* of them would have. Indeed, if a molecular cloud gives birth to a given number of stars, some of them will have low mass, some of them will have high mass – this is described by the so-called initial mass function, which is usually taken to be a power law. Weighting with this function, and using pre-computed stellar evolutionary models, one can – in principle – predict things about the population such as the total ionizing photon flux emitted, or the total mass ejected from stars (and its composition), or the number/energy of supernovae and other explosions (e.g. gamma-ray bursts, gravitational wave event rates). Indeed, the term *stellar feedback* refers to this in context of a star-forming region where young massive stars are present and contributing with their strong radiation and mass input – either

as a living, mass-ejecting massive star or as exploding supernovae. The term *supernova feedback* is used to refer to only that later process.

Detailed models vs. rapid models

Another confusion often arises when the literature talks about "following the evolution of a star/stellar population". *Following* in this context may mean either that *detailed* simulations are carried out with an evolutionary code, or that existing simulatons are applied (as tables/fitting formulae) serving as a basis for a *rapid* approach.

Examples of *detailed* stellar evolution codes include the 'Bonn' code[24] and Mesa (*Modules for Experiments in Stellar Astrophysics*[35–37]). Both of these codes are state-of-the-art, see the panel on the right. Mesa has the advantage of being open source, modular and extendible[38,39,19,40–42].

Examples of *rapid* codes include the one I have been involved with as a theoretical expert, called Compas (*Compact Object Mergers: Population Astrophysics and Statistics*)*. While it has been used in word-leading studies on gravitational-wave emitting merger rates[43–46,6,7], it relies on rather simplistic fitting formulae[47] and is therefore not a very flexible populations

> The **Bonn Code** is a leading stellar evolution code which, amongst other things, is especially suited to simulating massive stars due to the large nuclear reaction network and the high spacial resolution it applies[10,25–28]. The most recent addition to the code was the so-called **BoOST project** (*Bonn Optimized Stellar Tracks*, Szécsi+22[29]), in which I made large model grids publicly available in the form of full, well-maintained tables (cf. **Hab1**). These tables are now widely used in the community[30–34].

synthesis tool – with its only possible application being the merger rate predictions. Despite its many advantages therefore, including exceptionally strong statistical packages, a recent open release**, as well as active development and great user support, its current version would not be able to account for the stellar feedback in e.g. forming star-clusters (e.g. **Hab3/4**).

Why do we need *population sythesis* in gravitational-wave research?

Gravitational-wave-emitting compact object mergers start their lives as two massive stars in a binary system. We detect gravitational waves from the entirety of our vast Universe. Therefore, making predictions about them is an inherently statistical endeavour. A common approach is to build **synthetic populations of binary stars** based on theoretical stellar models[48–57,20,58,43,59–61,7]. The results, which are to be interpreted statistically, will depend on the underlying stellar *evolutionary* models quite delicately.

On the other hand, the evolution of massive stars, and especially that of metal-poor massive stars, has undergone significant development in recent years. New physical ingredients have been implemented and studied in **stellar evolution simulations** for example with the 'Bonn' code[62–64,27,28,10,29] and other codes[54,65,66,19,40,42] and due to these, our knowledge of metal-poor massive stars (single and binary) has grown substantially.

To predict gravitational-wave events as accurately as possible, we have to make sure that the synthetic population code we use bases its statistics on these most up-to-date stellar models – and future ones too (cf. **Hab2**).

The challenges of binary evolution

The interaction between binary companions is a complex issue[67–69], as these close-by stars may exchange their mass, merge with each other, and influence each others' lives in various other ways too (e.g. via creating gravitational tides, via impacting each others' orbit, via wind-collision and accretion etc.). All these processes are actively investigated. One of the most influential of them is the so-called *common envelope* phase, during which the two stars are encompassed by the same, extended

---

* Compas website: http://compas.science/
** Compas github: http://github.com/TeamCOMPAS/COMPAS

stellar envelope. Indeed, the presence of luminous supergiants (as predicted in metal-poor stellar models, **Hab3**, **Hab4**) can influence merger rate predictions significantly[57] due to these stars possibly undergoing common envelope evolution with their companions.

The inherent challenges in building synthetic populations

Existing population synthesis tools were usually created for certain specific purposes: some aim to predict gravitational-wave event rates (e.g. Compas[43,60,7], StarTrack[49,53,57], ComBinE[59], BPASS[50,20]), some aim to statistically predict observed stars' physical properties (Starmaker[52], Bonnsai[55], binary_c[48,51,56]), and some aim to provide input for other codes (e.g. by predicting the feedback on star-formation of a population of massive stars lying nearby; BPASS[54], synStars[13]). While all these codes have the same underlying idea – that is, weighting stellar evolutionary models with an initial mass function to predict some properties of a population of stars – none of them are able to *simultaneously* fulfill all the purposes mentioned.

Ideally, what we would need is the integrated values of *every* stellar property that state-of-the-art evolutionary models include, such as

- total energy emitted in radiation as a function of time
- total mass lost and its composition as a function of time
- total wind velocity as a function of time
- number of supernova explosions and their kinetic energy
- number of long-duration gamma-ray burst (e.g. estimated based on the collapsar scenario)
- masses of the compact objects that are produced
- number of gravitational-wave emitting mergers

and so on. Having all these predictions available simultaneously, from various populations of stars (i.e. with various metallicities, rotational velocity distributions and binary fractions), has been one of the main goals during my independent post-PhD career (**Hab1**).

In practice, creating a binary population synthesis code based on modern stellar models in a flexible way so that the outcome is *multi-purposefully* applicable not only for gravitational-wave event rate predictions but for several other fields of related research, **is a challenge**[39,70,71,29]. It certainly needs expertise in stellar evolution and binary population synthesis, but also some expertise in those other fields (star-formation and cosmological simulations). For example, the interpolation between two stellar evolutionary models is something that is typically needed[52,39] (unless one computes a very dense model grid[19]; this however is not only computationally expensive but requires *a lot* of humanpower for the maintenance of the grid). But interpolating is also a challenge, because these models are data sets of very high dimensions. Making sure that all their parameters change smoothly upon interpolation, is a serious task. And the situation gets even more complicated when one wants to work not only with single, but with **binary stars** too[41]: then the parameter space gets much larger because any two stars can be on a close orbit, or on a wide orbit, or anything in between – and their orbital distance influences the way they live their coupled lives.

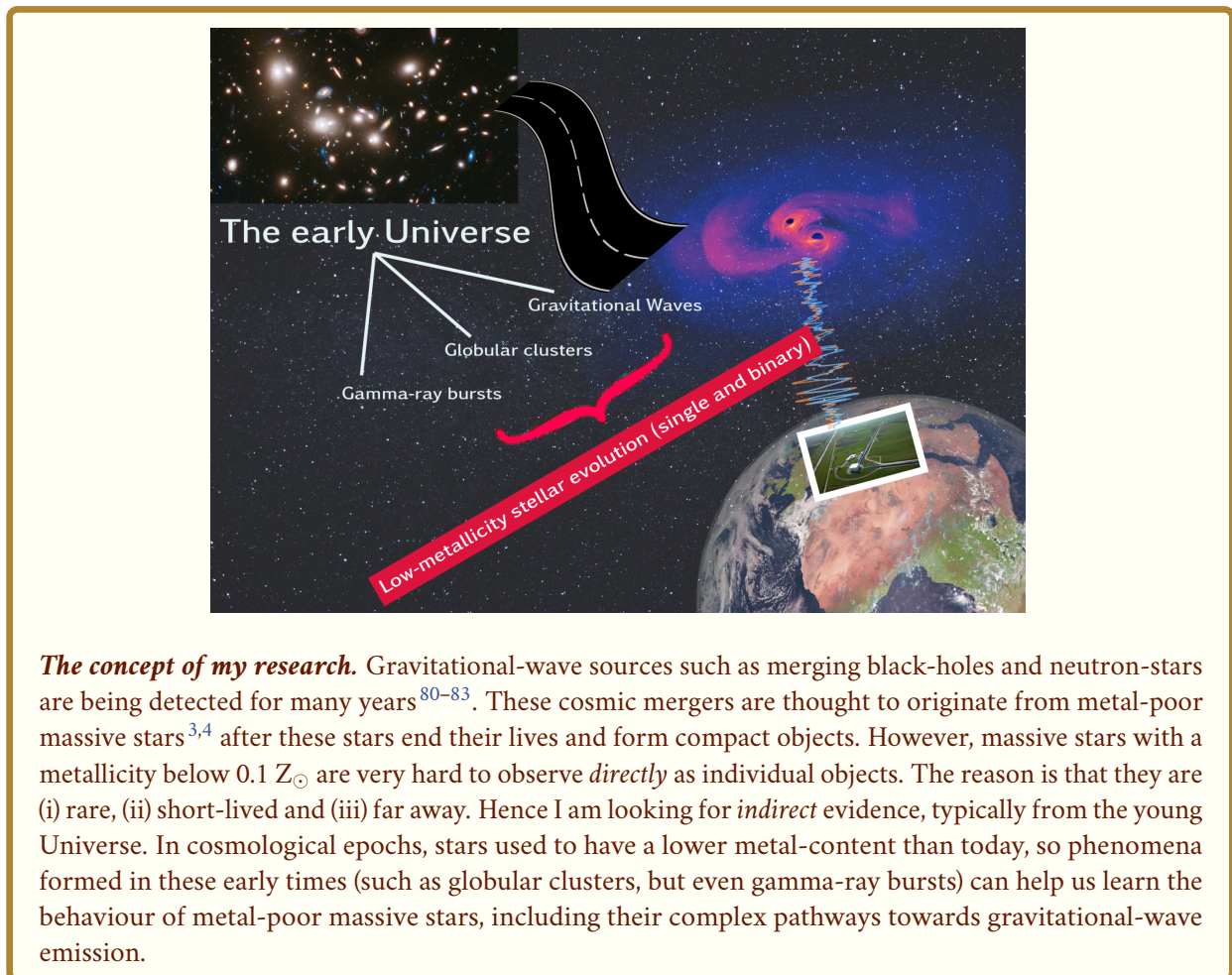## Stellar winds and how uncertain mass loss rates are

One of the most uncertain physical ingredients of the theory of massive stars is the nature of their mass loss, that is, their stellar winds. It is an established fact that massive stars eject material during their lives[1], and the exact amount strongly impacts their evolutionary behavior. However, it is not easy to predict the exact amount. Especially for those stars that have low metal content (i.e. those that we expect to be the progenitors of gravitational-wave emitting mergers), observational clues for how they are loosing their mass are hard to obtain. Nonetheless, great progress has been[72–74] and is being[75–77] done in this field of research – some of it is my own contribution, cf. **Hab5**[15].

Supernova types, and the issue of assigning them to stellar progenitor models

Evolutionary model sequences of massive stars do not always include the **phase of the final explosion**.

However, when translating them into populations, people need to assign some supernova type (and explosive energy released, and remnant mass left behind) to them. Since this problem is rather complex due to the explosion physics depending delicately on the structure of the exploding star[78,79], several simple solutions are used in practice.

For example, in the current version of the Compas binary population synthesis code, every star above a certain mass is supposed to explode as a supernova, and the final remnant's mass is simply determined from the core mass of the exploding star. This is a straightforward and effective, but also very simplistic and approximative, treatment of the problem. Similarly, it is a common approach to assume that every massive star in a population explodes as a supernova with a uniform kinetic energy of 10^{51} erg, which is another simple treatment of this complex issue (**Hab1**).

The concept of my research. Gravitational-wave sources such as merging black-holes and neutron-stars are being detected for many years[80–83]. These cosmic mergers are thought to originate from metal-poor massive stars[3,4] after these stars end their lives and form compact objects. However, massive stars with a metallicity below 0.1 $Z_\odot$ are very hard to observe *directly* as individual objects. The reason is that they are (i) rare, (ii) short-lived and (iii) far away. Hence I am looking for *indirect* evidence, typically from the young Universe. In cosmological epochs, stars used to have a lower metal-content than today, so phenomena formed in these early times (such as globular clusters, but even gamma-ray bursts) can help us learn the behaviour of metal-poor massive stars, including their complex pathways towards gravitational-wave emission.

Gamma-ray bursts: what are they, and how do they enter the picture?

Long-duration gamma-ray bursts are energetic phenomena accompanying a supernova with a rapidly rotating progenitor star[62,63,4]. Relying on the distribution of specific angular momentum of the stellar model in the late phases of evolution, it is possible to infer if such a burst will or will not happen[25] for any given model. This opens the door to include gamma-ray burst research into my efforst of understanging metal-poor massive stars: these explosions have been both theoretically and observationally associated with low-metallicity environments[14,4].

Short-duration gamma-ray bursts happen when two neutron stars (or a black hole and a neutron star) collides. Naturally, this should be **accompanied by a gravitational-wave emission**. The nominal distinction of long vs. short is at 2 sec.

Gamma-ray bursts are observed on a daily basis by special satellites such as *Fermi*[84,85] and SWIFT[86], and occasionally followed up by large ground-based telescopes[87–90]. As of today, there is a sample of

about ∼500 long-duration gamma-ray bursts with measurement of the redshift of their host galaxies[91]. After translating between redshift and metallicity, this observational data could be used to constrain the physics of metal-poor massive stars, i.e. telling us **the ratio of TWUIN stars (Hab5) vs. normal stars as a function of metallicity** – provided that the final fates of the stars are properly assigned in our synthetic populations.

> **Globular clusters: how do they enter the picture?**

Metal-poor massive stars, including those that are supposedly progenitors to gravitational-wave emitting mergers, do not exist in our Galaxy anymore. However, they might have existed here in the past – and we may indeed see their traces in ancient, metal-poor galactic globular clusters. **Anomalous light element ratios** have been observed in almost all globular clusters[5], ratios that can only be synthesised deep inside massive or intermediate-mass stars where the temperature is high enough.

Metal-poor massive stars can play a crucial role in this process. In particular, metal-poor *luminous supergiants* have various ways to contribute (cf. **Hab3** and **Hab4**). When simulating the forming globular cluster, it is commonly supposed that it starts out as a young massive cluster (YMC)[92,93]. To take into account the influence of the first generation of massive stars, state-of-the-art evolutionary models (with an assumed initial mass function) can be applied. The second generation of new stars form from the wind-material (or, depending on the scenario assumes, possibly its mixture with the pristine gas).

Observational comparisons can be performed using archival data, e.g. of the *Gaia* satellite's ESO/UVES survey[94] and other spectroscopic surveys. Contributing to the field of globular clusters this way **enhances our understanding of metal-poor massive stars** too, for there is not many ways one can observationally constrain theories of these stars – and comparing model predictions to abundance measurements in globular clusters, even if indirect, is one of them. Indeed, the number of predicted black hole mergers depends delicately both on the number of supergiants as well as on the nature of the mass transfer. Thus, testing synthetic populations in globular cluster research *simultaneously* with their predictions about aLIGO/Virgo detections is a unique research idea which is made possible by my habilitation achivements (cf. **Hab1–3**).

III.   DESCRIPTION OF PUBLICATIONS

(Hab1)   **Szécsi**, D., Agrawal, P., Wünsch, R., Langer, N.: *'Bonn' Optimized Stellar Tracks (BoOST). Simulated Populations of Massive and Very Massive Stars as Input for Astrophysical Applications*, A&A 658, A125 (2022). [LINK] [arXiv:2004.08203] [*Media Release*] – 22 pages.

Quick overview.   Publicly available stellar evolutionary models of massive stars, computed with the Bonn Code, and published and optimized for astrophysical applications. Such a complete set of models – that include massive and very massive stars (9–500 $M_\odot$) and cover a broad range in metallicity ($Z_\odot$–1/250 $Z_\odot$) in a user-friendly way – is **quite unique in the literature**. In addition to providing stellar models in an optimized format, I also provide a dense grid of interpolated tracks based on them. These now serve as input for many studies[30–34], from 3D dwarf galaxy simulations to dust formation.

How it fits into my Habilitation.   Publishing the models I have created and tested (**Hab2-4**) so that others can also apply them in their *own* studies is a cornerstone of my activities. The more angle we study metal-poor massive stars from, the better we can hopefully understand them. While I am using these models to tackle my special research interests (gravitational wave astrophysics, globular clusters, gamma-ray busts), there are, necesarily, more places out there where such stars contribute. Providing a **broadly applicable dataset for the community** is, therefore, key if my goal is to properly explore their role in the Universe.

My role.   I am the PI of this study; the person who carried out the vast majority of the work. My co-

authors helped with programming and double-checking the models for inconsistencies, but everything else was done by me. These include the simulation and pre-processing of stellar models, the design of the grids, the invention of a novel way to overcome numerical difficulties, the post-processing of all models into a user-friendly format, and writing the article.

Most important results.   The panels below (page 9) show a few examples of the models published in **Hab1**. Two features stand out. First, the presense/absence of very luminous supergiants at low/high metallicity: this is due to the metal-rich models having stronger mass loss rates, and thus loosing their envelopes in the stellar wind becoming hot Wolf-Rayet stars instead. Second, the presense/absense of a so-called blue loop at lower metallicities: this phenomenon is tightly linked to internal mixing[95]. The models include stellar wind yields for 34 isotopes: ^{1}H, ^{2}H, ^{3}He, ^{4}He, ^{6}Li, ^{7}Li, ^{7}Be, ^{9}Be, ^{8}B, ^{10}B, ^{11}B, ^{11}C, ^{12}C, ^{13}C, ^{12}N, ^{14}N, ^{15}N, ^{16}O, ^{17}O, ^{18}O, ^{19}F, ^{20}Ne, ^{21}Ne, ^{22}Ne, ^{23}Na, ^{24}Mg, ^{25}Mg, ^{26}Mg, ^{26}Al, ^{27}Al, ^{28}Si, ^{29}Si, ^{30}Si, and ^{56}Fe, as well as a complete coverage of the core-hydrogen and core-helium-burning phases.
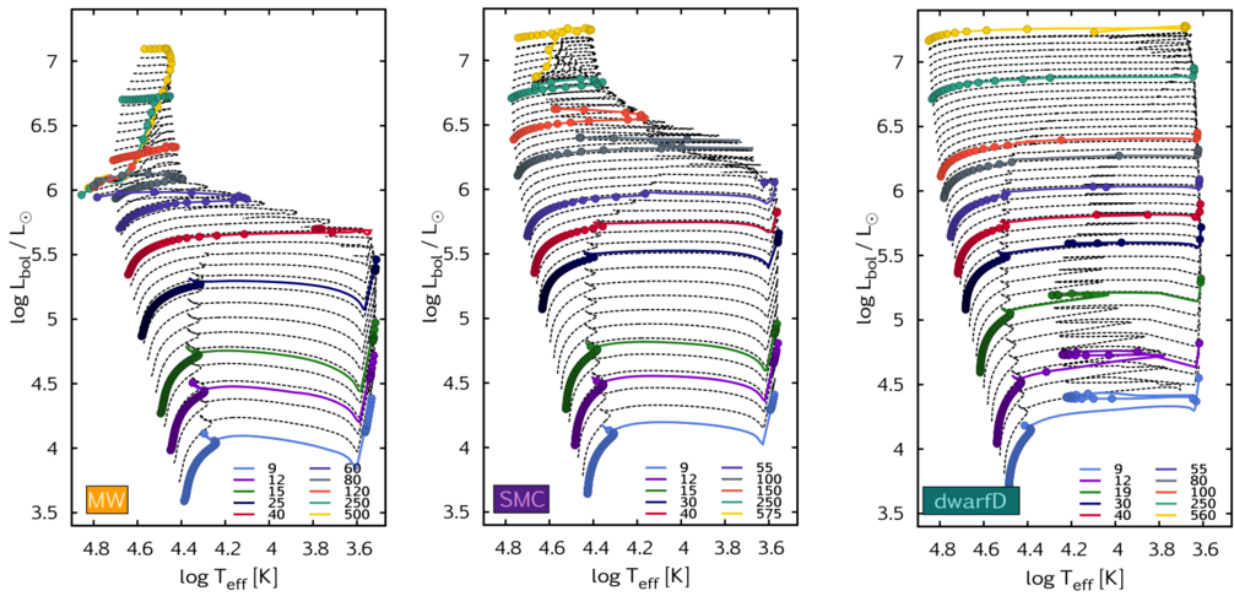
Example of the models published in the BoOST project (**Hab1**)[24] in the Hertzsprung–Russell diagram. Initial mass is color-coded (between 9 and ∼500 $M_\odot$), initial metallicity corresponds to that of the Milky Way (MW), the Small Magellanic cloud (SMC, $Z_{SMC} = 0.002$) and a metal-poor dwarf galaxy ($Z_{dwarfD} = 0.0001$). Circles mark every 10^5 yr of evolution along the stellar models. Dashed black lines represent interpolated tracks, based on which synthetic stellar populations are created. ● *In the BoOST project, 9 full grids of similar constitution are published in a user-friendly data format (**Hab1**)[24] facilitating easy application of metal-poor stellar models in gravitational-wave research and beyond.*

This work now serves as a basis for a number of astrophysical studies[30–34] – and will serve more in the future – harvesting the true potential of stellar evolutionary modelling, and crowning my habilitation achievements.

(Hab2)   Agrawal, P.; <u>Szécsi</u>, D.; Stevenson, S.; Hurley, J.: *Explaining the differences in massive star models from various simulations*, MNRAS Vol.512, Issue 4, pp.5717-5725 (2022). [LINK] [arXiv:2112.02800] – 9 pages.

Quick overview.   When comparing the BoOST models (**Hab1**[24]) to other 1D simulations of massive stars in the literature, I realized that above 40 $M_\odot$ serious discrepancies arise in *all* the datasets. The physical reasons for the discrepancies are explained here, and a strong message is sent to the community about treating *any* stellar simulations above 40 $M_\odot$ with caution, as the physics of these models have not yet reached scientific consensus.

How it fits into my Habilitation.   Libraries of stellar models are often treated as black boxes by people applying them. Since I myself publish such a library in **Hab1**[24], adding the necessary warning is the scientifically valid next step. As a use-case, we also investigate how **gravitational-wave predictions are influenced** by the uncertainties. We find a discrepancy as high as 20 $M_\odot$: a serious caveat for anyone who wants to connect merging black holes to their theoretical progenitors[96].

My role.   I am sharing first authorship with my then-PhD student, P. Agrawal. The original idea way mine, as was the presentation of the results and a fair share of the calculations. Yet I offered my student to be leading author because, similarly to any young researcher wanting to build a career in science, her publication list needed to be strengthened to get a post-doctoral position. Nonetheless, I consider this paper as **one of the most significant contribution of mine** to massive star theory: it explains a long-standing problem around modelling in a widely accessible way, and raises people's attention to the fact that *any* set of published data is subject of certain modelling uncertainties.
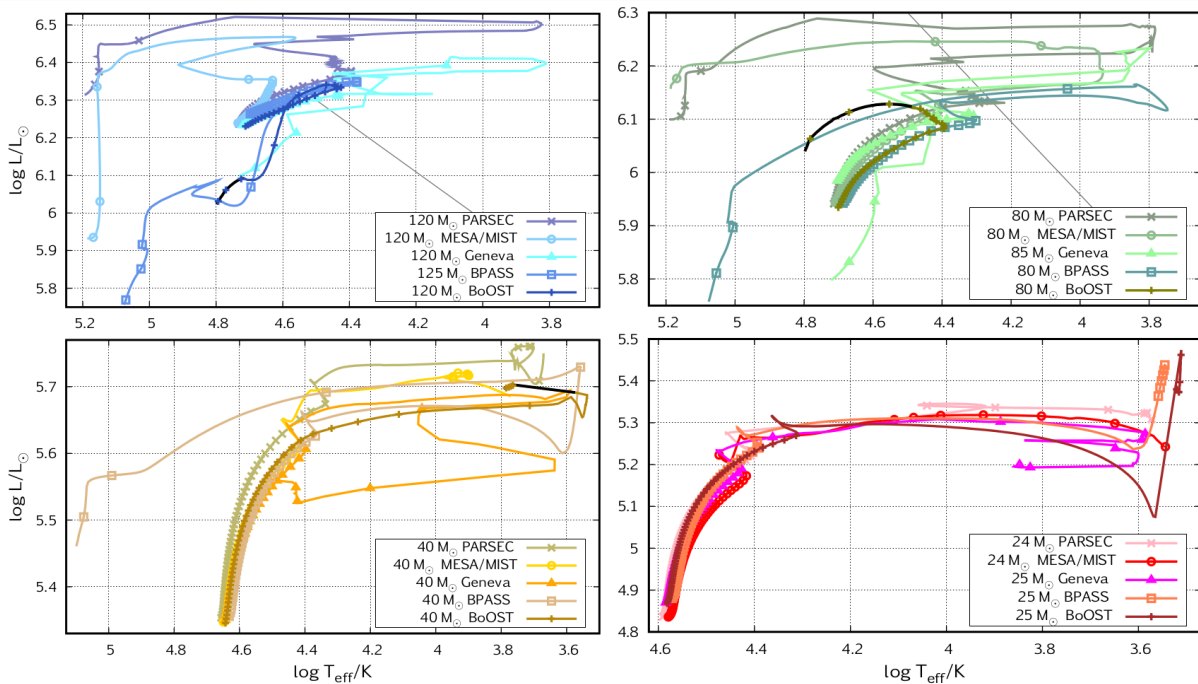
HR diagrams of massive single star models near-solar composition. Figure is reproduced from **Hab2**[23]. Symbols mark every 10^5 yr of evolution. Only the core-hydrogen- and core-helium-burning phases are plotted. Thin grey line marks the observational Humphreys–Davidson limit[97] where relevant. The tracks become more varied with increasing initial mass. This is because the codes apply various treatments for the numerical instabilities associated with the Eddington-limit proximity, leading to a variation of about 20 $M_\odot$ in the remnant masses between the stellar models from various simulations.
- *Based on all this, we warn that gravitational-wave studies need to apply stellar models with caution.*

Most important results.   We present a comparison between five published sets of stellar models from the PARSEC, MIST/MESA, Geneva, BPASS and BoOST/Bonn simulations at near-solar composition, see the panels (page 10). We find that different pragmatic methods adopted by the stellar evolution codes when the Eddington-limit is exceeded inside massive stars can result in up to 18% difference in terms of ionizing radiation coming from stellar populations. Even more alarmingly, the mass of the remaining black hole can vary up to 20 $M_\odot$ between various sets of models (as shown in the figure on the right). These
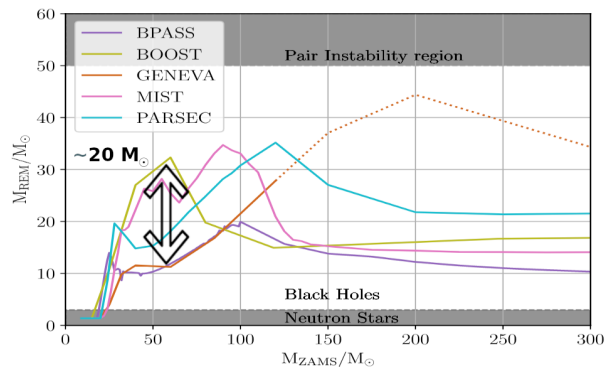

Predicted mass of the remnants. The models apply for Solar metallicity only; at lower metallicities the masses would reach the pair-instability zone (cf. Fig.3 of **Hab2**[23]). ● *The discrepancy between the model sets can be as large as 20 $M_\odot$.*

differences are important, as they can lead to strikingly different results when translated into stellar populations – such as when accounting for gravitational-wave event rates.

(**Hᴀʙ3**)   **Szécsi**, D. and Wünsch, R.: *Role of supergiants in the formation of globular clusters*, ApJ 871, 20 (2019). [ADS] [arXiv:1809.01395] – 21 pages.

Quick overview.   This is an interdisciplinary accomplishment that combines, for the first time, state-of-the-art massive star evolution with cluster hydrodynamics simulations. The result is a fully developed model for the formation of globular clusters. We drew an unprecedentedly complex picture about these clusters. In particular, we uncovered how and why **supergiants could be responsible** for the observed abundance anomalies. The paper was very well received by both of the relevant communities, and I am currently working on follow-up studies that rely on the methods presented here.

How it fits into my Habilitation.   The paper uses my metal-poor massive star models (and populations) published in **Hᴀʙ1**. Some of these stars go on to become black holes and neutron stars (cf. **Hᴀʙ2**), e.g. progenitors of gravitational waves in these clusters. Therefore, these stars' role in the cluster formation process needs to be understood.
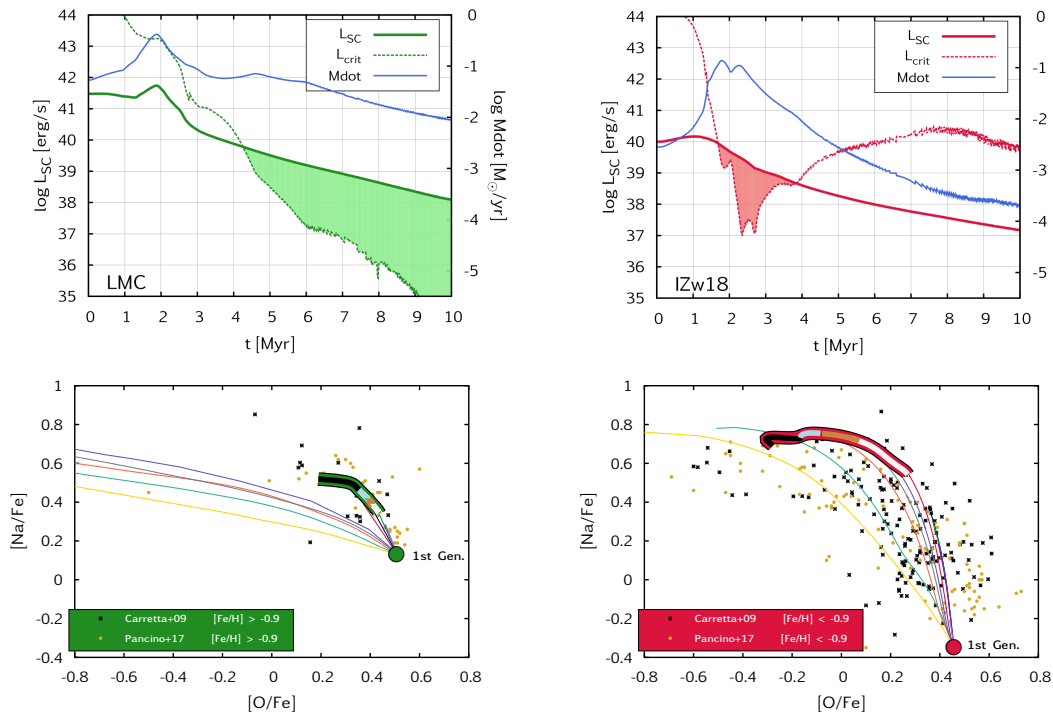
My theory explaining globular cluster formation using state-of-the-art models of metal-poor massive stars. Figure is an updated version from **Hᴀʙ3**[13]. ● *Top:* Time evolution of the cluster wind for two initial compositions: a higher-metallicity one of the Large Magellanic Cloud (LMC) and a low-metallicity one of a dwarf galaxy I Zwicky 18. Whenever the cluster wind luminosity L_{SC} exceeds the critical luminosity L_{crit}, wind-mass accumulates into the cluster center (these phases are marked with shading). In the low-Z cluster, mass accumulation happens early on: before the first supernovae explode at 4 Myr, providing a "window" for undisturbed formation of the second generation. ● *Bottom:* Surface composition of GC stars, showing anticorrelations between oxygen and sodium. Observational data is taken from the FLAMES-UVES survey[98] and *Gaia*/ESO-UVES survey[94]. Observational error is typically between $0.05-0.12$ dex. Overplotted are the theoretical predictions from my scenario. Mass accumulated in the cluster center has a composition shown by the thick line. The four colored stripes (black, blue, brown and white) mark the four quadrants of the total mass (i.e. every 25%, starting with the black and ending with the white). Thin lines show the surface composition of the original stellar models during all their evolution; the accumulated mass may mix with the original gas in the center. My scenario is able to explain the whole spread, and even the trend of the measurements. More technical details are given in my **Hᴀʙ3** paper[13].

My role.   I was the PI of this study, responsible for computing and maintaining stellar models, in charge

of the observational comparisons, as well as the drawing of scientific conclusions and the presentation of the work. My co-author, R. Wünsch provided the semi-analitical cluster simulations, and helped with interpreting the outcome.

Most important results.   We find that the strong winds of the first generation of massive stars collide, get shocked, cool down, and fall into the cluster center[99–102]. Here the second generation of stars form from the mixture of the wind-material and the pristine gas, also with a regular mass function. The results are shown in the panels below (page 11). The most important contribution is coming from the luminous supergiants at low metallicity: which means that the whole star-formation process takes place *before* the first supernovae explode – note that many of these metal-poor massive stars fall into black holes directly without an explosion.

(**Hab4**)   **Szécsi**, D., Mackey, J. and Langer, N.: *Supergiants and their shells in young globular clusters*, A&A 612, A55 (2018). [LINK] [arXiv:1711.04007] – 13 pages.

Quick overview.   New scenario to explain how stars of anomalous composition may have formed in ancient globular clusters. This scenario predicts that low-mass stars with anomalous surface abundances were formed in *photoionization-confined shells* around massive supergiants. It was the first time that metal-poor supergiant models were suggested as a source of abundance anomalies in globular clusters.

How it fits into my Habilitation.   Similarly to **Hab3**, here I attempt to build a theory of how globular clusters could have formed, under the influence of metal-poor massive stars from my simulations. However, in this case I suggest another possible scenario (which is actually not contradicting **Hab3** but can be combined with it): the so-called PICO shell theory. PICO stands for *photoionization-confined*: such a shell is **found around the famous close-by supergiant, Betelgeuse**[103]. We simulate a shell like that around a metal-poor supergiant (see the figure on page 12), and find that it becomes unstable against gravitational collapse on a short enough timescale to form new stars. The composition of the shell **fits that of second generation stars observed in globular cluster**. This is a very unique and exciting theory, if a bit hard to prove or disprove in lack of seeing any those early supergiants (they are obviously dead now, we only see the old, low-mass stars in globular clusters). While I elaborated on my globular cluster theories later on in **Hab3**, I consider this an important contribution too, especially since the central supergiants would form black holes and thus potentially contribute to gravitational-wave emissions coming from globular clusters.
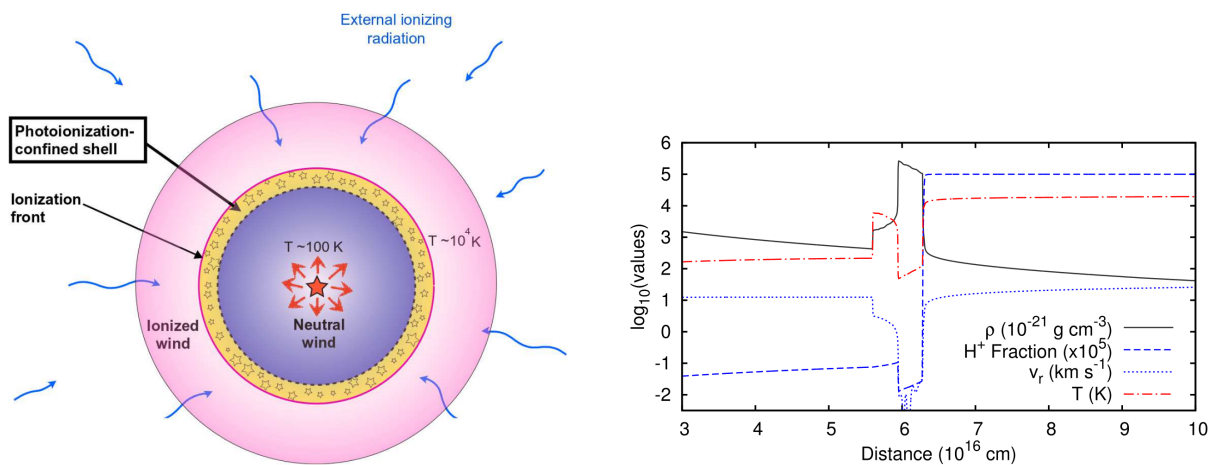
Photoionization-confined (PICO) shell around a metal-poor supergiant. *Left*: theoretical set-up. *Right*: simulation results.

My role.   I was the PI of this study. I computed the stellar evolutionary models of the supergiants on which the simulation of the photoionization-confined shell relies. I performed all the observational

comparisons, and derived the scientific conclusions.

Most important results.   The figure on page 12 shows both the theoretical set-up and the simulation results of a PICO-shell around one of my metal-poor massive star models. The ionization is provided by the hot, chemically-homogeneously evolving stars (so-called TWUIN stars, the topic of **Hᴀʙ5**). Our simulation shows that a dense and long-lived shell develops at the ionization front composed of the stellar-wind material of the central supergiant. The distance of the shell from the central star is 0.02 pc ($6 \cdot 10^{16}$ cm). The central supergiant itself has a radius of 5000 $R_\odot$, 170 times smaller than the sphere of the shell. We show in the paper that the shell becomes unstable, and possibly forms new stars of solar and sub-solar mass, the chemical abundance patterns of which fits those observed in globular clusters.

(**Hᴀʙ5**)   Kubátová, B.; <u>Szécsi</u>, D.; Sander, A. A. C.; Kubát, J.; Tramper, F.; Krtička, J.; Kehrig, C.; Hamann, W.-R.: *Low-metallicity massive single stars with rotation. II. Predicting spectra and spectral classes of chemically homogeneously evolving stars*, A&A, 623, A8 (2019). [LINK] [arXiv:1810.01267] – 33 pages.

Quick overview.   Synthetic spectra of a broad set of chemically-homogeneously evolving hot stars (so-called TWUIN stars) are presented at low-metallicity, computed with the PoWR stellar atmosphere code. Spectral classification of these predicted stars are performed. We conclude that extremely hot, early-O type stars in a low-metallicity galaxies could be the result of chemically-homogeneous evolution, and might therefore be progenitors of gravitational-wave emitting compact-object mergers.
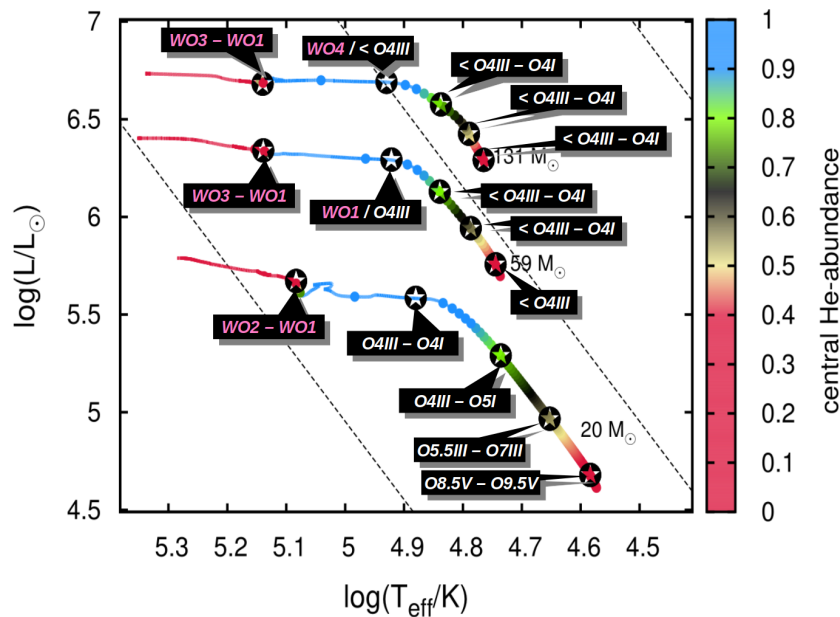
HR diagram of the stellar models for which synthetic spectra was computed with the PoWR code in **Hᴀʙ5**. Figure is based on the one in **Hᴀʙ5** [104] but updated to show the final result of the spectral classification (cf. Table 4 of the paper). Chemically-homogeneously evolving stars are indeed "TWUIN stars" during most of their lives: meaning, now we know, hot O-type stars of early class. Only in their post-main-sequence phase they become Wolf–Rayet stars with emission lines: and of WO type at that, instead of WC as previously thought. • *In other words, gravitational-wave progenitors are predicted to show up as early O stars most of their lives, and only develop Wolf–Rayet features (including high He II ionizing emission) in the last 10% of their lifetimes.*

How it fits into my Habilitation.   TWUIN stars (Transparent Wind Ultraviolet INtense stars) are a special object predicted by my metal-poor stellar models. These stars are candidates for gravitational-wave progenitors. While I showed in my PhD, based on simplictic estimates, that **these stars are in fact *not* Wolf–Rayet stars** despite them being hot and located exactly at the same place in the HR-diagram, a more conclusive study with a more precize technique was necessary to support this statement. **As**

a post-doc therefore, I forged a new collaboration with experts in stellar atmosphere modelling. The result is this paper. We simulate the complete spectrum of TWUIN stars predicted by my evolutionary models. We analyse their line features, provide information on their ionizing radiation, and classify them according to the standard approach.

My role.   I share first authorship with B. Kubátová. While I designed the project and provided the models that consist the basis of the whole study, she created the synthetic spectra with the PoWR code, which we then analysed together. We derived conclusions and wrote the paper as a joint effort. I am proud of **building such a close and fruitful collaboration with experts outside of my field**: although similar at first glance, stellar evolutionary modelling and stellar atmosphere modelling are *very* different techniques with different jargon and different ways of thinking. I consider this paper a crucial piece or research in my overall habilitation goal of understanding metal-poor massive stars – and, especially, the gravitational-wave progenitors amongst them.

Most important results.   We find that the simple estimate about chemically-homogeneously evolving stars having transparent winds is more or less correct: during the main-sequence (i.e. core-hydrogen burning) phase **TWUIN stars *look like* very hot O-stars** of some early class (taking into account the uncertainties around mass loss). On the other hand, during the post-main-sequence (core-helium burning), but only then, they would indeed look like Wolf–Rayet stars – although **of type WO, not WC**, as commonly assumed before.

As chemically-homogeneously evolving stars are theoretical progenitors of **gravitational-wave emission**[18,3], predicting what they look like during their lives is a key contribution to the field. Future observational campaigns can now specifically search for these stars in e.g. local dwarf galaxies.

## IV.   CONCLUSIONS: A PIONEER APPROACH IN MY FIELD

Due to the research I carried out in **Hab1–5**, it is now possible to combine information from gravitational-wave detections with star-cluster formation, stellar archeology and even gamma-ray burst research. This is done by the inventive computational tool I developed, described below. Since obtaining any kind of *direct* observational evidence of metal-poor massive stars is extremely difficult, my approach of combining pieces of *indirect* evidence is more than just practical: it constitutes an outstanding contribution to the field of astrophysics.

My own population synthesis queue: *PopSy*

Having won an NCN OPUS grant to build my own research group, I have incorporated all my habilitation achievements (**Hab1–5**) into a unified framework, the so-called *PopSy* queue, so that my group can apply it in various research cases (cf. Sect. 7/a). The *PopSy* queue is basically a multi-purpose population synthesis tool. The cartoon on page 15 shows its setup. The queue fulfils the following three requirements:

- First, the **stellar models** need to have high enough resolution and in a flexible way so that the right physical ingredients can be explored.

- Second, the stellar populations need to be **synthesised in a special way** to account for *both* their lives and their deaths while retaining flexibility – a highly non-trivial job, as anyone who has attempted to create such populations would attest[39,70,71,24].

- And third, one needs specific codes via which these populations can be used in the various **observational studies** – so that actual scientific conclusions can be drawn.

I have all three assets in the *PopSy* queue. While a few other groups in the world have similar tools, **no one has it the exact way I do**: my queue has been uniquely designed to work in cluster-formation (both globular and YMC) *and* gravitational-wave / gamma-ray burst research *in the same time* – and, importantly, it is flexible, as explained below.
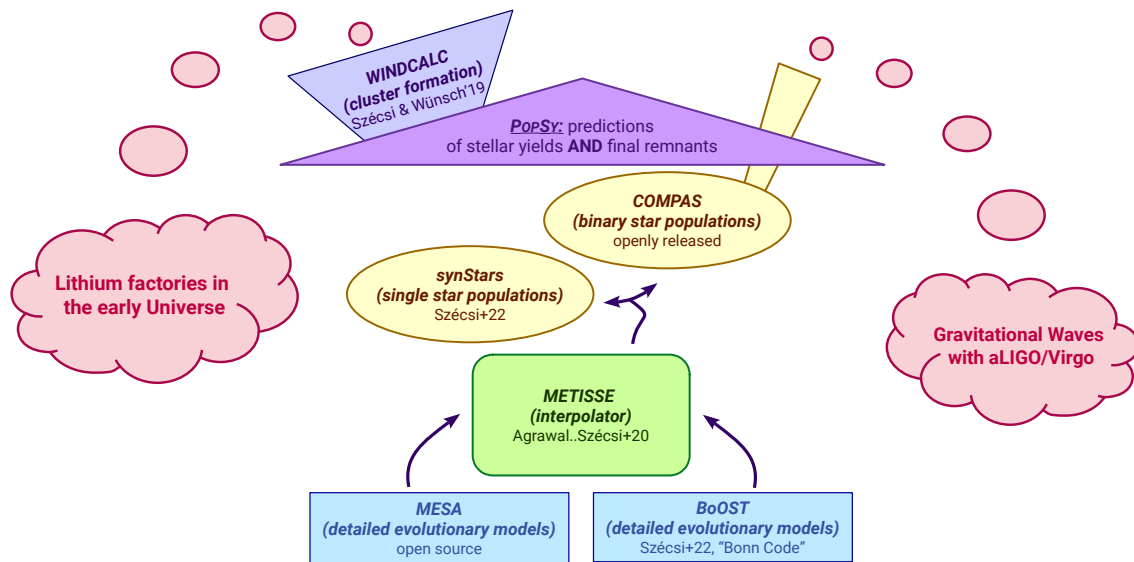
*Design of the PopSy queue, the population synthesis (& application) method which incorporates my habilitation achievements (**Hab 1–5**) into one unified computational framework.*

It will be used by my newly established OPUS research group in Toruń (see Sect. 7/a on my future plans).

The central building block is the interpolator tool *Metisse*, created by my ex-student (now post-doc) P. Agrawal[71]. The capabilities of *Metisse* allow the user to feed in any MESA-models as well as models from other codes such as the Bonn Code. The output of *Metisse* is a carefully interpolated set of stellar tracks which **preserve the detailed properties of both the living stars *and* the remnants**.

Having such a set of tracks, the *PopSy* queue's next step is to perform population synthesis. For single stars, it is done with the simple population synthesis tool *synStars* (published in Szécsi+22[29]). For binaries, the Compas code will be used[43–46,6,7]. In fact, the *Metisse* pipeline has beed specifically optimized to work with Compas.

Thus the *PopSy* queue provides me with synthetic populations – of either single or binary stars – which I can **directly apply** in globular cluster research via the method developed in Szécsi & Wünsch'19[13] (called WINDCALC, now an integral part of the queue), as well as, since I am using Compas, in gravitational-wave research.

A big advantage of my method is its ***flexibility***: any new grid of models can be computed with MESA (or other codes), and converted into synthetic populations. Another big advantage is its multi-purposeness: the *PopSy* queue's outcome delivers ***simultaneously*** the detailed isotopic abundance yields (e.g. lithium & other elements) and the remant mass statistics (to be tested against aLIGO/Virgo and upcoming GW-detections).

But the biggest advantage is that via *PopSy*, I can test the same theoretical stellar populations against several, ***completely independent*** observational phenomena. Whatever I learn from one observational comparison, can be straight away tested in the others: so anything I figure out about the physics of massive stars, can be directly converted back into models via the *PopSy* queue, and re-implemented into *the rest of* the sub-projects.

This means that with *PopSy* I can design various future tests (e.g. from cosmology or from dwarf galaxies or from gamma-ray burst research) to study the nature of metal-poor massive stars. In Sect. 7/a, I overview the research I am planning to carry out with my OPUS group in the coming years.

> **In conclusion, my habilitation achievements uncovered the roles that gravitational-wave progenitors – that is, metal-poor massive stars – played/play in various places of the Universe. While doing this, I have significantly expanded our understanding of the physics of these objects, pioneered new and unique pathways to study such exotic stars, and built bridges between various subfields of astrophysics.**

5. Presentation of significant scientific activity carried out at more than one university, scientific or cultural institution, especially at foreign institutions

2.5 years	**Alexander von Humboldt Individual Research Fellow**, *University of Cologne, Germany*, 04.2019 – 09.2021.
1.5 years	**Research assistant (PD)**, *Institute of Gravitational Wave Astronomy and School of Physics and Astronomy, University of Birmingham, UK*, 10.2017 – 03.2019.
1 year	**Research assistant (PD)**, *Astronomical Institute of the Czech Academy of Sciences*, 08.2016 – 09.2017.
3 months	**Post-doctoral Fellow**, *Argelander-Instutut für Astronomie of the University Bonn, Germany*, 04.2016 – 07.2016.
3 months	**Research assistant**, *Konkoly Observatory of the Hungarian Academy of Sciences*.
4 years	**Intern**, *Non-paid research internship at the Hungarian research group OTKA-77795*.

6/a. Presentation of teaching achievements

summer semester 2022	**Gravitational-wave progenitors**, *Special ('monographic') lecture at the Master in Astronomy program (3 ECTS)*, Nicolaus Copernicus University, Link to curriculum.
2021 –	**Currently supervising <u>two PhD students</u> in Toruń**, *R. Sarwar, H. Stinshoff*, Acting as primary advisor. Astronomica Copernicana Grad-School, NCU, Toruń.
2018 – 2021	**External PhD supervisor**, *of Dr. Poojan Agrawal*, Swinburne University of Technology, Australia, Date of successful defence: 24/11/2021. *Now holding a PD researcher position at the University of North Carolina at Chapel Hill, USA.*
2020 – 2021	**Scientific Writing in Astrophysics**, *Self-developed special lecture for PhD and Master students*, University of Cologne, Germany & Nicolaus Copernicus University, Poland, Link to curriculum.
2017 – 2018	**Two Master students at the University of Birmingham**, *N. Bennett, S. Ratcliff*, Date of successful defence: May 2018.
2013 – 2014	**Teaching Assistant**, *Master's class 'Stellar Structure and Evolution'*, University of Bonn, Germany, Winter Semester 13/14.
IFS-Mentoring	**Mentoring Program for International Female Scholars (IFS)**, *participating regularly as a Mentor*, current mentee: A. Baby (Uni Köln), previous mentee: A.M. Babaei (Uni Köln), Link.

6/b. Presentation of organizational achievements

Grant management	**Principal Investigator of the NCN grant OPUS 2021/41/B/ST9/00757**, *Starting date: 01/02/2022*, People paid from the grant: 2 (one PD researcher and one PhD student).
Group leader	**Newly established 'Gravitational-wave progenitors' group in Toruń**, *Current group positions: two PhD students (H. Stinshoff, R. Sarwar), one PD researcher (K. Sen), one paid intern (Sz. Żywica), Past member: PD fellow (Á. Szabó).*
Workshop at EAS 2021	**Early Career Astronomers & their supporters**, *Senior SOC member*, Date of workshop: 28.06.2021, Website and program.

Conference 'MathFiz'	**'Actual Problems in Mathematics and Physics 2021'**, *SOC member*, Date of conference: 26.08.2021, Website and program.
Conference 'MOBSTER-1'	**MOBSTER-1 2020 Conference on Magnetism in Massive Stars**, *VOC (Virtual Organizing Committee) member*, Date: 13-17 July 2020, Website and program.
Journal Club	**Main organizer, 2016-2017**, *Interdepartmental monthly meeting of the Astronomical Institute of the Czech Academy of Sciences.*
Chair of S11 at EWASS 2017	**Symposium 11 at the European Week of Astronomy and Space Sciences (EWASS)**, *Chair and main organizer*, Date: 26-27 June 2017, Website and program.

6/c. Achievements in popularizing science

Telescope night	**Presenting Moon and planets with a 102/500mm Rich Field Refractor (80x)**, *Public event*, 12 Aug 2021, Budapest, Hungary.
Astronomy on Tap Köln	**How big are stars?**, *Outreach talk on Youtube Live*, 5 Nov 2020, Organized by the 'Astronomy on Tap Köln' community, Link to video.
Astro in the City Birmingham	**How big are stars?**, *Outreach talk organized by the University of Birmingham, 17 Oct 2018, Birmingham, United Kingdom*, Presentation.
Girls in STEM Talk	**A tale of Super Giant Stars and Shells**, *Talk at 'Girls in STEM' Open Day*, 12 Sep 2018, Birmingham, United Kingdom, Link to presentation.
Outreach Article	**Who lives in Globular Clusters?**, *Public outreach article in Hungarian. Published in 'Élet és Tudomány' (in print, October, 2018).*
Public talk Budapest	**Starforming supergiant shells**, *Outreach talk given at: Polaris Public Observatory, 6 Feb 2018, Budapest, Hungary*, Presentation.
Outreach Article	**A new method for measuring the expansion of the Universe**, *Public outreach article published (in Hungarian): csillagaszat.hu & index.hu (May 2010).*
Outreach Article	**Jitter radiation causes gamma-ray bursts?**, *Public outreach article published (in Hungarian): csillagaszat.hu & index.hu (January 2010).*

7/a. Current group activities and future plans

As an NCN OPUS grant holder, I am now continuing my research activities as a group leader. Below I discuss the current scientific goals of my young group in Toruń.

Testing massive star physics againt GW-detections

Now that the gravitational-wave detector systems aLIGO/Virgo operate at an ever increasing efficiency[80,22,105] and new detectors are being added to the network[106,107], it is of crucial importance that the observed gravitational-wave event rates are matched by the most up-to-date stellar physics as in e.g. the 'Bonn' models (**Hab1**) or Mesa.

Indeed, it has been shown that chemically-homogeneously evolving TWUIN stars (cf. **Hab5**) can lead to gravitational-wave emissions in a binary[16–19,108]. Additionally, the presence of luminous supergiants (as predicted in metal-poor stellar evolution[10], cf. **Hab3/4**) can also influence merger rate predictions significantly[57] due to these stars possibly undergoing common envelope evolution with their companions. With PopSy, both of these scenarios can be tested.
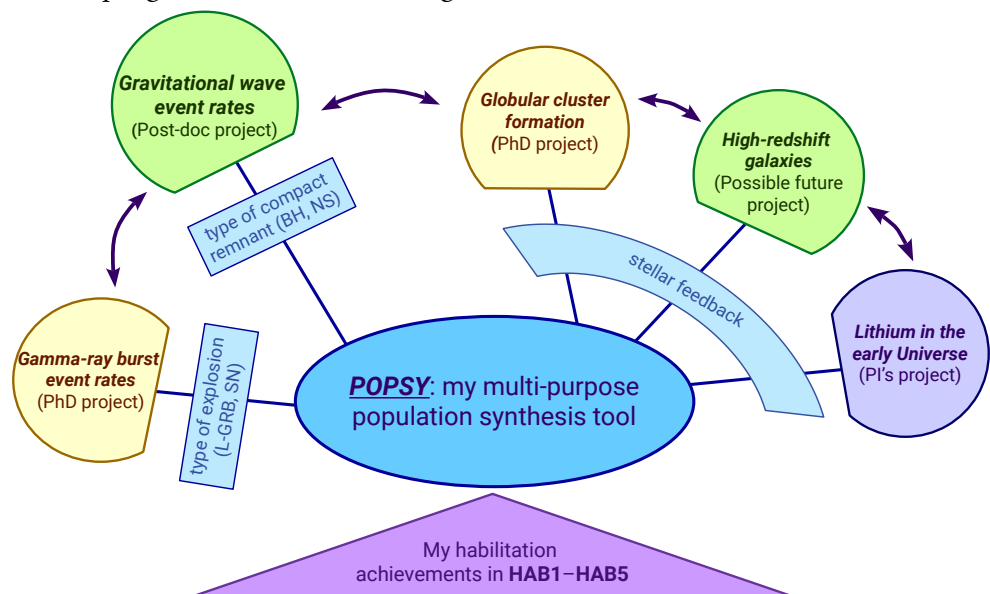
Relying on the flexibility of the *PopSy* queue, newly created Bonn/BoOST and Mesa models can be added to it over and over again. One of the biggest uncertainties in massive star evolution, mass-loss,

can be investigated this way, by creating model sets with various mass-loss rate prescriptions and comparing them to each other, as well as to aLIGO/Virgo detections. Also, we can test the effect of other relevant sources of uncertainty (e.g. mixing processes such as convection and semi-convection[95,109], and their role in the physical stablity of the stars near the Eddington-limit[110–112]; or magnetic fields[42]). This flexibility is what makes our work extremely beneficial for the scientific community. Additionally, adding new Mesa models with fast-rotation will come in handy when accounting for gamma-ray bursts, as follows.

Gamma-ray bursts and supernovae: final fate predictions

To achieve this goal, we are **developing a new tool *FINFAT*** to automatically decide what kind of *final fate* a given star in the population is expected to undergo. This includes various types of supernovae (e.g. regular core-collapse, electron-capture, pair-instability, pulsational pair-instability etc.) with estimates about their explosion energy and approximate ejecta mass – following the preparatory work I have done[113,11] and leaving room for future updates[78,114,115,113,116–118,11,21]. While this will be extremely beneficial for all those who need **supernova feedback predictions** from my models, I want to pay a special attention to an important, yet not widely accounted for phenomenon: long-duration gamma-ray bursts, of which the progenitors are fast rotating massive stars (TWUIN stars, **Hab5**).

If a massive star forms an iron-core, nuclear fusion cannot maintain its stability anymore: it collapses and falls in due to gravity. Normally, the outer layers bounce back from the surface of the newly-forming neutron star (this initiates a core-collapse type supernova explosion). However, if the core is compact enough to form a black hole directly, the super-

nova is said to 'fail' and the material falls right into the black hole[119]. If the progenitor star was rotating fast (such as in some of my chemically-homogeneously evolving metal-poor models, the so-called TWUIN stars, cf. **Hab5**), we can have a set-up where **the black hole is fed by the infalling material while the polar regions are emptied out, forming two jets (the so-called 'collapsar')**. In the near-vacuum of the jets, the particles that are accelerated to relativistic speeds emit syncrotron radiation. Therefore, in case the jet is directed towards us, we may observe a (long-duration) gamma-ray burst[4]. In practice, to decide whether a given stellar model is the progenitor of such a burst is done by analysing its internal angular momentum[25]. Short-duration gamma-ray bursts on the other hand are **associated with gravitational-wave emitting compact object mergers**[3]: in case there is barionic material in the system during the merger, it may be accelerated to relativistic speeds, and we may observe it as a shorter (but spectrally harder) gamma-ray burst event.

The cosmic rate of gamma-ray bursts has been predicted with this method using single stars[25] and tide-influenced binaries[120]; but such a prediction with accurate, rotating stellar models is a necessarily outcome of our binary populations with PopSy. Thus, the project will allow my research group to contribute to the **blooming field of gamma-ray burst progenitors** with our important new results.

Binary stars in globular clusters

Massive interactive *binary* stars have been shown to possibly contribute to the anomalous element ratios in globular clusters [121,122] in case their mass-transfer is non-conservative. Nonetheless, no comprehensive population synthesis study has ever been performed to test this scenario. With my habilitation achievements, I am in the best place to do this, since *PopSy* allows me to create binary populations with complex chemical networks included.

Moreover, **I have the cluster-code *WINDCALC* at my disposal.** *WINDCALC* is a semi-analytic code that simulates the thermodynamic conditions in young massive clusters, and predicts the composition of the newly forming stars. This is the code I used in **Hab3** to study the role of – single – supergiants [13].

Having complex binary populations from *PopSy* available, I can apply them right away in *WINDCALC*. This may lead to the realization that – as I tend to suspect due to the lack of detection of such luminous supergiants [123,109] in currently forming young clusters – instead of single massive stars with strong winds, it is massive interactive binaries with non-conservative mass transfer that are responsible for the formation of globular clusters.

Lithium factories of the early Universe

Measurements of lithium abundance in old halo stars seems to have a constant value: the so-called **Spite-plateu** at around $A(Li) \sim 2.2$. The stars in the plateau are *quite close to* primordial (second or third or fourth – anyway very early [124–126] – generation; also called 'pop-II' stars), while their ^7Li content has always thought to come from the Big Bang nucleosynthesis.

The problem however is that researchers constantly find a factor-of-3 discrepancy between what is measured in old stars and what is predicted from the Big Bang nucleosynthesis (namely, $A(Li) \sim 2.7$). This is called the **"cosmic lithium problem"** [127–131] which has long been motivating researchers to look beyond the Standard Model and come up with various exotic alternatives [132–136].

But these close-to-primordial stars in the plateau are *not* the first stars. They do already contain *some* heavy elements. Which means that their composition has been influenced by previous generations of (metal-poor and/or metal-free) massive stars.

Massive stars are known to be one of the most effective chemists in the Universe [1]. Yet hardly anyone considered them to be lithium factories before, the consensus mistakenly being that they are *obviously* too hot to preserve this fragile element. But what if the consensus is wrong? In fact, **my simulations show that this might indeed be the case**.

My fiducial simulations were created with the Bonn Code and published in **Hab1** [137,10,24]. To double check, we run another set of simulations with MESA [35–37] using similar input physics. With both codes, we found that ^7Li is being *produced* under certain circumstances during the life of the star, and in a large amount.

If massive stars are able to produce lithium during their lives, this means they could be responsible – partly or wholly – for the Spite-plateau*. First, they of course destroy the primordial lithium because they are, well, hot. ***But then they re-create some of it*** via the newly discovered process and – as they do with countless other elements – eject it into their surroundings where subsequent generations of stars can form.

If so, the pop-II stars that constitute the Spite-plateau may not be a good way to estimate the baryonic density of the Universe [139] and should not be used as direct constrain to the Standard Model – perhaps metal-poor massive stars can solve the cosmic lithium problem instead? With all the tools I now possess due to my habilitation achievements (**Hab1-5** & the *PopSy* queue), I hope to soon figure out.

---

*Additionally, some globular clusters display intriguing values of lithium [138] too, which motivates me to study the origin of Li^7 further.

## 7/b. Description of research not included in Section 4.

- **Szécsi**, D., Bagoly, Z., Kóbori, J., Horváth, I., Balázs, L.G.: *Direction dependent background fitting for the Fermi GBM data*, A&A v.557, A8 (2013). [LINK] [arXiv:1306.3812] – 16 pages.

Overview. This paper presents **my own data reducing technique** which allows one to analyise the data collected by gamma-ray satellites in an accurate way.

I was PI of this A&A article as a Master student (in Hungary), so it is a completely independent achievement both from my PhD (in Germany) and from my Habilitation papers.

The technique is original and inventive. As an undergrad, I wanted to study the lightcurve and the physical properties of gamma-ray bursts and do statistical analyses on them. However, it soon became clear that the data contains a systematic background noise. I realized that the noise originates from the proper motion of the satellite. There were no computational tools available at that point to filter it out. **So I invented one.** The figure on page 20 shows the results: my own data reducing technique to make gamma-ray burst observations more reliable.

Most important results. I analysed the complex motion effects of the *Fermi* satellite, and as a result, I developed a new data-filtering method called 'direction dependent background fitting'. I wrote a code to fit the data with a high-order hyper-surface (see the figure) that takes the orbital parameters of the satellite's 3D-position into account.
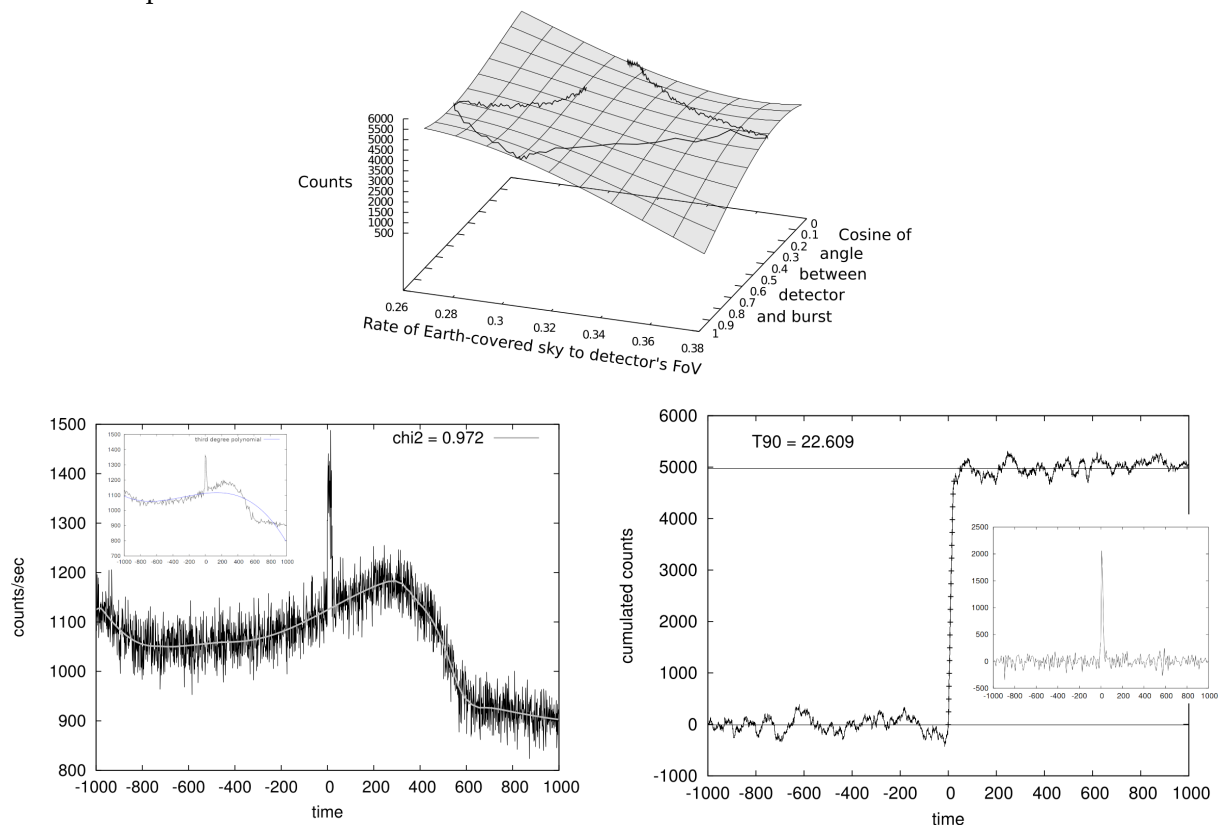
Example of how my data reduction technique works. The data (lightcurve in the *bottom left* panel showing photon counts as a function of time in seconds) sometimes contain a systematic background which is impossible to model with a simple polynomial fit (the traditional method before my paper, shown in the *embedded* panel). After realizing that the source of the background is associated with the celestial direction of the satellite, **I defined a hypersurface based on the proper motion parameters (*top* panel) and fit *that* on the data instead of a polynomial**. The white line overplotted on the lightcurve shows this fit: it follows all the background variations perfectly. After removal, we arrive to the panel on the *bottom right*: embedded figure shows the background-removed lightcurve, while the photon count is measured and the duration value ($T_{90} = 22.6$ s) is derived from the cumulative plot. This particular example is for the *Fermi* burst GRB091030.613 but the method is automatic and has been applied for many other events. • *The paper and the data reducing method is an independent achievement from both my PhD and my Habilitation activities.*

7/c. Other information: grants, prizes, fellowships & awards

Description and Funding Source	Amount	Date / Period
OPUS research grant awarded by the National Science Centre, Poland (NCN) – *sponsoring: PI, PhD & PD positions for 4 years*	**1.446.310 PLN** $\approx 300.000\ EUR$	Febr. 2022 – Jan. 2026
PhD position supervised at the grad. shool Academia Copernicana, supported by the Center of Excellence Astrophysics and Astrochemistry	$\approx 60k\ PLN/yr \times 4$: $\approx 52.000\ EUR$	Jan. 2022 – Dec. 2025
Humboldt 'Return' Fellowship offered by the Humboldt Foundation, Germany	**6.500 EUR**	Apr. 2022 – March 2023
Humboldt Individual Research Fellowship offered by the Alexander von Humboldt Foundation	**104.100 EUR**	Apr. 2019 – Sept. 2021
Jan Frič Premium for Young Researchers awarded by the Astronomical Institute of the Czech Academy of Sciences	80.000 CZK $\approx$ **3.100 EUR**	year 2017
Honours Branch (H2) Scholarship of the Bonn-Cologne Graduate School (BCGS) of Physics and Astronomy	**12.400 EUR**	Oct. 2013 – July 2016
PhD Fellowship offered by Alexander-von-Humbold-Professor N. Langer	**71.700 EUR**	Sept. 2012 – March 2016
Erasmus exchange scholarship offered by Eötvös University, Budapest and Wuppertal University, Germany	**1.733 EUR**	Oct. 2011 – Febr. 2012
First prize of Young Researcher's National Competition in Hungary	–	29 April 2011

REFERENCES

[1] N. Langer. *ARA&A*, 50:107–164, September 2012.

[2] D. Garcia, ..., **Szécsi** et al. *Experimental Astronomy*, 51(3):887–911, June 2021.

[3] D. **Szécsi**. *Contributions of the Astronomical Observatory Skalnate Pleso*, 47:108–115, July 2017.

[4] D. **Szécsi**. *Proceedings of Science, PoS(MULTIF2017)065, 2017*, October 2017.

[5] N. Bastian and C. Lardo. *Annual Review of Astronomy and Astrophysics*, 56:83–136, sept 2018.

[6] Neijssel, Vigna-Gómez, ..., et al. *MNRAS*, 490(3):3740–3759, December 2019.

[7] Stevenson, ..., **Szécsi**, et al. *ApJ*, 882:121, September 2019.

[8] F. Tramper, G. Gräfener, O. E. Hartoog, et al. *A&A*, 559:A72, November 2013.

[9] M. Garcia, A. Herrero, F. Najarro, et al. *MNRAS*, 484:422–430, March 2019.

[10] D. **Szécsi**, N. Langer, S.-C. Yoon, et al. *A&A*, 581:A15, September 2015.

[11] D. **Szécsi**. *The Evolution of Low-Metallicity Massive Stars*. PhD thesis, Mathematisch-Naturwissenschaftlichen Fakultät der Universität Bonn, July 2016.

[12] D. **Szécsi**, J. Mackey, and N. Langer. *A&A*, 612:A55, April 2018.

[13] D. **Szécsi** and R. Wünsch. *ApJ, Vol. 871, nr. 1*, 2019.

[14] D. **Szécsi**, N. Langer, D. Sanyal, et al. In *Proceedings of Wolf-Rayet Stars Workshop, Potsdam, Germany, p.189*, 2015.

[15] Kubátová & **Szécsi** et al. *A&A*, 623:A8, March 2019.

[16] S. E. de Mink, M. Cantiello, N. Langer, et al. *A&A*, 497:243–253, April 2009.

[17] S. E. de Mink and I. Mandel. *MNRAS*, 460:3545–3553, August 2016.

[18] I. Mandel and S. E. de Mink. *MNRAS*, 458:2634–2647, May 2016.

[19] P. Marchant, N. Langer, P. Podsiadlowski, et al. *Astronomy & Astrophysics*, 588:A50, April 2016.

[20] J. J. Eldridge and E. R. Stanway. *MNRAS*, 462:3302–3313, November 2016.

[21] D. R. Aguilera-Dena, N. Langer, T. J. Moriya, and A. Schootemeijer. *ApJ*, 858:115, May 2018.

[22] The LIGO Scientific Collaboration, the Virgo Collaboration, B. P. Abbott, et al. *Phys. Rev. D*, 100(2):024017, July 2019.

[23] Poojan Agrawal, Dorottya Szécsi, Simon Stevenson, et al. *MNRAS*, 512(4):5717–5725, June 2022.

[24] Dorottya **Szécsi**, Poojan Agrawal, Richard Wünsch, and Norbert Langer. *A&A*, 658:A125, February 2022.

[25] S.-C. Yoon, N. Langer, and C. Norman. *A&A*, 460:199–208, December 2006.

[26] S.-C. Yoon, A. Dierks, and N. Langer. *A&A*, 542:A113, June 2012.

[27] I. Brott, S. E. de Mink, M. Cantiello, et al. *A&A*, 530:A115, June 2011.

[28] K. Köhler, N. Langer, A. de Koter, et al. *A&A*, 573:A71, January 2015.

[29] Dorottya Szécsi, Poojan Agrawal, Richard Wünsch, and Norbert Langer. *A&A*, 658:A125, February 2022.

[30] M. Kourniotis, R. Wünsch, S. Martínez-González, et al. *MNRAS*, 521(4):5686–5698, June 2023.

[31] Natalia Lahén, Thorsten Naab, Guinevere Kauffmann, et al. *MNRAS*, 522(2):3092–3116, June 2023.

[32] A. Romagnolo, K. Belczynski, J. Klencki, et al. *arXiv e-prints*, page arXiv:2211.15800, November 2022.

[33] Sergio Martínez-González, Richard Wünsch, Guillermo Tenorio-Tagle, et al. *ApJ*, 934(1):51, July 2022.

[34] Annika Franeck, Richard Wünsch, Sergio Martínez-González, et al. *Accepted by ApJ*, page arXiv:2201.12339, January 2022.

[35] B. Paxton, L. Bildsten, A. Dotter, et al. *ApJS*, 192:3, January 2011.

[36] B. Paxton, M. Cantiello, P. Arras, et al. *ApJS*, 208:4, September 2013.

[37] B. Paxton, P. Marchant, J. Schwab, et al. *ApJS*, 220:15, September 2015.

[38] J. Choi, A. Dotter, C. Conroy, et al. *ApJ*, 823:102, June 2016.

[39] A. Dotter. *ApJS*, 222:8, January 2016.

[40] P. Marchant, N. Langer, P. Podsiadlowski, et al. *A&A*, 604:A55, August 2017.

[41] Y. Götberg, S. E. de Mink, J. H. Groh, et al. *A&A*, 629:A134, September 2019.

[42] Z. Keszthelyi, G. Meynet, M. E. Shultz, et al. *MNRAS*, 493(1):518–535, March 2020.

[43] S. Stevenson, A. Vigna-Gómez, I. Mandel, et al. *Nature Communications*, 8:14906, April 2017.

[44] J. W. Barrett, S. M. Gaebel, C. J. Neijssel, et al. *MNRAS*, 477:4685–4695, July 2018.

[45] A. Vigna-Gómez, C. J. Neijssel, S. Stevenson, et al. *MNRAS*, 481:4009–4029, December 2018.

[46] F. S. Broekgaarden, S. Justham, S. E. de Mink, et al. *MNRAS*, September 2019.

[47] J. R. Hurley, O. R. Pols, and C. A. Tout. *MNRAS*, 315:543–569, July 2000.

[48] R. G. Izzard, L. M. Dray, A. I. Karakas, et al. *A&A*, 460:565–572, December 2006.

[49] K. Belczynski, V. Kalogera, F. A. Rasio, et al. *ApJS*, 174:223–260, January 2008.

[50] J. J. Eldridge, R. G. Izzard, and C. A. Tout. *MNRAS*, 384:1109–1118, March 2008.

[51] R. G. Izzard, E. Glebbeek, R. J. Stancliffe, and O. R. Pols. *A&A*, 508:1359–1374, December 2009.

[52] I. Brott, C. J. Evans, I. Hunter, et al. *A&A*, 530:A116, June 2011.

[53] M. Dominik, K. Belczynski, C. Fryer, et al. *ApJ*, 759:52, November 2012.

[54] J. J. Eldridge and E. R. Stanway. *MNRAS*, 419:479–489, January 2012.

[55] F. R. N. Schneider, N. Langer, A. de Koter, et al. *A&A*, 570:A66, October 2014.

[56] C. Abate, O. R. Pols, R. J. Stancliffe, et al. *A&A*, 581:A62, September 2015.

[57] K. Belczynski, D. E. Holz, T. Bulik, and R. O'Shaughnessy. *Nature*, 534:512–515, June 2016.

[58] Kruckow, ..., **Szécsi** et al. *Astronomy & Astrophysics*, 596:A58, November 2016.

[59] M. U. Kruckow, T. M. Tauris, N. Langer, et al. *MNRAS*, 481:1908–1949, December 2018.

[60] Vigna-Gómez, ..., **Szécsi** et al. *MNRAS*, 481:4009–4029, December 2018.

[61] Mario Spera, Michela Mapelli, Nicola Giacobbo, et al. *MNRAS*, 485(1):889–907, May 2019.

[62] S.-C. Yoon and N. Langer. *A&A*, 443:643–648, 2005.

[63] S. E. Woosley and A. Heger. *ApJ*, 637:914–921, February 2006.

[64] M. Cantiello, S.-C. Yoon, N. Langer, and M. Livio. *A&A*, 465:L29–L33, April 2007.

[65] F. I. Pelupessy, A. van Elteren, N. de Vries, et al. *A&A*, 557:A84, September 2013.

[66] E. R. Stanway, J. J. Eldridge, and G. D. Becker. *MNRAS*, 456:485–499, February 2016.

[67] N. Ivanova, S. Justham, X. Chen, et al. *A&A Rev.*, 21:59, February 2013.

[68] A. Menon and A. Heger. *MNRAS*, 469:4649–4664, August 2017.

[69] A. Menon, ..., D. **Szécsi**, et al. *MNRAS*, 507(4):5013–5033, November 2021.

[70] Simon Portegies Zwart and Steve McMillan. *Astrophysical Recipes; The art of AMUSE*. IOP Publishing, 2018.

[71] Agrawal, ..., **Szécsi** et al. *MNRAS*, 497(4):4549–4564, October 2020.

[72] J. Puls, J.S. Vink, and F. Najarro. *A&A Rev.*, 16:209–325, December 2008.

[73] B. Šurlan, W.-R. Hamann, A. Aret, et al. *A&A*, 559:A130, November 2013.

[74] N. Smith. *Annual Reviews of A&A*, (52), 2014.

[75] R. Björklund, J. O. Sundqvist, J. Puls, and F. Najarro. *arXiv e-prints*, page arXiv:2008.06066, August 2020.

[76] Andreas A. C. Sander and Jorick S. Vink. *MNRAS*, 499(1):873–892, November 2020.

[77] Jorick S. Vink, Erin R. Higgins, Andreas A. C. Sander, and Gautham N. Sabhahit. *MNRAS*, March 2021.

[78] A. Heger and S. E. Woosley. *ApJ*, 567:532–543, March 2002.

[79] A. Heger, C. L. Fryer, S. E. Woosley, et al. *ApJ*, 591:288–300, July 2003.

[80] B. P. Abbott, R. Abbott, T. D. Abbott, et al. *The Astrophysical Journal Letters*, 818(2):L22, 2016.

[81] B. P. Abbott, R. Abbott, T. D. Abbott, et al. *Physical Review Letters*, 116(6):061102, February 2016.

[82] B. P. Abbott, R. Abbott, T. D. Abbott, et al. *Physical Review Letters*, 116(24):241103, June 2016.

[83] The LIGO Scientific Collaboration, the Virgo Collaboration, B. P. Abbott, et al. *Physical Review Letters*, June 2017.

[84] D. **Szécsi**, Z. Bagoly, J. Kóbori, et al. *A&A*, 557:A8, September 2013.

[85] M. Ajello, M. Arimoto, M. Axelsson, et al. *ApJ*, 878:52, June 2019.

[86] A. Lien, T. Sakamoto, S. D. Barthelmy, et al. *ApJ*, 829:7, September 2016.

[87] J. Hjorth, D. Watson, J. P. U. Fynbo, et al. *Nature*, 437:859–861, October 2005.

[88] N. Kawai, G. Kosugi, K. Aoki, et al. *Nature*, 440:184–186, March 2006.

[89] C. C. Thöne, L. Christensen, J. X. Prochaska, et al. *MNRAS*, 441:2034–2048, July 2014.

[90] O. E. Hartoog, D. Malesani, J. P. U. Fynbo, et al. *A&A*, 580:A139, August 2015.

[91] I. Horvath, D. **Szécsi**, J. Hakkila, et al. *MNRAS*, 498(2):2544–2553, October 2020.

[92] S. F. Portegies Zwart, S. L. W. McMillan, and M. Gieles. *ARA&A*, 48:431–493, September 2010.

[93] S. N. Longmore, J. M. D. Kruijssen, N. Bastian, et al. *Protostars and Planets VI*, pages 291–314, 2014.

[94] E. Pancino, D. Romano, B. Tang, et al. *A&A*, 601:A112, May 2017.

[95] A. Schootemeijer, N. Langer, N. J. Grin, and C. Wang. *A&A*, 625:A132, May 2019.

[96] E. Laplace, Y. Götberg, S. E. de Mink, et al. *A&A*, 637:A6, May 2020.

[97] R. M. Humphreys and K. Davidson. *ApJ*, 232:409–420, September 1979.

[98] E. Carretta, A. Bragaglia, R. Gratton, and S. Lucatello. *A&A*, 505:139–155, October 2009.

[99] S. Silich, G. Tenorio-Tagle, and A. Rodríguez-González. *ApJ*, 610:226–232, July 2004.

[100] R. Wünsch, S. Silich, J. Palouš, et al. *ApJ*, 740:75, October 2011.

[101] S. Silich and G. Tenorio-Tagle. *MNRAS*, 465:1375–1383, February 2017.

[102] R. Wünsch, J. Palouš, G. Tenorio-Tagle, and S. Ehlerová. *ApJ*, 835:60, January 2017.

[103] J. Mackey, S. Mohamed, V. V. Gvaramadze, et al. *Nature*, 512:282–285, August 2014.

[104] B. Kubátová, D. **Szécsi**, A. A. C. Sander, et al. *A&A*, 623:A8, March 2019.

[105] The LIGO Scientific Collaboration, the Virgo Collaboration, R. Abbott, et al. *arXiv e-prints 2004.08342*, April 2020.

[106] J. Aasi, B. P. Abbott, R. Abbott, et al. *Phys. Rev. D*, 89(12):122004, June 2014.

[107] B. P. Abbott, R. Abbott, T. D. Abbott, et al. *Living Reviews in Relativity*, 21(1):3, April 2018.

[108] J. J. Eldridge, E. R. Stanway, and P. N. Tang. *MNRAS*, 482:870–880, January 2019.

[109] Avishai Gilkis, Tomer Shenar, Varsha Ramachandran, et al. *MNRAS*, February 2021.

[110] N. Langer. *Luminous Blue Variables: Massive Stars in Transition. ASP Conference Series. Ed. A.Nota, H.Lamers.*, 120:83, 1997.

[111] G. Gräfener, S. P. Owocki, and J. S. Vink. *A&A*, 538:A40, February 2012.

[112] D. Sanyal, ..., D. **Szécsi**, et al. *A&A*, 597:A71, January 2017.

[113] D. **Szécsi**, N. Langer, S.-C. Yoon, et al. In *Fast Outflows in Massive Stars. EWASS 2014 Simposia 7. Geneva, Switzerland*, june 2014.

[114] E. O'Connor and C. D. Ott. *ApJ*, 730:70, April 2011.

[115] M. Ugliano, H.-T. Janka, A. Marek, and A. Arcones. *ApJ*, 757:69, September 2012.

[116] O. Pejcha and T. A. Thompson. *ApJ*, 801:90, March 2015.

[117] T. Sukhbold and S. E. Woosley. *ApJ*, 783:10, March 2014.

[118] T. Sukhbold, T. Ertl, S. E. Woosley, et al. *ApJ*, 821:38, April 2016.

[119] A. I. MacFadyen and S. E. Woosley. *ApJ*, 524:262, 1999.

[120] A. A. Chrimes, E. R. Stanway, and J. J. Eldridge. *MNRAS*, 491(3):3479–3495, January 2020.

[121] S. E. de Mink, O. R. Pols, N. Langer, and R. G. Izzard. *A&A*, 507:L1–L4, November 2009.

[122] N. Bastian, I. Cabrera-Ziri, and M. Salaris. *MNRAS*, 449:3333–3346, May 2015.

[123] N. E. Britavskiy, A. Z. Bonanos, A. Herrero, et al. *A&A*, 631:A95, November 2019.

[124] K. Lind, J. Melendez, M. Asplund, et al. *A&A*, 554:A96, June 2013.

[125] Tilman Hartwig, Miho N. Ishigaki, Ralf S. Klessen, and Naoki Yoshida. *MNRAS*, 482(1):1204–1210, January 2019.

[126] A. Mucciarelli, L. Monaco, P. Bonifacio, et al. *A&A*, 661:A153, May 2022.

[127] E. A. Maugeri, S. Heinitz, R. Dressler, et al. *Journal of Instrumentation*, 12(2):P02016, February 2017.

[128] N. Rijal, I. Wiedenhöver, J. C. Blackmon, et al. *Phys. Rev. Lett.*, 122(18):182701, May 2019.

[129] B. Davids. *Mem. d.Soc. Astron.Ital.*, 91:20, January 2020.

[130] Cyril Pitrou, Alain Coc, Jean-Philippe Uzan, and Elisabeth Vangioni. *Nature Reviews Physics*, 3(4):231–232, January 2021.

[131] E. M. Tursunov, S. A. Turakulov, and A. S. Kadyrov. *Nuclear Physics A*, 1006:122108, February 2021.

[132] Kanji Mori and Motohiko Kusakabe. *Mem. d.Soc. Astron.Ital.*, 91:26, January 2020.

[133] G. J. Mathews, A. Kedia, N. Sasankan, et al. *Mem. d.Soc. Astron.Ital.*, 91:29, January 2020.

[134] G. R. Farrar. In *American Astronomical Society Meeting Abstracts #235*, volume 235 of *American Astronomical Society Meeting Abstracts*, page 133.04, January 2020.

[135] Kanji Mori, Motohiko Kusakabe, A. Baha Balantekin, et al. *MNRAS*, 503(2):2746–2753, May 2021.

[136] Yini Lu and Motohiko Kusakabe. *ApJ*, 926(1):L4, February 2022.

[137] I. Brott, S. E. de Mink, M. Cantiello, et al. *A&A*, 530:A115, June 2011.

[138] Valentina D'Orazi, Sara Lucatello, Raffaele Gratton, et al. *ApJ*, 713(1):L1–L5, Apr 2010.

[139] S. Q. Hou, T. Kajino, T. C. L. Trueman, et al. *ApJ*, 920(2):145, October 2021.

LIST OF SCIENTIFIC ACHIEVEMENTS

DOROTTYA SZÉCSI

───── Information on scientific achievements – set out in Art. 219 para 1.2 of the Act

Cycle of scientific articles related thematically (art. 219 para 1. point 2b of the Act):

(Hᴀʙ1) **Szécsi**, D., Agrawal, P., Wünsch, R., Langer, N.: *'Bonn' Optimized Stellar Tracks (BoOST). Simulated Populations of Massive and Very Massive Stars as Input for Astrophysical Applications*, A&A 658, A125 (2022). [LINK] [arXiv:2004.08203] [***Media Release***] – 22 pages.

(Hᴀʙ2) Agrawal, P.; **Szécsi**, D.; Stevenson, S.; Hurley, J.: *Explaining the differences in massive star models from various simulations*, MNRAS Vol.512, Issue 4, pp.5717-5725 (2022). [LINK] [arXiv:2112.02800] – 9 pages.

(Hᴀʙ3) **Szécsi**, D. and Wünsch, R.: *Role of supergiants in the formation of globular clusters*, ApJ 871, 20 (2019). [ADS] [arXiv:1809.01395] – 21 pages.

(Hᴀʙ4) **Szécsi**, D., Mackey, J. and Langer, N.: *Supergiants and their shells in young globular clusters*, A&A 612, A55 (2018). [LINK] [arXiv:1711.04007] – 13 pages.

(Hᴀʙ5) Kubátová, B.; **Szécsi**, D.; Sander, A. A. C.; Kubát, J.; Tramper, F.; Krtička, J.; Kehrig, C.; Hamann, W.-R.: *Low-metallicity massive single stars with rotation. II. Predicting spectra and spectral classes of chemically homogeneously evolving stars*, A&A, 623, A8 (2019). [LINK] [arXiv:1810.01267] – 33 pages.

───── Infomation on scientific or artistic activity

List of articles published in scientific journals (including the articles not mentioned in Sect. 1):

After PhD

(1.) Geen, S.; ...; Sarwar, R.; Stinshoff, H.; ...; **Szécsi**, D.; et al.: *Bringing Stellar Evolution and Feedback Together: Summary of Proposals from the Lorentz Center Workshop*, Publ. of the Astron. Society of the Pacific, Vol.135, Issue 1044, id.021001, (2023). [LINK] [arXiv:2301.13611] – 17 pages.

(2.) Agrawal, P.; Stevenson, S.; **Szécsi**, D.; Hurley, J.: *A systematic study of super-Eddington layers in the envelopes of massive stars*, A&A, Vol.668, id.A90, (2022). [LINK] [arXiv:2112.02800] – 15 pages.

(3.) Martinez-Gonzalez, S., Wünsch, R., Tenorio-Tagle, G., Silich, S., **Szécsi**, D., and Palous, J.: *Dust Grain Growth & Dusty Supernovae in Low-Metallicity Molecular Clouds*, ApJ Vol.934, Issue 1, id.51 (2022). [ADS] [arXiv:2206.06382] – 8 pages.

(4.) Agrawal, P.; **Szécsi**, D.; Stevenson, S.; Hurley, J.: *Explaining the differences in massive star models from various simulations*, MNRAS Vol.512, Issue 4, pp.5717-5725 (2022). [LINK] [arXiv:2112.02800] – 9 pages.

(5.) Franeck, A.; Wünsch, R.; Martínez-González, S.; Orlitová, I.; Boorman, P.; Svoboda, J.; **Szécsi**, D.; Douna, V.: *X-ray emission from star cluster winds in starburst galaxies*, ApJ 927 212 (2022). [ADS] [arXiv:2201.12339] – 18 pages.

(6.) **Szécsi**, D., Agrawal, P., Wünsch, R., Langer, N.: *'Bonn' Optimized Stellar Tracks (BoOST). Simulated Populations of Massive and Very Massive Stars as Input for Astrophysical Applications*, A&A 658, A125 (2022). [LINK] [arXiv:2004.08203] [***Media Release***] – 22 pages.

(7.) Tanvir, N. R.; Le Floc'h, E.; Christensen, L.; [...] **Szécsi**, D.; Toth, L. V.; Urata, Y.; Vergani, S.; Zane, S.: *Exploration of the high-redshift universe enabled by THESEUS*, Experimental Astronomy, Vol. 52, Issue 3, p.219-244 (2021). [ADS] [arXiv:2104.09532] – 14 pages.

(8.) Menon, A.; de Mink, S.E.; Langer, N.; Justham, S.; **Szécsi**, D.; Sen, K.; de Koter, A.; Abdul-Masih, M.; Sana, H.; Mahy, L.; Marchant, P.: *Detailed evolutionary models of massive contact binaries: I. Model grids and synthetic populations for the Magellanic Clouds*, MNRAS, Vol.507, Issue 4, pp.5013-5033 (2021). [ADS] [arXiv:2011.13459] – 23 pages.

(9.) Horvath, I., **Szécsi**, D., Hakkila, J., Szabó, Á., Racz, I.I., Tóth, L.V., Pintér, S., Bagoly, Z.: *The clustering of gamma-ray bursts in the Hercules – Corona Borealis Great Wall: the largest structure in the Universe?* MNRAS 498, 2544 (2020). [ADS] [arXiv:2008.03679] – 12 pages.

(10.) Agrawal, P.; Hurley, J.; Stevenson, S.; **Szécsi**, D.; Flynn, C.: *The fates of massive stars: exploring uncertainties in stellar evolution with METISSE*, MNRAS 497,4549 (2020). [arXiv:2005.13177] – 18 pages.

(11.) Neijssel, C. J.; Vigna-Gómez, A.; Stevenson, S.; Barrett, J.W.; Gaebel, S.M.; Broekgaarden, F.; de Mink, S.E.; **Szécsi**, D.; Vinciguerra, S.; Mandel, I.: *The effect of the metallicity-specific star formation history on double compact object mergers*, MNRAS, Vol. 490, Issue 3, p.3740 (2019). [arXiv:1906.08136] – 22 pages.

(12.) Garcia, M.; Evans, C. J.; Bestenlehner, J. M.; [...] **Szécsi**, D.; [...] Vink, J.; Wofford, A.: *Massive stars in extremely metal-poor galaxies: A window into the past*, Experimental Astronomy, Vol.51, Issue 3, p.887 (2021). [arXiv:1908.04687] – 21 pages.

(13.) Stevenson, S.; Sampson, M.; Powell, J.; Vigna-Gómez, A.; Neijssel, C. J.; **Szécsi**, D.; Mandel, I.: *The Impact of Pair-instability Mass Loss on the Binary Black Hole Mass Distribution*, ApJ, 882/2, 121 (2019). [arXiv:1904.02821] – 16 pages.

(14.) **Szécsi**, D. and Wünsch, R.: *Role of supergiants in the formation of globular clusters*, ApJ 871, 20 (2019). [ADS] [arXiv:1809.01395] – 21 pages.

(15.) Kubátová, B.; **Szécsi**, D.; Sander, A. A. C.; Kubát, J.; Tramper, F.; Krtička, J.; Kehrig, C.; Hamann, W.-R.: *Low-metallicity massive single stars with rotation. II. Predicting spectra and spectral classes of chemically homogeneously evolving stars*, A&A, 623, A8 (2019). [arXiv:1810.01267] – 33 pages.

(16.) Vigna-Gómez, A.; Neijssel, C. J.; Stevenson, S.; Barrett, J.W.; Belczynski, K.; Justham, S.; de Mink, S.E.; Müller, B.; Podsiadlowski, P.; Renzo, M.; **Szécsi**, D.; Mandel, I.: *On the formation history of Galactic double neutron stars*, MNRAS 481, p.4009 (2018). [arXiv:1805.07974] – 23 pages.

(17.) Stratta, G.; Ciolfi, R.; Amati, L.; [...] **Szécsi**, D.; [...] Patricelli, B.; Bernardini, M.: *THESEUS: a key space mission for Multi-Messenger Astrophysics*, Advances in Space Research, vol. 62, issue 3, p. 662-682 (2018). [arXiv:1712.08153] – 25 pages.

(18.) **Szécsi**, D., Mackey, J. and Langer, N.: *Supergiants and their shells in young globular clusters*, A&A 612, A55 (2018). [arXiv:1711.04007] – 13 pages.

(19.) Amati, L.; O'Brien, P.; Goetz, D.; [...] **Szécsi**, D.; [...] Watson, D.; Zicha, J.: *The Transient High Energy Sky and Early Universe Surveyor (THESEUS)*, Advances in Space Research, Vol. 62, Issue 1, p.191-244 (2018). [arXiv:1710.04638] – 69 pages.

(20.) **Szécsi**, D.: *Single and binary stellar progenitors of long-duration gamma-ray bursts (GRB Progenitor Review Series Part II.)*, Proceedings of Science, PoS(MULTIF2017)065 (2017). [arXiv:1710.05655] – 13 pages.

(21.) **Szécsi**, D.: *How may short-duration GRBs form? A review of progenitor theories. (GRB Progenitor Review Series Part I.)*, Contributions of the Astronomical Observatory Skalnaté Pleso, vol. 47, no. 2, p.108-115 (2017). [arXiv:1710.05356] – 8 pages.

(22.) Sanyal, D.; Langer, N.; **Szécsi**, D.; Yoon, S-C; Grassitelli, L.: *Metallicity dependence of envelope inflation in massive stars*, A&A 597, A71 (2017). [arXiv:1611.07280] – 16 pages.

Before PhD

(23.) Kruckow, M.U.; Tauris, T.M.; Langer, N.; **Szécsi**, D.; Marchant, P.; Podsiadlowski, P.: *Common-envelope ejection in massive binary stars. Implications for the progenitors of GW150914 and GW151226*, A&A 596, A58 (2016). [arXiv:1610.04417] – 13 pages.

(24.) Bagoly, Z., **Szécsi**, D., Balázs, L.G., Csabai, I., Horváth, I., Dobos, L., Lichtenberger, J., Tóth, L.V.: *Searching for electromagnetic counterpart of LIGO gravitational waves in the Fermi GBM data with ADWO*, A&A 593, L10 (2016). [arXiv:1603.06611] – 4 pages.

(25.) **Szécsi**, D; Langer, N.; Sanyal, D.; Evans, C. J.; Bestenlehner, J. M.; Raucq, F.: *Do rapidly-rotating massive stars at low metallicity form Wolf-Rayet stars?*, Wolf-Rayet Stars: Proceedings of an International Workshop. Edited by Wolf-Rainer Hamann, Andreas Sander, Helge Todt. Universitätsverlag Potsdam, 2015., p.189-192. [ADS]

(26.) **Szécsi**, D., Langer, N., Yoon, S.-C., Sanyal, D., Mink, S.E., Dermine, T.: *Low metallicity massive single stars with rotation. I. Evolutionary models applicable to I Zw 18*, A&A 581, A15 (2015). [arXiv:1506.09132] – 34 pages.

During University

(27.) **Szécsi**, D., Bagoly, Z., Kóbori, J., Horváth, I., Balázs, L.G.: *Direction dependent background fitting for the Fermi GBM data*, A&A v.557, A8 (2013). [arXiv:1306.3812] – 16 pages.

(28.) **Szécsi**, D., Bagoly, Z., Mészáros, A., Balázs, L.G., Veres, P., and Horváth, I.: *New background-filtering algorithm based on the motion of the Fermi Gamma-ray Space Telescope*, Memorie della Societa Astronomica Italiana v.21, p.214 (2012). [ADS] – 4 pages.

(29.) **Szécsi**, D., Bagoly, Z., Horváth, I., Balázs, L.G., Veres, P., Mészáros, A.: *GRB duration distribution considering the position of the Fermi*, Acta Polytechnica, 52, 43 (2012). [arXiv:1202.2592] – 4 pages.

Information on presentations given at national or international scientific conferences / seminars

Invited conference talks:

1. *Metal-poor massive stars.* **Keynote speech.** International Conference for Young Professionals in Physics and Technology (ICYPPT, V.N. Karazin Kharkiv National University, 30th April 2021, Kharkiv, Ukraine) [Slides]

2. *Metal-poor massive stars: The theory linking gravitational waves, star-formation and the dawn of the Universe* 'Actual Problems in Mathematics and Phyisics', Conference at the Deartment of Natural Sciences, University of Public Service (1 September 2020, Budapest, Hungary) [Recorded-Talk] [Slides]

3. *Low-Z massive stars vs high-Z massive stars of an M51-like galaxy*, SILCC Workshop (14-15 March 2019, Bad Neuenahr-Ahrweiler, Germany) [LINK]

4. *Tracking the Yeti in the snow — Looking for metal-poor massive stars*, Frontiers of the Physics of Massive Stars (16-20 July 2018, Ensenada, Mexico) [LINK] [Video-1] [Video-2]

5. *GRBs and stellar evolution: a review of progenitor theories*, European Week of Astronomy and Space Science (EWASS, 26-30 June 2017, Prague, Czech Republic) [LINK]

6. *Progenitors of GRBs*, Multifrequency Behaviour of High Energy Cosmic Sources - XII (12-17 June 2017, Palermo, Italy) [LINK]

7. *How may GRBs form? An overview of progenitor theories*, 14th INTEGRAL/BART Workshop (3-7 April 2017, Karlovy Vary, Czech Republic) [LINK]

Contributing conference talks:

1. *Massive stars from various simulations: why so different?* 'Actual Problems in Mathematics and Phyisics 2021', Second Conference at the Deartment of Natural Sciences, University of Public Service (26 August 2021, Budapest, Hungary) [Slides]

2. *How to use THESEUS' high-redshift GRB data to constrain the physics of Pop-II and Pop-III progenitors*, Talk given at: THESEUS CONFERENCE 2021 (23-26 March 2021, Virtual) [Presentation] [Video] [Poster]

3. *The BoOST project: 'Bonn' Optimized Stellar Tracks. Simulated Populations of Massive and Very Massive Stars for Astrophysical Applications*, Talk given at: MOBSTER-1 virtual conference (12-17 July 2020, Globally) [Video-Presentation] [Slides]

4. *What if massive stars could procude lithium?*, Talk given at the Conference 'Lithium in the Universe: To Be or not to Be?' (18-22 November 2019, Observatory of Rome, Italy) [LINK]

5. *Metal-poor massive stars: What are they? Why to care? And... how can we find them?*, Talk given at the Network Meeting of the Alexander von Humboldt Foundation (6-8 November 2019, Hamburg, Germany) [LINK]

6. *Life and death of metal-poor massive stars – a new vision for THESEUS' science*, Cosmology and multi-messenger astrophysics with Gamma-Ray Bursts, EWASS 2019, Symposium S4 (24-28 June 2019, Lyon, France) [LINK]

7. *Do chemically homogeneously evolving stars exist?* EWASS 2019, Special Session SS17 'Key ingredients in massive star evolution' (24-28 June 2019, Lyon, France) [LINK]

8. *CHE stars – as the source of photoionization and C-IV emission in dwarf galaxies* VFTS Workshop (13-15 May 2019, Edinburgh, UK) [LINK]

9. *The first, and second, and third... massive stellar generations in the early Universe*, Rise and Shine — Galaxies in the Epoch of Reionisation (18-22 June 2018, Strasbourg, France) [LINK]

10. *The winds of the hot massive stars in I Zwicky 18*, Blowing in the wind (7-13 August 2016, ICISE, Quy Nhon, Vietnam) [LINK]

11. *Core-hydrogen burning red supergiants in the early globular clusters*, Stellar Behemots – Red supergiants across the local Universe. IAU General Assembly 2015 Focus Meeting 16 (3-5 August 2015, Honolulu, Hawaii) [LINK]

12. *The Life and Death of Massive Stars in the Starburst Galaxy IZw18*, Stellar explosions in an everchanging environment. IAU General Assembly 2015 Focus Meeting 10 (11-13 August 2015, Honolulu, Hawaii) [LINK]

13. *Fast rotating massive stars at low metallicity: WR stars?*, International Workshop on Wolf-Rayet Stars (1-5 June 2015, Potsdam, Germany) [LINK]

14. *Stellar evolution in I Zw 18*, VLT FLAMES Meeting (22-24 March 2015, Sheffield, UK [LINK]

15. *Globular Cluster Abundane Anomalies and the Massive Binary Polluter Scenario*, Binary systems, their evolution and environments (1-5 September 2014, Ulaan Baatar, Mongolia) [LINK] [Video]

16. *Consequences of Mass Loss on the Final Fates of Massive Stars*, Fast Outflows in Massive Stars. EWASS 2014 Simposia 7 (30 June - 4 July 2014, Geneva, Switzerland) [LINK]

17. *Evolution of Massive Stars in Blue Compact Dwarf Galaxies: model tracks, Wolf-Rayet stars and final fates*, Galaxies meet GRBs at Cabo de Gata (23-27 September 2013, Cabo de Gata, Spain) [LINK]

18. *Investigating the Motion of the Fermi Satellite – Considering the Background Levels Superposed on the Gamma-ray Burst Data*, Conference of the Hungarian National Scientific Students' Associations (Young Scientist Competition – 1st Prize), Astrophysics Section (27-29 April 2011, Nyíregyháza, Hungary) [LINK]

Invited talks at international seminars/colloquia:

1. *A unified & metallicity-dependent theory of Globular Clusters and Gravitational Waves*, KU Leuven, ***Belgium***, (3rd May 2023) [LINK]

2. *Gravitational Wave Progenitors solving the Cosmic Lithium Problem*, University College ***London***,

(18th April 2023, London, UK) [LINK]

3. *Massive stars from various simulations: different, but why?*, Astrophysical Seminar, Jagiellonian University, **Krakow**, Poland (26 Oct. 2022) [LINK]

4. *Massive stars from various simulations: different, but why?*, European Southern Observatory, **Chile** (11th Aug 2022, Santiago, Chile) [LINK]

5. *Metal-poor massive stars: Linking gravitational waves, star-formation and the dawn of the Universe*, Astronomical Center of the Polish Academy of Sciences (CAMK PAN) in **Warsaw** (8th December 2021, Warsaw, Poland) [LINK]

6. *Role of metal-poor massive stars in galaxies near and far*, **Swinburne** University of Technology (29th April 2021, Melbourne, Australia) [LINK]

7. *When gravity meets radiation: the stellar Eddington limit*, Seminar of the SILCC group, University of Cologne (27th April 2021, Cologne, Germany) [LINK]

8. *The theory linking gravitational waves, star-formation and the dawn of the Universe*, Colloquium talk at the Nicolaus Copernicus University (30 November 2020, Torun, Poland) [LINK] [Video-1] [Video-2] [Video-3]

9. *Metal-poor massive stars*, Seminar talk at the Astronomy Student's Association Meeting, Nicolaus Copernicus University (10th November 2020, Torun, Poland) [LINK]

10. *The impossible GW190521* Seminar of the SILCC group, University of Cologne (6th October 2020, Cologne, Germany) [LINK]

11. *Gamma-ray bursts*, Seminar of the SILCC group, University of Cologne (30th June 2020, Cologne, Germany) [LINK] [Video]

12. *The theory linking gravitational waves, star-formation and the dawn of the Universe*, Anton Pannekoek Institut for Astronomy, University of **Amsterdam** (13 March 2020, Amsterdam, The Netherlands) [LINK] [Video-1] [Video-2] [Video-3]

13. *Lithium in massive stars*, Seminar of the SILCC group, University of Cologne (14th January 2020, Cologne, Germany) [LINK] [Video]

14. *Metal-poor massive stars – The progenitors of gravitational waves*, **Hamburg** Observatory, (8 January 2020, Hamburg, Germany) [LINK]

15. *Scientific Writing in Astrophysics – Tips and Tricks*, University of Cologne (8 October 2019, Cologne, Germany) [LINK]

16. *Massive stars in the metal-poor Universe*, Eötvös University (3 January 2019, Budapest, Hungary) [LINK]

17. *Role of supergiants in the formation of globular clusters*, University of Surrey (29 November 2018, **Guildford**, UK) [LINK]

18. *Role of supergiants in the formation of globular clusters*, Royal Observatory Edinburgh (10 October 2018, **Edinburgh**, UK) [LINK]

19. *Tracking the Yeti in the snow — Looking for metal-poor massive stars*, Argelander-Institut für Astronomie (8 February 2018, Bonn, Germany) [LINK] [Video-1] [Video-2]

20. *Supergiants and their shells in young globular clusters*, Konkoly Observatory (1 February 2018, **Budapest**, Hungary) [LINK]

21. *Tracking the Yeti in the snow — Looking for metal-poor massive stars in and around the Milky Way*, **Jan Frič Prize Talk** (29 January 2018, Ondřejov, Czech Republic) [LINK] [Video-1] [Video-2]

22. *Scientific Writing in Astrophysics—Tips and Tricks*, Seminar at the University of Birmingham (22 November 2017, Birmingham, United Kingdom) [LINK]

23. *Homogeneous evolution and binarity: the progenitor behind various cosmic explosions*, University of Birmingham (23 May 2017, **Birmingham**, United Kingdom) [LINK]

24. *The evolution of low-metallicity massive stars*, Masaryk University (17 October 2016, **Brno**, Czech Republic) [LINK]

25. *The evolution of low-metallicity massive stars*, Charles University (5 October 2016, **Prague**, Czech Republic) [LINK]

26. *The evolution of low-metallicity massive stars*, Autumn Institute Meeting of the Astronomical Institute of the Czech Academy of Sciences (3 October 2016, Ondřejov, Czech Republic) [LINK]

27. *The final fate of the hot massive stars in IZw18*, Seminar of the Stellar Physics group (2 June 2016, Bonn, Germany) [LINK]

28. *Hot massive stars in I Zwicky 18*, Seminar in the Stellar Department of the Astronomical Institute of the Czech Academy of Sciences (25 May 2016, Ondřejov, Czech Republic) [LINK]

29. *Globular Cluster Abundance Anomalies and the Massive Binary Polluter Scenario*, Anton Pannekoek Institute, University of *Amsterdam* (1 April 2016, Amsterdam, The Netherlands) [LINK] [Video]

30. *Low Metallicity Massive Stars*, Seminar of the Stellar Physics group (22 October 2015, Bonn, Germany) [LINK]

31. *Low Metallicity Massive Stars*, Gravitation & Relativity Group Seminar, University of Cologne (20 October 2015, Cologne, Germany) [LINK]

32. Consequences of Mass Loss on the Final Fates of Massive Stars (Part I); The BEC Interface (Part II), Seminar of the Stellar Physics group (12 June 2014, Bonn, Germany) [LINK]

33. *Stellar winds*, PhD Seminar of Stellar physics students (12 November 2013, Bonn, Germany) [LINK]

34. *Admission to the PhD honors program (H2)*, Bonn-Cologne Graduate School of Physics and Astronomy (7 October 2013, Cologne, Germany) [LINK]

35. *Evolution of Massive Stars in Blue Compact Dwarf Galaxies: model tracks, Wolf-Rayet stars and final fates*, Seminar of the Stellar Physics group (12 September 2013, Bonn, Germany) [LINK]

36. *Grid of evolutionary models of low metallicity massive stars*, Seminar of the Stellar Physics group (17 January 2013, Bonn, Germany) [LINK]

37. *The Henyey Method (in Hungarian)*, Theoretical Astrophysics Seminar at the Eötvös University (11 April 2012, Budapest, Hungary) [LINK]

38. *Cosmic Rays measured at the ISS: the Alpha Magnetic Spectrometer*, Seminar on the Foundations of Elementary Particle and Astroparticle Physics (GETA) at the Bergische Universität Wuppertal (19 January 2012, Wuppertal, Germany) [LINK]

39. *Dinamics of Planets on Keplerian Orbits (in Hungarian)*, Seminar on Computer Simulations at the Eötvös University (14 December 2012, Budapest, Hungary) [LINK] [Video-1-Mercury-orbit] [Video-2-Inner-planets] [Video-3-Outer-planets]

40. *Investigating the Motion of the Fermi Satellite (in Hungarian)*, Young Scientist' Competition at the Eötvös University, Department of Astronomy (2 December 2010, Budapest, Hungary) – **Won 1st prize.** [LINK]

41. *Introduction to Cosmology*, Astrophysics Seminar at the Eötvös University (8 October 2010, Budapest, Hungary) [LINK]

42. *Studying Gamma-ray Bursts (in Hungarian)*, Young Scientist' Competition/Conference at the Eötvös University, Department of Astronomy (2 December 2009, Budapest, Hungary) [LINK]

43. *Gravitational lenses as cosmic rulers (in Hungarian)*, Astronomy Seminar at the Eötvös University (29 March 2010, Budapest, Hungary) [LINK]

44. *Cosmology – and the science behind it (in Hungarian)*, Speaker Competition of the Hungarian Association of Physics Students (10 April 2010, Budapest, Hungary) – Evaluation: 2nd prize [LINK]

45. *The jitter radiation paradigm (in Hungarian)*, Astronomy Seminar at the Eötvös University (17 November 2009, Budapest, Hungary) [LINK]

46. *A "Swift" in Space (in Hungarian)*, Speaker Competition of the Hungarian Association of Physics Students (4 April 2009, Budapest, Hungary) – Won 3rd prize [LINK]

Information on participation in organizational and scientific committees at national or international conferences

Workshop at EAS 2021 — **Early Career Astronomers & their supporters**, *Senior SOC member*, Date of workshop: 28.06.2021, Website and program.

Conference 'MathFiz'	**'Actual Problems in Mathematics and Physics 2021'**, *SOC member*, Date of conference: 26.08.2021, Website and program.
Conference 'MOBSTER-1'	**MOBSTER-1 2020 Conference on Magnetism in Massive Stars**, *VOC (Virtual Organizing Committee) member*, Date: 13-17 July 2020, Website and program.
Chair of S11 at EWASS 2017	**Symposium 11 at the European Week of Astronomy and Space Sciences (EWASS)**, *Chair and main organizer*, Date: 26-27 June 2017, Website and program.

Participation in projects financed through national and international competitions

NCN OPUS	**Principal Investigator of the NCN grant OPUS 2021/41/B/ST9/00757**, *Starting date: 01/02/2022*, People paid from the grant: 2 (one PD researcher and one PhD student), *1.446.310 PLN*.
Humbold 'Return'	**Humboldt 'Return' Fellowship**, *offered by the Alexander von Humboldt Foundation, Germany*, Apr. 2022 – March 2023, *6500 EUR*.
Humbold Fellowhsip	**Humboldt Individual Research Fellowship**, *offered by the Alexander von Humboldt Foundation, Germany*, Apr. 2019 – Sept. 2021, *104.100 EUR*.

Information on participation in European or other international programmes

GAMOW Consortium	**Member of the Polish Science Support Team of the GAMOW Satellite Mission**, *MIDEX proposal submitted to NASA.*.
THESEUS Consortium	**Member of the THESEUS Satellite Mission proposal**, *short-listed at ESO (see here)*, Link to webpage: LINK.

Information on internships completed in scientific institutions

Leuven	2-3 May 2023: Visit at KU Leuven. Colloquium given.
London	24-30 April 2023: Visit at UCL London. Colloquium given.
Amsterdam	16-20 March 2020: Visit at UvA, Amsterdam. Colloquium given.
Potsdam	15-17 January 2019: University of Potsdam, Germany. Colloquium given.
Utrecht	24-26 May 2018: Utrecht, The Netherlands. Colloquium given.
Spořilov/Prague	15-18. April. 2018: Spořilov/Prague. Purpose of visit: collaboration on globular clusters.
Bonn	08-09. February 2018: Bonn. Purpose of visit: Discussion with N. Langer, J. Mackey and G. Gräfener. Seminar talk given.
Budapest	01-07. February 2018: Budapest. Purpose of visit: Collaboration with Gamma-ray burst group. Seminar talk given at the Konkoly Observatory.
Ondřejov/Prague	25-31. January 2018: Ondřejov/Prague. Purpose of visit: receiving prize '**Jan Frič Premium for young researchers** by the Astronomical Institute of the Czech Academy of Sciences'. Giving a prize talk.

Hamburg	18-21. December 2017: Hamburg. Purpose of visit: Attending a seminar ("Introduction to Supergravity") at the Differential Geometry group in the Center for Mathematical Physics.
Budapest	14-17. July, 2017: Budapest. Purpose of visit: scientific discussion with local researcher Carolyn Doherty (Konkoly Observatory) and visiting researcher Athira Menon (Monash University).
Birmingham	22-25. May, 2017: Birmingham. Purpose of visit: start of collaboration with Gravitational Wave Group. Seminar talk given.
Brno	17. October, 2016: Brno. Seminar talk given at the Department of Theoretical Physics and Astrophysics at the Faculty of Science, Masaryk University.
Budapest	29-30. August, 2016: Budapest. Purpose of visit: discussion, visiting Konkoly Observatory, plan of organizing an EWASS workshop.
Prague/Ondřejov	23-27. May, 2016: Prague/Ondřejov. Purpose of visit: starting collaboration, discussion. Seminar talk given in Ondřejov.
Amsterdam	28. March – 01. April, 2016: Amsterdam. Purpose of visit: discussion on binary stars and globular clusters. Seminar talk given.
Cologne	20. October, 2015: Cologne. Purpose of visit: giving a talk at the Gravitation & Relativity Group Seminar, lead by Prof. C. Kiefer.
Liège	22. May, 2015: Liège. Purpose of visit: collaboration with F. Raucq on CMFGEN model spectra.
Hamburg	07-08. August, 2014: Hamburg. Purpose of visit: discussion with members of Differential Geometry group in the Center for Mathematical Physics.
Budapest	05-07. May, 2014: Budapest. Purpose of visit: discussion about future plans of the GRB group.
Cologne	07. October, 2013: Cologne. Purpose of visit: application for admission to the PhD honors program (H2) of the Bonn-Cologne Graduate School of Physics and Astronomy. Talk given.
Budapest	20-27. August, 2013: Budapest. Purpose of visit: submission of my Master research paper to the journal A&A.
Bonn	23. January, 2012: Bonn. Purpose of visit: first discussion of a PhD project with Prof. N. Langer. Soon afterwards a PhD scholarship was offered and accepted.
State College	10-15. June, 2011: State College. Informal visit at Péter Mészáros at Penn State University, PA, USA. Discussion of gamma-ray bursts and career prospects.

Information on scientific or artistic works reviewed, in particular those published in international journals

A&A	3x
MNRAS	2x
Science	1x

Membership in teams assessing applications for financing of research projects, applications for scientific awards, applications in other competitions of scientific or didactic character

Hubble Panel Member	**Hubble Space Telescope's Cycle #27 – Review Panel Member – Stellar Physics**, *Date of board meeting: 10-12 June 2019.*

JWST reviewer   **James Webb Space Telescope Cycle 2 – External Panel Review**, *2022/3.*

──────────   ## Scientometric information

Impact   **A&A**: 9 articles, IF 6.240, MP 140
Factors (IF)   **MNRAS**: 6 articles, IF 5.235, MP 140
and   **ApJ**: 4 articles, IF 5.521, MP 140
Ministerial   **Exp. Astron.**: 2 articles, IF 2.155 , MP 100
Points (MP)   **Adv. in Space Research**: 2 articles, IF 2.611, MP 70
               Acta Polytechnica: 1 article, IF 1.02, MP 40
               Publ. of Astro Soc. of Pacific: 1 article, IF 5.842, MP 140

PhD year: **2016** – Total number of citations: **1180** – Excluding self-citations: **1058** – Total number of papers: **57** – Total number of refereed journal papers: **29** – Total number of reads: **18738** – h-index: **14**

(Data is based on NASA ADS metrics on 27.06.2023.)

PUBLICATIONS (HAB1-HAB5) CONSTITUTING THE HABILITATION

Astronomy
&
Astrophysics

Bonn Optimized Stellar Tracks (BoOST)

Simulated populations of massive and very massive stars for astrophysical applications[*]

Dorottya Szécsi[1,2] , Poojan Agrawal[3,4,5] , Richard Wünsch[6] , and Norbert Langer[7]

[1] Institute of Astronomy, Faculty of Physics, Astronomy and Informatics, Nicolaus Copernicus University, Grudziądzka 5, 87-100 Toruń, Poland
  e-mail: dorottya.szecsi@gmail.com
[2] I. Physikalisches Institut, Universität zu Köln, Zülpicher-Strasse 77, 50937 Cologne, Germany
[3] Center for Astrophysics and Supercomputing, Swinburne University of Technology, Hawthorn, Victoria 3122, Australia
[4] OzGrav: The ARC Center of Excellence for Gravitational Wave Discovery, Hawthorn, Australia
[5] McWilliams Center for Cosmology, Department of Physics, Carnegie Mellon University, Pittsburgh, PA 15213, USA
[6] Astronomical Institute of the Czech Academy of Sciences, Boční II 1401, 141 00 Prague 4, Czech Republic
[7] Argelander-Institut für Astronomie der Universität Bonn, Auf dem Hügel 71, 53121 Bonn, Germany

ABSTRACT

Massive and very massive stars can play important roles in stellar populations by ejecting strong stellar winds and exploding in energetic phenomena. It is therefore imperative that their behavior be properly accounted for in synthetic model populations. We present nine grids of stellar evolutionary model sequences, together with finely resolved interpolated sequences and synthetic populations, of stars with 9–500 $M_\odot$ and with metallicities ranging from Galactic metallicity down to $1/250\,Z_\odot$. The stellar models were computed with the Bonn evolutionary code with consistent physical ingredients, and covering core hydrogen- and core helium-burning phases. The interpolation and population synthesis were performed with our newly developed routine SynStars. Eight of the grids represent slowly rotating massive stars with a normal or classical evolutionary path, while one grid represents fast-rotating, chemically homogeneously evolving models. The grids contain data on stellar wind properties such as estimated wind velocity and kinetic energy of the wind, as well as common stellar parameters such as mass, radius, surface temperature, luminosity, mass-loss rate, and surface abundances of 34 isotopes. We also provide estimates of the helium and carbon-oxygen core mass for calculating the mass of stellar remnants. The Bonn Optimized Stellar Tracks (BoOST) project is published as simple tables that include stellar models, interpolated tracks, and synthetic populations. Covering the broadest mass and metallicity range of any published massive star evolutionary model sets to date, BoOST is ideal for further scientific applications such as star formation studies in both low- and high-redshift galaxies.

Key words. stars: massive – stars: evolution – stars: formation – gravitational waves – stars: black holes – methods: numerical

1. Introduction

Stellar evolutionary model sequences provide the basis for several astrophysical investigations. These investigations include the simulation of galaxies close (e.g., Gatto et al. 2017) and far (e.g., Rosdahl et al. 2018), obtaining mass and age of observed stars (e.g., Schneider et al. 2014; Grin et al. 2017; Ramírez-Agudelo et al. 2017), studying the formation of ancient globular clusters (e.g., de Mink et al. 2009a; Szécsi & Wünsch 2019), and predicting the outcome of binary populations in terms of gravitational wave event rates (e.g., Kruckow et al. 2018). Because massive (>9 $M_\odot$) and very massive (>100 $M_\odot$) stars can play important roles in stellar populations by ejecting strong stellar winds and exploding in energetic phenomena, it is very important that their behaviour is properly accounted for in synthetic populations (Agrawal et al. 2020). For example if the early Universe is to be studied, very massive stars are key: the first few generations of galaxies at cosmic dawn might have formed them

in larger numbers and with higher initial mass than what is typical today.

The Bonn code[1] has been used in the past decades to compute stellar evolutionary model sequences with the most recent input physics. Amongst other things, it is especially suited to simulating massive stars due to the large nuclear reaction network and the high spacial resolution it applies. Stellar grids of massive stars with various chemical composition and various rotational properties have been created and analyzed (Yoon et al. 2006, 2012; Brott et al. 2011; Köhler et al. 2015; Szécsi et al. 2015), occasionally including detailed binary models (de Mink et al. 2009a,b; Yoon 2015).

Nonetheless, the models published so far can be further optimized. Consistency in the initial parameter space, as well as a reliable treatment of the late phases of evolution, is necessary in order to make these models applicable within a wide range of astrophysical studies. The Bonn code has been used to create and publish four grids of rotating single-star models. Their initial compositions correspond to the Milky Way (MW; Brott et al. 2011), the Large and Small Magellanic Clouds (LMC

---

[1] Also known as the Binary Evolutionary Code.

and SMC; Brott et al. 2011; Köhler et al. 2015), and the dwarf galaxy I Zwicky 18 (IZw18; Szécsi et al. 2015). In the current project, we extend the mass range of all published Bonn grids up to very massive stars. The metallicity range of the models is also extended down to the lowest metallicities observed in ancient globular clusters.

We publish stellar evolutionary model predictions as well as synthetic populations based on published and unpublished results of the Bonn code in a physically consistent way. That is, the Bonn Optimized Stellar Tracks (BoOST) project provides the following three types of published data:

(a) Grids: Nine grids of stellar models with initial masses of $9-500$ $M_\odot$ each. The metallicities of the grids are equally distributed between Galactic[2] ([Fe/H] $\lesssim$ 0.0) and very low ([Fe/H] $=-2.4$) metallicities. These grids are in part based on published stellar models (MW, LMC, SMC, IZw18, and IZw18-CHE), while four new grids have been computed for the present work and cover various sub-SMC metallicities. These are typical for dwarf galaxies and the early Universe. The models have been post-processed into equivalent evolutionary phase format.

(b) Tracks: Interpolated sets of tracks[3] corresponding to all nine grids, which can serve as the basis of synthetic stellar populations. We publish them as simple tables.

(c) Populations: After weighting the interpolated sets of tracks with a Salpeter initial mass function, the result are synthetic populations of massive and very massive stars for an instantaneous starburst episode at age 0. The total mass of the populations is set to 10^7 $M_\odot$. The populations are published as tables, up to $\sim$25 Myr (when the 9 $M_\odot$ stars die).

This is the first time that stellar evoluionary predictions for massive and very massive stars in such a broad metallicity range are published. The models in eight of the grids (a) have been computed with moderate rotation rates leading to normal or classical stellar evolution (i.e., initial rotational velocity of 100 km s^{-1} uniformly), while one of the grids corresponds to extreme rotation rates leading to chemically homogeneous evolution (CHE; initial rotational velocity of 500 km s^{-1}). In addition to the usual surface properties (mass, temperature, luminosity, mass-loss rate, etc.), detailed information about the chemical composition (yields of 34 isotopes) and kinetic energy of the stellar winds is provided at various metallicities as a function of time. Additionally, estimates for the helium and carbon-oxygen core masses are provided to facilitate predictions for the mass of the remnant.

Moreover, we present the newly developed stellar population synthesis tool SYNSTARS, which performs spline-based interpolation on the precomputed stellar models based on the initial mass of the star. In addition to performing the interpolation, SYNSTARS also creates the time-dependent synthetic populations by weighting the tracks with a Salpeter initial mass function and integrating over the stellar feedback (total mass in the wind, total kinetic energy in the wind, etc.). To facilitate reproducibility, the

current version of SYNSTARS is also available along with the model data.

With their broad range in mass and metallicity, the BoOST model populations are suitable for applications in star formation studies, for instance. They can also be used to simulate the formation and evolution of young clusters, dwarf galaxies, and high-redshift galaxies, where the feedback from massive stellar winds play a crucial and metallicity dependent, role.

This paper is organized as follows. In Sect. 2 we present nine grids of stellar models computed with the Bonn code. In Sect. 3.1 we describe how we identified the equivalent evolutionary phases (EEPs), while in Sects. 3.2 and 3.3, we present our new tool SYNSTARS and use it to interpolate between the stellar models and perform population synthesis. In Sect. 4 we discuss the models that did not converge due to numerical instabilities and our novel solution for including their contributions into the populations. In Sect. 5 we explain our method for defining the mass of the final stellar cores, which is a proxy for the mass of the compact object remnant. In Sect. 6 we discuss similarities to previous projects, suggest possible astrophysical applications, and describe future plans. In Sect. 7 we conclude.

2. Grids of stellar models

2.1. Physical ingredients

The BoOST project relies on stellar evolutionary models created with the Bonn code. Some of these models have been published earlier (Brott et al. 2011; Köhler et al. 2015 and Szécsi et al. 2015), but most are newly computed. A description of the input physics implemented in the version of the Bonn code we use here was given by Heger et al. (2000), Heger & Langer (2000), Petrovic et al. (2005), Brott et al. (2011), Yoon et al. (2012), Szécsi et al. (2015) and references therein. To summarize, the models follow the prescription from Vink et al. (2000) for hot wind-driven mass loss of OB stars and Nieuwenhuijzen & de Jager (1990) for cool dust-driven mass loss of supergiants. As for the naked helium star phase – i.e., Wolf–Rayet stars or Transparent Wind UV-Intense (TWUIN) stars; cf. Kubátová et al. 2019 –, they follow the rates from Hamann et al. (1995) reduced by a factor of ten (Yoon & Langer 2005). A metallicity dependence of $\sim Z^{0.86}$ (Vink et al. 2001) was applied. Convective mixing was included based on the mixing-length theory approach (Böhm-Vitense 1958) with a mixing length parameter $\alpha_{\mathrm{MLT}} = 1.5$. For convective overshooting, step overshooting was employed with a parameter $\alpha_{\mathrm{over}} = 0.335$ as calibrated by Brott et al. (2011) for massive stars in the LMC. Convective boundaries were determined using the Ledoux criterion with a semiconvective mixing parameter of $\alpha_{\mathrm{sc}} = 1.0$. Rotationally induced mixing of chemical elements was treated with an efficiency parameter $f_c = 0.0228$ (Heger et al. 2000; Heger & Langer 2000, calibrated by Brott et al. 2011). Furthermore, transport of angular momentum by magnetic fields due to the Spruit–Taylor dynamo (Spruit 2002; Heger et al. 2005) was included.

Table 1 provides a summary of all the BoOST grids and their initial compositions. The already published and the newly created models were computed with the same version of the code, that is, the same input physics as above were applied consistently. As for the previous publications, Brott et al. (2011) published stellar models with an MW, LMC, and SMC composition between $9-60$ $M_\odot$. Köhler et al. (2015) extended the LMC grid with main-sequence models up to 500 $M_\odot$. Szécsi et al. (2015) published models with the much lower IZw18 metallicity

---

[2] By Galactic metallicity, we mean the metallicity of MW stars as defined and applied to stellar models by Brott et al. (2011), cf. their Tables 1 and 2: $Z_{\mathrm{MW}} = 0.0088$. This is somewhat lower than the solar metallicity, which is $Z_\odot \sim 0.012$. See Brott et al. (2011) for a discussion of this definition.

[3] We use the term 'stellar model' to mean a detailed evolutionary model sequence computed in a stellar evolution code from first principles. In turn, we use the term 'track' to mean synthetically created (here: interpolated) evolutionary models. Similarly, we consistently use the term 'grid' to mean a grid of stellar models, and the term 'set' to mean a set of interpolated tracks.

Table 1. Nine BoOST grids published here, and their compositions in various units.

	MW [a]	LMC [b]	SMC [a]	dwarfA SMC/2	dwarfB SMC/5	IZw18 [c] SMC/10	dwarfD SMC/20	dwarfE SMC/50	IZw18-CHE [c] SMC/10
Z_{MW}	1	~1/2.5	~1/5	~1/10	~1/25	~1/50	~1/100	~1/250	~1/50
Z_{SMC}	~5	~2	1	0.5	0.2	0.1	0.05	0.02	0.1
[Fe/H]	$\lesssim 0.0$	~−0.4	−0.7	−1.0	−1.4	−1.7	−2.0	−2.4	−1.7
Z	0.0088	0.0047	0.0021	0.00105	0.00042	0.00021	0.00011	0.00005	0.00021

Notes. The values Z_{MW} = 0.0088, Z_{LMC} = 0.0047, and Z_{SMC} = 0.0021 were defined by Brott et al. (2011, see their Tables 1 and 2). For dwarf galaxy grids dwarfA...E (including IZw18 and IZw18-CHE), the initial metallicity is scaled down from that of the SMC by a factor given in the table header. [a]Models between 9–60 $M_\odot$ were published in Brott et al. (2011). [b]Models between 9–60 $M_\odot$ were published in Brott et al. (2011), and the main-sequence phase of the models between 60–500 $M_\odot$ in Köhler et al. (2015). [c]The main-sequence phases of the models between 9–300 $M_\odot$ were published in Szécsi et al. (2015).

(corresponding to $0.1 \times Z_{SMC}$) in the mass range of 9−300 $M_\odot$, also on the main sequence. All other models, as well as the post-main-sequence phases when needed, were newly computed by us.

We consistently used the moderate initial rotational rate of 100 km s⁻¹ because this rotational rate is representative of non-rotating or slowly rotating massive stars. Additionally, one of our grids was composed of chemically homogeneous models, which have a very fast initial rotation rate, 500 km s⁻¹.

2.2. Design of the grids

To be able to create synthetic populations out of these models in a consistent way, we extended the parameter space. In particular, we (i) computed new models up to 500 $M_\odot$ in all the grids, (ii) computed new grids for a good metallicity coverage with equal steps, and (iii) either simulated the post-main-sequence evolution or provided a reliable approximation for this phase. Thus we designed eight consistent grids with equal log-metallicity steps from Galactic down to the most metal-poor clusters observed. Additionally, (iv) we provide one grid with chemically homogeneous evolution.

Every grid contains ten stellar models, starting with 9 $M_\odot$. We did not fix any consistent value for the mass steps between the ten models in the grids. Instead, their initial masses were chosen in a way that facilitated the best interpolation between them. For example, we ensured that we properly covered the part of the HR diagram in which the models show blue loops or luminous blue variable-type features. Indeed, because these effects are highly metallicity dependent, the design of the grids was kept flexible in terms of the mass step, so that abrupt changes in the models were followed properly.

(i) New models up to 500 $M_\odot$. We extended the published grids (MW, LMC, SMC, and IZw18) with very massive models (up to around 500 $M_\odot$). For consistency, all these new models also had an initial rotational rate of 100 km s⁻¹, and all their physical ingredients were the same as in the published models. The only two exceptions were the models with 250 and 500 $M_\odot$ at MW metallicity, for which the initial rotational rate was set to 0 km s⁻¹ for convenience. We find that this does not make any practical difference in the evolution: at this mass and metallicity, mass loss is so strong already at the beginning of the main sequence that these stars would spin down very soon in any case.

(ii) New grids for a good metallicity coverage. We present here four new grids (cf. Table 1). Two of them were designed so that the metallicity gap between SMC and IZw18 is filled. The other two belong to metallicities below IZw18, down to

1/250th Z_{MW}. Because these metallicities are typical of star-forming dwarf galaxies, we call these grids dwarfA, dwarfB, dwarfD, and dwarfE (dwarfC is consistent with the IZw18 grid). With these, our models allow studying the formation of even the lowest-metallicity globular clusters (with [Fe/H] ∼ −2.3).

(iii) Late phases of evolution. Most of the models in this work were computed with the Bonn code until core-helium exhaustion. In some cases, however, this was not possible due to numerical reasons. High-metallicity models above ∼40 or 60 $M_\odot$ and lower-metallicity models above ∼100 $M_\odot$ have inflated envelopes, and in this state, the computations become numerically challenging[4]. It is difficult to ensure that all our models completely include the post-main-sequence phase (i.e., core-helium-burning). Here we offer a new solution that is described in Sect. 4. With this new method, we approximate for the remaining evolution, completing the last phases of our stars.

(iv) Models with chemically homogeneous evolution. We provide one grid of fast-rotating, chemically homogeneously evolving models with [Fe/H] = −1.7 called IZw18-CHE. In this grid, the initial composition of the models is the same as in the IZw18 grid, but the initial rotational velocity is 500 km s⁻¹ (except in the case of the 9 $M_\odot$ model, where it is somewhat lower, 450 km s⁻¹, to avoid reaching critical rotation). The main-sequence phase of these models (up to 300 $M_\odot$) was published and analyzed by Szécsi et al. (2015), and their atmospheres were studied by Kubátová et al. (2019). Here we complete this grid with two new very massive models (388 $M_\odot$ and 575 $M_\odot$) as well as the post-main-sequence phase of all of the models (computed properly for almost all of them, except for the highest mass, where we had to include the remaining phases in an approximate way; cf. Sect. 4).

We only included core hydrogen- and core helium-burning in our published stellar models. This is justified by the fact that core carbon-burning and subsequent burning phases constitute only $\lesssim 1\%$ of a massive star's life, during which no significant contribution to stellar feedback is expected (except for the supernova explosion; cf. Sect. 5). For example, by simulating the core carbon-burning phase of the 26 $M_\odot$ model in our IZw18 grid, we find that this lasts for ∼7300 years, which is a mere 0.12% of the total 6.21 Myr lifetime of the model. The mass that is lost during this time is about 0.02 $M_\odot$, which is an order of magnitude less than what is lost during the whole evolution. Because

---

[4] The massive and very massive LMC and IZw18 models in Köhler et al. (2015) and Szécsi et al. (2015) were only computed and published up to the end of the main sequence mainly for this same reason.

some of our models experience numerical difficulties in their late phases in any case (we approximate for them in Sect. 4), omitting carbon-burning and beyond from the present version of BoOST is not expected to cause additional discrepancies in our simulated populations from the point of view of stellar feedback and wind properties.

We publish the stellar model grids as simple tables. They include the following quantities as functions of time (cf. also the Readme file attached to the table, as well as Appendix A): the stellar mass, M as a function of time, the effective temperature of the surface, T_{eff}, the bolometric luminosity, L_{bol}, the stellar radius, R, the mass loss, $\dot{M}$, the logarithm of the surface gravity, $\log(g)$, the rotation velocity at the surface at the equator, v_{surf}, the critical rotation velocity, v_{crit}, the Eddington factor, Γ, and abundances of 34 isotopes at both the stellar surface and in the center of the star, as listed below. Additionally, the mass of the final He core and CO core are included as a proxy for the mass of the compact object remnant (cf. Sect. 5).

The Bonn code simulates nuclear reaction networks for the following 34 isotopes: ^{1}H, ^{2}H, ^{3}He, ^{4}He, ^{6}Li, ^{7}Li, ^{7}Be, ^{9}Be, ^{8}B, ^{10}B, ^{11}B, ^{11}C, ^{12}C, ^{13}C, ^{12}N, ^{14}N, ^{15}N, ^{16}O, ^{17}O, ^{18}O, ^{19}F, ^{20}Ne, ^{21}Ne, ^{22}Ne, ^{23}Na, ^{24}Mg, ^{25}Mg, ^{26}Mg, ^{26}Al, ^{27}Al, ^{28}Si, ^{29}Si, ^{30}Si, and ^{56}Fe. They are all included in the published tables.

2.3. HR diagrams

Hertzsprung–Russell diagrams of all the BoOST stellar models are shown in Fig. 1. Additionally, Figs. 2–4 present various diagnostic diagrams showing important properties of stellar feedback such as mass-loss rate, wind velocity, and kinetic energy of the winds. As expected, both the zero-age main sequence and the supergiant branch shift to higher effective temperatures when the metallicity is lower due to the lower opacities. Furthermore, there are two features that gradually change from high to low metallicity: very luminous supergiants at high masses, and blue supergiants at lower masses (in the blue loop of the evolutionary models).

The luminous supergiants are the natural result of envelope inflation in these massive stars. As explained by Sanyal et al. (2015), for example, in stellar models close to the Eddington limit (Langer 1997), density and pressure-inversion regions can develop in the outer regions. In the absence of any user intervention (cf. the discussion in Sect. 4.1), the code deals with this by increasing the physical extent of the star, that is, by inflating the envelope and thus producing luminous supergiants (cf. also Sect. 5 of Szécsi et al. 2015 as well as Sanyal et al. 2017). These special supergiants have been shown to possibly contribute to the formation of globular clusters (in two different scenarios, the first presented by Szécsi et al. 2018 and the second in Szécsi & Wünsch 2019). Thus, with the metallicity coverage the BoOST grids provide, the door opens to studying the role of these supergiants in cluster and star formation research and beyond.

The blue loop is known to be sensitive to any change in physical parameters during the evolution. For example, Schootemeijer et al. (2019) presented stellar models with an SMC composition between $9-100\,M_\odot$ using various semiconvective and overshooting parameters. They showed that the presence or absence of blue loops depends on these parameters, as well as on the applied rotational velocity. In short, the phenomenon was found to be tightly linked to internal mixing. They did not study the effect of metallicity, but our models show that this influences blue loops as well. With both semiconvection and overshooting fixed ($\alpha_{sc} = 1.0$ and $\alpha_{over} = 0.335$; cf.

Sect. 2.1), and with the same initial rotational velocity chosen for all the models (100 km s^{-1}), we find no blue loops at metallicities above that of the SMC (consistent with Schootemeijer et al. 2019), while with decreasing metallicity, the feature becomes increasingly prominent. This may provide a way to improve our models in the future: because blue supergiants are observed in the SMC (Humphreys et al. 1991; Kalari et al. 2018), a next version of the BoOST grids, for example, may be computed with testing a higher semiconvective parameter.

3. Interpolation and population synthesis: Presenting SYNSTARS

We have developed the simple stellar population synthesis code SYNSTARS written in Python with libraries NUMPY (Oliphant 2006) and SCIPY (Virtanen et al. 2020). In addition to the actual population synthesis (to be discussed in Sect. 3.3), SYNSTARS is also able to interpolate between our precomputed stellar models (those presented in Sect. 2). Below we describe how the interpolation of the tracks is implemented (including preprocessing in Sect. 3.1) and what the published tables contain in Sect. 3.2.

3.1. Finding equivalent evolutionary phases

A stellar population consists of stars of varying initial masses. To construct them, we interpolate between the precomputed stellar models from Sect. 2. During the process, it is important to ensure that the resulting set of interpolated tracks shows only gradual changes. However, the evolutionary models of stars vary significantly between non-neighboring masses, especially within the wide mass range covered in this project. For example, a star with $9\,M_\odot$ has a different evolutionary path in the HR diagram from a star with $60\,M_\odot$ or from a star with $500\,M_\odot$. To correctly interpolate the evolutionary sequence of a star using sequences of neighboring masses, it is thus common to determine EEPs (Prather 1976; Bergbusch & Vandenberg 1992, 2001; Pietrinferni et al. 2004) between stellar models. EEPs are identified by using evolutionary features that occur across the range of stellar tracks, such as the amount of hydrogen burned in the core, and they represent different phases during the evolution of a star.

For our models we identified seven EEPs (labeled A to G). Each EEP was further subdivided into an equal number of points, so that each phase of stellar evolution was represented by a fixed number of points (i.e., lines in the data file) to ensure that the nth point in one model has a comparable interpretation in another model. The seven EEPs for different stellar models are shown in Figs. 5–7. The method of identifying these EEPs is explained below.

The first EEP (A) is the zero-age main sequence (excluding the initial hook phase caused by hydrogen ignition). The second EEP (B) is the local minimum of the mass-loss rate corresponding to the bistability jump, that is, when it occurs during the main sequence. If the local minimum of the mass-loss rate occurs after the main sequence ends, we chose the second EEP simply to be at about three-fourths of the main-sequence lifetime. Assigning our second EEP to the local minimum of the mass-loss rate ensures that the interpolation behaves nicely at quick changes in mass loss, which is an important requirement when these models are to be applied to studying their feedback on star formation.

The third EEP (C) is the tip of the hook at the end of the main sequence. However, for very massive stars, this hook is not visible; in this case, we simply chose a point close to core hydrogen-exhaustion. The fourth EEP (D) is the bottom
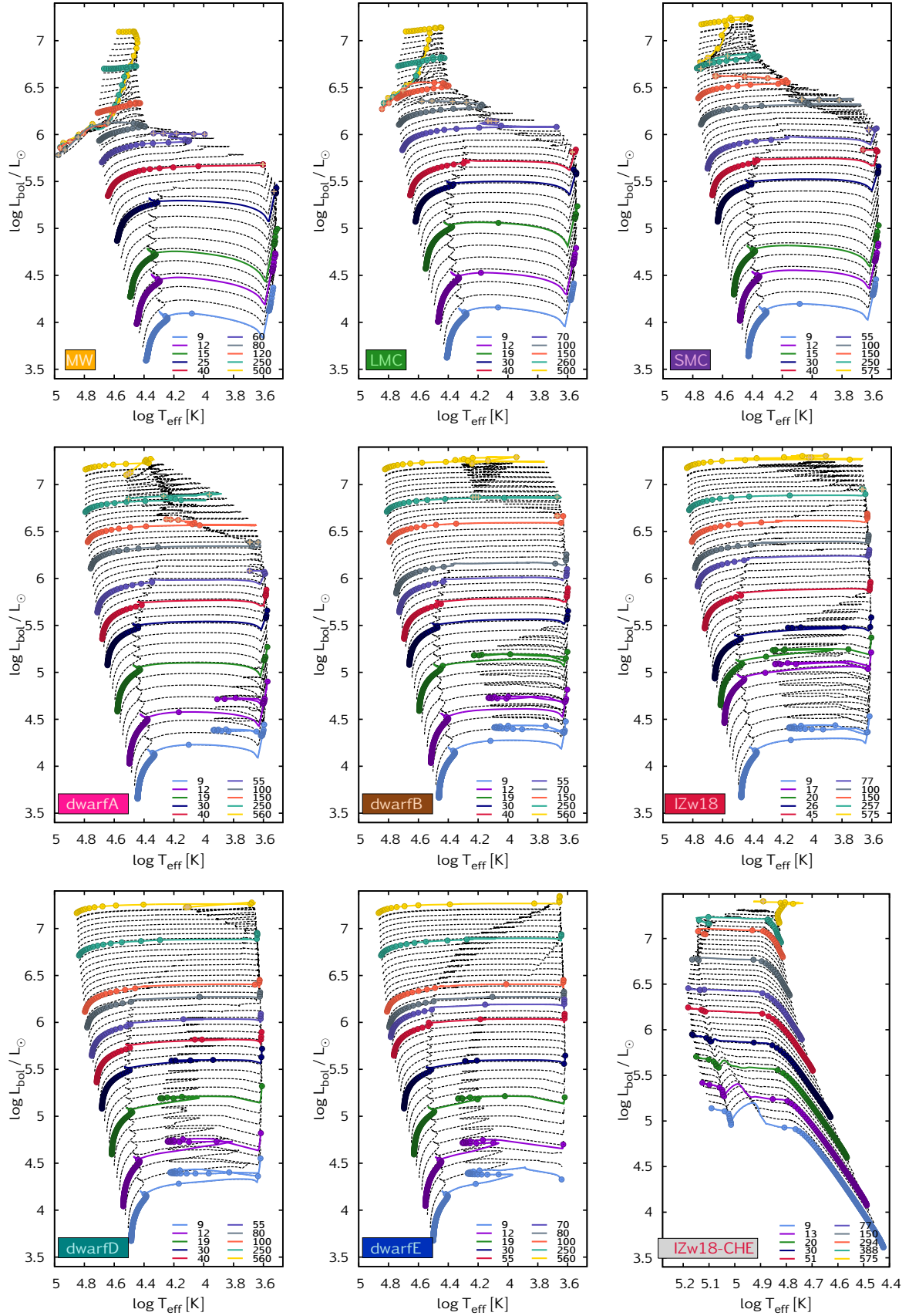
Fig. 1. Hertzsprung–Russell diagrams. Initial mass is color-coded (between 9 and ∼500 $M_\odot$); dots mark every 10^5 yr of evolution along the stellar models. Dashed black lines represent interpolated tracks (up to 500 $M_\odot$); brown crosses mark the phases in which the direct extension method (Sect. 4) has been applied. For details about the models and their postprocessing, see Sects. 2 and 4, respectively, and for details about the interpolated tracks, see Sect. 3.
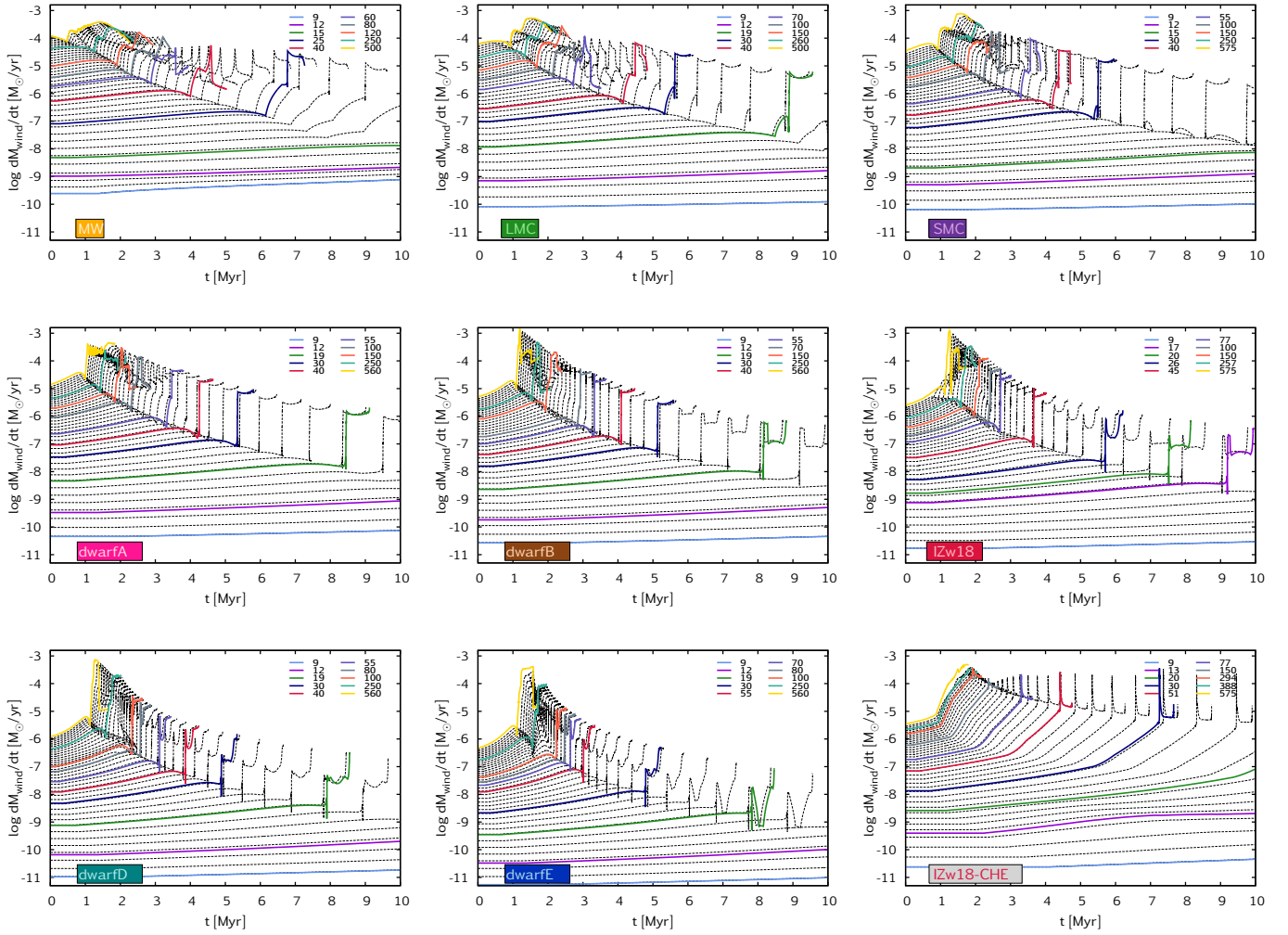
Fig. 2. Time evolution of the mass-loss rate. The initial mass is color-coded (between 9 and ~500 $M_\odot$). The dashed black lines represent interpolated tracks (up to 500 $M_\odot$); cf. Fig. 1.. While here only shown until 10 Myr, the files published in the BoOST project contain data until the end of the lifetimes of the longest-living model in the population (~30 Myr).

of the red supergiant branch where the luminosity has a local minimum. If this was not visible, for instane, in the case of an extreme blue loop without a base at the red supergiant branch, a point in the middle of the loop blueward progression was chosen. Some examples are shown in Fig. 6.

The fifth EEP (E) is the middle of the helium-burning phase. It corresponds to the hottest point of the blue loop if there is one, otherwise, $Y_C \sim 0.5$. The sixth EEP (F) is chosen near the end of core helium-burning when the model has a small dip in luminosity. If this was not visible, we chose a point at around $Y_C \sim 0.1$. The seventh EEP (G) is the end of the helium-burning phase where $Y_C = 0.0$, and we did not include carbon burning in our models.

For the most massive models at high metallicities, we chose the EEPs to be equally distributed in time during the luminous blue variable phase because these stars have no systematically recognizable surface features except for their extremely strong winds. Some examples are shown in Fig. 7.

The precomputed stellar evolutionary models were filtered so that the published files are in EEP format. To choose the number of points between each EEP, we followed the convention established by Choi et al. (2016). Our EEPs occur at lines 1, 151, 252, 403, 429, 505, and 608 for each stellar track. We did not include the pre-main-sequence phase of stars in our models:

all models start their evolution at the zero-age main sequence. Consequently, BoOST models have 200 fewer lines than those in Choi et al. (2016). The simulation of the pre-main-sequence phase for these very massive stars is hardly physical because a clear picture of how they form in reality is still lacking. Thus, following a pre-main-sequence path that imitates the behavior of low-mass stars on the pre-main-sequence is not more realistic than starting out with a homogeneous zero-age main-sequence model and evolving the star from there on, as we did.

3.2. Interpolation with SYNSTARS

The precomputed and EEP-filtered stellar models were read in by SYNSTARS for each model characterized by its initial mass, M_0. Several additional quantities were calculated by SYNSTARS, namely, the velocity of the stellar wind, v_{wind}, was determined with the procedure suggested by Lamers & Cassinelli (1999) and Vink et al. (2001) following from the theory of line-driven winds,

$$v_{wind} = \begin{cases} 1.3v_{esc} & \text{for} \quad T_{eff} < 21 \text{ kK} \\ 2.6v_{esc} & \text{for} \quad T_{eff} > 21 \text{ kK} \end{cases}, \tag{1}$$

where $v_{esc} = (2GM/R)^{(1/2)}$ is the escape velocity from the stellar surface and G is the constant of gravity. Additionally, following
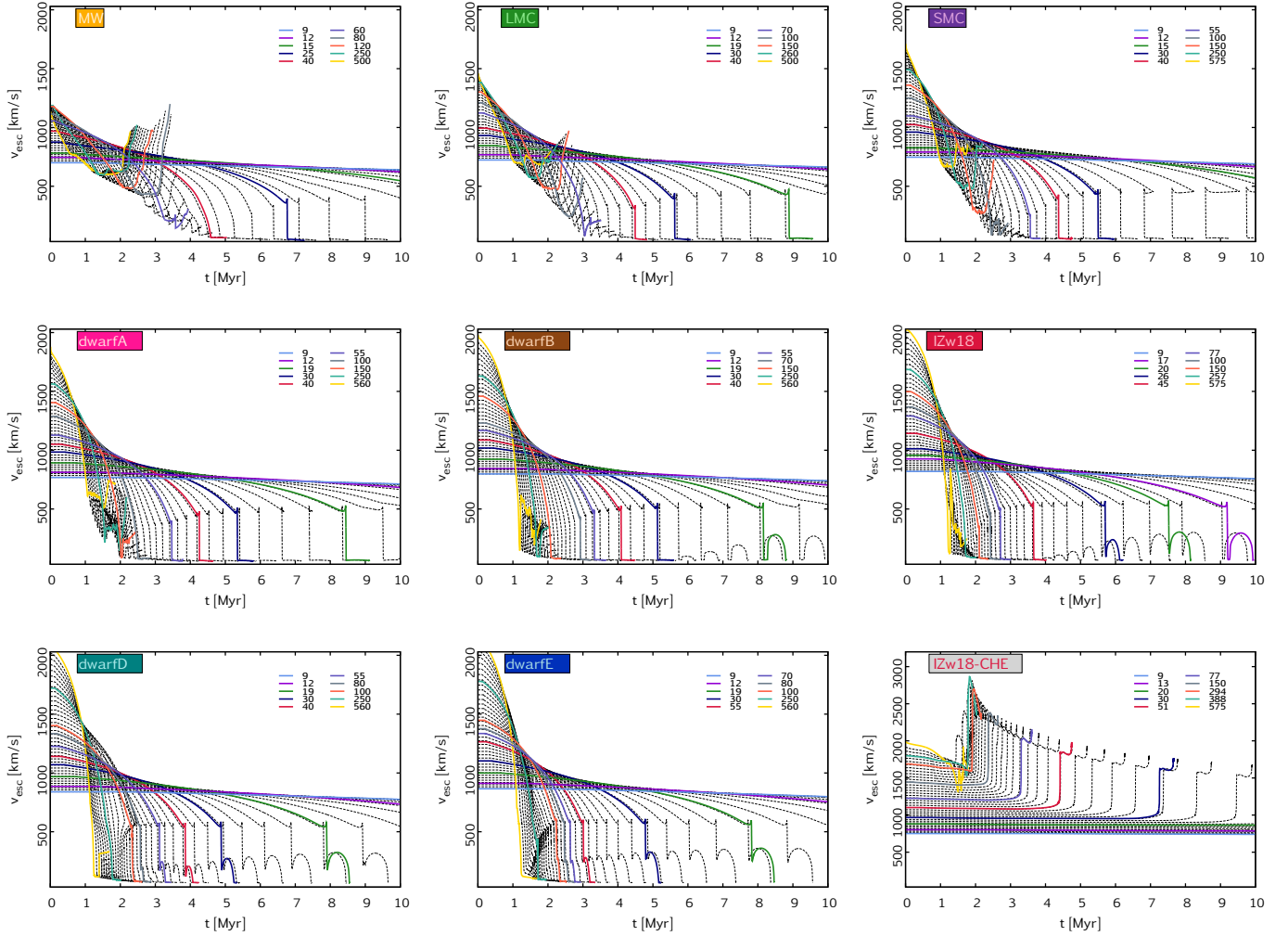
Fig. 3. Time evolution of the escape velocity; cf. Eq. (1). The initial mass is color-coded (between 9 and ~500 $M_\odot$). The dashed black lines represent interpolated tracks (up to 500 $M_\odot$); cf. Figs. 1 and 2. While here only shown until 10 Myr, the files published in the BoOST project contain data until the end of the lifetimes of the longest-living model in the population (~30 Myr).

Leitherer et al. (1992), for instance, the wind velocity was corrected for the metallicity of the wind material, Z, by multiplying it by a factor $(Z/Z_\odot)^{0.13}$. Furthermore, the wind power was given by $L_{mech} = \dot{M}v^2_{wind}/2$.

Interpolated tracks with M_0 between the EEP-filtered models were then calculated with SYNSTARS. The interpolation was performed separately for the stellar age, t, and for all the other quantities, using the SCIPY function INTERPOLATED-UNIVARIATESPLINE implementing the spline interpolation method of a given order. The stellar age, $t(M_0)$, was interpolated in the $\log(t) - \log(M_0)$ space using splines of the second order by default. This default can be changed by the user; however, we found while testing various choices that the first-order interpolation can lead to unphysical discontinuities in quantities integrated over the stellar population (cf. Cerviño et al. 2001, who documented a similar effect). All the other quantities, $Q(M_0)$, were also interpolated in the $\log(Q) - \log(M_0)$ space, but the default order for them is 1, that is, the interpolation is linear, to avoid errors due to overshooting for quantities that change abruptly (e.g., abundances).

The interpolated tracks computed with SYNSTARS are presented in Fig. 1 in the HR-diagram, and in Figs. 2–4 in terms of mass-loss rate, wind velocity, and kinetic energy deposition rate of the wind. As these quantities are typically needed to study

stellar feedback in star formation, we especially ensured that they did not include any numerical artifacts.

We used only the initial mass as the basis for the interpolation. In some of the grids we used stellar models with 560 or 575 $M_\odot$ as the highest mass (cf. Sect. 2.2), but still took the upper limit $M_{top} = 500 \, M_\odot$ for the interpolated set of tracks to be consistent.

We tested the validity of our interpolation method by comparing interpolated tracks and their corresponding original models in Fig. 8. The largest difference in terms of surface temperature is 0.47 dex, and in terms of luminosity, the difference is 0.08 dex, meaning that the interpolated tracks match the original models well within the error margins of massive star evolution.

We publish the interpolated (synthetic) tracks as one large data table per grid. These files contain 1856 records between 9 $M_\odot$ and 498.4 $M_\odot$, equally distributed in $\log(M_0)$, all having 608 lines. (Figures 1–4 only show every 50th interpolated track for clarity.) Thus, the size of this data file is about 800 MB. Tracks are marked by their initial mass values before their record starts (in $M_\odot$ and in cgs units). The following columns are provided (cf. the Readme file next to the published tables): initial mass, time, actual mass, wind velocity, kinetic energy generation rate of the wind, luminosity, radius, effective temperature, mask, type of interpolation, surface rotational velocity,
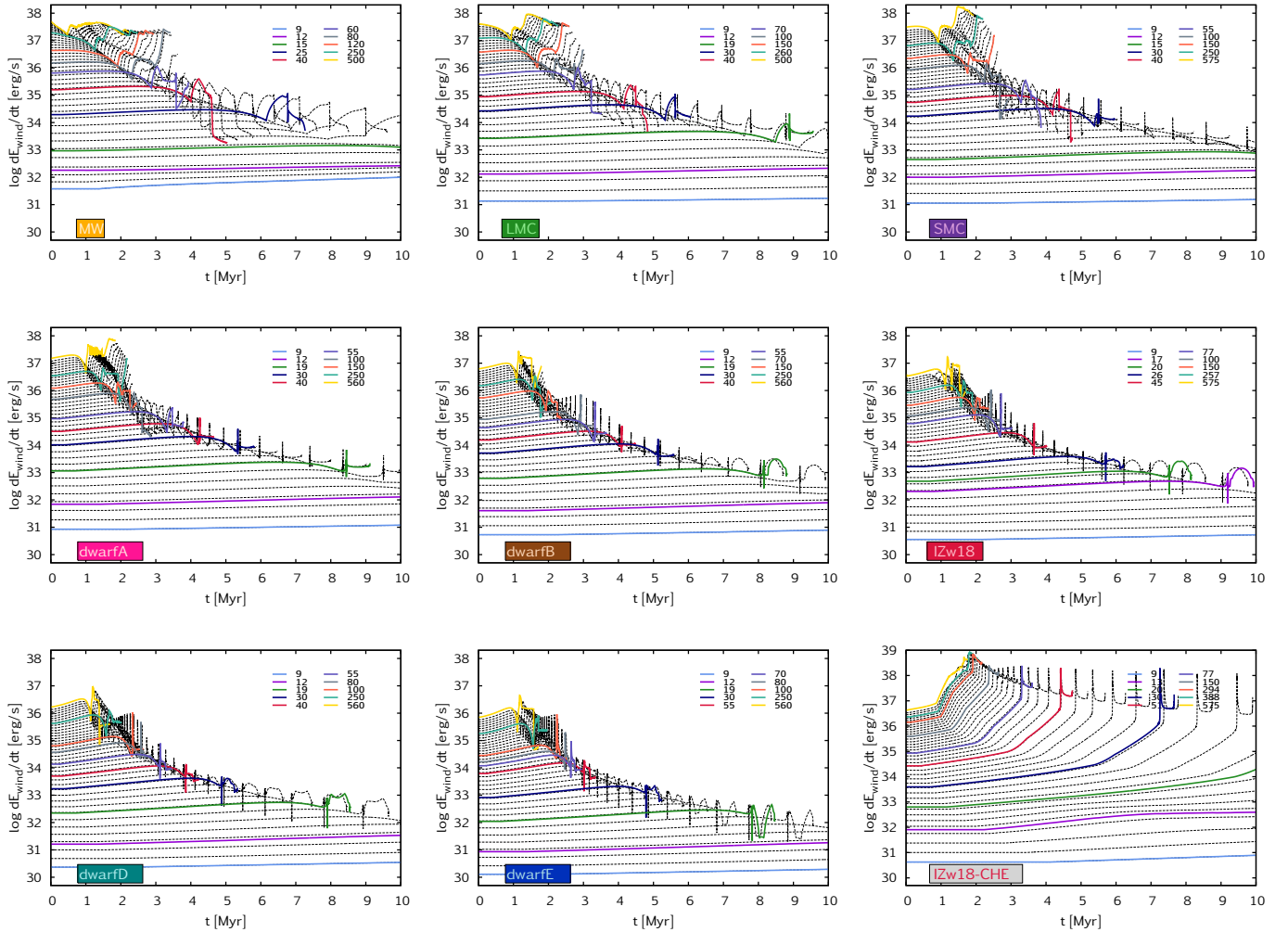
Fig. 4. Time evolution of the wind kinetic energy rate. The initial mass is color-coded (between 9 and ~500 $M_\odot$). The dashed black lines represent interpolated tracks (up to 500 $M_\odot$); cf. Figs. 1–3. While here only shown until 10 Myr, the files published in the BoOST project contain data until the end of the lifetimes of the longest-living model in the population (~30 Myr).

critical rotational velocity, Eddington factor, flag marking whether the phase includes the direct extension method of Sect. 4 or not, helium-core mass, carbon-oxygen core mass, and surface mass fraction of the same 34 isotopes as in the original stellar models.

3.3. Synthetic populations

Synthetic populations of single massive and very massive stars are also computed with SYNSTARS based on the interpolated tracks. The population data we publish here represent massive star clusters with a total mass of 10^7 $M_\odot$ that were formed as the result of a single, burst-like star formation event in which the initial mass function follows a classical Salpeter distribution (with an upper mass limit of 500 $M_\odot$). The evolution of these populations is presented in the data files with equal time-steps up to ~25 Myr, that is, when the life of the longer-living star of our models (the star with 9 $M_\odot$) ends. After this, such a cluster will only contain stars below 9 $M_\odot$, the contribution of which to feedback processes can typically be neglected. In addition, the compact object remnants of the dead massive stars are also expected to still be within the cluster (see Sect. 5, and we note that remnant types are not specifically listed in the published tables, only final core masses are).

The current version of SYNSTARS is attached to the published data. Thus if needed, the user can feed the precomputed stellar grids to it and create their own interpolated tracks or their own synthetic populations. For example, the interpolated tracks and populations computed here have an upper mass of 500 $M_\odot$, but the user may need populations with an upper mass limit that is lower than this. Thus they can create their own synthetic population with 150 or 250 $M_\odot$ as an upper mass, for example, and even change the index of the mass function and the total mass of the stellar cluster. (For the highest mass achievable with SYNSTARS, see the precomputed models with the highest mass in the grids, Sect. 2.2.) A typical run of SYNSTARS creating thousands of tracks takes a few minutes on a normal workstation.

Alternatively, the user may wish to use their own population synthesis tool. This is also a possibility because one of the outputs of SYNSTARS is the set of interpolated stellar tracks, and their resolution (bin size) can be defined simply as a command line input. These interpolated tracks can then be fed into any population synthesis code, thus providing great flexibility for the user.

In the synthetic population data files created by SYNSTARS (not the same as the interpolated track data tables), the following quantities are given as a function of time (also see the Readme file attached to the tables): mass lost from stars in the form of fast
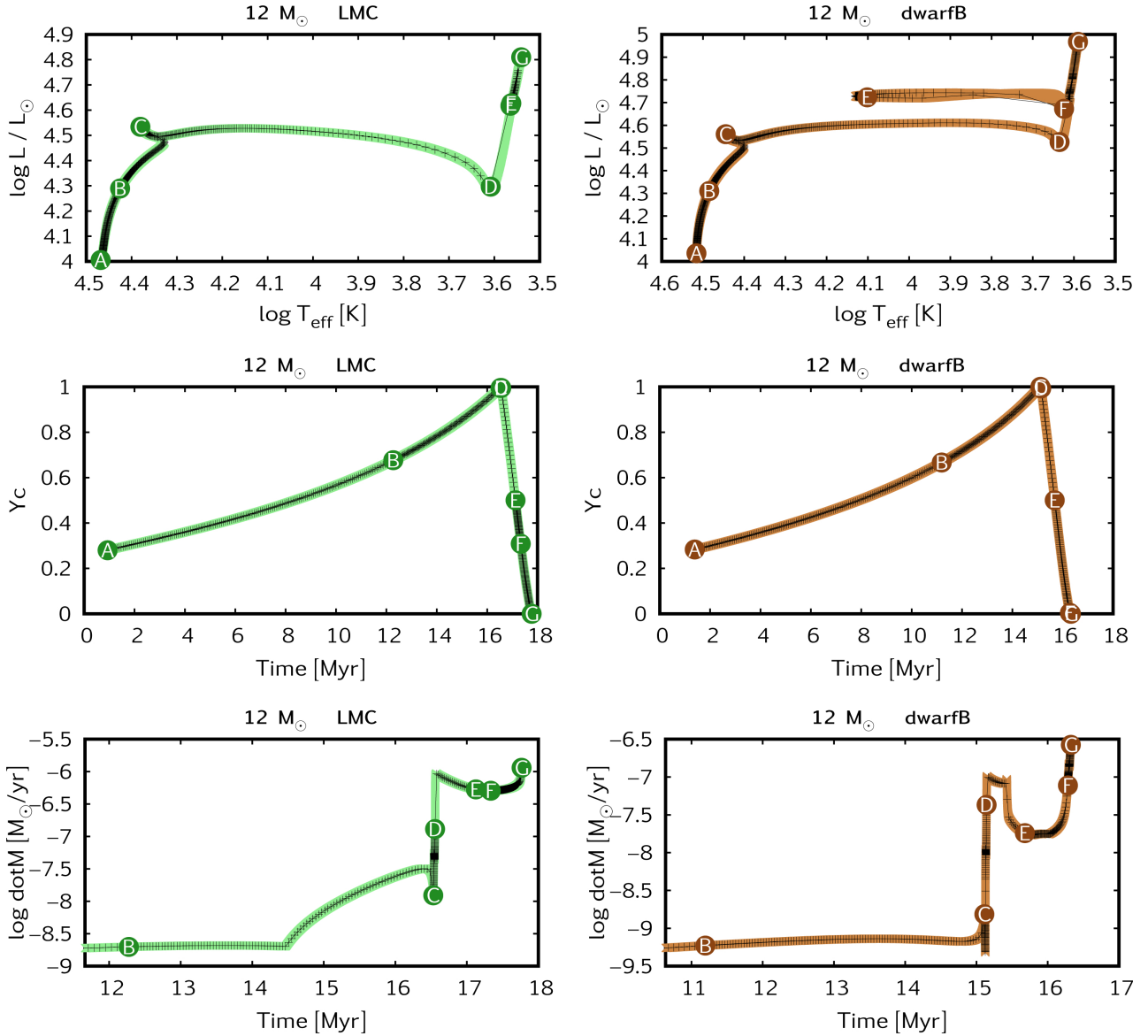
Fig. 5. Position of EEPs (i.e., fixed points in evolution) during the lifetime of some typical models. Colored lines represent the original output of our computations with the Bonn code, and black lines and crosses mark the filtered version (consistently containing the same number of dots between EEPs). The seven EEPs are labeled A–G; our method of choosing them is explained in the text.

stellar wind (i.e., faster than 100 km s^{-1}), mass lost from stars in the form of slow stellar wind (i.e., slower than 100 km s^{-1}), kinetic energy in the fast winds, integrated bolometric luminosity, integrated UV flux (including corrections for optically thick stellar winds, following the method presented in Szécsi 2016, cf., Chapt. 4.5.1), time-integrated values of Ṁ and Ė, that is, the total mass and mechanical energy produced (in the form of winds and their power) by the all stars up to a given time, as well as the mass fraction of all 34 isotopes in the wind (i.e., integrated over the population).

3.4. Red supergiant luminosity histogram

To test our stellar populations against observations, we created a luminosity histogram as in Neugent et al. (2020). Our results are shown in Fig. 9 for an MW composition, to be compared with two sets of super-solar M31 observations (Neugent et al. 2020; Massey et al. 2021). Following the method presented in Neugent et al. (2020, see their Fig. 11c), we normalized the num-

ber of red supergiant stars in our theoretical sample to 1000. We defined red supergiants as log T_{eff} < 3.7 (Neugent 2021, priv. comm.).

As Fig. 9 attests, our models reproduce the observations of red supergiant luminosities as closely as other published sets of stellar models. Because we worked only with massive stars, our stellar models have a lower mass limit at 9 $M_\odot$, meaning that our data do not contain any assymptotic giant branch stars. Therefore our theoretical histogram does not reach below $L \sim 4.2$.

4. Numerically problematic late phases of stellar evolution

4.1. Role of the Eddington limit

The maximum luminosity that can be transported by radiation while maintaining hydrostatic equilibrium is called the Eddington luminosity (Eddington 1926). However, in the envelopes of massive stars, where the density is low, changes in the elemental
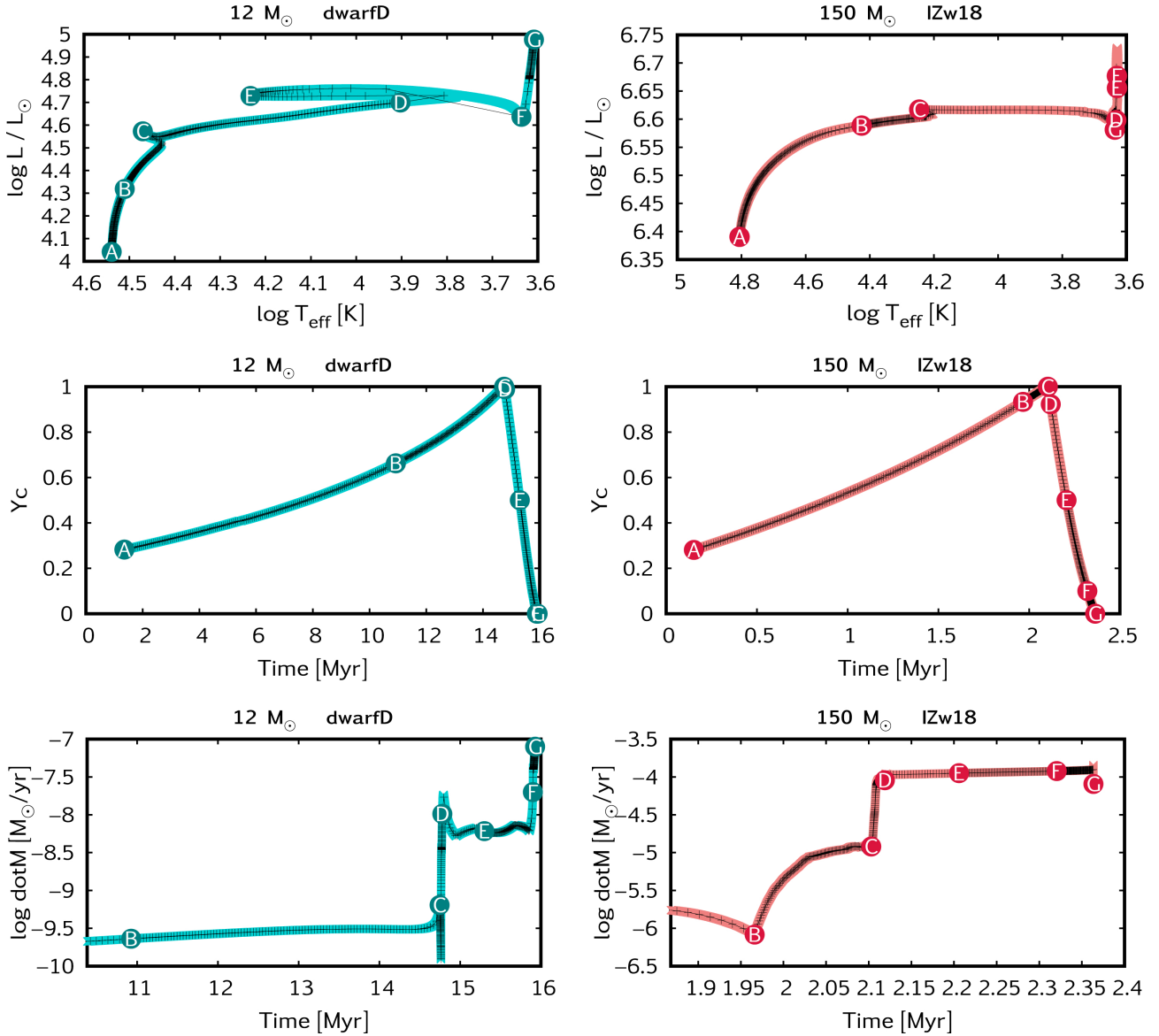
Fig. 6. Same as Fig. 5 but for a model with prominent blue loop (without a starting point in the red supergiant branch, *left*) and one with inflated envelope (*right*). For more details on the latter, which is a core-hydrogen-burning supergiant, we refer to e.g. Sanyal et al. (2015, 2017), Szécsi et al. (2015, 2018), Szécsi & Wünsch (2019).

opacities can cause the local radiative luminosity to exceed this Eddington luminosity (Langer 1997; Sanyal et al. 2015). To maintain hydrostatic equilibrium, density and pressure inversions develop in such envelopes. In the absence of efficient convection (which is also typical for the low-density envelopes of massive stars, Grassitelli et al. 2016), this can lead to numerical difficulties in 1D stellar evolution codes (Paxton et al. 2013), meaning in practice that the time-steps become exceedingly small, preventing further computation of the model. While less massive and less metal-rich stars are only affected by this issue in their late evolutionary phases, more massive and high-metallicity stars (at $\gtrsim 40\,M_\odot$ for solar composition) can exceed the Eddington limit inside their envelopes already during the core hydrogen-burning phase (Gräfener et al. 2012; Sanyal et al. 2015).

Stellar evolution codes employ pragmatic solutions to avoid or overcome the above-mentioned numerical difficulties (Agrawal et al. 2021b). For example, in the PARSEC stellar models, an artificial limit is set for the temperature gradient (see Sect. 2.4 of Chen et al. 2015, as well as Alongi et al. 1993), which ensures that the density gradient never becomes negative and thus inefficient convection is prevented. Additionally, a mass-loss enhancement following (Vink et al. 2011) is applied whenever the total luminosity of the star approaches the Eddington luminosity. On the other hand, in the MIST stellar models (Choi et al. 2016) computed with the MESA code (Paxton et al. 2013), density inversions are suppressed through the MLT++ formalism: the actual temperature gradient is artificially reduced to make it closer to the adiabatic temperature gradient whenever the radiative luminosity exceeds the Eddington luminosity above a predefined threshold. Radiative pressure at the surface of the star is also enhanced. This approach again increases the convective efficiency, helping the stars to overcome density inversions. Yet another pragmatic solution is employed in the GENEVA models (see Sect. 2.3 of Ekström et al. 2012): the mixing length is set to be comparable with the density scale height, which helps avoid density inversions (Nishida & Schindler 1967; Maeder 1987), while the mass-loss rates are increased by a factor of three
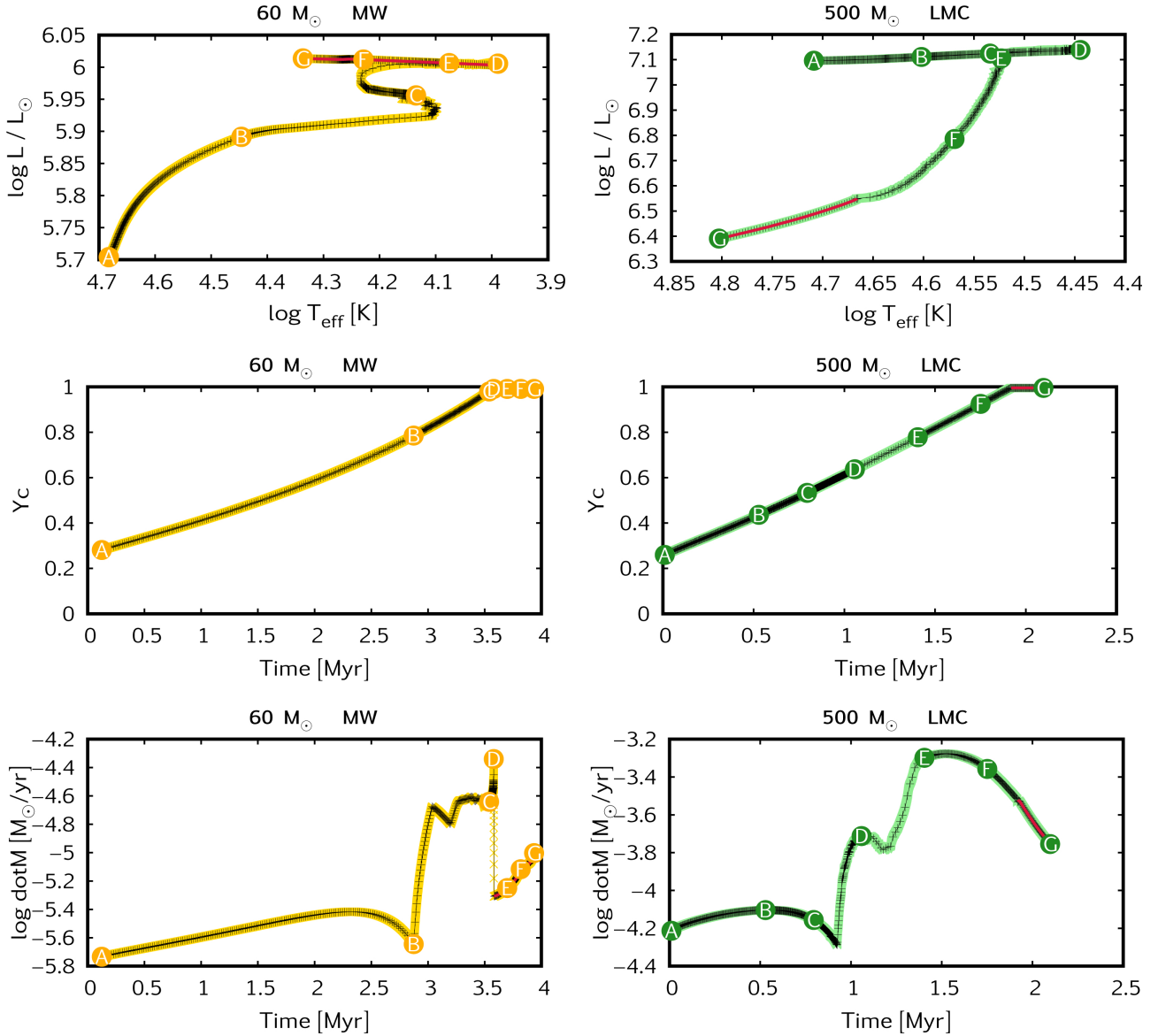
Fig. 7. Same as Fig. 5 but for models that show features associated with a luminous blue variable phase before becoming Wolf-Rayet stars. In both cases, we use our newly developed method for a direct extension in the post-main-sequence phase (that is, removing mass layers one by one from the last computed model's envelope and correcting for the values of the surface properties, as explained in Sect. 4). Red line marks this phase of stellar life.

whenever the local luminosity in any of the layers of the envelope is higher than five times the local Eddington luminosity.

Most of the stellar models in this work are not effected by the above-mentioned numerical difficulties, and are thus computed with the Bonn code without interruption until their core helium is exhausted. However, the very massive high-metallicity models do develop density inversion regions due to their proximity to the Eddington limit. Instead of artificially avoiding or surpassing these density inversions, we employed another solution.

4.2. Another solution: Inflated envelopes and the direct extension method

If the density and pressure inversions are not avoided in some pragmatic way (as above), the envelope grows (or inflates, Gräfener et al. 2012; Sanyal et al. 2015, 2017), and the star may become a core hydrogen-burning cool supergiant (cf. Sect. 5 of Szécsi et al. 2015). These cool supergiants might explain

globular cluster formation (Szécsi et al. 2018; Szécsi & Wünsch 2019). Because we wish our models to be applicable in this field of research, and because for these masses, the available observational constraints cannot exclude the existence of stars with such inflated envelopes, we continue the approach of the previously published Bonn models, and let the envelope of all our stars inflate as well. This makes our BoOST models special amongst other stellar evolutionary models, but it comes at a cost.

In some models (those with very high mass and high metallicity), the time-steps become exceedingly small and the computation is halted before the end of core helium-burning is reached. These models need to be further treated in postprocessing (we call this the direct extension method, see below), to make them ready to still serve as a proxy for the chemical yields and radiation of the remaining lifetimes. In terms of stellar populations, the missing phases comprise less than 3% of the stellar lifetimes because the Eddington-limit proximity only influences the most massive models, which live shorter lives. Moreover, the lower
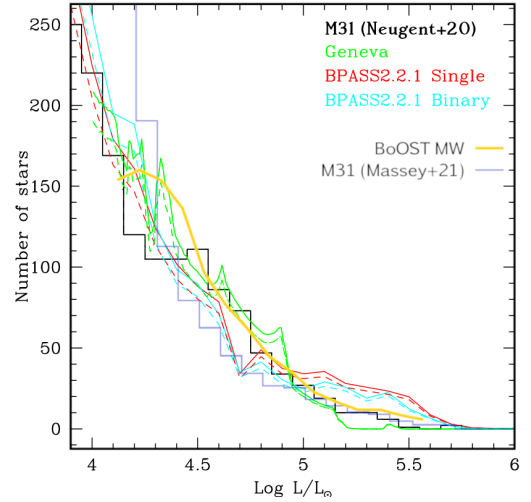
Fig. 9. Luminosity histogram of our BoOST models with an MW composition (yellow). The original is taken from Neugent et al. (2020), including M31 observations (black) and theoretical predictions from the Geneva (green) and BPASS stellar models (red and blue) for solar metallicity. An even larger and more recent dataset of M31 observations from Massey et al. (2021) is overplotted (violet). Our MW population follows the observed luminosity histograms as closely as the Geneva and BPASS stellar models. See Sect. 3.4 for further details.

are computed in the code, including the chemical composition of the layer. When the computation was halted due to the above-mentioned numerical difficulties, we postprocessed the data by removing mass from the surface layer by layer from the last computed structure model. This approach allows us to predict the composition of the material ejected by the stellar winds even during the phases for which the code did not converge.

We continued to remove layers until the projected lifetime of the star ended. The projected lifetime was estimated as follows. If the model had already burned away at least 2% of helium when the simulation stopped, the remaining lifetime was calculated by linearly extrapolating the central helium abundance as a function of time until it reached zero. If the model had not burned that much helium, but stopped before this (e.g., at the terminal-age main sequence), the remaining lifetime was simply defined as 10% of the main-sequence lifetime. In five cases (cf. Table B.2) was the terminal-age main sequence not reached: here first we established the projected main-sequence lifetime by quadratically extrapolating the central helium mass fraction as a function of time, and then again assumed that the post-main sequence lasts for 10% as long as the main sequence. We ensured that the whole process, including the quadratic extrapolation, provided a good estimation for the projected lifetimes by testing it on existing models. For stars that lose much mass, however, the process may only provide a lower limit because the lifetime of stars is inversely proportional to the actual mass.

Mass-loss rates. During the direct extension phase, the same mass-loss rate prescriptions were applied as in the stellar evolution code. Namely, Nieuwenhuijzen & de Jager (1990) rates were applied for supergiants with $T_{\rm eff} < 22\,500$ and $X_{\rm surf} > 0.45$, and Hamann et al. (1995) scaled by ten (which is consistent with Nugis & Lamers 2000 and is representative of Wolf–Rayet stars) otherwise. In both cases, a metallicity dependence of $\sim Z^{0.86}$ was included, following Vink et al. (2001).

HR diagram and radius. If mass layers are removed from a stellar model, this is expected to change the stellar structure

Fig. 8. Validating the interpolation. Colored lines represent the original stellar models (IZw18 grid), dotted black lines represent the interpolated tracks created by removing the corresponding original while performing these test interpolations. See also Sect. 3.2.

the metallicity, the less relevant this effect: for example, in our lowest metallicity grid called dwarfE, all the models, even the inflated ones, are properly computed until the end. In Fig. 1, crosses mark the models that were postprocessed with the direct extension method, and the tables in Appendix B.2 provide some quantitative summary. Eight of the 90 models have evolved past the end of the main sequence, but stopped short of completing core helium-burning, and 27 of the models stopped at the end of the main sequence. These are therefore the models for which we developed the method below. The remaining 58 models are complete.

4.3. The method

A 1D stellar evolutionary model sequence consists of consecutive stellar models (structure models, or profiles) belonging to a certain age. One such structure model consists of about 1500 grid points (layers) between the core and the surface. For every layer, physical variables such as local temperature and density
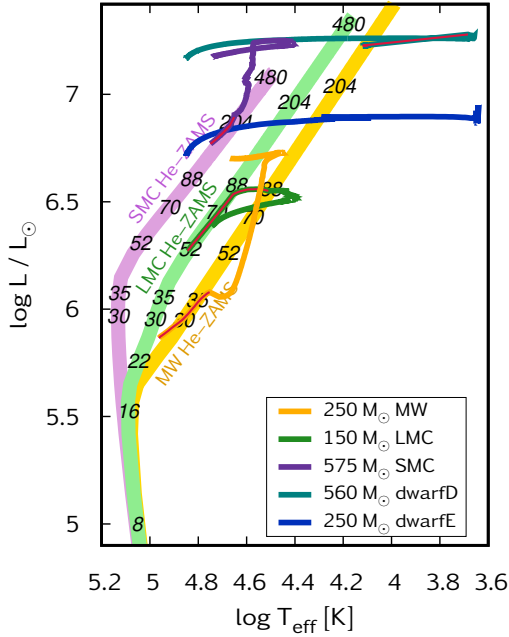
Fig. 10. Example of the results of the direct extension method (Sect. 4). The complete evolution of five stellar models (see the key legend) is plotted. The direct extension phase (typically lasting for 9% of the lifetime of these particular models) is marked with red in four of them (MW, LMC, SMC, and dwarfD); the fifth model (dwarfE) was properly computed without interruption, and is shown here as reference. During the direct extension phase, the models converge to their corresponding helium ZAMS position while loosing mass from their surface layers (cf. Sect. 4.3). Helium ZAMS positions in the HR diagram are shown for MW, LMC, and SMC compositions. The details of constructing these lines are given in Appendix B.1. Numbering indicates stellar masses (in $M_\odot$).

and thus influence surface temperature and luminosity, and hence not only the radius of the star, but also the total ionizing radiation, which is important for stellar feedback predictions. We accounted for this by causing these quantities to transition towards the so-called helium zero-age main sequence (helium ZAMS, cf. Appendix B.1) in the HR diagram. To achieve smoothness, we took the surface temperature and the surface luminosity to be log-linear functions of the surface helium mass fraction. The stellar radius was calculated from these according to the Stefan-Boltzmann law. When a layer was removed, the helium mass fraction of the next layer was used as a weight to find the new surface temperature and luminosity values between the old ones and those of the helium ZAMS given the new total mass of the star. In this way, the stellar models in the HR diagram converged smoothly and directly towards the helium ZAMS while losing mass from the surface layers. Examples are shown in Fig. 7 and Fig. 10.

4.4. Caveats

Numerical difficulties in stellar modeling are a known issue (Aarseth et al. 2008); we have summarized some of the solutions offered by modelers in Sect. 4.1. The common feature of all these solutions is that they are pragmatic: technical maneuvers usually need to be employed for models to evolve without interruption. In the absence of a homogeneous sample of massive stars observed through various metallicities and various evolutionary phases, based on which 1D stellar evolutionary models could be

constrained, none of the solutions can be established as preferable over the others. Our solution, in which the inflated envelope develops and the remaining life is continued by carefully post-processing the models when numerical issues are encountered, is just one possible way to solve the common issue in stellar evolution modeling pragmatically. The inflated-envelope phase has special astrophysical applications (Moriya & Langer 2015; Szécsi et al. 2015, 2018; Szécsi & Wünsch 2019) that make our BoOST models especially useful in globular cluster research, for example.

While our direct extension method is quite robust and provides an acceptable approximation for the late phases of very massive stars, there necessarily are some caveats. Removing layers from the last computed structure model involves the assumption that no more mixing occurs during the remaining lifetime. This may not be true. The evolution of stars near the Eddington limit is unclear, and the projected lifetimes ignore remaining changes in the model until the end of helium burning. As no nuclear reactions are simulated for this phase, the central quantities in our output files are simply kept the same as in the last simulated structure model. We add a flag to all our published tables to indicate when this is the case. All these caveats should be kept in mind when using BoOST populations.

Helium stars are expected to evolve away from the helium ZAMS during their nuclear burning lifetime. In the absence of properly computed helium star evolutionary models in a sufficiently wide mass range (as explained in Appendix B.1), we approximate the post-main-sequence position of our helium stars simply by the helium ZAMS position. This is still within the error bars of massive star physics. In other words, the fact that the mass-loss rates of these stars so unconstrained, for example, introduces a larger uncertainty in any grid of stellar models than our simple treatment of the direct extension towards the helium ZAMS.

We emphasize that the direct extension method did not need to be applied for most of the published data (in terms of stellar lifetimes, >97% of the published data are properly computed with the code; also cf. Fig. 1, where crosses indicate when the method is applied). Even at high metallicities, only the latest phases of the tracks are influenced; and at low metallicies, we hardly had to apply it at all, as shown by the tables in Appendix B.2. The reason for this is that envelope inflation starts at higher masses when the metallicity is low (Sanyal et al. 2017). In our lowest-metallicity grid with $1/250\,Z_{MW}$, even the highest-mass star of 560 $M_\odot$ is computed with the Bonn code without any numerical issues until the end of core-helium exhaustion, making the grid called dwarfE perfectly complete; and for applications in which the upper mass in the population is chosen to be 150 $M_\odot$, the IZw18 grid can be used without problem as well because up to this mass, it is not influenced by the DEM treatment.

5. Final-fate predictions

5.1. Final core-mass estimates

The core mass of a pre-supernova star before the collapse (defined either as the helium-rich or the carbon-oxygen-rich central region) is often used as an estimated upper limit for the mass of the compact remnant (Belczynski et al. 2002, 2008; Fryer et al. 2012). While our modeling stops before carbon burning begins, we provide a proxy for these pre-supernova core-mass values based on the status of the model at the end of core-helium burning. Our models develop a carbon- and

oxygen-rich core in this phase already because helium mainly burns into carbon and oxygen. We define the He core mass to be the mass coordinate where the mass fraction of everything but helium drops below 12%, and the CO core mass where the mass fraction of everything but carbon and oxygen drops below 12%.

During the remaining evolution, the inner regions of the core would undergo nuclear processing, and the core mass would change somewhat: for a naked helium star because mass is lost in the hot wind, and for a hydrogen-rich star because shell helium-burning replenishes the core with more carbon and oxygen. However, because core carbon-burning and the subsequent burning phases last for about 1% of the life of a massive star, these changes are expected to be minor enough for an order-of-magnitude estimate. For example, Chieffi & Limongi (2013) reported that in their Solar metallicity models (computed with the FRANEC code, see their Table 1), stars in the mass range of $13-40\ M_\odot$ change their CO core mass during the post-helium-burning phases by merely $1-4\%$ in terms of the initial mass; and stars in the mass range of $60-120\ M_\odot$ do so typically by $3-8\%$. (The situation is further complicated by the technical difficulty of defining core masses throughout the life of a star; we refer to Sect. 3.3 of Kruckow et al. 2018 for further discussions and references.) We therefore suggest that the pre-carbon-burning core mass values we provide for our models can serve as an order-of-magnitude estimate for the pre-supernova values.

In the case of the models for which the direct extension method was applied (Sect. 4), the definitions above do not always hold because the core composition may not yet have reached the required amount of carbon and oxygen. Therefore, we define the CO core mass for these models as 0.8 times the He core mass. We chose this value because we found that the CO cores of models that are not treated with the direct extension method are about 0.7–0.8 times as massive as their corresponding He cores.

5.2. Assigning supernova types to stellar models

Associating supernova types with stellar models is a complex task, hence simplifying assumptions are often made. In star formation studies, for example, when the feedback from supernova explosions is included, it is commonly assumed that all massive stars explode as core-collapse supernovae (e.g., Gatto et al. 2017). Moreover, the kinetic energy of the explosion is sometimes simply taken uniformly to be 10^{51} erg. We suggest caution with this approach, especially when our very massive BoOST models are applied, for the following reasons.

In the case of very massive CO cores, stellar models are known to undergo pair-creation related instability during their oxygen-burning phases (Burbidge et al. 1957; Langer 1991; Heger et al. 2003; Langer et al. 2007; Kozyreva et al. 2014). This is in fact what would occur in our very massive models as well if their simulations were continued after the helium burning. Thus, simply associating such a stellar model with a core-collapse supernova explosion is inaccurate. Instead, very massive models are expected to undergo one of the following final fates (relying on the work of Heger & Woosley 2002; Woosley et al. 2007 and Chatzopoulos & Wheeler 2012).

For core masses higher than $130\ M_\odot$, the star will directly collapse into a black hole without a supernova explosion.

For core masses between $65-130\ M_\odot$, the model will explode as a pair-instability supernova. This will completely disrupt the whole star, leaving no remnant. The brightness of such a supernova depends strongly on the amount of nickel that is synthesized (Herzig et al. 1990; Dessart et al. 2013), but according to

the analysis of Kasen et al. (2011), some of these supernovae should be observable out to large distances. The total explosive energy in such a stellar model is about $10^{51}-10^{52}$ erg.

For core masses between $40-65\ M_\odot$, the model will undergo pair instability but should not explode in a pair-instability supernova explosion. Such a model may be associated with large pulsations leading to mass ejection and flashes of emitted light, which is called a pulsational pair-instability supernova (Woosley et al. 2007; Sukhbold et al. 2016; Stevenson et al. 2019). However, these models will continue their evolution until an iron core forms, and will then explode as a core-collapse supernova.

For core masses below $40\ M_\odot$, iron core collapse is expected, which may lead to a regular core-collapse supernova.

Since research on core-collapse supernovae, pair-instability supernovae, and pulsational pair-instability supernovae is currently ongoing, we suggest that the user investigate the related literature for further developments before assigning supernova types to our models. No core-collapse type supernova explosions should be assigned to models with cores above $130\ M_\odot$ in any case: these certainly do not explode, as explained above. We also suggest to refrain from assigning remnant masses to models with cores between $65-130\ M_\odot$: these do explode, but leave no remnant.

The situation for our chemically homogeneously evolving grid IZw18-CHE may become even more complicated due to the fast rotation of these models. Models with core masses of $\sim12-30\ M_\odot$ may be progenitors of long-duration gamma-ray bursts in either the collapsar or the magnetar scenario, as explained in Szécsi (2017); also cf. Chapter 4.7 of Szécsi (2016). For the pair-instability processes in them, we refer to Aguilera-Dena et al. (2018).

6. Discussion

6.1. Comparison to other synthetic populations based on the Bonn code

The four Bonn grids that existed before the BoOST project (MW, LMC, SMC, and IZw18) have already been applied in population synthesis codes. Examples include *Bonnsai* (Schneider et al. 2014, in which the ages of observed massive stars can be established) and *ComBinE* (Kruckow et al. 2018, in which predictions of gravitational wave event rates are made). While the basic method of creating a synthetic population out of a stellar grid is the same in these two projects and in ours, the details tend to depend on many things. For one, the mass range of the models depends on the actual scientific question: *Bonnsai* and *ComBinE* worked with stars only up to $100\ M_\odot$. We intend the BoOST models for astrophysical applications such as star formation studies in clusters and galaxies in which the contribution from very massive stars may be important, therefore we extended the grids to $500\ M_\odot$. In order to study the early universe (e.g., high-redshift galaxies and the origin of globular clusters), a good metallicity coverage including sub-IZw18 metallicities is achieved here.

BoOST populations also differ from earlier population synthesis studies in that the models and the interpolated tracks are optimized for smoothness and consistency. For example, in *Bonnsai*, only the main-sequence phases of the massive single-star models were included, while for star formation studies, the main-sequence phase and the post-main-sequence phase should be included (i.e., the role of massive supergiants and pure helium stars may be relevant).

6.2. Future updates

We foresee possible future updates of BoOST models as follows. The first possible update concerns stellar rotation. In the present work we uniformly set all rotational velocities to a 100 km s^{-1} initial value; however, massive stars rotate with various rotational rates that can to some extent change the predictions in terms of chemical yields, radiation, final core mass, etc. While the 100 km s^{-1} value we use here is typical for massive stars (as observed in the MW and the Magellanic Clouds, cf., e.g., Hunter et al. 2008; Dufton et al. 2013; Ramírez-Agudelo et al. 2013, 2017), a possible future update of BoOST may be carried out by including stellar models with various rotational velocities.

Similarly, the initial composition of the BoOST grids could be refined. While the current version of the grids covers a broad range in metallicities from Galactic down to 1/250 lower, we provide only eight metallicity values. This constitutes quite a discrete binning. One possible future endeavor is to simulate grids with a much better resolution in metallicity than this, for instance, by either computing stellar models with metallicities in between or performing interpolation between the grids published here.

The same is true for the post-helium-burning phases of our models: while they were omitted in the present version for consistency (and for not being relevant for stellar feedback related applications), a possible update may include these phases.

We certainly plan to provide in an updated version of BoOST the chemical yields retained in the stellar envelope (to be released by a stripping of the envelope due to binary interaction). This would allow combining binary population synthesis studies with star formation studies in a powerful way.

Finally, we encourage future studies in the direction of solving the convergence issues in the inflated envelope near the Eddington limit in a reliable and physically consistent way in the Bonn code and in other stellar evolution codes such as MESA (cf. Agrawal et al. 2021a). While our method of direct extension for the phases in which the models are numerically unstable is quite robust and produces an acceptable result, it is of course not free of caveats (as discussed in Sect. 4.4). Therefore, when stellar evolutionary models become available in which these inflated phases are reliably computed, we will update our interpolated tracks and synthetic populations accordingly.

7. Conclusions

The BoOST project covers the mass-metallicity parameter space with an unprecedented resolution for the first time. We presented nine grids of massive stars between Galactic and 1/250 lower metallicities, including interpolated tracks and synthetic populations. They are available under this link as simple tables. The stellar models were computed with the Bonn evolutionary code and were post-processed with methods optimized for massive and very massive stars. Interpolated tracks and synthetic populations were created by our newly developed stellar population synthesis code SYNSTARS. Eight of the grids represent slowly rotating massive stars with normal or classical evolution, while one grid represents fast-rotating, chemically homogeneously evolving models. In addition to the common stellar parameters such as mass, radius, surface temperature, luminosity, and mass-loss rate, we present stellar wind properties such as the estimated wind velocity and kinetic energy of the wind. Additionally, we provide chemical yields of 34 isotopes, and the mass of the core at the end of the stellar lifetimes.

The BoOST models (grids, tracks, and populations) are thus suitable for further scientific applications, for example, in simulations of star formation in various environments. Future updates are planned in terms of adding models with various rotational rates, and with various initial compositions (i.e., a better resolution in metallicity). Post-helium-burning phases will also be added in future work, as will chemical yields retained in the envelope.

In the future we plan to apply the BoOST grids to study the formation and early evolution of globular clusters and young massive clusters in a metallicity-dependent way (following Wünsch et al. 2017; Szécsi & Wünsch 2019). Beyond this, however, BoOST models open the door for testing the effect of stellar metallicity in many astrophysical contexts in a simple and straightforward way. By optimizing the models for an easy application by the user, our BoOST project harvests the full scientific potential of the Bonn stellar evolutionary code and will contribute to a new era of studying massive stars and their roles in various fields of astrophysics.

References

Aarseth, S. J., Tout, C. A., & Mardling, R. A. 2008, The Cambridge N-Body Lectures, 760 (Netherlands: Springer)
Agrawal, P., Hurley, J., Stevenson, S., Szécsi, D., & Flynn, C. 2020, MNRAS, 497, 4549
Agrawal, P., Stevenson, S., Szécsi, D., & Hurley, J. 2021a, MNRAS, submitted [arXiv:2112.02801]
Agrawal, P., Szécsi, D., Stevenson, S., & Hurley, J. 2021b, MNRAS, submitted [arXiv:2112.02800]
Aguilera-Dena, D. R., Langer, N., Moriya, T. J., & Schootemeijer, A. 2018, ApJ, 858, 115
Alongi, M., Bertelli, G., Bressan, A., et al. 1993, A&AS, 97, 851
Belczynski, K., Kalogera, V., & Bulik, T. 2002, ApJ, 572, 407
Belczynski, K., Kalogera, V., Rasio, F. A., et al. 2008, ApJS, 174, 223
Bergbusch, P. A., & Vandenberg, D. A. 1992, ApJS, 81, 163
Bergbusch, P. A., & Vandenberg, D. A. 2001, ApJ, 556, 322
Böhm-Vitense, E. 1958, Z. Astrophys., 46, 108
Brott, I., de Mink, S. E., Cantiello, M., et al. 2011, A&A, 530, A115
Burbidge, E. M., Burbidge, G. R., Fowler, W. A., & Hoyle, F. 1957, Rev. Mod. Phys., 29, 547
Cerviño, M., Gómez-Flechoso, M. A., Castander, F. J., et al. 2001, A&A , 376, 422
Chatzopoulos, E., & Wheeler, J. C. 2012, ApJ, 748, 42
Chen, Y., Bressan, A., Girardi, L., et al. 2015, MNRAS, 452, 1068
Chieffi, A., & Limongi, M. 2013, ApJ, 764, 21
Choi, J., Dotter, A., Conroy, C., et al. 2016, ApJ, 823, 102
de Mink, S. E., Pols, O. R., Langer, N., & Izzard, R. G. 2009a, A&A, 507, L1
de Mink, S. E., Cantiello, M., Langer, N., et al. 2009b, A&A, 497, 243
Dessart, L., Waldman, R., Livne, E., Hillier, D. J., & Blondin, S. 2013, MNRAS, 428, 3227
Dufton, P. L., Langer, N., Dunstall, P. R., et al. 2013, A&A, 550, A109
Eddington, A. S. 1926, The Internal Constitution of the Stars
Ekström, S., Georgy, C., Eggenberger, P., et al. 2012, A&A, 537, A146
Fryer, C. L., Belczynski, K., Wiktorowicz, G., et al. 2012, ApJ, 749, 91
Gatto, A., Walch, S., Naab, T., et al. 2017, MNRAS, 466, 1903
Gräfener, G., Owocki, S. P., & Vink, J. S. 2012, A&A, 538, A40
Grassitelli, L., Fossati, L., Langer, N., et al. 2016, A&A, 593, A14
Grin, N. J., Ramírez-Agudelo, O. H., de Koter, A., et al. 2017, A&A, 600, A82

Hamann, W.-R., Koesterke, L., & Wessolowski, U. 1995, A&A, 299, 151
Heger, A., & Langer, N. 2000, ApJ, 544, 1016
Heger, A., & Woosley, S. E. 2002, ApJ, 567, 532
Heger, A., Langer, N., & Woosley, S. E. 2000, ApJ, 528, 368
Heger, A., Fryer, C. L., Woosley, S. E., Langer, N., & Hartmann, D. H. 2003, ApJ, 591, 288
Heger, A., Woosley, S. E., & Spruit, H. C. 2005, ApJ, 626, 350
Herzig, K., El Eid, M. F., Fricke, K. J., & Langer, N. 1990, A&A, 233, 462
Humphreys, R. M., Kudritzki, R. P., & Groth, H. G. 1991, A&A, 245, 593
Hunter, I., Lennon, D. J., Dufton, P. L., et al. 2008, A&A, 479, 541
Kalari, V. M., Carraro, G., Evans, C. J., & Rubio, M. 2018, ApJ, 857, 132
Kasen, D., Woosley, S. E., & Heger, A. 2011, ApJ, 734, 102
Kippenhahn, R., & Weigert, A. 1990, Stellar Structure and Evolution (Springer)
Köhler, K., Langer, N., de Koter, A., et al. 2015, A&A, 573, A71
Kozyreva, A., Blinnikov, S., Langer, N., & Yoon, S.-C. 2014, A&A, 565, A70
Kruckow, M. U., Tauris, T. M., Langer, N., Kramer, M., & Izzard, R. G. 2018, MNRAS, 481, 1908
Kubátová, B., Szécsi, D., Sander, A. A. C., et al. 2019, A&A, 623, A8
Lamers, H., & Cassinelli, J. 1999, Introduction to Stellar Winds (Cambridge University Press)
Langer, N. 1991, A&A, 252, 669
Langer, N. 1997, in Luminous Blue Variables: Massive Stars in Transition, eds. A. Nota, & H. Lamers, ASP Conf. Ser., 120, 83
Langer, N., Norman, C. A., de Koter, A., et al. 2007, A&A, 475, L19
Leitherer, C., Robert, C., & Drissen, L. 1992, ApJ, 401, 596
Maeder, A. 1987, A&A, 178, 159
Massey, P., Neugent, K. F., Dorn-Wallenstein, T. Z., et al. 2021, ApJ, 922, 177
Moriya, T. J., & Langer, N. 2015, A&A, 573, A18
Neugent, K. F., Massey, P., Georgy, C., et al. 2020, ApJ, 889, 44
Nieuwenhuijzen, H., & de Jager, C. 1990, A&A, 231, 134
Nishida, M., & Schindler, A. M. 1967, PASJ, 19, 606
Nugis, T., & Lamers, H. 2000, A&A, 360, 227
Oliphant, T. 2006, Guide to NumPy (USA: Trelgol Publishing)

Paxton, B., Cantiello, M., Arras, P., et al. 2013, ApJS, 208, 4
Petrovic, J., Langer, N., Yoon, S.-C., & Heger, A. 2005, A&A, 435, 247
Pietrinferni, A., Cassisi, S., Salaris, M., & Castelli, F. 2004, ApJ, 612, 168
Prather, M. J. 1976, Ph.D. Thesis, Yale University, New Haven, CT, USA
Ramírez-Agudelo, O. H., Simón-Díaz, S., Sana, H., et al. 2013, A&A, 560, A29
Ramírez-Agudelo, O. H., Sana, H., de Koter, A., et al. 2017, A&A, 600, A81
Rosdahl, J., Katz, H., Blaizot, J., et al. 2018, MNRAS, 479, 994
Sanyal, D., Grassitelli, L., Langer, N., & Bestenlehner, J. M. 2015, A&A, 580, A20
Sanyal, D., Langer, N., Szécsi, D., Yoon, S. C., & Grassitelli, L. 2017, A&A, 597, A71
Schneider, F. R. N., Langer, N., de Koter, A., et al. 2014, A&A, 570, A66
Schootemeijer, A., Langer, N., Grin, N. J., & Wang, C. 2019, A&A, 625, A132
Spruit, H. 2002, A&A, 381, 923
Stevenson, S., Sampson, M., Powell, J., et al. 2019, ApJ, 882, 121
Sukhbold, T., Ertl, T., Woosley, S. E., Brown, J. M., & Janka, H.-T. 2016, ApJ, 821, 38
Szécsi, D. 2016, Ph.D. Thesis Mathematisch-Naturwissenschaftlichen Fakultät der Universität Bonn, Germany
Szécsi, D. 2017, Proceedings of Science, PoS(MULTIF2017)065, 2017
Szécsi, D., & Wünsch, R. 2019, ApJ, 871, 1
Szécsi, D., Langer, N., Yoon, S.-C., et al. 2015, A&A, 581, A15
Szécsi, D., Mackey, J., & Langer, N. 2018, A&A, 612, A55
Vink, J., de Koter, A., & Lamers, H. 2000, A&A, 362, 295
Vink, J., de Koter, A., & Lamers, H. 2001, A&A, 369, 574
Vink, J., Muijres, L. E., Anthonisse, B., et al. 2011, A&A, 531, A132
Virtanen, P., Gommers, R., Oliphant, T. E., et al. 2020, Nat. Methods, 17, 261
Woosley, S. E., Blinnikov, S., & Heger, A. 2007, Nature, 450, 390
Wünsch, R., Palouš, J., Tenorio-Tagle, G., & Ehlerová, S. 2017, ApJ, 835, 60
Yoon, S.-C. 2015, PASA, 32, 15
Yoon, S.-C., & Langer, N. 2005, A&A, 443, 643
Yoon, S.-C., Langer, N., & Norman, C. 2006, A&A, 460, 199
Yoon, S.-C., Dierks, A., & Langer, N. 2012, A&A, 542, A113

Appendix A: Columns in the BoOST data files

BoOST data files are available under this link. The authors welcome feedback from the community, in particular, if there are physical quantities that a next version of our BoOST stellar models and populations should provide in order to serve the community's scientific goals better. Our aim is to provide a flexible model set that can be used in several astrophysical applications.

The current version (v1.3) of BoOST tables contain the columns described below.

A.1. Stellar models

All data files contain 608 lines. The *n*th line in one model data file has a comparable evolutionary interpretation in another model data file. Columns are

1. Time [yr]
2. Actual mass [$M_\odot$]
3. Surface temperature [K]
4. Surface luminosity [$\log L_\odot$]
5. Radius [$R_\odot$]
6. Mass-loss rate [$\log M_\odot$ yr^{-1}]
7. Surface gravity [$\log$ cm s^{-2}]
8. Surface rotational velocity [km s^{-1}]
9. Critical velocity (assuming an Eddington factor for pure electron scattering) [km s^{-1}]
10. Eddington Γ_e factor calculated for pure electron scattering
11. Flag marking whether the phase is simulated [0] or approximated with the direct extension method [1] (cf. Sect. 4)
12. – 24. Surface abundances of elements (by summing the abundance of all corresponding isotopes): ϵ(H), ϵ(He), ϵ(Li), ϵ(Be), ϵ(B), ϵ(C), ϵ(N), ϵ(O), ϵ(F), ϵ(Ne), ϵ(Na), ϵ(Mg), ϵ(Al), where ϵ(X) = N_X/N_H+12, and N_X is the number fraction of element X
25. Helium-core mass [$M_\odot$]
26. Carbon-oxygen core mass [$M_\odot$]
27. – 60. Surface mass fraction of isotopes: ^{1}H, ^{2}H, ^{3}He, ^{4}He, ^{6}Li, ^{7}Li, ^{7}Be, ^{9}Be, ^{8}B, ^{10}B, ^{11}B, ^{11}C, ^{12}C, ^{13}C, ^{12}N, ^{14}N, ^{15}N, ^{16}O, ^{17}O, ^{18}O, ^{19}F, ^{20}Ne, ^{21}Ne, ^{22}Ne, ^{23}Na, ^{24}Mg, ^{25}Mg, ^{26}Mg, ^{26}Al, ^{27}Al, ^{28}Si, ^{29}Si, ^{30}Si, and ^{56}Fe.
61. – 94. Core mass fraction of isotopes: ^{1}H, ^{2}H, ^{3}He, ^{4}He, ^{6}Li, ^{7}Li, ^{7}Be, ^{9}Be, ^{8}B, ^{10}B, ^{11}B, ^{11}C, ^{12}C, ^{13}C, ^{12}N, ^{14}N, ^{15}N, ^{16}O, ^{17}O, ^{18}O, ^{19}F, ^{20}Ne, ^{21}Ne, ^{22}Ne, ^{23}Na, ^{24}Mg, ^{25}Mg, ^{26}Mg, ^{26}Al, ^{27}Al, ^{28}Si, ^{29}Si, ^{30}Si, and ^{56}Fe.

A.2. Interpolated tracks

The table contains 1856 tracks, and all tracks contain 608 lines. Thus, this data file has about 1.1 M lines (file size: ~ 800 MB). Tracks are marked by their initial mass values before their record starts (in $M_\odot$ and in cgs units). The following columns are provided:
1. Initial mass [cgs units]
2. Time [cgs units]
3. Actual mass [cgs units]
4. Mass-loss rate [cgs units]
5. Wind velocity [cgs units]
6. Kinetic energy generation rate of the wind [cgs units]
7. Luminosity [cgs units]
8. Stellar radius [cgs units]
9. Surface temperature [K]
10. Mask [integer]
11. Type of interpolation [integer]
12. Surface rotational velocity [km s^{-1}]

13. Critical rotational velocity [km s^{-1}]
14. Eddington factor (see column 10. in Sect. A.1 above)
15. Flag marking whether the phase includes the direct extension method [1] or not [0] (cf. Sect. 4)
16. Helium-core mass [$M_\odot$]
17. Carbon-oxygen core mass [$M_\odot$]
18. – 50. Surface mass fraction of isotopes: ^{1}H, ^{2}H, ^{3}He, ^{4}He, ^{6}Li, ^{7}Li, ^{7}Be, ^{9}Be, ^{8}B, ^{10}B, ^{11}B, ^{11}C, ^{12}C, ^{13}C, ^{12}N, ^{14}N, ^{15}N, ^{16}O, ^{17}O, ^{18}O, ^{19}F, ^{20}Ne, ^{21}Ne, ^{22}Ne, ^{23}Na, ^{24}Mg, ^{25}Mg, ^{26}Mg, ^{26}Al, ^{27}Al, ^{28}Si, ^{29}Si, ^{30}Si, and ^{56}Fe.

A.3. Synthetic populations

These files contain 608 lines (inherited from the stellar models, see above) plus 50 extra lines to ensure the interpolated quantities behave well. The following columns are provided:
1. Time [cgs units]
2. Mass lost from all massive stars in the form of stellar wind [cgs units]
3. Mass lost from all massive stars in the form of dynamical ejection [cgs units] (set to zero for all BoOST models in this paper)
4. Kinetic energy in the winds [cgs units]
5. Integrated bolometric luminosity of the population [cgs units]
6. Integrated UV flux [cgs units]
7. Total mass released in stellar winds (accumulated) [cgs units]
8. Total mechanical energy produced in the stellar winds [cgs units]
9. – 56. Mass fraction of isotopes in the winds: ^{1}H, ^{2}H, ^{3}He, ^{4}He, ^{6}Li, ^{7}Li, ^{7}Be, ^{9}Be, ^{8}B, ^{10}B, ^{11}B, ^{11}C, ^{12}C, ^{13}C, ^{12}N, ^{14}N, ^{15}N, ^{16}O, ^{17}O, ^{18}O, ^{19}F, ^{20}Ne, ^{21}Ne, ^{22}Ne, ^{23}Na, ^{24}Mg, ^{25}Mg, ^{26}Mg, ^{26}Al, ^{27}Al, ^{28}Si, ^{29}Si, and ^{30}Si.

Appendix B: Technical details of the direct extension method

B.1. Establishing the helium zero-age main sequence

To be able to apply the direct extension method (Sect. 4), we need to establish the point toward which the stellar models converge in terms of surface temperature and luminosity (and thus radius) when they lose mass in their late evolution. This point is the helium ZAMS, that is, the position in the HR diagram at which homogeneous, thermally adjusted helium stars are predicted to be by simulations.

The position of the helium ZAMS is well known for massive stars, but it is less well known for very massive stars. Model grids were computed with the Bonn code only for MW and SMC metallicity up to masses of 25 and 109 $M_\odot$, respectively. They are presented in Fig. 19 of Köhler et al. (2015). In this figure, the 35 $M_\odot$ point of the MW helium ZAMS was obtained by linearly extrapolating the data above 25 $M_\odot$ (D. Sanyal 2019, private communication). No helium ZAMS data for the LMC (and for sub-SMC metallicities) are available.

Some of our very massive models in the MW grid retain as much as 44 $M_\odot$ when the simulation stops and those in the SMC grid as much as 170 $M_\odot$. Additionally, we have models with LMC and sub-SMC metallicities. This means that even if we rely on the helium-ZAMS data in Fig. 19 of Köhler et al. (2015), we still have to supplement it to cover our parameter space.

The helium-ZAMS models from Fig. 19 of Köhler et al. (2015) themselves are unpublished but have kindly been provided by D. Sanyal (2019, private communication). We

extrapolated the MW and SMC data in terms of M, $\log T_{\mathrm{eff}}^{(M)}$, and $\log(L/L_\odot^{(M)})$ up to 500 $M_\odot$. We also interpolated between these two data sets using $\log(Z)$ as the interpolation parameter to obtain data for the LMC. The results are shown in Fig. 10.

When supplementing the MW and SMC data, we applied linear extrapolation and also reduced all quantities by a factor of 3. We chose this number for the following reasons. First, the helium-ZAMS models are initial models with a homogeneous composition, while our models would in reality become helium-ZAMS stars with a relaxed composition (i.e., nuclear burning would be ongoing inside). The surface temperature of such relaxed models is typically somewhat higher, while the surface luminosity is somewhat lower than those of unrelaxed models. Second, extrapolating linearly above 100 $M_\odot$ using the original data leads to highly unphysical results. For example, a 200 $M_\odot$ helium-star in the LMC grid would have a surface temperature of ~3300 K with an extrapolation like this. This is hardly physically possible because massive stars (including very massive stars) are not expected to have a surface temperature lower than ~4000 K (cf. the Hayashi line, Kippenhahn & Weigert 1990). Third and most conclusively, the helium-ZAMS lines we would obtain by a simple linear extrapolation of the original data lie at higher surface temperatures than the lines in the last computed stages of some of our most massive stellar models. During the late phases of evolution, our models should evolve to higher and not lower surface temperatures when they lose mass (and thereby uncover helium-rich layers). For all these reasons and after testing several values, we decided that including a reduction of a factor of 3 in our linearly extrapolation of the helium-ZAMS lines in the HR diagram gives the most physically consistent result. Examples are presented in Fig. 10.

B.2. Fraction of the data that includes the direct extension method

Tables B.1 provide the percentage of the lifetime influenced by the treatment of direct extension method (DEM) and the central helium mass fraction Y_{cen} of the last computed structure model (cf. Sect. 4). An asterisk denotes if the value is reached during the main sequence (as opposed to the post-main-sequence, which is the most common case). The corresponding lines of the published data files are flagged with [1] in the relevant column (Column 11, cf. Sect. A).

Table B.1. Fraction of the data that includes the direct extension method, cf. Sects. 4 and B.2

MW	'DEM'	Y_{cen}
9 $M_\odot$	0.0%	0.00
12 $M_\odot$	0.0%	0.00
15 $M_\odot$	0.0%	0.00
25 $M_\odot$	1.3%	0.17
40 $M_\odot$	8.8%	0.99
60 $M_\odot$	8.9%	0.99
80 $M_\odot$	9.0%	0.99
120 $M_\odot$	9.0%	0.99
250 $M_\odot$	9.0%	0.99
500 $M_\odot$	9.0%	0.99
LMC	'DEM'	Y_{cen}
9 $M_\odot$	0.0%	0.00
12 $M_\odot$	0.0%	0.00
19 $M_\odot$	0.0%	0.00
30 $M_\odot$	0.0%	0.01
40 $M_\odot$	3.0%	0.41
70 $M_\odot$	8.6%	1.00
100 $M_\odot$	8.5%	1.00
150 $M_\odot$	9.7%	0.98
260 $M_\odot$	8.6%	1.00
500 $M_\odot$	8.5%	1.00

Table B.1. Continued.

dwarfB	'DEM'	Y_{cen}
SMC	'DEM'	Y_{cen}
9 $M_\odot$	0.0%	0.00
12 $M_\odot$	0.0%	0.00
15 $M_\odot$	0.0%	0.00
30 $M_\odot$	0.0%	0.00
40 $M_\odot$	0.9%	0.10
55 $M_\odot$	3.2%	0.40
100 $M_\odot$	8.8%	0.99
150 $M_\odot$	8.4%	1.00
250 $M_\odot$	11.2%	0.97*
575 $M_\odot$	8.3%	1.00
dwarfA	'DEM'	Y_{cen}
9 $M_\odot$	0.0%	0.00
12 $M_\odot$	0.0%	0.00
19 $M_\odot$	0.0%	0.00
30 $M_\odot$	0.0%	0.00
40 $M_\odot$	0.0%	0.00
55 $M_\odot$	0.9%	0.07
100 $M_\odot$	8.7%	0.99
150 $M_\odot$	8.2%	1.00
250 $M_\odot$	9.4%	0.99
560 $M_\odot$	15.1%	0.92*
9 $M_\odot$	0.0%	0.00
12 $M_\odot$	0.0%	0.00
19 $M_\odot$	0.0%	0.00
30 $M_\odot$	0.0%	0.00
40 $M_\odot$	0.0%	0.00
55 $M_\odot$	0.0%	0.00
70 $M_\odot$	0.0%	0.00
150 $M_\odot$	5.0%	0.56
250 $M_\odot$	15.3%	0.92*
560 $M_\odot$	10.4%	0.97*
IZw18	'DEM'	Y_{cen}
9 $M_\odot$	0.0%	0.00
17 $M_\odot$	0.0%	0.00
20 $M_\odot$	0.0%	0.00
26 $M_\odot$	0.0%	0.00
45 $M_\odot$	0.0%	0.00
77 $M_\odot$	0.0%	0.00
100 $M_\odot$	0.0%	0.00
150 $M_\odot$	0.0%	0.00
257 $M_\odot$	6.1%	0.68
575 $M_\odot$	10.0%	0.98
dwarfD	'DEM'	Y_{cen}
9 $M_\odot$	0.0%	0.00
12 $M_\odot$	0.0%	0.00
19 $M_\odot$	0.0%	0.00
30 $M_\odot$	0.0%	0.00
40 $M_\odot$	0.0%	0.00
55 $M_\odot$	0.0%	0.00
80 $M_\odot$	0.0%	0.00
100 $M_\odot$	0.0%	0.00
250 $M_\odot$	0.0%	0.00
560 $M_\odot$	18.9%	0.88*
dwarfE	'DEM'	Y_{cen}
9 $M_\odot$	0.0%	0.00
12 $M_\odot$	0.0%	0.00
19 $M_\odot$	0.0%	0.00
30 $M_\odot$	0.0%	0.00
55 $M_\odot$	0.0%	0.00
70 $M_\odot$	0.0%	0.00
80 $M_\odot$	0.0%	0.00
100 $M_\odot$	0.0%	0.00
250 $M_\odot$	0.0%	0.00
560 $M_\odot$	0.0%	0.00
IZw18-CHE	'DEM'	Y_{cen}
9 $M_\odot$	0.0%	0.00
13 $M_\odot$	0.0%	0.00
20 $M_\odot$	0.0%	0.00
30 $M_\odot$	0.0%	0.00
51 $M_\odot$	0.0%	0.00
77 $M_\odot$	0.0%	0.00
150 $M_\odot$	0.0%	0.00
294 $M_\odot$	0.0%	0.00
388 $M_\odot$	0.0%	0.00
575 $M_\odot$	8.0%	1.00

Explaining the differences in massive star models from various simulations

Poojan Agrawal [1,2,3]★ Dorottya Szécsi,[4,5] Simon Stevenson [1,2] Jan J. Eldridge [6] and
Jarrod Hurley [1,2]

[1]*Centre for Astrophysics and Supercomputing, Swinburne University of Technology, Hawthorn, VIC 3122, Australia*
[2]*OzGrav: The ARC Centre of Excellence for Gravitational Wave Discovery, Hawthorn, VIC 3122, Australia*
[3]*McWilliams Center for Cosmology, Department of Physics, Carnegie Mellon University, Pittsburgh, PA 15213, USA*
[4]*Institute of Astronomy, Faculty of Physics, Astronomy and Informatics, Nicolaus Copernicus University, Grudziadzka 5, PL-87-100 Torun, Poland*
[5]*I. Physikalisches Institut, Universität zu Köln, Zülpicher-Str 77, D-50937 Cologne, Germany*
[6]*Department of Physics, University of Auckland, Auckland 1142, New Zealand*

ABSTRACT

The evolution of massive stars is the basis of several astrophysical investigations, from predicting gravitational-wave event rates to studying star formation and stellar populations in clusters. However, uncertainties in massive star evolution present a significant challenge when accounting for these models' behaviour in stellar population studies. In this work, we present a comparison between five published sets of stellar models from the BPASS (Binary Population and Spectral Synthesis), BoOST (Bonn Optimized Stellar Tracks), Geneva, MIST (MESA Isochrones and Stellar Tracks), and PARSEC (PAdova and TRieste Stellar Evolution Code) simulations at near-solar metallicity. The different sets of stellar models have been computed using slightly different physical inputs in terms of mass-loss rates and internal mixing properties. Moreover, these models also employ various pragmatic methods to overcome the numerical difficulties that arise due to the presence of density inversions in the outer layers of stars more massive than $40 \, M_\odot$. These density inversions result from the combination of inefficient convection in the low-density envelopes of massive stars and the excess of radiative luminosity to the Eddington luminosity. We find that the ionizing radiation released by the stellar populations can change by up to 18 per cent, the maximum radial expansion of a star can differ between 100 and $1600 \, R_\odot$, and the mass of the stellar remnant can vary up to $20 \, M_\odot$ between the five sets of simulations. We conclude that any attempts to explain observations that rely on the use of models of stars more massive than $40 \, M_\odot$ should be made with caution.

Key words: gravitational waves – stars: evolution – stars: formation – stars: massive – galaxies: stellar content.

1 INTRODUCTION

Stellar evolutionary model sequences serve as input for a broad range of astrophysical applications: from star formation (e.g. Gatto et al. 2017) to galaxy evolution (e.g. Weinberger, Springel & Pakmor 2020); from cluster dynamics (e.g. Heggie & Hut 2003) to gravitational-wave (GW) studies (e.g. Vigna-Gómez et al. 2018). These sequences provide an easy and powerful way to account for both individual stars (e.g. Schneider et al. 2014) and stellar populations (e.g. Brott et al. 2011b) in a given astrophysical environment.

1D model sequences (from now on: *stellar models*) can be computed from first principles (Kippenhahn & Weigert 1990) and have become a household tool in astrophysical research. However, when it comes to stars more massive than $\sim 9 \, M_\odot$ – those that, despite being rare, provide the bulk of the radiation, chemical pollution, and the most exotic death throes in the Universe (Woosley, Heger & Weaver 2002) – stellar models are still riddled with large uncertainties.

High-mass stars are born less often than their low-mass counterparts (Salpeter 1955) and have comparatively shorter lives (Crowther 2012). Consequently, observational constraints on their evolution are more difficult to obtain. The situation is further complicated by many massive stars being observed to be fast rotators (Ramírez-Agudelo et al. 2013), which breaks down perfect symmetry, and to have a close-by companion star (Sana et al. 2012), breaking the assumption of perfect isolation. Even for isolated, non-rotating single stars, the physical conditions both inside (Heger, Langer & Woosley 2000) and around (Lamers & Cassinelli 1999) the star are so peculiar and complex that developing appropriate numerical simulations becomes highly challenging. This is why the evolution of massive stars remains an actively studied field to this day.

Much progress has been made in the last few decades concerning massive stars and their evolution. Mass-loss in the form of high-velocity winds from massive stars is being intensively studied and accounted for in the models (Smith 2014; Sander & Vink 2020). Observations of massive stars from the Large and Small Magellanic Clouds are being used to constrain the efficiency of interior mixing processes (Brott et al. 2011a; Schootemeijer et al. 2019). 1D stellar models have also been updated to account for the effects of rotation (Maeder 2009; Costa et al. 2019) and magnetic fields (Heger,

★ E-mail: pagrawal@astro.swin.edu.au

Woosley & Spruit 2005; Maeder & Meynet 2005; Takahashi & Langer 2021) that can significantly change their evolutionary paths (Walder, Folini & Meynet 2012; Petit et al. 2017; Groh et al. 2020).

Despite the progress, there are still many open questions surrounding the lives of massive ($\gtrsim 9\,M_\odot$) and 'very' massive (here designated as $\gtrsim 40\,M_\odot$) stars, and in the absence of well-defined answers, stellar evolution codes make use of different assumptions. Earlier studies comparing models of massive stars from different codes (e.g. Martins & Palacios 2013; Jones et al. 2015) have already established that the differences in the physical parameters such as mixing and mass-loss rates adopted by various stellar evolution codes can affect the evolutionary outcome of these stars.

Here, we highlight another major uncertainty arising due to the numerical treatment of low-density envelopes of very massive stars. These stars have luminosities close to the Eddington limit, so changes in the elemental opacities during their evolution can lead to the formation of density and pressure inversions in the stellar envelope (Langer 1997). The presence of these density inversions can cause numerical instabilities for 1D stellar evolution codes. To deal with these instabilities, the codes use different pragmatic solutions whose interplay with mixing and mass-loss can further vary the evolution of massive stars.

The role of the Eddington limit and the associated density inversions in massive stars is well known within the stellar evolution community but remains relatively unknown outside the field. With the surge in the use of massive star models, for example, in GW event rate predictions and supernova studies, it has become important to be aware of this issue. Our goal is to present the broader community with a concise overview, including how it affects the evolutionary properties such as the radial expansion and the remnant mass of very massive stars. To this end, we compare models of massive and very massive stars from five published sets created with different evolutionary codes: (i) models from the PAdova and TRieste Stellar Evolution Code (PARSEC; Bressan et al. 2012; Chen et al. 2015); (ii) the MESA Isochrones and Stellar Tracks (MIST; Choi et al. 2016) from the Modules for Experiments in Stellar Astrophysics (MESA; Paxton et al. 2011); (iii) models (Ekström et al. 2012; Yusof et al. 2013) from the Geneva code (Eggenberger et al. 2008); (iv) models from the Binary Population and Spectral Synthesis (BPASS; Eldridge et al. 2017) project; and (v) the Bonn Optimized Stellar Tracks (BoOST; Szécsi et al. 2022) from the 'Bonn' code.

We describe the major physical ingredients used in computing each set of models in Sections 2 and 3. In Section 4, we compare the predictions from each set of models in the Hertzsprung–Russell (HR) diagram and in terms of the emitted ionizing radiation, as well as the predictions for the maximum radial expansion of stars, and their remnant masses. Finally, we draw conclusions in Section 5.

2 PHYSICAL INPUTS

2.1 Chemical composition

The chemical composition of the Sun is often used as a yardstick in computing the metal content of other stars. However, the exact value remains inconclusive and has undergone several revisions since 2004 (see Basu 2009; Asplund, Amarsi & Grevesse 2021, for an overview). Therefore, different stellar models often make use of different abundance scales.

The BPASS, PARSEC, Geneva, and MIST models base their chemical compositions on the Sun, while the BoOST models use a mixture tailored to the sample of massive stars from the FLAMES survey (Evans et al. 2005) with $Z_{\rm Gal} = 0.0088$. For stellar winds and

opacity calculations, BoOST models use $Z = 0.017$ from Grevesse, Noels & Sauval (1996) as the reference solar metallicity. The BPASS models use solar abundances from Grevesse & Noels (1993) with $Z_\odot = 0.02$. The PARSEC models follow Grevesse & Sauval (1998) with revisions from Caffau et al. (2011) and $Z_\odot = 0.015\,24$. Geneva models use Asplund, Grevesse & Sauval (2005) abundances with Ne abundance from Cunha, Hubeny & Lanz (2006) and $Z_\odot = 0.014$ while, finally, the MIST models base their abundance on Asplund et al. (2009) with $Z_\odot = 0.014\,28$.

For the purpose of comparison here, we use $Z = 0.014$ models for each set except for BoOST where we use the Galactic composition, $Z = 0.0088$ as the closest match. Iron is an important contributor to metallicity, as numerous iron transition lines dominate both opacity and mass-loss rates, therefore directly affecting the structure of massive stars (e.g. Puls, Springmann & Lennon 2000). The stellar models compared here have similar iron content, with the normalized number density $[A_{\rm Fe} = \log(N_{\rm Fe}/N_{\rm H}) + 12.0]$ ranging from 7.40 (for BoOST models) to 7.54 (for MIST models).

2.2 Mass-loss rates

Stellar mass is a key determinant of a star's life and evolutionary outcome. It can, however, change as stars lose their outer layers in the form of stellar winds, and through interactions with a binary companion. Consequently, mass-loss not only can affect the structure and chemical composition of the star, but is also important in determining its final state (Renzo et al. 2017).

For massive stars, the effects of mass-loss are even more pronounced. The mass-loss experienced by hot massive stars (O type stars and Wolf–Rayet stars) is known to be line-driven (Lamers & Cassinelli 1999) while that of cool massive stars (red supergiants; Levesque 2017) is suggested to be dust-driven. Both types of mass-loss are an intensively studied subject. However, the complexity of the problem of atomic and molecular transitions in the wind together with the rarity of stars at these high masses means that the model assumptions are usually based either on a few observations (a small sample of stars) or on what we know about the wind properties of low-mass stars.

All models in this study follow Vink et al. (2000, 2001) for hot wind-driven mass-loss. The PARSEC, Geneva, BPASS, and MIST models follow de Jager et al. (1988) for cool dust-driven mass-loss and Nugis & Lamers (2000) for mass-loss in the naked helium star phase. The Geneva models further switch to Crowther (2000) for hydrogen-rich stars with $\log T_{\rm eff}/K \leq 3.7$. They also use the maximum of Vink et al. (2001) and Gräfener & Hamann (2008) for stars with surface hydrogen mass fraction between 0.3 and 0.05, before switching to Nugis & Lamers (2000) when the surface hydrogen mass fraction falls below 0.05. The BoOST models follow Nieuwenhuijzen & de Jager (1990) for cool winds and Hamann et al. (1995; reduced by a factor of 10) for stars with surface hydrogen mass fraction < 0.3. For computing mass-loss rates of stars with surface hydrogen mass fraction between 0.3 and 0.6, BoOST models linearly interpolate between the mass-loss rates of Vink et al. (2001) and Hamann et al. (1995; reduced by a factor of 10).

To account for the dependence of the mass-loss rates on the chemical composition, BoOST, MIST, and BPASS models scale the mass-loss rates by a factor of $Z^{0.85}$ (Vink et al. 2001).[1] Geneva

---

[1]Note that for some models the factor $Z^{0.69}$ is quoted, depending on whether the dependence of the terminal velocity on Z is explicitly considered or not.

Table 1. Summary of input parameters used in the computation of the models of massive stars from different codes. See Section 2 for details.

Stellar model	$Z_\odot$	Hot wind	Cool wind	Wolf–Rayet wind	Convective boundary	α_{MLT}	Overshoot type	α_{ovs}	α_{semi}
BPASS	0.020	Vink, de Koter & Lamers (2000, 2001)	de Jager, Nieuwenhuijzen & van der Hucht (1988)	Nugis & Lamers (2000)	Schwarzschild (1958)	2.0	Pols et al. (1998)	0.12^e	–
BoOST	0.008^a	Vink et al. (2000, 2001)	Nieuwenhuijzen & de Jager (1990)	Hamann, Koesterke & Wessolowski (1995)^b	Ledoux (1947)	1.5	Step	0.335	1.0
Geneva	0.014	Vink et al. (2000, 2001)	de Jager et al. (1988)^c	Nugis & Lamers (2000)	Schwarzschild (1958)	1.6^d	Step	0.1	–
MIST	0.014	Vink et al. (2000, 2001)	de Jager et al. (1988)	Nugis & Lamers (2000)	Ledoux (1947)	1.82	Herwig (2000)	0.016^e	0.1
PARSEC	0.015	Vink et al. (2000, 2001)	de Jager et al. (1988)	Nugis & Lamers (2000)	Schwarzschild (1958)	1.74	Bressan, Chiosi & Bertelli (1981)	0.5^e	–

^{a}For calculating mass-loss rates and opacities, $Z_\odot = 0.017$ is used.
^{b}Reduced by a factor of 10.
^{c}For $\log T_{eff}/K \leq 3.7$, mass-loss rates from Crowther (2000) are used.
^{d}For stars with initial mass $\geq 40\,M_\odot$, $\alpha_{MLT} = 1.0$ is used but with a different scale height (see Section 3).
^{e}The rough equivalent in the step overshooting formalism is 0.2, 0.25, and 0.4 for the MIST, PARSEC, and BPASS models, respectively.

and PARSEC models also use additional mass-loss as described in Section 3.

2.3 Convection and overshooting

Internal mixing processes such as convection and overshooting play an important role in determining both the structure and evolution of massive stars (see e.g. Sukhbold & Woosley 2014). Similar to mass-loss, these processes represent another major source of uncertainty in massive stellar evolution (Schootemeijer et al. 2019; Kaiser et al. 2020). In 1D stellar evolution codes convection is modelled using the mixing-length theory (MLT; Böhm-Vitense 1958) in terms of the mixing-length parameter α_{MLT}. However, 3D simulations suggest that convection in massive stars might be more sophisticated and turbulent than described by MLT (Jiang et al. 2015).

The BoOST, Geneva, PARSEC, and BPASS models used here follow standard MLT (Cox & Giuli 1968) for convective mixing with mixing-length parameter $\alpha_{MLT} = (1.5, 1.6, 1.74, 2.0)$, respectively. MIST follows a modified version of MLT given by Henyey, Vardya & Bodenheimer (1965) with $\alpha_{MLT} = 1.82$. Convective boundaries in PARSEC, Geneva, and BPASS models are determined using the Schwarzschild criterion (Schwarzschild 1958). BoOST and MIST use the Ledoux criterion (Ledoux 1947) for determining convective boundaries with semiconvective mixing parameters of 1.0 and 0.1, respectively. For determining convective core overshoot, Geneva and BoOST use step overshooting with overshoot parameter $\alpha_{ov} = (0.1, 0.335)$. MIST uses exponential overshooting following Herwig (2000) with $\alpha_{ov} = 0.016$. PARSEC uses overshoot from Bressan et al. (1981) with $\alpha_{ov} = 0.5$. BPASS uses the overshoot prescription from Pols et al. (1998) with $\alpha_{ov} = 0.12$. For comparison, the rough equivalent in the step overshooting formalism would be 0.2, 0.25, and 0.4 for the MIST, PARSEC, and BPASS models, respectively (see Pols et al. 1998; Bressan et al. 2012; Choi et al. 2016, for details of each method).

MIST and PARSEC also include small amounts of overshoot associated with convective regions in the envelope. However, apart from modifying surface abundances, envelope overshoot has a negligible effect on the evolution of the star (Bressan et al. 2012).

Rotational mixing also plays an important role in the evolution of massive stars. In fact, the calibration of the free parameters in the stellar codes is often based on their rotating models. For simplicity, we only compare non-rotating models for PARSEC, MIST, Geneva, and BPASS in this study. Although, for BoOST, in the absence of non-rotating models for stars more massive than $60\,M_\odot$, we do use slowly rotating ($100\,km\,s^{-1}$) models. As shown by Brott et al. (2011a), this small difference in the initial rotation rate is not relevant from the point of view of the overall evolutionary behaviour.

Major input parameters used in each set of models are summarized in Table 1.

3 EDDINGTON LUMINOSITY AND THE NUMERICAL TREATMENT OF DENSITY INVERSIONS

The Eddington luminosity is the maximum luminosity that can be transported by radiation while maintaining hydrostatic equilibrium (Eddington 1926). In the low-density envelopes of massive stars changes in the elemental opacities during the evolution of stars can cause the local radiative luminosity to exceed the Eddington luminosity (Langer 1997; Sanyal et al. 2015). To maintain hydrostatic equilibrium, density, and pressure inversion regions form in the stellar envelope. In the absence of efficient convection (which is also typical for the low-density envelopes; Grassitelli et al. 2016), this can lead to convergence problems for 1D stellar evolution codes (Paxton et al. 2013). Owing to numerical difficulties, the time-steps become exceedingly small, preventing further evolution of the star. While less-massive stars are only affected by this process in their late evolutionary phases (Harpaz 1984; Lau et al. 2012), very massive stars can exceed the Eddington limit already during the core-hydrogen-burning phase (Gräfener, Owocki & Vink 2012; Sanyal et al. 2015) and inhibit computation of their evolution. Therefore, 1D stellar evolution codes have to employ various solutions to compute further evolution of very massive stars.

In PARSEC models, density inversions and the consequent numerical difficulties are avoided by limiting the temperature gradient such that the density gradient never becomes negative (see section 2.4 of

Chen et al. 2015; Alongi et al. 1993). Limiting the temperature gradient prevents inefficient convection and the evolution of the stars proceeds uninterrupted. Also, the models include a mass-loss enhancement following Vink (2011) whenever the total luminosity of the star approaches the Eddington luminosity.

MIST models suppress density inversions through the MLT++ formalism (Paxton et al. 2013) of MESA. In this method, the actual temperature gradient is artificially reduced to make it closer to the adiabatic temperature gradient whenever radiative luminosity exceeds the Eddington luminosity above a pre-defined threshold. This approach again increases convective efficiency, helping stars to overcome density inversions. Additionally, radiative pressure at the surface of the star is also enhanced in the MIST models to help with convergence (Choi et al. 2016).

In the extended envelopes of massive stars, the density scale height is much larger compared to the pressure scale height (which is typically used for computing the mixing length). Therefore, setting the mixing length to be comparable with the density scale height helps avoid density inversion (Nishida & Schindler 1967; Maeder 1987). The Geneva models include this treatment when computing models with initial masses greater than $40\,M_\odot$ with $\alpha_{MLT} = 1.0$ (see section 2.3 of Ekström et al. 2012). Additionally, the mass-loss rates for the models are increased by a factor of 3 whenever the local luminosity in any of the layers of the envelope is higher than five times the local Eddington luminosity.

BoOST models do not include any artificial treatment to prevent massive stars from encountering density inversions. Instead, their models undergo envelope inflation when massive stars reach the Eddington limit (Sanyal et al. 2015). On encountering the density inversions in their envelopes, the computation of very massive stars becomes numerically difficult. Further evolution of such stars is then computed through post-processing. It involves removing layers from the surface of the star (which would anyway happen due to regular mass-loss) while correcting for surface properties such as effective temperature and luminosity (Szécsi et al. 2022).

BPASS models also allow density inversions to develop in the envelope of massive stars. However, these models are able to continue the evolution without numerical difficulties, most likely due to the use of a non-Lagrangian mesh (see Stancliffe 2006, for an overview) and the resolution factors being lower than in other models (Eggleton 1973; Eldridge et al. 2017).

4 COMPARING THE MODELS

4.1 Differences between models in the Hertzsprung–Russell diagram

The evolution of stars can be easily represented through tracks on the HR diagram, depicting the evolutionary paths followed by a series of stars. Fig. 1 presents the HR diagram of stars of various initial masses from the five simulation approaches. The observational analogue to the Eddington limit is the Humphreys–Davidson limit or HD limit (Humphreys & Davidson 1979). Since the luminosity of a star depends on its mass, more massive stars also are more luminous. This means they can easily exceed the Eddington limit, develop density inversions, and require the use of numerical solutions as discussed in Section 3.

From Fig. 1, we see that the tracks of the $25\,M_\odot$ (or $24\,M_\odot$ in some cases) stars agree well during most of the evolution. This is because stars of this mass do not exceed the Eddington limit and are thus not affected by the related numerical treatments. The minor differences in their tracks are due to the difference in physical inputs (Section 2) be-

tween the simulations. For example, the differences in the position of the main-sequence (MS) hook feature in the HR diagram arise due to the varied extent of convective overshoot used in each set of models.

A $40\,M_\odot$ star is clearly affected by the numerical treatment employed during the post-main-sequence phase of its evolution, as evidenced by the difference in the tracks in the HR diagram shown in Fig. 1. More massive stars, i.e, those with initial masses $80/85\,M_\odot$ and $120/125\,M_\odot$, can exceed the Eddington limit in their envelopes while on the MS and therefore their simulations differ significantly from each other. At these masses, the mass-loss rates can be as high as 10^{-3}–$10^{-4}\,M_\odot\,\mathrm{yr}^{-1}$, completely dominating over every other physical ingredient in determining the evolutionary path. While all tracks have been computed with similar prescriptions for wind mass-loss (cf. Section 2), the actual rates can be strongly modified by the numerical methods adopted by each code in response to numerical instabilities (Section 3), resulting in vast differences in the tracks.

4.2 Ionizing radiation and synthetic populations

The ionization released by a stellar population in e.g. a cluster or galaxy is influenced by the contribution of the most massive stars (Topping & Shull 2015). As shown above, however, these are the stars for which the simulations give the most diverse predictions.

To demonstrate this effect, we calculate the ionizing radiation emitted by a simple stellar population, supposing a Salpeter (1955) initial mass function with an upper mass of $120\,M_\odot$ and a star-forming region of $10^7\,M_\odot$ total mass – which is aimed to represent either a typical starburst galaxy, or a young massive cluster in the Milky Way. In Table 2, we list the Lyman photon flux predicted by the individual stellar models analysed here. To simplify the population synthesis calculations, the table provides time-averaged values, that is, the photon number flux emitted over the whole evolution is divided by the lifetime. This way the emission coming from the population is estimated by simply weighting the time-averaged values by the initial mass function (i.e. without needing to follow the time evolution of the modelled cluster or galaxy). The results of these simple population syntheses are also reported in Table 2. In the absence of spectral synthesis models computed for all five sets (cf. Wofford et al. 2016), we have opted to simply use blackbody estimation. To correct for optically thick winds, we follow the method explained in chapter 4.5.1 of Szécsi (2016, which relies on Langer 1989).

We find that, in terms of how much Lyman flux is emitted by a given synthetic population, the model predictions can differ as much as ∼18 per cent between simulations. This supports earlier findings (e.g. Topping & Shull 2015) that relying on the ionizing properties of massive stars from evolutionary models should be done with caution. Indeed one should keep in mind that the behaviour of the most massive models, those that dominate the radiation profile of any star-forming region, is weighted with large uncertainties – the source of which is the treatment of the Eddington limit, explained in Section 3.

4.3 Predictions of maximum stellar radii

The radial expansion of a star plays a significant role in determining the nature of binary interaction as it can lead to episodes of mass transfer in close interacting binaries. Recent studies indicate that most of the massive stars occur in binaries (Sana et al. 2012; Moe & Di Stefano 2017). Therefore, predictions of stellar radii become even more important for determining the binary properties of massive stars.

Fig. 2 shows the maximum radial expansion achieved by massive stars from each simulation. For stars with initial mass up to $30\,M_\odot$, all
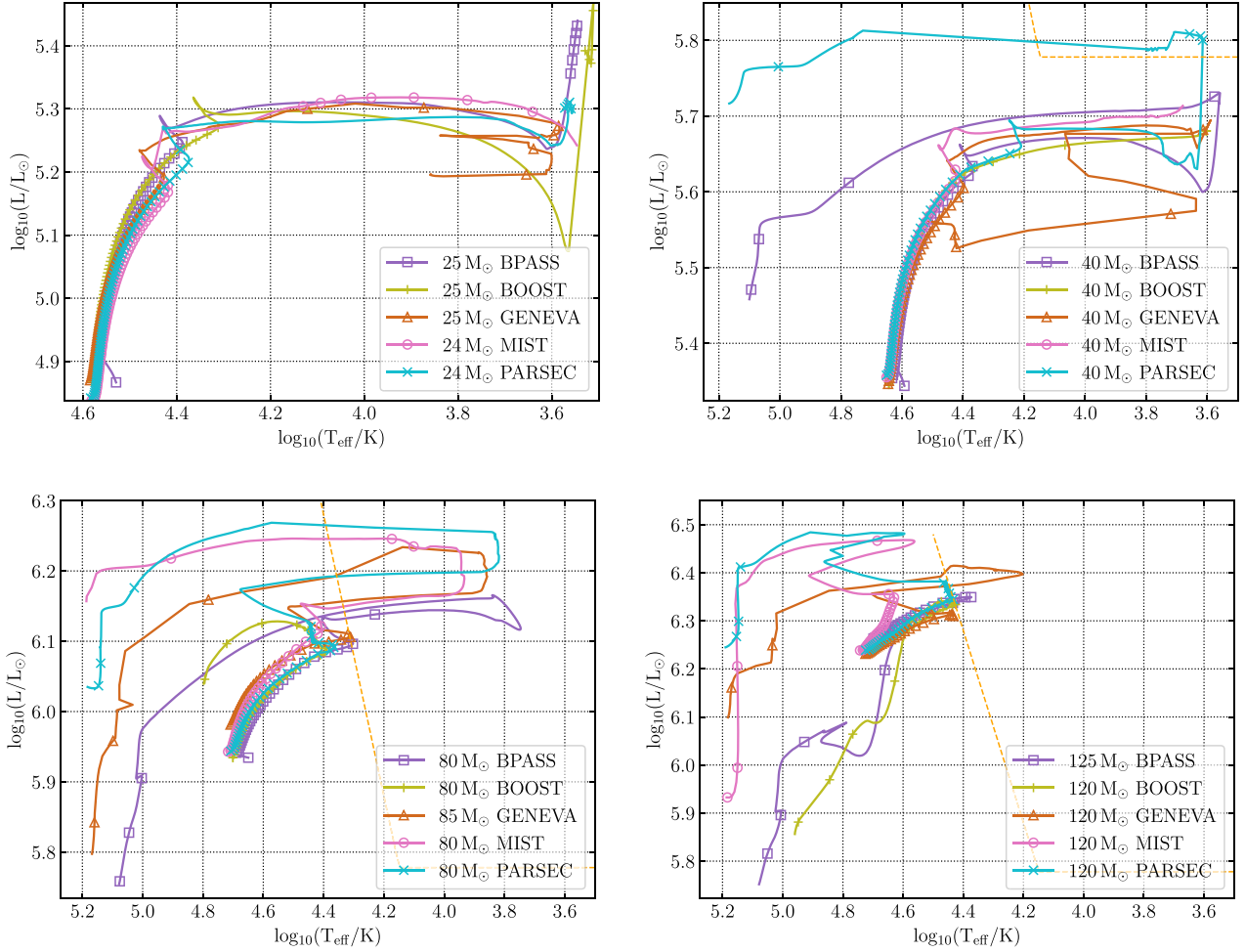
Figure 1. HR diagrams of the massive single star models analysed in this work. All models have near-solar composition. Symbols mark every 10^5 yr of evolution. Only the core-hydrogen- and core-helium-burning phases are plotted. The dashed red line marks the observational Humphreys–Davidson limit (Humphreys & Davidson 1979) where relevant. The tracks become more varied with increasing initial mass. This is because the codes apply various treatments for the numerical instabilities associated with the Eddington-limit proximity, cf. Section 3.

Table 2. Time-averaged ionizing photon number flux [s^{-1}] in the Lyman continuum emitted by the stellar models during their lives *on average*, cf. Section 4.2. The last column provides the amount of Lyman radiation (number of photons [s^{-1}]) that a 10^7 M$_\odot$ population (e.g. a starburst galaxy or a young massive cluster in the Milky Way) containing these massive stars would emit.

M_{ini} [M$_\odot$]	24/25	40	80/85	120/125	pop.
PARSEC	3.7×10^{48}	1.3×10^{49}	5.5×10^{49}	1.0×10^{50}	1.08×10^{54}
MIST	3.3×10^{48}	1.5×10^{49}	5.1×10^{49}	1.1×10^{50}	1.06×10^{54}
Geneva	3.5×10^{48}	1.2×10^{49}	5.1×10^{49}	8.5×10^{49}	9.90×10^{53}
BPASS	3.6×10^{48}	1.3×10^{49}	4.5×10^{49}	7.7×10^{49}	9.34×10^{53}
BoOST	3.7×10^{48}	1.2×10^{49}	4.2×10^{49}	6.9×10^{49}	8.89×10^{53}

simulations predict the formation of a red supergiant. The maximum difference in the radius predictions here is $\lesssim 1000$ R$_\odot$. For higher initial masses, the predictions for maximum stellar radii become more divergent as proximity to the Eddington limit increases and numerical treatments adopted by each code modify the mass-loss rates.

The greatest difference in the maximum radius predictions ($\gtrsim 1000$ R$_\odot$) occurs for stars with initial masses between 40 and 100 M$_\odot$. Above ~ 100 M$_\odot$, stars have even higher mass-loss rates

that can completely strip a star of its envelope before it can become a red-supergiant. Such stars evolve directly towards the naked helium star phase and have much smaller radii. Therefore, for stars with initial masses more than 100 M$_\odot$, the difference between the maximum radius predictions by each simulation reduces to $\lesssim 100$ R$_\odot$. The predictions in this mass range seem to further converge into two main groups: PARSEC and MIST represent one group predicting smaller radii compared to the second group that consists of BoOST and BPASS models. The maximum radii in this mass range are
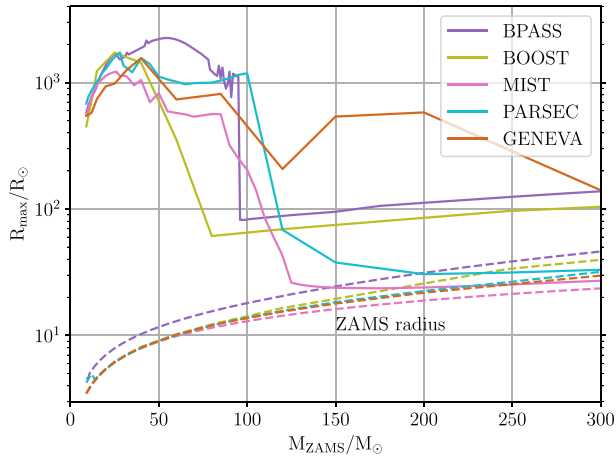
Figure 2. Maximum stellar radii as a function of the initial mass of the star. Similar to Fig. 1, differences in the physical inputs and the numerical methods adopted by each code can lead to a difference of more than 1000 $R_\odot$ in predictions in terms of the maximum radial expansion achieved by the stars.

predicted by the Geneva models. This is due to the difference in the mass-loss rates adopted during the naked helium phase of the star, as explained in the next section.

4.4 Remnant mass predictions

Stellar evolutionary models provide an easy way of estimating the properties of stellar remnants such as black holes and neutron stars, which are needed in many fields including supernova studies (e.g. Aguilera-Dena et al. 2018; Raithel, Sukhbold & Özel 2018), gamma-ray bursts progenitors (e.g. Yoon, Langer & Norman 2006; Szecsi 2017), and GW event rate predictions (e.g. Stevenson et al. 2019; Mapelli et al. 2020).

Following Belczynski et al. (2010), we show in Fig. 3 how the uncertainties in the models we compare here also pose a challenge for the predictions of remnant properties. Remnant masses have been calculated from the carbon-oxygen (CO) core mass and the total mass of the star at the end of the core helium-burning phase using the prescription of Belczynski et al. (2008; same as the StarTrack prescription in Fryer et al. 2012).

The Geneva models do not provide information on core masses in their publicly available data set. Therefore, the final CO-core mass for these models has been taken from Georgy et al. (2012; for stars with initial mass up to 120 $M_\odot$) and Yusof et al. (2013; for stars with initial mass more than 120 $M_\odot$). Note that in the Geneva models from Yusof et al. (2013), CO-core mass is defined as the mass of the core where the sum of mass fraction of carbon and oxygen exceeds 75 per cent, and is different to the definition used by Georgy et al. (2012).

The remnant masses are heavily influenced by the modelling assumptions (cf. Section 2) and the numerical methods (cf. Section 3) especially above $M_{ini} = 40\,M_\odot$ where the most massive black holes are predicted. For stars with initial masses between 9 and 120 $M_\odot$, we find that the mass of the black holes predicted by the different sets of models can differ by $\sim 20\,M_\odot$. The maximum black hole mass varies from about 20 $M_\odot$ for BPASS models to about 35 $M_\odot$ for MIST and PARSEC models, and 32 $M_\odot$ for the BoOST models. BPASS models consistently predict the lowest values of remnant mass for most of the massive stars while predictions from the BoOST, MIST, and
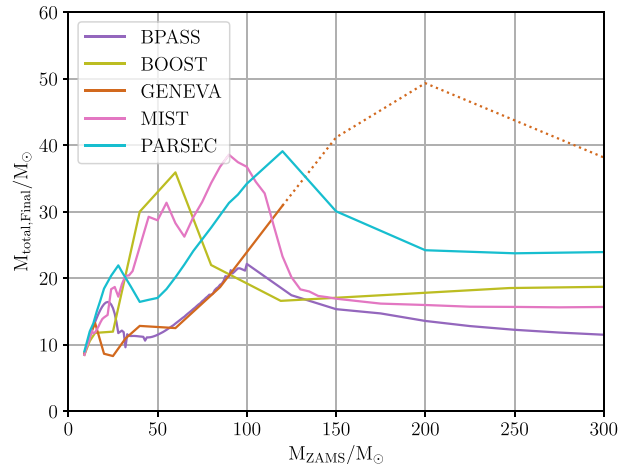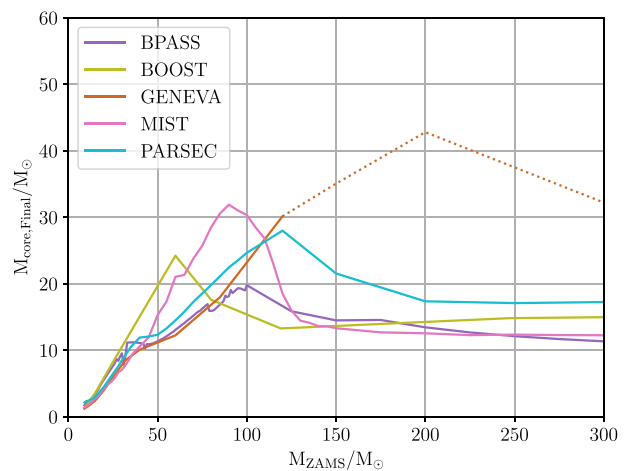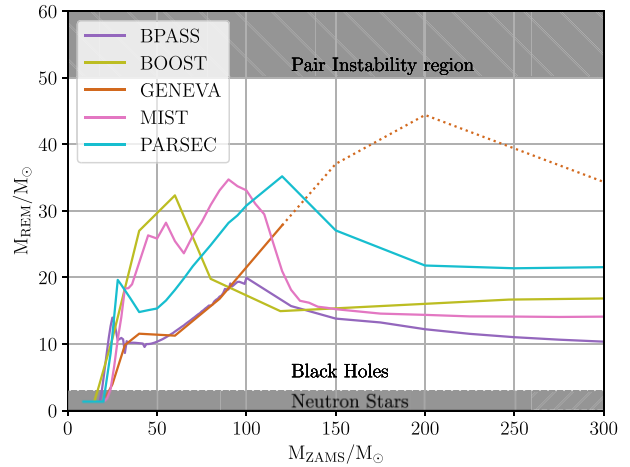
Figure 3. Final masses of stars as a function of their initial mass, M_{ZAMS}. The top panel shows the mass of stellar remnants as predicted by the different sets of stellar models. The middle panel shows the carbon-oxygen core mass and the bottom panel shows the total mass of the star, as used in the calculation of the remnant masses. For stars more massive than 120 $M_\odot$, the Geneva models from Yusof et al. (2013) use a different criteria for defining CO-core compared to the lower mass models from the same set (see Section 4.4 for details) and therefore, are represented using dotted line. Differences in the evolutionary parameters for massive stars can cause variations of about 20 $M_\odot$ in the remnant masses between the stellar models from various simulations.

PARSEC models peak at 60, 90, and $120\,M_\odot$ before flattening out at the higher initial masses.

For more massive stars, the variation in the remnant mass between BPASS, BoOST, MIST, and PARSEC models reduces to about $10\,M_\odot$. An interesting behaviour is shown by the Geneva models, which predict one of the lowest remnant masses for stars up to $120\,M_\odot$, reaching a maximum of only $28\,M_\odot$ at $120\,M_\odot$. These models, however, predict the highest values of remnant masses beyond $120\,M_\odot$. At their farthest, for a model with initial mass of $200\,M_\odot$, the predictions between the Geneva models and other models can be as high as $30\,M_\odot$. Similar variability is found in the core mass and the final total mass of the star (from which the remnant masses have been calculated).

The significantly higher remnant masses predicted by the Geneva models for stars with initial mass beyond $120\,M_\odot$ can be explained as follows. Due to their high luminosity, stars more massive than 100–$120\,M_\odot$ rapidly lose mass during the main-sequence phase and directly evolve towards the naked helium phase (cf. Fig. 1). The mass-loss prescriptions from both Nugis & Lamers (2000) and Hamann et al. (1995) predict that the highest mass-loss rates for stars occur during this naked helium phase. BPASS, MIST, and PARSEC models switch to mass-loss rates from Nugis & Lamers (2000) when the mass fraction of hydrogen at the surface of the star falls below 0.4, 0.4, and 0.5, respectively. BoOST models linearly interpolate between the mass-loss rates of Vink et al. (2001) and Hamann et al. (1995; reduced by a factor of 10) for stars with surface hydrogen mass fraction between 0.3 and 0.6, before completely switching to the mass-loss rate from Hamann et al. (1995; reduced by a factor of 10) for stars with surface hydrogen mass fraction less than 0.3.

Geneva models, on the other hand, switch to using mass-loss rates from Nugis & Lamers (2000) only when the mass fraction of hydrogen at the surface of the star falls below 0.05. For stars with surface hydrogen mass fraction between 0.3 and 0.05, they use the maximum of Vink et al. (2001) and Gräfener & Hamann (2008), which predict lower mass-loss rates compared to both Nugis & Lamers (2000) and Hamann et al. (1995) (see section 2.1 of Yusof et al. 2013). Thus, they do not lose as much mass as other models during the naked helium star phase and end with higher total mass and thus with the higher remnant mass.

Note that the Belczynski et al. (2008) prescription is one of several methods for predicting the remnant properties of the stars. Other methods for calculating the remnant masses may predict higher or lower values. For example, the remnant mass calculations based on the binding energy of the star (see e.g. Eldridge et al. 2017) are generally lower than those predicted here. However, all the models we study have near-solar metallicity and therefore rather high mass-loss rates; none of them stays massive enough at the end of their lives to undergo pair instability

5 CONCLUSIONS

We compare 1D evolutionary models of massive and very massive stars from five independent simulations. Focusing on near-solar composition, we find that the predictions from different codes can differ from each other by more than $1000\,R_\odot$ in terms of maximum radial expansion achieved by the stars, by ≈ 18 per cent in terms of ionizing radiation, and about $20\,M_\odot$ in terms of the stellar remnant mass. The differences in the evolution of massive stars can arise due to physical inputs like chemical abundances, mass-loss rates, and internal mixing properties. However, very massive stars, that is stars with initial masses $40\,M_\odot$ or more, show a larger difference in evolutionary properties compared to lower mass stars. For these

stars, the differences in the evolution can be largely attributed to the numerical treatment of the models when the Eddington limit is exceeded in their low-density envelopes.

The different methods used by 1D codes to compute the evolution of massive stars beyond density inversions (or to avoid the inversions) can modify the radius and temperature of the star, and can therefore affect the mass-loss rates. A phenomenological justification for the mass-loss enhancement comes from the fact that there are stars observed with extremely high, episodical mass-loss, i.e. luminous blue variables (Bestenlehner et al. 2014; Sarkisyan et al. 2020). However, other studies, such as the recent measurement of an approximately $20\,M_\odot$ black hole in the Galactic black hole high-mass X-ray binary Cyg X-1 (Miller-Jones et al. 2021), suggest that the mass-loss rates for massive stars at near-solar metallicity may be lower than usually assumed in the 1D stellar models (Neijssel et al. 2021). The exact nature of wind mass-loss for very massive stars remains disputed (Smith & Tombleson 2015). Moreover, variation in remnants masses in Fig. 3 shows that other uncertainties in massive star evolution can lead to differences at least as large as variations in mass-loss rates, which could also easily explain the formation of a $20\,M_\odot$ black hole in Cyg X-1 in the Galaxy.

None of the solutions that the BoOST, Geneva, MIST, and PARSEC models employ can currently be established as better than the others. In each case, they have been designed to address numerical issues in 1D stellar evolution. However, the interplay of these solutions with mass-loss rates and convection further adds to the uncertainties in massive stellar evolution. Therefore, a systematic study to untangle the effect of the treatment of the Eddington limit from other physical assumptions has been conducted in a companion paper (Agrawal et al. 2021).

In the case of BPASS, the stellar models evolve without requiring any numerical enhancement. Whether this is a result of using a non-Lagrangian mesh (the 'Eggletonian' mesh, which is more adaptive to changes in stellar structure) or whether this is an artefact of bigger time-steps (that helps stars skip problematic short-lived phases of evolution) is currently not known. A separate study to explore the effect of the 'Lagrangian' versus the 'Eggletonian' mesh structure for massive stars [similar to Stancliffe, Tout & Pols (2004) study for low- and intermediate-mass stars] is highly desirable.

In conclusion, it is crucial to be aware of the uncertainties resulting from numerical methods whenever the evolutionary model sequences of massive stars are applied in any scientific project, such as GW event rate predictions or star formation and feedback studies.

We only focus on massive stars as isolated single stars in this work. However, there is mounting evidence that massive stars are formed as binaries or triples, thus treating them as single stars might not be correct (e.g. Klencki et al. 2020; Laplace et al. 2021). Several studies have shown that binarity can heavily influence the lives of massive stars through mass and angular momentum transfer (de Mink et al. 2009; Marchant et al. 2016; Eldridge et al. 2017) and can therefore help in avoiding density and pressure inversion regions in stellar envelopes (Shenar et al. 2020).

We also limit our study to massive stars at near-solar metallicity, where due to high opacity, the numerical instabilities related to the proximity to the Eddington limit are maximum. Since opacity decreases with metallicity, opacity peaks become less prominent at lower metallicity. Nevertheless, stars with low metal content also reach the Eddington limit, although at higher initial masses (Sanyal et al. 2015, 2017). While progenitors of currently detectable GW sources may have been born in the early Universe where the metal content is sub-solar (cf. Santoliquido et al. 2021), high star formation rates at near-solar metallicities offer a fertile ground for the formation

of more GW sources, although less massive compared to sub-solar metallicity (Neijssel et al. 2019). As such, there is good motivation for studying the behaviour and reliability of massive star models across a wide range of metallicities (Agrawal et al. 2021).

Collecting observational data as well as improvements in 3D and hydrodynamical modelling will help us better constrain the models of massive stars in the future. Until then, however, we urge the broader community to treat any set of stellar models with caution. Ideally, one would implement all available simulations as input into any given astrophysical study, and test the outcome also in terms of stellar evolution-related uncertainties. With tools such as METISSE (Agrawal et al. 2020) and SEVN (Spera et al. 2019), this task is becoming feasible.

DATA AVAILABILITY

All the stellar models used in this work are publicly available:

PARSEC: people.sissa.it/∼sbressan/parsec.html;

MIST: waps.cfa.harvard.edu/MIST/;

Geneva: obswww.unige.ch/Research/evol/tables_grids2011/Z014;

BPASS: bpass.auckland.ac.nz/9.html;

BoOST: boost.asu.cas.cz.

REFERENCES

Agrawal P., Hurley J., Stevenson S., Szécsi D., Flynn C., 2020, MNRAS, 497, 4549

Agrawal P., Stevenson S., Szécsi D., Hurley J., 2021, preprint (arXiv:2112.02801)

Aguilera-Dena D. R., Langer N., Moriya T. J., Schootemeijer A., 2018, ApJ, 858, 115

Alongi M., Bertelli G., Bressan A., Chiosi C., Fagotto F., Greggio L., Nasi E., 1993, A&AS, 97, 851

Asplund M., Grevesse N., Sauval A. J., 2005, in Barnes T. G., III, Bash F. N., eds, ASP Conf. Ser. Vol. 336, Cosmic Abundances as Records of Stellar Evolution and Nucleosynthesis. Astron. Soc. Pac., San Francisco, p. 25

Asplund M., Grevesse N., Sauval A. J., Scott P., 2009, ARA&A, 47, 481

Asplund M., Amarsi A. M., Grevesse N., 2021, A&A, 653, A141

Basu S., 2009, in Dikpati M., Arentoft T., González Hernández I., Lindsey C., Hill F., eds, ASP Conf. Ser. Vol. 416, Solar-Stellar Dynamos as Revealed by Helio- and Asteroseismology: GONG 2008/SOHO 21. Astron. Soc. Pac., San Francisco, p. 193

Belczynski K., Kalogera V., Rasio F. A., Taam R. E., Zezas A., Bulik T., Maccarone T. J., Ivanova N., 2008, ApJS, 174, 223

Belczynski K., Bulik T., Fryer C. L., Ruiter A., Valsecchi F., Vink J. S., Hurley J. R., 2010, ApJ, 714, 1217

Bestenlehner J. M. et al., 2014, A&A, 570, A38

Böhm-Vitense E., 1958, Z. Astrophys., 46, 108

Bressan A. G., Chiosi C., Bertelli G., 1981, A&A, 102, 25

Bressan A., Marigo P., Girardi L., Salasnich B., Dal Cero C., Rubele S., Nanni A., 2012, MNRAS, 427, 127

Brott I. et al., 2011a, A&A, 530, A115

Brott I. et al., 2011b, A&A, 530, A116

Caffau E., Ludwig H. G., Steffen M., Freytag B., Bonifacio P., 2011, Sol. Phys., 268, 255

Chen Y., Bressan A., Girardi L., Marigo P., Kong X., Lanza A., 2015, MNRAS, 452, 1068

Choi J., Dotter A., Conroy C., Cantiello M., Paxton B., Johnson B. D., 2016, ApJ, 823, 102

Costa G., Girardi L., Bressan A., Marigo P., Rodrigues T. S., Chen Y., Lanza A., Goudfrooij P., 2019, MNRAS, 485, 4641

Cox J., Giuli R., 1968, Principles of Stellar Structure: Physical Principles, Principles of Stellar Structure. Gordon & Breach, New York https://books.google.com.au/books?id = TdhEAAAAIAAJ

Crowther P. A., 2000, A&A, 356, 191

Crowther P., 2012, Astron. Geophys., 53, 4.30

Cunha K., Hubeny I., Lanz T., 2006, ApJ, 647, L143

de Jager C., Nieuwenhuijzen H., van der Hucht K. A., 1988, A&AS, 72, 259

de Mink S. E., Cantiello M., Langer N., Pols O. R., Brott I., Yoon S.-C., 2009, A&A, 497, 243

Eddington A. S., 1926, The Internal Constitution of the Stars, Cambridge Science Classics. Cambridge Univ. Press, Cambridge

Eggenberger P., Meynet G., Maeder A., Hirschi R., Charbonnel C., Talon S., Ekström S., 2008, Ap&SS, 316, 43

Eggleton P. P., 1973, MNRAS, 163, 279

Ekström S. et al., 2012, A&A, 537, A146

Eldridge J. J., Stanway E. R., Xiao L., McClelland L. A. S., Taylor G., Ng M., Greis S. M. L., Bray J. C., 2017, Publ. Astron. Soc. Aust., 34, e058

Evans C. J. et al., 2005, A&A, 437, 467

Fryer C. L., Belczynski K., Wiktorowicz G., Dominik M., Kalogera V., Holz D. E., 2012, ApJ, 749, 91

Gatto A. et al., 2017, MNRAS, 466, 1903

Georgy C., Ekström S., Meynet G., Massey P., Levesque E. M., Hirschi R., Eggenberger P., Maeder A., 2012, A&A, 542, A29

Gräfener G., Hamann W. R., 2008, A&A, 482, 945

Gräfener G., Owocki S. P., Vink J. S., 2012, A&A, 538, A40

Grassitelli L., Fossati L., Langer N., Simón-Díaz S., Castro N., Sanyal D., 2016, A&A, 593, A14

Grevesse N., Noels A., 1993, in Prantzos N., Vangioni-Flam E., Casse M., eds, Origin and Evolution of the Elements. Proceedings of a symposium in honour of H. Reeves, held in Paris, June 22-25, 1992, Cambridge University Press, p. 15

Grevesse N., Sauval A. J., 1998, Space Sci. Rev., 85, 161

Grevesse N., Noels A., Sauval A. J., 1996, in Holt S. S., Sonneborn G., eds, ASP Conf. Ser. Vol. 99, Cosmic Abundances. Astron. Soc. Pac., San Francisco, p. 117

Groh J. H., Farrell E. J., Meynet G., Smith N., Murphy L., Allan A. P., Georgy C., Ekstroem S., 2020, ApJ, 900, 98

Hamann W. R., Koesterke L., Wessolowski U., 1995, A&A, 299, 151

Harpaz A., 1984, MNRAS, 210, 633

Heger A., Langer N., Woosley S. E., 2000, ApJ, 528, 368

Heger A., Woosley S. E., Spruit H. C., 2005, ApJ, 626, 350

Heggie D., Hut P., 2003, The Gravitational Million-Body Problem: A Multidisciplinary Approach to Star Cluster Dynamics. Cambridge Univ. Press, Cambridge

Henyey L., Vardya M. S., Bodenheimer P., 1965, ApJ, 142, 841

Herwig F., 2000, A&A, 360, 952

Humphreys R. M., Davidson K., 1979, ApJ, 232, 409

Jiang Y.-F., Cantiello M., Bildsten L., Quataert E., Blaes O., 2015, ApJ, 813, 74

Jones S., Hirschi R., Pignatari M., Heger A., Georgy C., Nishimura N., Fryer C., Herwig F., 2015, MNRAS, 447, 3115

Kaiser E. A., Hirschi R., Arnett W. D., Georgy C., Scott L. J. A., Cristini A., 2020, MNRAS, 496, 1967

Kippenhahn R., Weigert A., 1990, Stellar Structure and Evolution. Springer-Verlag, Berlin

Klencki J., Nelemans G., Istrate A. G., Pols O., 2020, A&A, 638, A55

Lamers H., Cassinelli J., 1999, Introduction to Stellar Winds. Cambridge Univ. Press, Cambridge

Langer N., 1989, A&A, 210, 93

Langer N., 1997, in Nota A., Lamers H., eds, ASP Conf. Ser. Vol. 120, Luminous Blue Variables: Massive Stars in Transition. Astron. Soc. Pac., San Francisco, p. 83

Laplace E., Justham S., Renzo M., Götberg Y., Farmer R., Vartanyan D., de Mink S. E., 2021, A&A, 656, A58

Lau H. H. B., Gil-Pons P., Doherty C., Lattanzio J., 2012, A&A, 542, A1

Ledoux P., 1947, ApJ, 105, 305

Levesque E. M., 2017, Astrophysics of Red Supergiants. IOP Publishing, Bristol, UK, p. 2514

Maeder A., 1987, A&A, 173, 247

Maeder A., 2009, Physics, Formation and Evolution of Rotating Stars. Springer-Verlag, Berlin

Maeder A., Meynet G., 2005, A&A, 440, 1041

Mapelli M., Spera M., Montanari E., Limongi M., Chieffi A., Giacobbo N., Bressan A., Bouffanais Y., 2020, ApJ, 888, 76

Marchant P., Langer N., Podsiadlowski P., Tauris T. M., Moriya T. J., 2016, A&A, 588, A50

Martins F., Palacios A., 2013, A&A, 560, A16

Miller-Jones J. C. A. et al., 2021, Science, 371, 1046

Moe M., Di Stefano R., 2017, ApJS, 230, 15

Neijssel C. J. et al., 2019, MNRAS, 490, 3740

Neijssel C. J., Vinciguerra S., Vigna-Gómez A., Hirai R., Miller-Jones J. C. A., Bahramian A., Maccarone T. J., Mandel I., 2021, ApJ, 908, 118

Nieuwenhuijzen H., de Jager C., 1990, A&A, 231, 134

Nishida M., Schindler A. M., 1967, PASJ, 19, 606

Nugis T., Lamers H. J. G. L. M., 2000, A&A, 360, 227

Paxton B., Bildsten L., Dotter A., Herwig F., Lesaffre P., Timmes F., 2011, ApJS, 192, 3

Paxton B. et al., 2013, ApJS, 208, 4

Petit V. et al., 2017, MNRAS, 466, 1052

Pols O. R., Schröder K.-P., Hurley J. R., Tout C. A., Eggleton P. P., 1998, MNRAS, 298, 525

Puls J., Springmann U., Lennon M., 2000, A&AS, 141, 23

Raithel C. A., Sukhbold T., Özel F., 2018, ApJ, 856, 35

Ramírez-Agudelo O. H. et al., 2013, A&A, 560, A29

Renzo M., Ott C. D., Shore S. N., de Mink S. E., 2017, A&A, 603, A118

Salpeter E. E., 1955, ApJ, 121, 161

Sana H. et al., 2012, Science, 337, 444

Sander A. A. C., Vink J. S., 2020, MNRAS, 499, 873

Santoliquido F., Mapelli M., Giacobbo N., Bouffanais Y., Artale M. C., 2021, MNRAS, 502, 4877

Sanyal D., Grassitelli L., Langer N., Bestenlehner J. M., 2015, A&A, 580, A20

Sanyal D., Langer N., Szécsi D., -C Yoon S., Grassitelli L., 2017, A&A, 597, A71

Sarkisyan A. et al., 2020, MNRAS, 497, 687

Schneider F. R. N., Langer N., de Koter A., Brott I., Izzard R. G., Lau H. H. B., 2014, A&A, 570, A66

Schootemeijer A., Langer N., Grin N. J., Wang C., 2019, A&A, 625, A132

Schwarzschild M., 1958, Structure and Evolution of the Stars. Princeton Univ. Press, Princeton, NJ

Shenar T., Gilkis A., Vink J. S., Sana H., Sander A. A. C., 2020, A&A, 634, A79

Smith N., 2014, ARA&A, 52, 487

Smith N., Tombleson R., 2015, MNRAS, 447, 598

Spera M., Mapelli M., Giacobbo N., Trani A. A., Bressan A., Costa G., 2019, MNRAS, 485, 889

Stancliffe R. J., 2006, MNRAS, 370, 1817

Stancliffe R. J., Tout C. A., Pols O. R., 2004, MNRAS, 352, 984

Stevenson S., Sampson M., Powell J., Vigna-Gómez A., Neijssel C. J., Szécsi D., Mandel I., 2019, ApJ, 882, 121

Sukhbold T., Woosley S., 2014, ApJ, 783, 10

Szécsi D., 2016, PhD thesis, Mathematisch-Naturwissenschaftlichen Fakultät der Universität Bonn

Szecsi D., 2017, in Giovannelli F., Sabau-Graziati L., eds, XII Multifrequency Behaviour of High Energy Cosmic Sources Workshop (MULTIF2017). Proceedings of Science, Sissa Medialab, Trieste, Italy, p. 65

Szécsi D., Agrawal P., Wünsch R., Langer N., 2022, A&A, 658, A125

Takahashi K., Langer N., 2021, A&A, 646, A19

Topping M. W., Shull J. M., 2015, ApJ, 800, 97

Vigna-Gómez A. et al., 2018, MNRAS, 481, 4009

Vink J. S., 2011, Ap&SS, 336, 163

Vink J. S., de Koter A., Lamers H. J. G. L. M., 2000, A&A, 362, 295

Vink J. S., de Koter A., Lamers H. J. G. L. M., 2001, A&A, 369, 574

Walder R., Folini D., Meynet G., 2012, Space Sci. Rev., 166, 145

Weinberger R., Springel V., Pakmor R., 2020, ApJS, 248, 32

Wofford A. et al., 2016, MNRAS, 457, 4296

Woosley S. E., Heger A., Weaver T. A., 2002, Rev. Mod. Phys., 74, 1015

Yoon S.-C., Langer N., Norman C., 2006, A&A, 460, 199

Yusof N. et al., 2013, MNRAS, 433, 1114

This paper has been typeset from a TeX/LaTeX file prepared by the author.

Role of Supergiants in the Formation of Globular Clusters

Dorottya Szécsi[1,2] and Richard Wünsch[3]
[1] Institute of Gravitational Wave Astronomy and School of Physics and Astronomy, University of Birmingham, Edgbaston, Birmingham B15 2TT, UK
[2] Astronomical Institute of the Czech Academy of Sciences, Fričova 298, 25165 Ondřejov, Czech Republic
[3] Astronomical Institute of the Czech Academy of Sciences, Boční II 1401, 141 00 Prague 4, Czech Republic

Abstract

Multiple stellar populations are observed in almost all globular clusters, but the origin of this phenomenon is still debated. We investigate the role cool supergiants may have played. To do this, we combine two investigative methods: state-of-the-art massive stellar evolution and calculations of the hydrodynamic structure of the cluster gas. This approach allows us to study how star formation in young massive clusters depends on the energy and mass input of the first generation of stars, while predicting the chemical composition of the second generation. We find that the presence of massive (9–500 $M_\odot$) metal-poor supergiants in the young cluster leads to a star formation episode within the first 4 Myr of the cluster's lifetime, that is, *before* the first core-collapse supernovae explode or the gas is expelled. The stellar winds accumulate in the cluster center, forming the second generation there. Its composition is predicted to show variations in O and Na abundances, consistently with observations. The abundance of helium is, similarly to other scenarios involving massive stars, higher than what is inferred from observations. Supposing dynamical removal of stars from the outskirts of the cluster, or applying a top-heavy initial mass function, we can predict a number ratio of the second generation as high as 20%–80%. The effect of metallicity is shown to be important, as the most luminous supergiants are only predicted at low metallicity, thus limiting—but not excluding—the extent of a polluted second generation at high metallicity. These massive stars becoming black holes suggest globular clusters hosting gravitational-wave progenitors. Our scenario predicts a correlation between the mass of the cluster and the extent of the multiple-population phenomenon.

Key words: galaxies: star clusters: general – globular clusters: general – stars: abundances – stars: formation – stars: massive – supergiants

1. Introduction

Young massive clusters (YMCs) are compact star-forming regions with a radius of only a few parsecs (Portegies Zwart et al. 2010; Longmore et al. 2014). Since their projected lifetimes are consistent with those of old globular clusters (GCs; Maíz-Apellániz 2002), they have been suggested to become GC-like objects eventually. In turn, old GCs, observed to populate the bulges and halos of many galaxies, including our own, are hypothesized to start out as massive clusters (Brodie & Strader 2006; Andersen et al. 2016).

Both YMCs and GCs, as well as their suggested connection, are surrounded by observational puzzles. For example, why do we see multiple stellar populations in practically all GCs (e.g., Yong et al. 2003; Gratton et al. 2004; Harris 2010; Da Costa et al. 2013; Bastian & Lardo 2018), and possibly in other clusters with ages up to 2 Gyr (e.g., Martocchia et al. 2018a)? Since one of the main indications that a cluster harbors multiple populations is the anomalous ratios of light elements—e.g., the observed ratio of sodium and oxygen, which can only be synthesized at temperatures as high as 60–100 MK—it has long been suggested that a first generation of massive or intermediate-mass stars is responsible for the formation of an anomalous second generation. But responsible in which sense? What are the conditions under which a second star formation episode can happen that feeds on the material ejected from the first generation? Or, to turn the question around, is the amount

of material ejected from the first-generation stars enough to produce the observed number of second-generation stars? The latter puzzle is usually referred to as the "mass budget problem," since most scenarios suggested so far do struggle to answer yes.

It all may have something to do with metallicity, as we know that massive stellar evolution strongly depends on this (e.g., Meynet & Maeder 2002; Yoon et al. 2006; Brott et al. 2011; Georgy et al. 2013; Sanyal et al. 2017; Vink 2018). But how does the metallicity of the cluster influence the second-generation star formation? In particular, how does the hydrodynamic structure of the cluster gas depend on the metallicity of the first stellar generation? How does the composition of the second generation depend on that?

Recently, Szécsi et al. (2018) suggested that cool supergiants may play a role in the formation of the multiple populations in GCs. They investigated a scenario in which the second generation forms in a photoionization-confined shell around such cool supergiants and speculated that the mass budget problem may be solved by only forming low-mass stars—which, contrarily to some of the other scenarios that assumed the same (e.g., de Mink et al. 2009b; D'Ercole et al. 2010), is better justified in these exotically shaped star-forming regions (see Section 4.7 of Szécsi et al. 2018). Nevertheless, they also suggested that even without such a shell, the wind of supergiant stars may play an important role in GCs that shall be more closely inspected—and this is the objective of present work.

Here we investigate these questions by combining up-to-date theories of massive stellar evolution (those that predict cool supergiants) with calculations of the cluster's hydrodynamic structure. Earlier studies involving massive or intermediate-mass

stellar evolution were able to predict e.g., chemical pollution and element ratios (e.g., Karakas et al. 2006; Decressin et al. 2007b; de Mink et al. 2009b; Denissenkov & Hartwick 2014; Szécsi et al. 2018), but not able to say too much about the hydrodynamic behavior of the gas in the cluster or, for that matter, under which conditions the formation of the second generation of stars happens. On the other hand, studies of the gas reinserted by massive stars within young clusters and its eventual accumulation leading to secondary star formation (e.g., Silich et al. 2004; Tenorio-Tagle et al. 2005; Wünsch et al. 2011, 2017; Palouš et al. 2014; Martínez-González et al. 2016; Silich & Tenorio-Tagle 2017) have hardly ever taken into account newly found peculiar aspects of stellar evolution. Combining these two research areas is therefore a viable and auspicious approach.

To that end, we use hydrodynamical, semianalytic calculations of the cluster structure (taken from Wünsch et al. 2017), which account for the winds of the first stellar generation as an input. We apply two different sets of single stellar evolutionary models for this first generation (taken from Brott et al. 2011; Köhler et al. 2015; Szécsi et al. 2015). They correspond to metallicities of the Large Magellanic Cloud (LMC) and of the low-metallicity dwarf galaxy I Zwicky 18 (I Zw 18). Thus, we are able to investigate both the questions of when and with which composition the second generation of stars may form in a YMC. Additionally, we are able to study the process's dependence on metallicity, as well as the role that cool supergiants play in it.

This paper is organized as follows. The semianalytic hydrodynamic code that determines the cluster structure, as well as the stellar evolutionary models, is described in Section 2. The synthetic population of stars that we created from the massive stellar models is discussed in Section 3. In Section 4 we perform calculations of the cluster's hydrodynamic structure applying the synthetic populations. We also discuss the conditions under which a second generation of stars may form. Section 5 then investigates the chemical composition of this second generation. Section 6 deals with the mass budget. Section 7 discusses caveats and future directions, while Section 8 summarizes and concludes the work.

2. Methods

2.1. Rapidly Cooling Shocked Winds

YMCs include large populations of massive stars concentrated in a rather small volume. Thus, their stellar winds are expected to collide with each other and heat up to high ($\sim 10^6$–10^7 K) temperatures. The overpressure of this hot gas then drives a star cluster (SC) wind (Chevalier & Clegg 1985). If the cluster is massive and compact, and hence the density of the hot gas within it is high, the gas becomes thermally unstable, cools down to $\sim 10^4$ K, and forms dense clumps. The clumps are initially warm and ionized owing to the radiation of nearby massive stars, but a fraction of them falls into the cluster center owing to the cluster gravity, where the gas accumulates until its column density is high enough to self-shield against the ionizing radiation. Then, the gas cools further to lower temperatures and forms new stars. This scenario was explored extensively in a series of papers by Silich et al. (2003, 2004), Tenorio-Tagle et al. (2007), Wünsch et al. (2008, 2011), Palouš et al. (2013, 2014), and others.

Wünsch et al. (2017) studied this model of rapidly cooling shocked stellar winds by means of 3D hydrodynamic

simulations including gravity (of both stars and gas), radiative cooling of the hot gas, and EUV radiation of massive stars. They estimated a fraction of stellar winds that accumulates inside the cluster depending on various cluster parameters.

They compared the results of the 3D simulations to the outcome of a much simpler and much faster 1D semianalytic code (see below) that is also able to estimate the mass of the second stellar generation. They found a good agreement. As for the first stellar generation, they relied on the predictions of the stellar synthesis code *Starburst99* by Leitherer et al. (1999). They found that, using solar-metallicity *Starburst99* models of single stars up to $M_{\rm top} = 120\,M_\odot$ and a standard initial mass function (IMF), a substantially massive second generation of stars forms only if the heating efficiency,[4] an observationally poorly constrained parameter, is very low. Here we apply the updated version of the semianalytic code using stellar populations with different underlying physics (including different metallicities and $M_{\rm top}$). Below we shortly describe how the code works and what initial parameters we assume when running it.

In a gravitationally bound SC, it can safely be supposed that properties of the stellar winds vary on a much longer timescale than the cluster wind crossing time. Therefore, one can search for a stationary solution of a set of spherically symmetric (1D) hydrodynamic equations to describe the *SC wind* (Chevalier & Clegg 1985). If the cluster is massive and compact enough, the hot gas is subject to radiative cooling owing to its high density, and thus the set of stationary hydrodynamic equations to be solved should include the appropriate cooling term. A code to solve such a set with the assumption of spherical symmetry was developed first by Silich et al. (2004). Here we use a similar code described in Wünsch et al. (2011, 2017) updated with terms describing the effect of the SC gravity on the gas.

The set of stationary spherically symmetric hydrodynamic equations has the form

$$\frac{1}{r^2}\frac{d}{dr}(\rho u r^2) = q_m \tag{1}$$

$$\rho u \frac{du}{dr} = -\frac{dP}{dr} - q_m u - \rho \frac{d\Psi_\star}{dr} \tag{2}$$

$$\frac{1}{r^2}\frac{d}{dr}\left[\rho u r^2\left(\frac{u^2}{2} + \frac{\gamma}{\gamma - 1}\frac{P}{\rho}\right)\right] = q_e - Q - \rho u \frac{d\Psi_\star}{dr}, \tag{3}$$

where ρ, u, and P are the wind density, velocity, and pressure, respectively. The mass and energy input rate densities, q_m and q_e, respectively, represent stellar winds approximated by a spatially smooth source described with a generalized Schuster distribution ($\sim [1 + (r/R_c)^2]^{-\beta}$ for $r < R_{\rm SC}$), with parameters R_c, $R_{\rm SC}$, and β being the core radius, cutoff radius, and slope of the distribution, respectively. The gravitational potential $\Psi_\star$ includes only a contribution from stars (i.e., the gas gravity is ignored), and it is assumed that the mass is distributed with the same generalized Schuster distribution as the wind sources and that the total mass is $M_{\rm SM}$. The cooling term has a form $Q = n_i n_e \Lambda(T, a_j)$, where $n_i = n_e = \rho/\mu_{\rm H}$ are the ion and

---

[4] Heating efficiency means the fraction of the mechanical energy of stellar winds that is transformed into thermal energy of the hot shocked gas inside the cluster.

electron number densities and $\Lambda(T, a_j)$ is a cooling function calculated by Schure et al. (2009) with abundances of 15 species (H, He, C, N, O, Ne, Na, Mg, Al, Si, S, Ar, Ca, Fe, Ni), denoted a_j, calculated by the stellar population synthesis code (see Section 3.3) from surface abundances of stellar evolution models (see Section 2.2).

The solution of Equations (1)–(3) exists only in a subset of the parameter space. It is possible to define a critical luminosity L_{crit} so that the solution exists only if the total mechanical luminosity of all stellar winds is smaller than the critical value, $L_{SC} < L_{crit}$. The semianalytic code determines the critical luminosity iteratively by trying to solve Equations (1)–(3) for a given set of parameters: R_c, R_{SC}, β, and properties of the wind of a stellar population with a given mass, age, and chemical composition. It has been shown by Wünsch et al. (2017) that L_{crit} can also be used to estimate the rate of clump formation: the mass of clumps formed over time is the difference between $\dot{M}_{SC}$ and $\dot{M}_{crit}$, the former being the mass deposition rate of the cluster, and the latter the corresponding quantity but taking $L_{SC} = L_{crit}$. The mass accumulation rate, $\dot{M}_{acc}$, is then determined by taking into account only clumps that are formed with initial velocity (the same as the cluster wind velocity u) smaller than the escape velocity $u_{esc} \equiv \sqrt{2\Psi_\star}$.

As the semianalytic code models the SC using a smooth distribution of mass and energy sources, the calculations cannot represent discrete events such as supernova explosions or, therefore, the effect of the dust they produce. We discuss why and when it is justified to omit supernovae in our calculations in Section 3.5.

In this work, we discuss two cluster models differing in the initial chemical composition of massive stars (see Section 2.2). We assume that all first-generation stars are formed abruptly at $t = 0$, and we follow the cluster evolution for 10 Myr. The total mass of the first-generation stars is $M_{SC} = 10^7 \, M_\odot$ for both models; the stars are assumed to form with the standard IMF (Kroupa 2001), and they are represented by the stellar models described in Section 2.2. The second-generation stars are represented only as the accumulated mass (M_{acc}); they do not contribute to our calculations by, e.g., their stellar winds. The stellar density profile of the cluster is given by the generalized Schuster distribution with $R_c = 1$ pc, $R_{SC} = 3$ pc, and $\beta = 1.5$. As opposed to Wünsch et al. (2017), here we assume that all the mechanical energy of stellar winds is converted to the thermal energy of the hot gas (i.e., the heating efficiency is unity) and that the mass loading is zero. On the other hand, we use a different upper mass limit, M_{top}, from our first-generation stellar population, as explained in Section 3.3. Additionally, we carry out a parameter space study (details given in Section 6.2), where we vary the initial cluster mass, M_{SC}, and the index of the IMF for stars more massive than $1 \, M_\odot$.

2.2. Stellar Evolutionary Models

To account for the first generation of massive stars, we apply two sets of models, both computed with the BEC code (see, e.g., Heger et al. 2000; Yoon et al. 2012; Szécsi et al. 2015, and references therein). The models with initial composition of the LMC were created by Brott et al. (2011) and Köhler et al. (2015), representing a subsolar-metallicity environment with ~0.4 $Z_\odot$ (i.e., [Fe/H] ~ −0.4). Those with initial composition of the dwarf galaxy I Zw 18 were created by Szécsi et al. (2015, 2018), representing a low-metallicity environment with ~0.02 $Z_\odot$ (i.e., [Fe/H] ~ −1.7).

The low-metallicity models between $M_{ini} = 10$ and 300 $M_\odot$ have all been followed until the end of core helium burning (completing the work of Szécsi et al. 2015, who only followed them until the end of core hydrogen burning). From this point on, we mainly refer to the composition of the LMC as high metallicity and to that of I Zw 18 as low metallicity.

The most massive models ($>70 \, M_\odot$ in the high-metallicity set and $>300 \, M_\odot$ in the low-metallicity set) have been, however, only computed until core hydrogen exhaustion (i.e., terminal-age main sequence). Therefore, we extrapolate for how much mass they would lose during their remaining evolution if the mass-loss rate was the same as that at the end of the computation. This is clearly a simplistic approach that brings some additional uncertainty into our predictions.

As for rotation, all the models have zero or slow rotation (i.e., 0 or 100 km s^{-1} initially). They evolve with a distinct core envelope structure toward lower surface temperatures. It shall be a future task to add models that have more extreme rotation rates (and, e.g., evolve chemically homogeneously). Also, effects of binarity are omitted at this point, as we only apply single stellar models.

The wind velocity, v_{wind}, of any given stellar model is calculated from the escape velocity from the stellar surface as $v_{wind} = 1.3 \cdot v_{esc}$ and $v_{wind} = 2.6 \cdot v_{esc}$ for models below and above a surface temperature of 21 kK, respectively, following the theory of line-driven winds (Lamers & Cassinelli 1999). Additionally, following e.g., Leitherer et al. (1992), the wind velocity is corrected for the metallicity of the wind material, Z, by multiplying it by a factor $(Z/Z_\odot)^{0.13}$. Since supergiants' winds are not expected to be line driven, we checked that the outcome of our calculations is not, in fact, sensitive to the actual values of supergiant wind velocity we use, as long as they are below 80 km s^{-1}, which they indeed are.

3. Stellar Populations

3.1. Comparing the Two Sets of Models

Figure 1 shows the Hertzsprung–Russell diagrams of the two sets of models. The most important difference between the high-metallicity models (LMC) and the low-metallicity models (I Zw 18) is the presence of very massive ($\gtrsim 100 \, M_\odot$) cool supergiants in the latter case, populating the upper right corner of the diagram. The reason the very massive, high-metallicity models do not evolve to the supergiant branch is that their mass-loss rate during the main sequence is high enough to remove almost the whole envelope, turning them into hot stars such as luminous blue variables (LBVs) or Wolf-Rayet stars. As we show in Section 4.1, the presence of very massive supergiants at low metallicity is the key to forming a second generation of stars early enough so that they show chemical abundances attributed to a subsequent population.

Other differences between the high- and low-metallicity sets of models are as follows:

1. Both the zero-age main sequence and the terminal-age main sequence lie at lower surface temperatures when the metallicity gets higher.
2. Blue supergiants are found in the low-metallicity models with 9–30 $M_\odot$ during core helium burning (i.e., blue loop).
3. Red supergiants with 9–45 $M_\odot$ are found among the high-metallicity models; these are also core helium-burning objects.
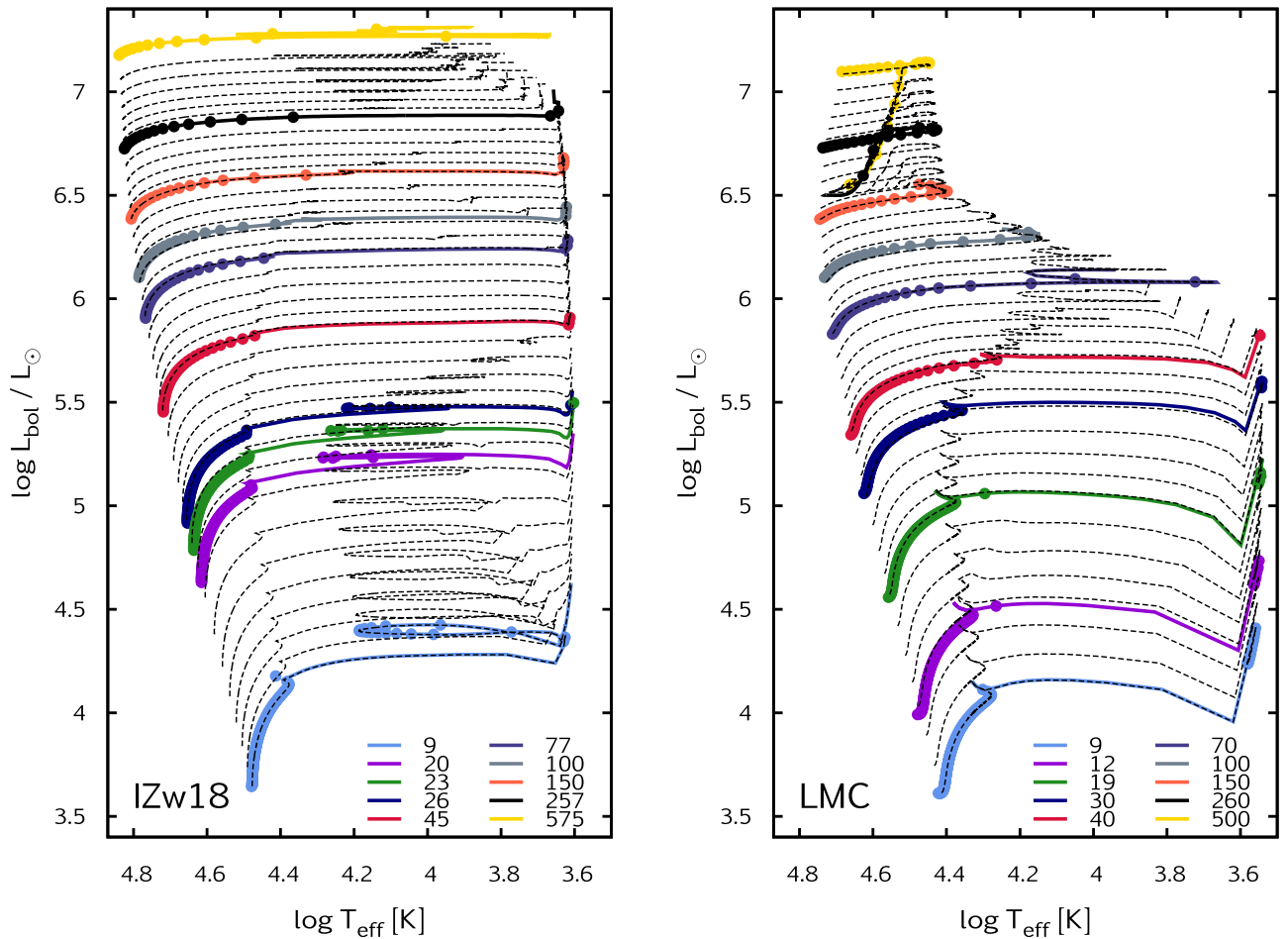
Figure 1. Hertzsprung–Russell diagrams of the two sets of models. Left: low-metallicity models; right: high-metallicity models. Initial masses are color-coded and indicated by the key legends (units in $M_\odot$). Black dashed lines mark interpolated tracks between the colored models; interpolation is performed between 0.1 and 500 $M_\odot$, resulting in ∼5000 tracks in this mass range.

4. The presence of LBVs at $M_{\rm ini} \sim$ 70–100 $M_\odot$ in the high-metallicity models; LBVs are found in the low-metallicity models only at masses above ≳300 $M_\odot$.

5. The presence of Wolf-Rayet stars at $M_{\rm ini} \gtrsim$ 100 $M_\odot$ in the high-metallicity models; no Wolf-Rayet stars are found in the low-metallicity models.

Since the very massive supergiants at low metallicity are the key objects responsible for the multiple-population phenomenon in our model, it is important to discuss them here a bit further.

3.2. Cool Supergiants

Low-metallicity models with $M_{\rm ini} \gtrsim 80\ M_\odot$ evolve to the supergiant branch even during their core hydrogen-burning phase owing to envelope inflation. This phenomenon has been investigated by Sanyal et al. (2015, 2017), who found that the reason these stars inflate their envelopes and thus expand is their proximity to the Eddington limit.

What is extremely intriguing in the context of the chemical composition and the multiple populations in SCs is that these massive stars becoming cool supergiants during their core hydrogen-burning phase means that they have a convective envelope. Convection mixes the material between the core—where the CNO cycle operates, together with side reactions that can synthesize Na and Al at the expense of O and Mg—and the

surface. The surface layers are then removed by the stellar wind, thus polluting the interstellar gas with nuclear ashes that have undergone hot hydrogen burning. Interestingly, the convective core does not reach down again into the burning regions during core helium burning (since these layers are much deeper inside than those of core hydrogen burning), thus avoiding the ejection of helium-burning products. This makes these supergiants quite ideal to be suggested as potential pollution sources in GCs.

Whether these stars exist in nature is a question for future investigations. Envelope inflation has been recently studied by several authors (Gräfener et al. 2012; Grassitelli et al. 2015a, 2015b; Sanyal et al. 2015, 2017). In particular, Moriya & Langer (2015) suggested that such supergiants may be responsible for some supernovae of the superluminous type. An additional caveat of using simulations of supergiants is that their mass-loss rates are, despite great efforts to constrain them, still quite uncertain. For a comprehensive discussion on the subject, we refer to Levesque (2017), as well as to the relevant literature on our stellar models (Section 5 in Szécsi et al. 2015 and Section 2.1 in Szécsi et al. 2018).

3.3. Population Synthesis

To create a synthetic population, we suppose that all the first-generation stars of the cluster were formed during a single starburst episode, almost instantaneously. We assume a

standard piecewise power-law IMF with three intervals (0.01–0.08 $M_\odot$, 0.08–0.5 $M_\odot$, and above 0.5 $M_\odot$) with indices -0.3, -1.3, and -2.3, respectively, suggested by Kroupa (2001). In Section 6.2 we explore how the results change if a top-heavy IMF is used, by introducing an additional fourth interval for masses above 1 $M_\odot$ with index α_4 varying between -2.3 and -1.1.

Since both sets of stellar evolutionary models only contain 10 models between 9 and 500 $M_\odot$, we need to interpolate between these tracks to get two smoothly changing grids (see dashed lines in Figure 1). We split the whole range of stellar masses (0.1–500 $M_\odot$)[5] equidistantly in the logarithmic scale into 5000 intervals. For intervals above 9 $M_\odot$ (there are ∼1800 of them) we apply the interpolated tracks, while stars less massive than that are taken into account only as mass holders. When interpolating between the stellar models, we use a logarithmic scale to interpolate linearly among age, mass, mass-loss rate, surface temperature, radius, and surface abundances, while bolometric luminosity, escape velocity, and wind energy rate are calculated as follows: $L_{\rm bol} = \sigma_{\rm SB} \cdot T_{\rm eff}^4 \cdot 4\pi \cdot R^2$, $v_{\rm esc}^2 = 2G \cdot M/R$, ,and $L = 0.5 \cdot \dot{M} \cdot v_{\rm esc}^2$. The tracks of this smooth grid are weighted with the IMF and interpolated for a selected age. Then sums of various quantities, such as mass and energy deposition rates, and mass-weighted mean abundances are calculated. This calculation is carried out for 500 points distributed uniformly throughout the followed period of the cluster evolution (10 Myr). The resulting time evolutions of these quantities are then used as the input for the semianalytic code (described in Section 2.1), which computes the structure of the SC wind and eventually the rate of the mass accumulation and its chemical composition for each point in time.

We sampled the stellar evolution models so that major steps occur more or less at the same evolutionary stage; in particular, since in our cluster calculations the most important property is the mass-loss rate, we made sure that the interpolated mass-loss rate behaves well around the bi-stability jump (i.e., at $T_{\rm eff} \sim 21$ kK, where the mass-loss rates change abruptly owing to an increase in the line acceleration of Fe III below the sonic point of the stellar wind; see Vink et al. 1999, 2000).

As opposed to earlier works on the same subject, such as Wünsch et al. (2017), who used $M_{\rm top} = 120\ M_\odot$, here we include very massive stars up to $M_{\rm top} = 500\ M_\odot$. This choice is motivated by the findings that low-metallicity stellar models between 150 and 500 $M_\odot$ display significant variations in their surface abundances of light elements (Szécsi et al. 2018). There are observational implications for the existence of stars up to 315 $M_\odot$ in the LMC (Crowther et al. 2010, 2016). At low metallicity, radiation-driven winds are less effective, so ideally even more massive stars than that may form.

3.4. Wind Properties of the Populations

Figure 2 presents the properties of the stellar wind such as its mass-loss rate, mechanical luminosity, and velocity for all model stars in the population. The mass-loss rate typically becomes higher with stellar mass. While slowly increasing in the first half of the stars' life, it then experiences a local minimum and then a sudden jump. This jump is attributed to certain changes in the wind structure at $T_{\rm eff} \sim 21$ kK, leading

to an increased mass loss. (It is called the bi-stability jump and concerns the fact that additional iron line transitions become effective in driving the wind under this temperature; see Vink et al. 1999). Soon after this, the stars reach their post-main-sequence phase, during which the mass-loss rates are 1–2 orders of magnitude higher than during the main-sequence phase. The models' evolution is computed until core hydrogen exhaustion, but subsequent evolutionary phases are very short (<1%) compared to the total lifetimes, so they can be safely omitted from considerations of stellar wind mass loss.

Models with low metallicity have typically lower mass-loss rates than their high-metallicity counterparts of the same mass. The reason is that the mass-loss rate is a function not only of stellar mass but also of metallicity (and, at some extent, of other stellar parameters such as radius and surface composition). The mass-loss rate's dependence on metallicity is prescribed as $\dot{M} \sim Z^{0.86}$ in both sets of models at every evolutionary phase, while its dependence on the actual stellar mass follows $\dot{M} \sim M^{1.13}$.

There is one evolutionary phase when the mass loss experienced by low-metallicity models is higher than that experienced by the high-metallicity ones: in the case of the most massive models' late evolution (i.e., above 100 $M_\odot$). Here the mass loss of the high-metallicity models follows a prescription typical for Wolf-Rayet stars, while that of the low-metallicity ones follows a prescription typical for red supergiants. While the latter does not predict significantly higher mass losses than the former, we have to take into account another effect also playing a role, namely, that since the mass-loss rates during the first half of the main sequence are lower in the case of low-metallicity models, these stars are typically more massive during their later phases than those predicted by high-metallicity models of the same initial mass, and therefore their mass-loss rates are now higher. The jumpy mass-loss rates visible, for example, during the late phases of the high-metallicity model with 70 $M_\odot$ or the low-metallicity model with 575 $M_\odot$ are due to these models being associated with an LBV phase. Models below 30 $M_\odot$ at low metallicity experience a blue loop during their core helium-burning phase. The mass loss attributed to this blue supergiant phase is typically lower than what is expected for a red supergiant, leading to a plateau in these models' post-main-sequence mass-loss rates.

The behavior of wind velocity of the models in Figure 2 can be understood as follows. Initially, the low-metallicity models are hotter than the high-metallicity ones owing to their surface opacity being lower. Therefore, these models are typically smaller in radial size. As wind velocity is computed from the escape velocity, it is expected that their wind velocity is higher than that of their high-metallicity counterparts. As the evolution progresses, however, the low-metallicity models evolve toward lower surface temperatures and larger radii; thus, their wind velocity drops. The same is happening with the high-metallicity models. One crucial difference is that while the low-metallicity models become supergiants, the high-metallicity ones, at least those above 70 $M_\odot$, become LBVs or W-R stars. These models' wind velocity is high. As for masses below 70 $M_\odot$, both grids predict supergiants—the low-metallicity grid blue supergiants below 40 $M_\odot$ with a loop in the wind velocity.

Energy flux of the wind is closely related to both the mass loss and the wind velocity, as it is computed by these two as $L_{\rm wind} = 1/2\dot{M}\, v_{\rm wind}^2$. From this we can calculate the mechanical

---

[5] We use a I Zw 18 model with 575 $M_\odot$ in the interpolation, but we still take the upper limit $M_{\rm top} = 500\ M_\odot$ for the synthetic population, to be consistent.
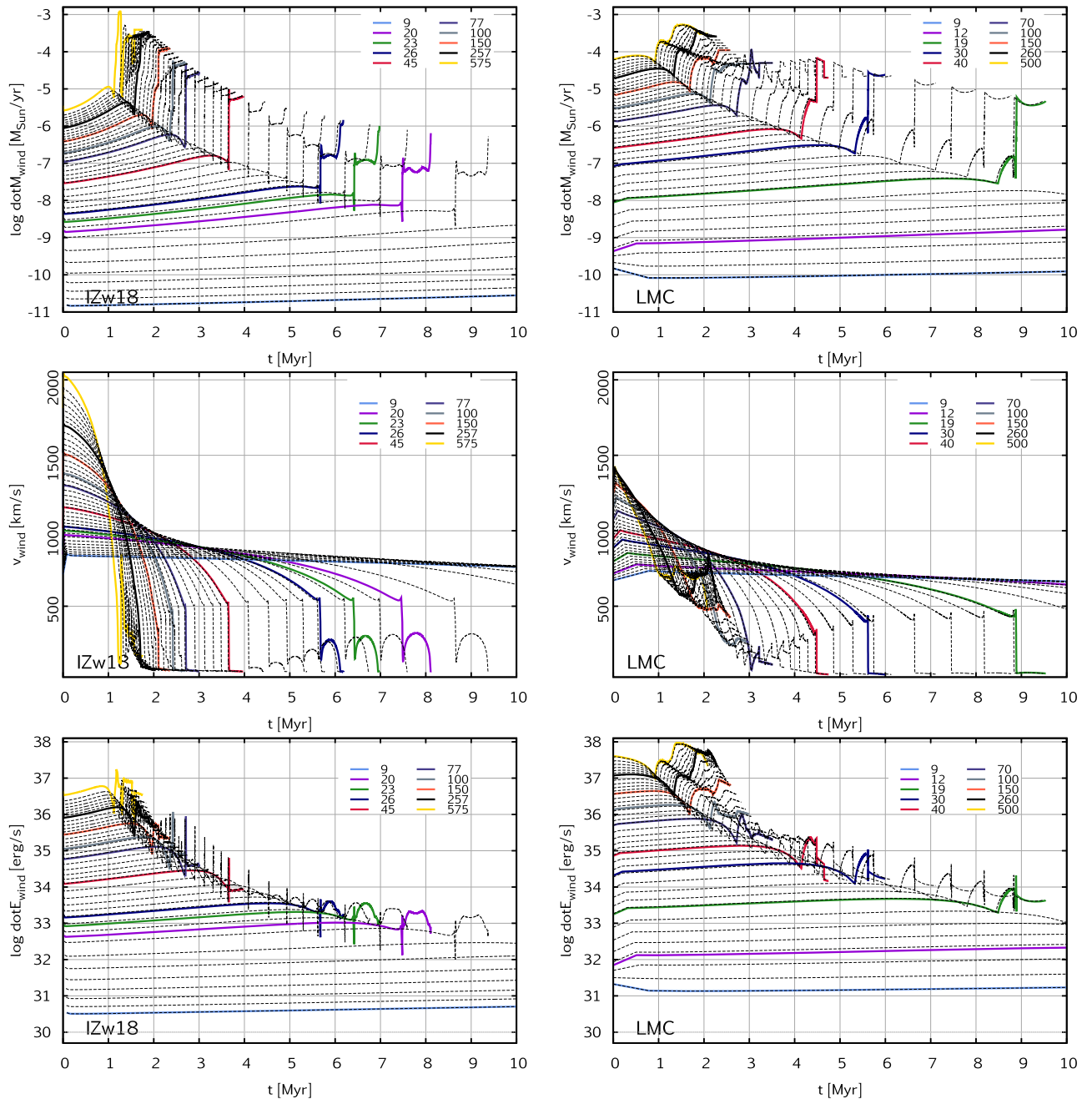
Figure 2. Time evolution of our low- and high-metallicity stellar populations (left and right panels, respectively) during the first 10 Myr of the clusters' life. Colored lines are taken from Szécsi et al. (2015, 2018), while black dashed lines are interpolated tracks. Top panels show the mass-loss rates in the models, middle panels show the terminal velocity of their stellar winds, and bottom panels show the energy flux these winds insert into the cluster gas.

luminosity inserted into the cluster by the first generation of stars, by properly considering every individual stellar model's contribution to the population (i.e., weighting with the IMF). Thus, we arrive at the value L_{SC} presented in Figure 3.

3.5. Supernova Explosions

Massive stars end their lives in various ways, depending on mass and metallicity. If supernova explosions happen, they may contribute to the cluster's subsequent evolution significantly. Core-collapse supernova explosions in particular may increase the cluster's iron content. For this to happen, however, a mechanism is needed that traps the (possibly very energetic) supernova ejecta inside the cluster's potential well. Such a

mechanism was suggested, e.g., by Tenorio-Tagle et al. (2013) and further studied by Martínez-González et al. (2018); however, its discussion is beyond the scope of this work.

Our semianalytic model does not include this effect. Therefore, we need to discuss when and what kind of supernova explosions we expect from our massive stellar models (if any) so that we can carefully evaluate the validity of our semianalytic approach. The majority of GCs show no variation in their iron content, so to account for them with our model, we need to pay extra attention to the time periods when a supernova's contribution enters the picture. Some GCs, such as ω Cen and M54, are peculiar in this regard, displaying variations in iron and even in their total sum of C, N, and O

6
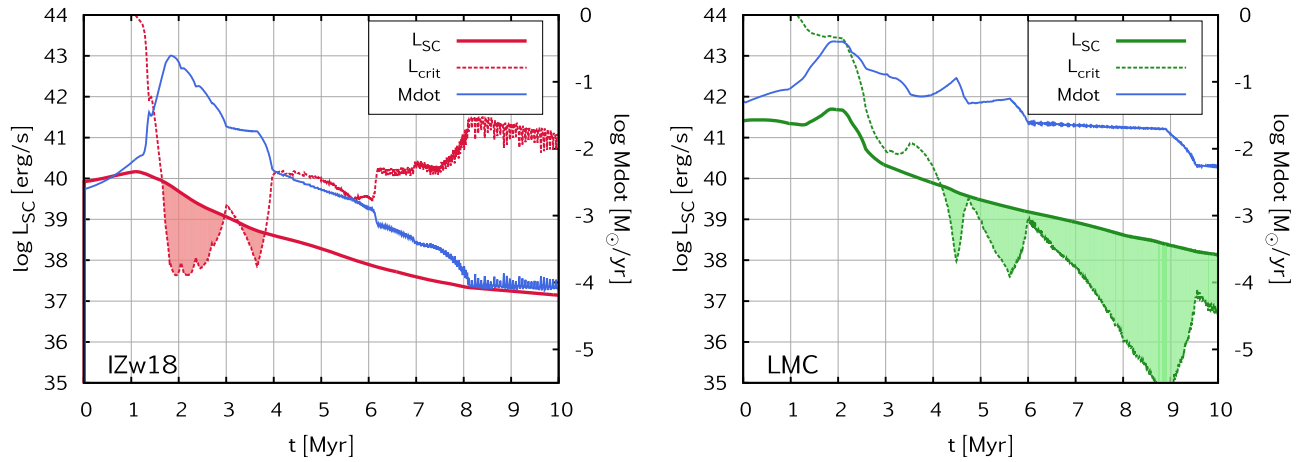
Figure 3. Time evolution of the cluster wind. Whenever the cluster wind luminosity L_{SC} exceeds the critical luminosity L_{crit}, wind mass is supposed to accumulate into the cluster center (marked by the shaded regions). The mass-loss rate of the stellar populations is also shown (blue lines, values on the right axis). In the I Zw 18 population, mass accumulation happens early on: before the first supernova explosions happen at 4 Myr. Thus, we conclude that this early mass accumulation episode provides a "window" for the undisturbed formation of a second generation of stars.

content. Still, their formation may have happened fundamentally differently from the average cluster (ω Cen in particular was suggested to start out as a dwarf galaxy; see Schiavon et al. 2017). Therefore, we only account for the majority of clusters here, those that do not exhibit star-to-star variations in iron abundance.

Connecting stellar models to supernova types is somewhat uncertain. It depends on both the model in question and the assumptions about the nature of the explosion. Here we simply rely on the work of Heger et al. (2003) and establish that, in the case of our low-metallicity population, the first supernova that may pollute the cluster with iron (which is a $40\,M_\odot$ star) explodes at a cluster age of 4.5 Myr. The reasons are the following.

In the low-metallicity population, massive stars up to an initial mass of $25\,M_\odot$ are expected to explode as core-collapse supernovae of Type II-P. The total lifetime of a $25\,M_\odot$ star is 7 Myr; those at lower masses live even longer. We expect them to form neutron stars as remnants. As for stars with an initial mass of 25–40 $M_\odot$, they are expected to explode as weak Type II-P supernovae and form black holes as remnants. The total lifetime of a $40\,M_\odot$ star is about 4.5 Myr.

Above this mass but below $140\,M_\odot$, it is expected that the metal-poor models do not explode but fall into a black hole directly owing to their immense self-gravity at the moment of iron core collapse. An initially $140\,M_\odot$ model has a total lifetime of 2.4 Myr. This means that stars with lifetimes between 2.4 and 4.5 Myr do not explode as supernovae, although they contribute to the (stellar-mass) black hole content of their clusters. The same fate awaits those stars that have an initial mass above $260\,M_\odot$—this means that many of our metal-poor models form black holes without an explosion.

Between 140 and 260 $M_\odot$ (i.e., total lifetimes of 1.9–2.4 Myr), the models in the low-metallicity set are again predicted to explode. This time, though, it is not due to iron core collapse but another effect: pair creation.[6] During their oxygen-burning phase, the creation of electron−positron pairs disturbs their hydrostatic stability and makes them explode

without leaving a remnant. Such a pair-instability supernova does not pollute the cluster with iron, as nuclear fusion has not yet produced an iron core. The core that explodes contains mainly carbon and oxygen, which undergo explosive burning during the supernova event, producing a unique nucleosynthetic signature (Burbidge et al. 1957; Langer 1991; Heger et al. 2003; Langer et al. 2007; Kozyreva et al. 2014).

A pair-instability supernova is expected only for a small number of all massive stars in our low-metallicity population (for a $10^7\,M_\odot$ cluster with the standard IMF, we expect about one such supernova every 270 yr). For our present purposes, we do not investigate how these supernovae may contribute to our cluster's structure or chemical composition, but we consider all stars above an initial mass of $40\,M_\odot$ (that is, an age of 4.5 Myr) not to pollute the cluster with iron. We also do not investigate the effect of pulsational pair instability (Woosley et al. 2007; Moriya & Langer 2015), pointing out that this process may also play some (yet to be investigated) role in polluting the cluster.

As for the high-metallicity set of models, the situation is quite different. Here we also expect Typee II-P supernovae from models with initial mass between 10 and 25 $M_\odot$, with stars between 25 and 40 $M_\odot$ ending up as Type II-L/b supernovae. But above that limit, instead of falling into a black hole owing to self-gravity or undergoing pair-creation-induced instability, stars are expected to explode as Type Ib/c supernovae—that is, owing to iron core collapse. The reason for the high-metallicity models exploding as core-collapse supernovae instead of some more exotic scenario is that they lose so much mass during their lifetimes that their final mass is in the range where neither is self-gravity strong for direct black hole formation nor is pair creation playing a role. Hence, all our high-metallicity stellar models undergo a core-collapse-induced supernova explosion that may, if the ejecta is trapped in the cluster, pollute the gas with iron. The first supernova, that of our most massive model (initial mass $500\,M_\odot$ but final mass only $34\,M_\odot$), explodes at the age of 2.1 Myr.

When discussing our results in the next sessions, we always point out where and when supernovae are expected. The extent to which the supernova ejecta stays trapped to mix with the gas remains a question. It may also depend on the nature of the explosions themselves, if they are weak ("failed") or strong

---

[6] It is not relevant to the present discussion, but those low-metallicity stars above $260\,M_\odot$ that fall into a black hole directly do so also because of pair-creation-induced instability and not an iron core collapse.

("successful") supernovae, a question currently undergoing some investigation (MacFadyen & Woosley 1999; O'Connor & Ott 2011; Smartt 2015). Also, it remains a question how the supernova feedback influences star formation of the second-generation stars. It may enhance it or stop it; with our current method, we have no way of knowing. Hence, all these questions around supernovae are left to be investigated in future work.

4. Cluster Wind and Secondary Star Formation

As explained in Section 2.1, mass accumulation happens when the cluster luminosity L_{SC} is lower than a certain critical luminosity L_{crit}. The former is simply the combined mechanical energy of all stellar winds, while the latter is determined by the hydrostatic structure of the cluster (computed in our semi-analytic model) and takes into account various effects such as cooling and the stability of the cluster wind. Mass accumulation means that mass is removed from the wind and is supposed to accrete onto forming protostars of a secondary generation—given, of course, that its velocity, inherited by the gas's velocity, is lower than the escape velocity from the cluster's gravitational potential.

Figure 3 shows how the cluster luminosity L_{SC} relates to the critical luminosity L_{crit} over the calculations. The phases when L_{SC} exceeds L_{crit} are are shaded in the figure; however, the size of the shaded area should not be taken as indicative of anything, especially not the efficiency of star formation; it only serves to help us see when and how long the star formation is going on.

4.1. Mass Accumulation at Low Metallicity

In the case of our low-metallicity stellar population, mass accumulation starts at ∼1.6 Myr and lasts until ∼3.9 Myr, resulting in a star formation episode that is ∼2.3 Myr long. Figure 3 also shows the total mass-loss rate of the cluster—that is, the mass-loss rate of all stars in the population combined. The mass accumulation episode coincides with a pronounced peak in the mass-loss rate, but this is not really a coincidence, as both effects are caused by the presence of cool supergiants in the population. Indeed, as discussed in Section 3.1, massive and very massive supergiants are present in the low-metallicity population (but are absent in the high-metallicity population). These stars have low surface temperature (and thus a slow stellar wind) and a high mass-loss rate. Therefore, they facilitate star formation by *not* heating the gas too much since they eject material with a small velocity and thus keep the cluster wind velocity also rather low. Additionally, they deposit a huge amount of mass into the cluster in just the right time for it to accumulate in the center.

As discussed in Section 3.5, the first core-collapse supernova explodes when the low-metallicity cluster is about 4.5 Myr old. Mass accumulation in this cluster happens before that age. Thus, we conclude that in our low-metallicity calculations the protostars of the second generation will have already been formed out of the stellar wind material before iron is deposited into the gas via supernova explosions.

Another caveat that this cluster avoids as a result of accumulating mass early is that, observationally, YMCs typically remove their gas by ∼4 Myr (Hollyhead et al. 2015). Figure 4 shows the mass that is lost in stellar winds (i.e., inserted in the cluster by stars, M_{ins}), as well as that

accumulated in the center (M_{acc}). The mass starts to accumulate when L_{crit} first exceeds L_{SC} (i.e., at ∼1.6 Myr). Almost all the mass that is inserted into the cluster wind accumulates in the center. When the process ends (at ∼3.9 Myr), the total accumulated mass is almost $10^5 M_\odot$. This is the mass budget from which a second generation of stars forms.

4.2. Mass Accumulation at High Metallicity

In the case of our high-metallicity stellar population in Figure 3, mass accumulation starts at a later time than at low metallicity, at 4.2 Myr. After this time, L_{SC} exceeds L_{crit} and keeps exceeding it until the end of our calculation.

In this case, however, we do not imply that a second generation of stars should be expected to form out of the accumulated mass. As mentioned in Section 3.5, this population experiences supernova explosions starting at the age of 2.1 Myr. Thus, our calculation should not be taken on face value after 2.1 Myr. We can nonetheless draw some interesting conclusions from it.

The reason this population does not produce a mass accumulation episode as early as the low-metallicity population is that the very luminous supergiants are practically absent. In this population, stars above 40 $M_\odot$ become LBVs or W-R stars (as discussed in Section 3.1), which are hot stars with fast winds. Hence, while the mass deposited into the gas from the stellar winds is high owing to the high mass-loss rates of LBVs and W-R stars (higher than in the low-metallicity population at any given point in time), the cluster wind luminosity does not exceed the critical value until the first red supergiants, those with ∼45–40 $M_\odot$ and below, appear. Indeed, the total lifetime of a 45 $M_\odot$ model is 4.2 Myr, marking the point where $L_{crit} > L_{SC}$ and the mass accumulation starts.

That is, if we disregard supernova explosions. It falls outside the scope of current work to investigate what happens to the supernova ejecta under the conditions in this cluster: whether it gets shocked and cools, staying and mixing with the gas, or leaves the cluster; and whether it enhances or stops star formation. What we can conclude from our calculation, nonetheless, is that mass accumulation starts ∼2.5 Myr later at high metallicity (i.e., in the absence of cool supergiants) than at low metallicity (when their contribution dominates). In the latter case, we expect that the accumulated mass forms a second generation of stars, whereas in the former case, we cannot be certain if a second generation forms without conducting 3D hydrodynamic simulations of the supernova ejecta and its contribution to star formation in the cluster.

5. Chemical Composition of the Second Generation

5.1. Light-element Variations

Light-element abundance variations are a well-established observational fact for practically all GCs that have been extensively studied spectroscopically (see, e.g., Bastian & Lardo 2018, for a recent review). In particular, Na over-abundance is always observed together with O depletion, while the sum of C, N, and O is constant, suggesting that the CNO cycle is operating. In some GCs, Al and Mg display variations as well. This implies that at least one population of low-mass stars (usually referred to as the second generation) is made up of material that has previously undergone hot hydrogen burning. This process is known to be active only in massive
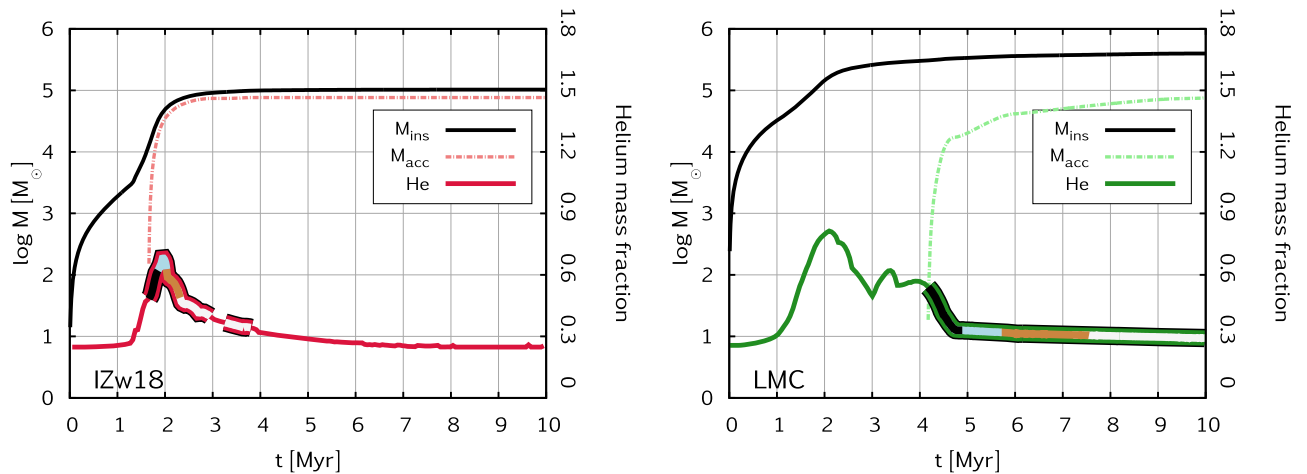
Figure 4. Time evolution of the mass lost from massive stars, i.e., inserted into the cluster wind by stellar winds, M_{ins}, and the mass that is accumulated into the cluster center, M_{acc}, both on a cumulative scale (left axis). Also shown is the helium mass fraction (right axis). The periods when mass is actually accumulated (see the shaded regions in Figure 3) are indicated with thick lines, the four colors (black, blue, brown, white) corresponding to every 25% of the total accumulated mass.

and intermediate-mass stars because low-mass stars' core temperatures are not high enough for that.

We do not study the contribution of intermediate-mass stars (i.e., asymptotic giant branch [AGB] stars) to our cluster, since their contribution happens after ∼30 Myr (while our computation ends at 10 Myr). Nonetheless, AGB stars have been used to account for the observed light-element variations (see, e.g., Cottrell & Da Costa 1981; Karakas et al. 2006; D'Ercole et al. 2010; Doherty et al. 2014). Here we focus only on massive stars but point out that AGB stars may contribute to the cluster gas's composition at later ages.

Figure 5 shows the observed anticorrelation between two pairs of light elements, O versus Na and Mg versus Al. The data are taken from Carretta et al. (2009), which is a FLAMES-UVES survey of ∼200 red giant stars in 17 GCs, as well as from Pancino et al. (2017) and E. Pancino et al. (2018, private communication), which contains ∼150 red giant stars in nine GCs with *Gaia*/ESO-UVES abundance measurements of all four elements in question. Since the abundance scales used by these two surveys differ, we took into account a small (compared to the internal spreads) offset of ∼0.10–0.15 dex when plotting the two data sets next to each other, as suggested by Pancino et al. (2017) and E. Pancino et al. (2018, private communication).

We account for low-metallicity and high-metallicity clusters in a simple way, by dividing the observational samples into two categories: one with [Fe/H] > −0.9 and another with <−0.9. The choice of this value is motivated by Figure 3 of Harris (2010), in which the metallicity histogram of a large catalog of GCs seems to show two peaks, with an arbitrary division at around −0.9. In future work this has to be refined by investigating a range of different metallicities, as discussed in Section 7.2. According to Figure 5, both anticorrelations are observed to be much more pronounced at low metallicity than at high, with no significant Mg depletion found among high-metallicity clusters whatsoever in these data sets.

When comparing our theoretical predictions to the observed spreads, we suppose that our low-metallicity cluster (with [Fe/H] = −1.7) is representative for all GCs below −0.9 and the same for our high-metallicity cluster (with −0.4) for those above −0.9. The stellar models do not use an α-enhanced mixture (as suggested for GC stars by, e.g., Decressin et al. 2007b;

see their Table 3), but a mixture suitable for certain galaxies; therefore, when creating Figure 5, the initial O, Na, Mg, and Al abundances of our models are scaled to match the composition of the unpolluted red giants. Below we discuss what our calculations predict for the composition of the second generation of stars (or, more precisely, as explained in Section 4.2, for that of the mass accumulated in the cluster center, out of which a second generation forms at low metallicity).

5.1.1. Na and O at Low Metallicity

Our calculation of a low-metallicity cluster predicts that the mass accumulated in the center has a high sodium value and a large range of oxygen values. In fact, about half of the accumulated mass has extremely low oxygen abundance with high sodium (see black and blue stripes), while another half is spread out in oxygen. This is related to *when* the mass is accumulated: if it is accumulated early, its composition is dominated by the winds of the most massive supergiants (which evolve to the supergiant branch earlier); if late, it is dominated by the less massive ones.

It is expected that in the center this material mixes with the pristine gas (out of which the first generation of stars formed). Thus, the mixture of the accumulated mass and the original gas can possibly produce the whole observed range of Na–O abundances in stars of low-metallicity clusters.

Such dilution of polluted gas with pristine gas is typically also invoked by other scenarios (e.g., in Equation (7) of Decressin et al. 2007a). One caveat here is that, observationally, YMCs have removed their gas by ∼4 Myr (Hollyhead et al. 2015), which presents a challenge for all models that form the second generation after this age. But in our low-metallicity cluster governed by the presence of supergiants, this caveat is avoided by the "window" for star formation opening between 1.6 and 3.9 Myr (as shown in Figure 3).

5.1.2. Na and O at High Metallicity

Metal-rich clusters show a smaller extent of both Na and O variations than metal-poor ones, with the lowest observed Na value being about 0.4 dex higher. As explained by Carretta et al. (2009), this is because the plateau of minimum Na
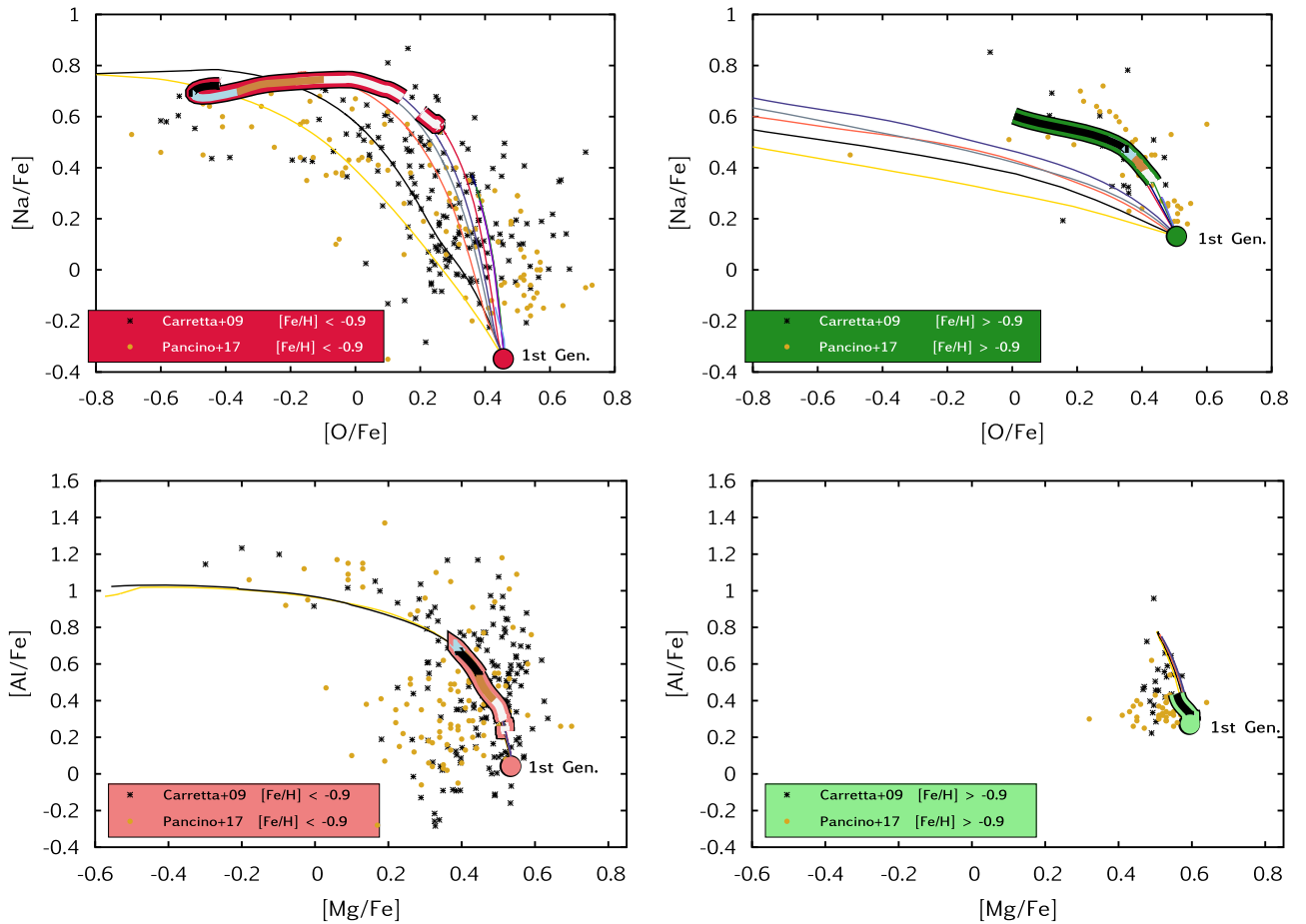
Figure 5. Surface composition of GC stars, showing the anticorrelations of oxygen–sodium and magnesium–aluminum. Observational data are taken from Carretta et al. (2009; FLAMES-UVES survey) and Pancino et al. (2017; *Gaia*/ESO-UVES survey). The data correspond to red giant stars in a total of 22 galactic GCs, with metallicities ranging from −0.9 to −2.3 in the left panels and from −0.4 to −0.9 in the right panels (in units of [Fe/H]). Observational error is typically between 0.05 and 0.12 dex. The composition of the pristine gas, that is, the composition we attribute to the first stellar generation in our calculation, is marked by the filled circle (labeled "1st Gen."). Our calculation predicts that the mass accumulated in the cluster center (see Figure 3) has a composition shown by the thick line. The four colored stripes overplotted on top of the thick line (black, blue, brown, and white) mark the four quadrants of the total mass (i.e., every 25%, starting with the black and ending with the white; see the same color-coding in Figure 4). Thin lines show the surface composition of the original stellar models during their entire evolution; for the meaning of the colors, see Figure 1. We expect that the accumulated mass will mix with the original gas in the center. Thus, if a star forms out of it (as we suppose is the case for the low-metallicity cluster; see Section 4.1), its composition will be a mixture of the pristine and the accumulated composition.

established by (a previous generation of) supernova nucleosynthesis is a function of the metallicity.

Although we cannot infer from our calculation of a high-metallicity cluster that a second generation of stars would form from the accumulated mass (due to the uncertainties associated with supernova explosions; see Section 3.5), it is nonetheless interesting to compare our predictions with observations of high-metallicity cluster stars in Figure 5. As opposed to the low-metallicity case discussed above, now the most massive stars' mass loss has no contribution to the accumulated mass, as mass accumulation starts when these are already dead. The composition in this case is dominated by supergiants of initial mass below 40 $M_\odot$. They do produce some Na by destroying some O, but to much less of an extent than higher-mass stars do, especially when it comes to destroying oxygen. This is in accordance with the observational data in Figure 5.

5.1.3. Al and Mg at Low Metallicity

This is the case where our calculation struggles to account for the whole extent of observations. While red giants in low-metallicity GCs display a broad spread in both Mg and Al, our

prediction is that the second generation of stars would have an Al spread of only about 0.6 dex, with almost no Mg being destroyed. This is so even though our most massive models do lose material with a very low Mg abundance (see yellow and black thin lines corresponding to stellar models with 257 and 575 $M_\odot$).

The reason for this lies in the specifics of the star formation episode. We accumulate mass in our calculation when the hydrodynamical conditions in the cluster are just right (see Section 4.1 and Figure 3). This means that we have a star formation episode that lasts from 1.6 to 3.9 Myr, during which the material lost by massive stars is integrated together (with proper weighting by the IMF) to produce the stripes in Figure 5. Our very massive models gradually lose their outer layers via their stellar winds, starting with those layers that are less effected by hot hydrogen burning. The first stars of the second generation form out of this material (black stripe). When these very massive stars are already losing their deeper, magnesium-deficient layers, lower-mass stars have evolved to the supergiant branch, contributing to the total composition significantly. The material of their surface layers is, therefore, accumulated together with the deeper layers of the very

massive stars, resulting in some slight decrease in the combined abundance (blue stripe) but clearly not enough to account for the whole observed spread in Mg. The later phases of star formation, when even lower-mass supergiants dominate the composition, produce a second generation with an even higher Mg (yellow and white stripes).

Nonetheless, all the extremely low Mg values were observed in the same cluster, NGC 2808 (in both data sets). As discussed by Carretta et al. (2009), there is a quite significant cluster-to-cluster variation when it comes to Mg and Al (see their Figure 6), with some clusters displaying large, and some displaying small, spread of these elements. Indeed, the phenomenon of magnesium depletion is not a common feature among GCs, but rather an exception, with extremely low magnesium abundances only observed in a handful of clusters (e.g., NGC 2419, NGC 2808), and even there the situation is further complicated by the phenomenon's apparent dependence on mass and metallicity (see Pancino et al. 2017).

Our calculation is way too simplistic to account for this cluster-to-cluster variation, as we use only two sets of single stellar models at two given metallicity values, together with some—reasonable, but certainly improvable—assumptions about the secondary star formation. We discuss ways to improve our theory in Section 7.2.

It is, for example, quite conceivable that some stars do form out of the pure material (that is, mixed neither with the other stars' ejecta nor with the pristine gas) of the most massive supergiants. Such a scenario was suggested by Szécsi et al. (2018) to possibly operate in the case of some very massive supergiants.

5.1.4. Al and Mg at High Metallicity

The high-metallicity models do not show the Mg–Al anticorrelation, not even in the most massive case (up to $500 \, M_{\odot}$). The reason for this is related to their core temperatures. To destroy magnesium and produce aluminum, the ^{24}Mg(p, g)^{25}Al chain should be active, which happens at a core temperature of ∼80–100 MK, according to Ventura et al. (2011). Below and above this temperature range, the reaction rate of the ^{24}Mg(p, g)^{25}Al chain is too small for it to produce any effect in stellar models.

But having the correct core temperature is not enough. In order to destroy lots of Mg, the right thermodynamical conditions should last for a long time (because the chain first creates ^{24}Mg $\rightarrow$ ^{25}Mg and then *slowly* destroys ^{25}Mg too; see Figure 1 of Ventura et al. 2011). Hence, we need stars that not only *pass through* the correct temperature range while, for example, collapsing or restructuring but also keep burning their fuel with exactly the right temperature *for a long time*. The longer the time that the core has the right temperature, the more Mg is destroyed and converted into Al.

This differentiates between the LMC models and the I Zw 18 models. For example, our LMC model with $M_{\mathrm{ini}} = 260 \, M_{\odot}$ has $T_c < 55$ MK during almost its entire main-sequence lifetime. It only reaches the range 80–100 MK when the core contracts to ignite helium, but this is a rather short phase in the star's life ($\lesssim$10 kyr), after which the temperature increases way above 100 MK. The I Zw 18 model with $257 \, M_{\odot}$, on the other hand, already starts its evolution with 60 MK and then slowly increases to 75 MK. Although the literature cites 80 MK as the nominal lower limit for the reaction to be effective, we find in our models that already at

>65 MK there is significant Mg depletion and Al production if this temperature lasts for a long time (in our $257 \, M_{\odot}$ model, for ∼0.6 Myr). This is in accordance with observations (Figure 5), which show that high-metallicity clusters have no significant variation in Mg.

5.2. C, N, O, and He Abundances

Observations of GCs typically show that carbon, nitrogen, and oxygen abundances are in accordance with the CNO cycle's equilibrium values. This means that the sum of these three atoms is constant; they simply act as catalysts in the cycle. Nonetheless, C and O drop and N increases in later populations owing to the CNO-equilibrium values being different from the abundances of the original gas.

This is confirmed by our theoretical calculations. Our massive stellar populations (at both low and high metallicity) do conserve the sum of C, N, and O, with their respective abundances being consistent with the CNO-equilibrium values. However, as the available C and N data for the first-generation stars are sparse and the interpretation of C and N variations is complicated by some evolutionary effects in the red giant branch phase (e.g., Boothroyd & Sackmann 1999; Gratton et al. 2000), we refrain from fitting the C–N anticorrelation here.

The helium mass fraction of the accumulated mass in our calculation is shown in Figure 4. It reaches a much higher value than what is inferred from observations of any GC (Bastian et al. 2015; Milone et al. 2017; Bastian & Lardo 2018). We discuss the implications of this finding in Section 7.1. Colored stripes in Figure 4 represent the same as in Figure 5, that is, the four quadrants of the mass accumulated in the cluster center. Comparing these two figures, we find that the most extreme oxygen depletion is produced together with a helium mass fraction, Y, ranging between 0.5 and 0.7 (i.e., black and blue stripes). This composition is a mixture of the material ejected from our most massive stars down to $150 \, M_{\odot}$. However, a less extreme oxygen depletion is possible to reach with a helium mass fraction between 0.3 and 0.5 (white stripe). This happens at the end of the star formation episode when the last 25% of the mass is accumulated. This mass is made of the winds of supergiants with an initial mass of 40–60 $M_{\odot}$. For further discussion on this issue, we refer to Section 7.1.

No helium-burning products, nor products of later burning phases, are found in our calculations at any metallicity.

6. Mass Budget

6.1. On the Mass Budget Problem and Dynamical Removal of Stars

The fraction of stars with anomalous chemical composition, i.e., the second generation, varies in the range of ∼30%–90% among GCs, with a mean value around 67% (Milone et al. 2017; Bastian & Lardo 2018). A difficulty of most models to predict such a high fraction of second-generation stars is called the mass budget problem.

In our calculation of a low-metallicity cluster with a total initial mass of $10^7 \, M_{\odot}$, we find that about $10^5 \, M_{\odot}$ is available to form second-generation stars. We emphasize that this is the mass that is ejected from massive stars via their winds and accumulated inside the cluster center—both processes accounted for in our calculations—and not, for example, the total mass in these massive stars. We took into account a standard IMF with an upper mass limit of $500 \, M_{\odot}$. As opposed

to earlier works accounting for the mass accumulation process (e.g., Wünsch et al. 2017), we did not include additional ad hoc parameters such as mass loading or heating efficiency, but found that the presence of supergiants already facilitates the process.

GCs today have a typical total mass of a few times $10^5 M_\odot$. If they indeed used to be massive clusters born with $10^7 M_\odot$, they must have lost $\gtrsim 90\%$ of their mass during their lives. It has been suggested (D'Ercole et al. 2008; Decressin et al. 2010; Vesperini et al. 2010; Khalaj & Baumgardt 2015) that clusters may lose a huge fraction of their stars via dynamical "evaporation." This process mainly effects stars located in the outskirts of the cluster.

In our calculations, mass accumulation happens in the center of the cluster.[7] This means that even if mass is removed from the cluster very efficiently by dynamical evaporation, the $\sim 10^5 M_\odot$ protostars of the second generation would be very hard to eject via this process, due to them being centrally located. For example, N-body simulations of the cluster's long-term dynamical evolution carried out by Khalaj & Baumgardt (2015) show that it is indeed possible to explain present-day observations by a cluster that contained a second-generation number fraction of 10% initially, on the conditions that a substantial amount of gas is kept after the formation of the second generation and that this gas is then expelled on a very short timescale. If such a process takes place in the cluster, leading to the loss of almost only first-generation stars, our low-metallicity model presented in Figure 4 is able to fulfill the mass budget, having already accumulated and converted $\sim 10^5 M_\odot$ into second-generation stars.

However, it is not conclusively established that the dynamical evolution leads to the loss of only first-generation stars. A recent study (Reina-Campos et al. 2018) suggests that while GCs have indeed lost 90%–95% of their initial masses, the present-day ratios of first versus second generation reflect the initial values. Another argument comes from Kruijssen (2015), who suggests that if mostly first-generation stars were lost owing to tidal interactions with the host galaxy, we should expect to observe GCs with increasing mass loss toward smaller galactocentric radii, with higher gas pressures at birth and with higher cluster metallicities (see Section 2.1.2 and especially argument (v) on page 1661 of the cited paper). While it could be insisted that the measurements of these quantities are significantly impacted by uncertainties, it is nonetheless clear that there are far too many open questions regarding the dynamical evolution during which YMCs become GCs for it to be called an established theory.

We have no means of solving any of these open questions here, due to us only focusing on the relatively short term phase of star formation. Indeed, our calculation only involves the first 10 Myr of the cluster's life, as we are mainly interested in the mass accumulation process. We predict that the mass is accumulated in the cluster center and that the second generation of stars forms there. Still, we cannot directly quantify which fraction of the first generation would be lost over the subsequent lifetime, nor, therefore, the final ratio of first versus second generation we may expect in today's GCs after them having undergone several gigayears of dynamical evolution.

---

[7] As shown by Wünsch et al. (2017), the outcome of the semianalytic code we use here is in accordance with 3D hydrodynamic simulations, which show that the cool gas falls toward the cluster center to accumulate there.
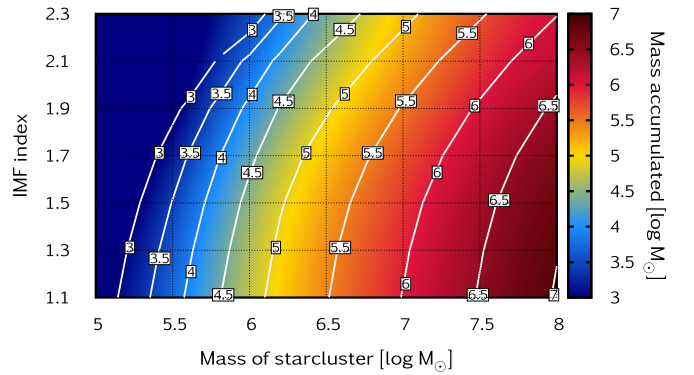

Figure 6. Results of our parameter space study. We vary the initial mass of the cluster, M_{SC}, shown on the X-axis, and the index of our IMF, shown on the Y-axis. Contours present the outcome of our calculation in terms of the amount of mass that is accumulated in the cluster center. Since the amount of accumulated mass (as well as the number of second-generation stars; see Figure 7) is an increasing function of the initial mass, we suggest that this may explain why we observe a correlation between today's GC masses and the extent of a polluted second generation.
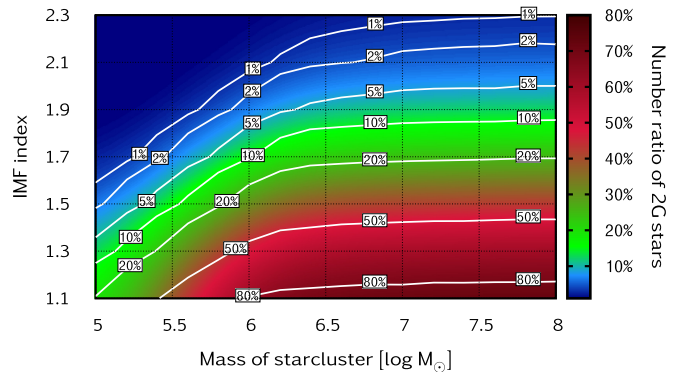

Figure 7. Same as Figure 6, but for the number ratio of low-mass stars in the second generation (i.e., $N_2/(N_1 + N_1)$, as explained in Section 6.4). Note that we do not suppose that only low-mass stars form in the second generation, but we apply a regular IMF with an index of -2.3.

We can nonetheless provide upper limits and predict some trends, by studying how our calculation is affected if we vary initial conditions such as the total mass of the cluster at birth or the IMF. This is done in what follows. We emphasize that from now on we do not suppose that the dynamical ejection process prefers the first generation. If it does, it helps our case, but there are also other options to alleviate the mass budget problem.

6.2. Parameter Space Study

We repeated our low-metallicity calculation by varying two of the input parameters, the total initial mass of the cluster, M_{SC}, and the high-mass index of the IMF, α_4 (our IMF is explained in Section 3.3). We vary M_{SC} between 10^5 and $10^8 M_\odot$ and α_4 between -1.1 and -2.3. The results are summarized in Figure 6 (and Section 6.3) for the amount of accumulated mass and in Figure 7 (and Section 6.4) for the number ratio of the second-generation stars versus the total, $N_2/(N_1 + N_2)$. Our motivation for testing the high-mass index of the IMF is that, recently, some attention has been paid to measuring this value in various star-forming regions with various methods. Some of these works report the finding of a top-heavy IMF (Kalari et al. 2018; Schneider et al. 2018a; Zhang et al. 2018), although the debate seems not to be over

(Bastian et al. 2010; Khorrami et al. 2016; De Masi et al. 2018; Farr & Mandel 2018; Hopkins 2018; Schneider et al. 2018b).

6.3. Mass Accumulation as a Function of Initial Cluster Mass and IMF

We find that the amount of accumulated mass is an increasing function of both the total initial mass and the number of massive stars in the population. Clusters in the upper left corner of Figure 6 do not accumulate a noteworthy amount of mass; in the case of a cluster with $M_{SC} = 10^5 \, M_\odot$ and a classical IMF index, no mass accumulation is taking place. This suggests that at least the lowest-mass GCs with multiple populations must have started out as more massive clusters and then gotten rid of some of their mass over their lives.

In the most extreme, probably hypothetical case of a $10^8 \, M_\odot$ cluster with an extremely top-heavy IMF, as much as $10^7 \, M_\odot$ is available to form the second generation. The consequences of this are discussed further in Section 6.6.

As for the chemical composition, we find the following. The *total* spreads predicted in Na and O, as well as those in Mg and Al, together with the high helium abundance (Section 5.2), are practically unchanged when varying the initial parameters. Nonetheless, more massive clusters produce more polluted gas, though with a less extreme *average* composition. To be able to quantitatively compare these results with observations, we would need to model the mixing with primordial gas, which will be done in future work. Here we only establish a correlation between the initial cluster mass and the amount of (polluted) mass accumulating in the cluster center. What this correlation means in terms of number of stars is discussed in the next sections.

6.4. The Ratio of Second- versus First-generation Stars

Figure 7 shows the same parameter study as before, but here we include assumptions about the number of stars formed out of the available mass, as follows. The number of low-mass stars in the first generation, N_1, is taken to be stars with masses between 0.08 and 0.8 $M_\odot$, as these are expected to be still alive after ~12 Gyr of cluster evolution, and thus to be observed today. To calculate N_1 then, we assume a first generation with mass M_{SC} and a given IMF (depending on α_4, with a mass range of 0.01–500 $M_\odot$). The number of low-mass stars in the second generation, N_2, is estimated from the amount of accumulated mass, M_{acc}, by assuming that all this mass is used to form the second generation *with a standard IMF*. Similarly to before, we apply an IMF between 0.01 and 500 $M_\odot$ and take the number of stars in the mass range 0.08–0.8 $M_\odot$ to be our N_2. The ratio of generations plotted in Figure 7 is then $N_2/(N_1 + N_2)$.

We find that, depending on the IMF index, the ratio of the generations can be anything between 1% and 80%. We emphasize again that we do not suppose a second generation forming stars only up to 0.8 $M_\odot$ (as done in, e.g., de Mink et al. 2009b), but apply a regular IMF that includes all stars, even massive and very massive stars. Additionally, the dynamical evolution of the SC should be taken into account: it may increase the $N_2/(N_1 + N_2)$ ratio even further, as the second generation is expected to be more centrally concentrated (see the discussion in Section 6.1). For observational evidence of a more centrally concentrated second generation, see, e.g., Milone et al. (2012) and Dalessandro et al. (2016).

Thus, we conclude that either a top-heavy IMF or the dynamical removal of the noncentrally located stars—or a combination of these two effects—is our suggested explanation for the observations of the second generation being as populous as ~30%–90%.

6.5. On the Correlation of Second Generation and Cluster Mass

It has been reported by several authors that the fraction of enriched stars in GCs strongly correlates with the cluster mass. See, e.g., Figures 14 and 16 of Carretta et al. (2010), Figure 20 of Milone et al. (2017), and Figure 7 of Carretta & Bragaglia (2018). To directly confirm these observations with our calculations, we would need to test the effects of two processes: the mixing with pristine gas (see Section 6.3) and the dynamical removal of stars (see Section 6.1). These tests fall outside the scope of the present study. However, we point out that both the total initial mass and the accumulated (i.e., enriched) mass do correlate with the number ratio of second-generation stars in our calculations. Thus, unless the processes mentioned above cancel out this correlation for some reason (e.g., ejecting only centrally located stars, or removing more mass from the more massive clusters, thus making the initial cluster mass strongly anticorrelate with the present-day cluster mass), we predict this trend to indeed be imprinted on GCs observed today.

6.6. More Than Two Generations?

In our model, we allow the second star formation episode to also create massive stars (see the discussion in Section 6.4). Thus, it is possible in principle that the whole scenario repeats another time. As seen in Figure 6, our most extreme cluster with $M_{SC} = 10^8 \, M_\odot$ can accumulate as much as 10^6–$10^7 \, M_\odot$ in the center—which may again form massive stars and thus repeat the cycle again. Without testing this possibility quantitatively here, we speculate that it may explain the fact that some clusters are observed to have more than two stellar generations (e.g., NGC 2808; see D'Antona et al. 2005; Milone et al. 2015).

7. Discussion

7.1. On the Helium Problem

Direct helium abundance measurements are difficult to obtain spectroscopically, since the relevant photospheric transitions need a much higher surface temperature than what red giant stars (those we have extensive spectroscopic studies of when it comes to light elements; see the data set plotted in Figure 5) have. Helium abundance is usually inferred indirectly from photometric measurements via fitting stellar models (isochrones) in the observed color–magnitude diagrams. These studies suggest that almost all GCs show variation in helium abundance, albeit rarely up to $Y_{obs} = 0.35$.

In Section 5.2 we show that our models overpredict helium at an extent ($Y \sim 0.5 - 0.7$) that is not reconcilable with observations. However, as pointed out by several authors already (Lochhaas & Thompson 2017; Bastian & Lardo 2018; Szécsi et al. 2018), this is a generic problem in the field. The current understanding of the nucleosynthetic origin of the second generation is that in order to reach the extremely low levels of, e.g., oxygen (together with the other extreme values

of light elements in Figure 5), hot hydrogen burning is needed because it has the relevant side reactions (namely, the Mg–Al chain and the Ne–Na chain) that produce the observed light-element ratios. But, of course, by burning hydrogen, helium is created.

These problems indicate that our general understanding of the multiple-population phenomenon is still far from perfect. For example, we may not have the complete picture of how the Mg–Al chain and the Ne–Na chain operate in massive and very massive stars. This would not be surprising, given the scarcity of observations when it comes to massive stars, especially at low metallicity (e.g., Section 1 in Kubátová et al. 2018).

Alternatively, there may be a way to separate Na, O, Mg, and Al from He either inside the first generation of massive stars or in the second generation of low-mass stars (gravitational settling of elements may play some role?). That said, there may be a missing ingredient in our theory of the cluster gas dynamics (e.g., the mixing of the pristine gas to the ejecta of massive stars may happen in an unexpected way; turbulence in particular, see Hopkins 2013, may play a role?) or even that of the star formation process itself. Also, the method of measuring He variations indirectly from photometry and isochrone fitting, although currently our most reliable method to infer He dispersions (Cassisi et al. 2017), may in the future undergo some not-yet-seen developments, leading to the revision of what we know about helium in GCs.

And finally, although some observational features are well explained by the hypothesis that a first generation of massive stars synthesized the observed element ratios, the problem around He may still mean that the massive star hypothesis needs to be looked beyond, and completely new hypotheses need to be suggested (see also the discussion in Section 2.2.2 of Bastian & Lardo 2018).

7.2. Directions for Future Work

We combined two research fields, massive stellar evolution and cluster gas dynamics; both have studied GCs so far mostly from their own perspectives. Combining them now opens up new pathways for investigation.

For example, we only applied single stellar models. But massive stars have a very high binary fraction (Sana et al. 2012). In a close binary, the interaction may lead to rather interesting outcomes, such as the formation of gravitational-wave progenitors (e.g., de Mink et al. 2009a; Belczynski et al. 2016; de Mink & Mandel 2016; Marchant et al. 2016, 2017; Szécsi 2017a, 2017b; Vigna-Gómez et al. 2018). In fact, interacting massive binaries have been suggested as the source of anomalous light-element ratios by de Mink et al. (2009b) and investigated further by Bastian et al. (2013) and Elmegreen (2017). We note that our single stellar models have been computed with very similar physical assumptions to the binary system in de Mink et al. (2009b). Therefore, we expect our stellar models to, upon putting them next to a companion in such a system, pollute the cluster at some extent via the binary channel as well. This, however, needs to be quantitatively investigated in the future, preferably by computing a set of detailed binary models. This would be a long-awaited completion of the work by de Mink et al. (2009b), who only computed one such system and extrapolated therefrom. Alternatively, although less elaborate, our set of single-star models may be applied in a synthetic binary population, similarly to what we did here for a synthetic single-star population, but with some necessary assumptions about the interaction of the companions. This binary population then can be applied as input for the cluster gas dynamics simulations, potentially allowing us to test uncertain parameters of stellar and binary evolution (e.g., mass transfer efficiency, nuclear reaction rates).

Another way to make use of our new method is to test the predictions of different pollution scenarios against each other. For example, the "fast spinning star" scenario (Decressin et al. 2007b) can be tested against ours, or the interactive binary scenario against these, etc., in terms of facilitating star formation and with which chemical composition. Alternatively, the role of rotation may be explored by using not only slow-rotating models of Szécsi et al. (2015) but also moderate, and even fast, rotators that predict chemically homogeneously evolution. These so-called "TWUIN stars" (Kubátová et al. 2018) are needed for the star-forming shell scenario of Szécsi et al. (2018) to operate. Hence, if we want to explain our present work's insufficient accounting for the high extent of Mg depletion by the shell scenario (as done in Section 5.1.3), we need to make sure that the contribution of hot TWUIN stars does not brake down our "window" of star formation by heating up the gas too much.

The role of metallicity should also be studied in more detail, as this may indeed be important, especially when it comes to the most fragile elements (e.g., magnesium). Also, the very massive supergiants, those responsible for accommodating the secondary star formation, are only predicted in our low-metallicity population and not in our high-metallicity one; however, the exact metallicity value below which supergiants start to play their role in the formation of GCs should be specified further in future work. We suggest to apply several sets of stellar models covering the range in metallicities between, and even above and below, the two values investigated here.

Our low-metallicity supergiants are theoretical predictions; if they indeed exist, their observational discovery is yet to be carried out. They are, of course, not expected to be found in GCs, because even if they used to be there, they are long dead now. As our models show, they are only expected to be present in clusters as young as between ∼2 and 4 Myr. Another caveat for their discovery is that their natal cloud needs to be sufficiently metal-poor and sufficiently massive to be able to form them at all. Nonetheless, from the models we know that they may be extremely bright objects. Szécsi et al. (2015, see their Section 5) explain that at the distance of 18 Mpc they would appear with a visual magnitude of 19 mag. It has been suggested that brightness variations due to pulsations (with periods of the order of months to years; see also Moriya & Langer 2015) may reveal them as stars rather than SCs in photometric multiepoch observations.

When it comes to the calculations of the cluster gas dynamics, there are ways to improve here too. We suggest, for example, to apply our stellar models (both the low- and high-metallicity ones) as input for 3D radiation-hydrodynamic simulations. There are basically two ways to do this. One is to compute the so-called smooth source hydrodynamics of the cluster (following Wünsch et al. 2017), that is, to suppose a population of several hundred massive stars providing energy and mass that is inserted smoothly into the cluster. Another, more elaborate but also computationally more expensive way is

to model the cluster evolution applying individual sources in the 3D simulations.

Less concerned with stellar evolution or cluster gas dynamics, ways to improve our general understanding of the multiple-population phenomenon have been pointed out throughout the text. To summarize these: the effect of supernovae on our star formation episode should be assessed (Section 3.5), the conditions for dynamical mass removal, including its effect on changing the ratio of first- versus second-generation stars, should be quantified (Section 6.1), and the extent of mixing the enriched material with the pristine gas in the cluster center should be investigated (Section 5.1.1). And last but not least, the issues around helium should be resolved (Section 7.1).

An interesting observational conundrum that arose recently is that there seems to be a cut in the occurrence of the multiple-population phenomenon at ~2 Gyr. Some clusters with this age, like NGC 1978, do show multiple populations, whereas slightly younger clusters with comparable present-day masses do not (Mucciarelli et al. 2008, 2014; Martocchia et al. 2018a, 2018b). If this proves to be an established fact in the future, any theoretical models should be able to account for it. It will need to be done, however, by including the investigation of the cluster's long-term dynamical evolution. As we have no means to do that yet (see also our discussion in Section 6.1), we leave this question open for now.

7.3. Gravitational Waves

With direct detections of gravitational waves (Abbott et al. 2016a, 2016b; Bagoly et al. 2016; Szécsi 2017a, 2017b; The LIGO Scientific Collaboration et al. 2017), many authors suggested GCs to be the host of these events (Rodriguez et al. 2015; Antonini et al. 2016; Belczynski et al. 2016; Askar et al. 2017). In Section 3.5, discussing the final fate and remnants of our supergiants, we pointed out that many of our stellar models are expected to form black holes or neutron stars after they explode; only those that explode as pair-instability supernova are not expected to leave any remnant. Thus, without quantitatively investigating this question, we point out that our scenario qualitatively predicts a significant number of these compact objects to be present in the YMC, and thus to potentially merge over the long lifetimes of these clusters via dynamical interactions. Our work is therefore an important motivation to look for gravitational-wave emission, as well as its compact object progenitors, in GCs. The same is true for short-duration gamma-ray bursts, the origin of which has been associated with gravitational-wave-emitting compact object mergers (Abbott et al. 2017).

8. Conclusions

We realized a novel synergy between two research fields, massive stellar theory and cluster gas dynamics. In particular, we explored whether the model of rapidly cooling shocked stellar winds combined with state-of-the-art stellar evolution models can contribute to the explanation of multiple stellar populations observed in GCs.

The model of rapidly cooling shocked stellar winds predicts that the hot gas within SCs can become thermally unstable and form warm clumps. These clumps fall into the cluster center, where they cool further and form a second generation of stars.

The new stars are necessarily enriched by the nuclear ashes synthesized in the first-generation massive stars.

We apply stellar evolutionary models as input for the calculations of the cluster gas dynamics. The models are computed for two chemical compositions: for low metallicity corresponding to [Fe/H] ~ −1.7, and for a higher but still subsolar metallicity corresponding to [Fe/H] ~ −0.4. By applying these two sets of models, we evaluate the impact of metallicity on the secondary star formation.

We find that at low metallicity, cool supergiant stars—predicted to have very high mass-loss rates and, at the same time, a low wind velocity—help to make the hot gas thermally unstable very early on. Their winds include products of hot hydrogen burning, thus making them a suitable candidate for explaining the multiple-population phenomenon.

Our calculations are run for the initial 10 Myr life of the clusters and predict the amount of mass accumulated inside the cluster center, as well as its chemical composition depending on the cluster mass, slope of the IMF, and metallicity. We draw the following conclusions:

1. *A "window" for undisturbed star formation.* At low metallicity, mass accumulation starts early (at ~1.6 Myr), and a significant amount of mass is available for star formation before the first supernovae start to explode (at around 4.5 Myr) or before the gas is expelled from YMCs (typically observed around 4 Myr). This is thanks to the slow winds of massive supergiants. At high metallicity, however, mass accumulation starts later, after ~4 Myr, thus limiting—but not necessarily excluding—our scenario to work.

2. *Agreement with light-element abundance ratios.* Our calculations reproduce the Na–O spread sufficiently well. Also, only hydrogen-burning products are ejected (i.e., the sum of the C, N, and O atoms are preserved, with C and O being depleted and N enhanced), but no products of helium burning or those of subsequent burning stages. The spread our calculations predict in Mg–Al is lower than observed; although the stellar models do provide the right chemical composition (i.e., heavily depleted in Mg and enriched in Al), it is not captured by our "window" of star formation. This, together with predicting higher-than-observed helium abundances, points to future directions of improvement.

3. *Cluster center captures all the mass of stellar winds.* Our metal-poor clusters with initial mass larger than several times $10^6 \, M_\odot$ capture almost all the mass ejected by stellar winds. This 10^4–$10^5 \, M_\odot$ material accumulates in the center of the cluster and forms new stars there. Thus, under the assumption that the massive cluster is evolving to become a GC by dynamically removing its not too centrally located (i.e., mainly first-generation) stars over several gigayears, we are able to consistently explain the mass budget of present-day GCs by applying a normal IMF for both the first and the second stellar generations.

4. *A top-heavy IMF helps though.* With a normal IMF ($\alpha_4 = -2.3$) our massive clusters form a second generation as populous as 1% of the total. But applying a top-heavy IMF with $\alpha_4 = -1.5$ raises this fraction to close to 50%, and a very extreme index of $\alpha_4 = -1.1$ up to 80%. This means that even without supposing dynamical removal of the first generation (see above), a top-heavy IMF can explain the observed high ratio of

second- versus first-generation stars. If both effects contribute, however, we suggest that a moderate amount of dynamical ejection, together with a moderately top-heavy IMF, is enough to account for the mass budget of present-day GCs.

5. *More than two generations?* In principle, our scenario is able to produce more than two stellar generations since we allow the newly formed generation to contain massive stars, thus possibly repeating the cycle.

6. *GCs as hosts of gravitational-wave emission.* In our scenario, the second generation is formed from the *winds* of massive stars. The massive stars themselves are predicted to end up mostly as compact objects, supporting the hypothesis that gravitational waves should be expected from GCs.

7. *Fraction of second generation correlates with GC mass.* We predict that both the amount of accumulated mass and the total initial mass of the cluster correlate with the number of low-mass stars in the second generation. This may lead to the observed correlation between the mass of the GC and the extent of the multiple-population phenomenon.

Our way of investigating the multiple-population phenomenon in GCs by combining stellar evolutionary models with calculations of cluster wind dynamics should be considered an important method of testing stellar theories in the future—especially those that are very hard to find observational evidence for. Such theories include metal-poor massive stars, in both single and binary systems. The potential of these systems in explaining exotic explosions (gravitational waves, gamma-ray bursts, several types of supernovae, and superluminous supernovae) is quite high; nonetheless, many of the existing theories await future tests. We suggest that studying GCs by combining stellar models with cluster wind dynamics is a viable new approach by which these tests could be done.

Software: Numpy.

ORCID iDs

Dorottya Szécsi ⬥ https://orcid.org/0000-0001-6473-7085
Richard Wünsch ⬥ https://orcid.org/0000-0003-1848-8967

References

Abbott, B. P., Abbott, R., Abbott, T. D., et al. 2016a, ApJL, 818, L22
Abbott, B. P., Abbott, R., Abbott, T. D., et al. 2016b, PhRvL, 116, 061102
Abbott, B. P., Abbott, R., Abbott, T. D., et al. 2017, PhRvL, 119, 161101
Andersen, M., Gennaro, M., Brandner, W., et al. 2016, arXiv:1602.05918
Antonini, F., Chatterjee, S., Rodriguez, C. L., et al. 2016, ApJ, 816, 65
Askar, A., Szkudlarek, M., Gondek-Rosińska, D., Giersz, M., & Bulik, T. 2017, MNRAS, 464, L36
Bagoly, Z., Szécsi, D., Balázs, L. G., et al. 2016, A&A, 593, L10
Bastian, N., Cabrera-Ziri, I., & Salaris, M. 2015, MNRAS, 449, 3333
Bastian, N., Covey, K. R., & Meyer, M. R. 2010, ARA&A, 48, 339
Bastian, N., Lamers, H., de Mink, S. E., et al. 2013, MNRAS, 436, 2398
Bastian, N., & Lardo, C. 2018, ARA&A, 56, 83
Belczynski, K., Holz, D. E., Bulik, T., & O'Shaughnessy, R. 2016, Natur, 534, 512
Boothroyd, A. I., & Sackmann, I.-J. 1999, ApJ, 510, 232
Brodie, J. P., & Strader, J. 2006, ARA&A, 44, 193
Brott, I., de Mink, S. E., Cantiello, M., et al. 2011, A&A, 530, A115
Burbidge, E. M., Burbidge, G. R., Fowler, W. A., & Hoyle, F. 1957, RvMP, 29, 547
Carretta, E., & Bragaglia, A. 2018, A&A, 614, A109
Carretta, E., Bragaglia, A., Gratton, R., & Lucatello, S. 2009, A&A, 505, 139
Carretta, E., Bragaglia, A., Gratton, R. G., et al. 2010, A&A, 516, A55
Cassisi, S., Salaris, M., Pietrinferni, A., & Hyder, D. 2017, MNRAS, 464, 2341
Chevalier, R. A., & Clegg, A. W. 1985, Natur, 317, 44
Cottrell, P. L., & Da Costa, G. S. 1981, ApJL, 245, L79
Crowther, P. A., Caballero-Nieves, S. M., Bostroem, K. A., et al. 2016, MNRAS, 458, 624
Crowther, P. A., Schnurr, O., Hirschi, R., et al. 2010, MNRAS, 408, 731
Da Costa, G. S., Norris, J. E., & Yong, D. 2013, ApJ, 769, 8
Dalessandro, E., Lapenna, E., Mucciarelli, A., et al. 2016, ApJ, 829, 77
D'Antona, F., Bellazzini, M., Caloi, V., et al. 2005, ApJ, 631, 868
Decressin, T., Baumgardt, H., Charbonnel, C., & Kroupa, P. 2010, A&A, 516, A73
Decressin, T., Charbonnel, C., & Meynet, G. 2007a, A&A, 475, 859
Decressin, T., Meynet, G., Charbonnel, C., Prantzos, N., & Ekström, S. 2007b, A&A, 464, 1029
De Masi, C., Vincenzo, F., Matteucci, F., et al. 2018, arXiv:1805.06841
de Mink, S. E., Cantiello, M., Langer, N., et al. 2009a, A&A, 497, 243
de Mink, S. E., & Mandel, I. 2016, MNRAS, 460, 3545
de Mink, S. E., Pols, O. R., Langer, N., & Izzard, R. G. 2009b, A&A, 507, L1
Denissenkov, P., & Hartwick, F. 2014, MNRAS, 437, L21
D'Ercole, A., D'Antona, F., Ventura, P., Vesperini, E., & McMillan, S. L. W. 2010, MNRAS, 407, 854
D'Ercole, A., Vesperini, E., D'Antona, F., McMillan, S. L. W., & Recchi, S. 2008, MNRAS, 391, 825
Doherty, C. L., Gil-Pons, P., Lau, H. H. B., et al. 2014, MNRAS, 441, 582
Elmegreen, B. G. 2017, ApJ, 836, 80
Farr, W. M., & Mandel, I. 2018, Sci, 361, aat6506
Georgy, C., Ekström, S., Eggenberger, P., et al. 2013, A&A, 558, A103
Gräfener, G., Owocki, S. P., & Vink, J. S. 2012, A&A, 538, A40
Grassitelli, L., Fossati, L., Langer, N., et al. 2015a, A&A, 584, L2
Grassitelli, L., Fossati, L., Simón-Díaz, S., et al. 2015b, ApJL, 808, L31
Gratton, R. G., Sneden, C., & Carretta, E. 2004, ARA&A, 42, 385
Gratton, R. G., Sneden, C., Carretta, E., & Bragaglia, A. 2000, A&A, 354, 169
Harris, W. E. 2010, arXiv:1012.3224
Heger, A., Fryer, C. L., Woosley, S. E., Langer, N., & Hartmann, D. H. 2003, ApJ, 591, 288
Heger, A., Langer, N., & Woosley, S. E. 2000, ApJ, 528, 368
Hollyhead, K., Bastian, N., Adamo, A., et al. 2015, MNRAS, 449, 1106
Hopkins, A. M. 2018, arXiv:1807.09949
Hopkins, P. F. 2013, MNRAS, 430, 1653
Kalari, V. M., Carraro, G., Evans, C. J., & Rubio, M. 2018, ApJ, 857, 132
Karakas, A. I., Fenner, Y., Sills, A., Campbell, S. W., & Lattanzio, J. C. 2006, ApJ, 652, 1240
Khalaj, P., & Baumgardt, H. 2015, MNRAS, 452, 924
Khorrami, Z., Lanz, T., Vakili, F., et al. 2016, A&A, 588, L7
Köhler, K., Langer, N., de Koter, A., et al. 2015, A&A, 573, A71
Kozyreva, A., Blinnikov, S., Langer, N., & Yoon, S.-C. 2014, A&A, 565, A70
Kroupa, P. 2001, MNRAS, 322, 231
Kruijssen, J. M. D. 2015, MNRAS, 454, 1658
Kubátová, B., Szécsi, D., Sander, A. A. C., et al. 2018, arXiv:1810.01267
Lamers, H., & Cassinelli, J. 1999, Introduction to Stellar Winds (Cambridge: Cambridge Univ. Press)
Langer, N. 1991, A&A, 252, 669
Langer, N., Norman, C. A., de Koter, A., et al. 2007, A&A, 475, L19
Leitherer, C., Robert, C., & Drissen, L. 1992, ApJ, 401, 596
Leitherer, C., Schaerer, D., Goldader, J. D., et al. 1999, ApJS, 123, 3
Levesque, E. M. 2017, Astrophysics of Red Supergiants (Bristol: IOP Publishing)
Lochhaas, C., & Thompson, T. A. 2017, MNRAS, 470, 977
Longmore, S. N., Kruijssen, J. M. D., Bastian, N., et al. 2014, Protostars and Planets VI, 291
MacFadyen, A. I., & Woosley, S. E. 1999, ApJ, 524, 262

Maíz-Apellániz, J. 2002, in IAU Symp. 207, Extragalactic Star Clusters, ed. D. P. Geisler, E. K. Grebel, & D. Minniti (Paris: IAU), 697
Marchant, P., Langer, N., Podsiadlowski, P., et al. 2017, A&A, 604, A55
Marchant, P., Langer, N., Podsiadlowski, P., Tauris, T. M., & Moriya, T. J. 2016, A&A, 588, A50
Martínez-González, S., Tenorio-Tagle, G., & Silich, S. 2016, ApJ, 816, 39
Martínez-González, S., Wünsch, R., Palouš, J., et al. 2018, ApJ, 866, 40
Martocchia, S., Cabrera-Ziri, I., Lardo, C., et al. 2018a, MNRAS, 473, 2688
Martocchia, S., Niederhofer, F., Dalessandro, E., et al. 2018b, MNRAS, 477, 4696
Meynet, G., & Maeder, A. 2002, A&A, 390, 561
Milone, A. P., Marino, A. F., Piotto, G., et al. 2015, ApJ, 808, 51
Milone, A. P., Piotto, G., Bedin, L. R., et al. 2012, ApJ, 744, 58
Milone, A. P., Piotto, G., Renzini, A., et al. 2017, MNRAS, 464, 3636
Moriya, T. J., & Langer, N. 2015, A&A, 573, A18
Mucciarelli, A., Carretta, E., Origlia, L., & Ferraro, F. R. 2008, AJ, 136, 375
Mucciarelli, A., Dalessandro, E., Ferraro, F. R., Origlia, L., & Lanzoni, B. 2014, ApJL, 793, L6
O'Connor, E., & Ott, C. D. 2011, ApJ, 730, 70
Palouš, J., Wünsch, R., Martínez-González, S., et al. 2013, ApJ, 772, 128
Palouš, J., Wünsch, R., & Tenorio-Tagle, G. 2014, ApJ, 792, 105
Pancino, E., Romano, D., Tang, B., et al. 2017, A&A, 601, A112
Portegies Zwart, S. F., McMillan, S. L. W., & Gieles, M. 2010, ARA&A, 48, 431
Reina-Campos, M., Kruijssen, J. M. D., Pfeffer, J., Bastian, N., & Crain, R. A. 2018, MNRAS, 481, 2851
Rodriguez, C. L., Morscher, M., Pattabiraman, B., et al. 2015, PhRvL, 115, 051101
Sana, H., de Mink, S. E., de Koter, A., et al. 2012, Sci, 337, 444
Sanyal, D., Grassitelli, L., Langer, N., & Bestenlehner, J. M. 2015, A&A, 580, A20
Sanyal, D., Langer, N., Szécsi, D.-C., Yoon, S., & Grassitelli, L. 2017, A&A, 597, A71
Schiavon, R. P., Johnson, J. A., Frinchaboy, P. M., et al. 2017, MNRAS, 466, 1010
Schneider, F. R. N., Sana, H., Evans, C. J., et al. 2018a, Sci, 359, 69
Schneider, F. R. N., Sana, H., Evans, C. J., et al. 2018b, Sci, 361, aat7032
Schure, K. M., Kosenko, D., Kaastra, J. S., Keppens, R., & Vink, J. 2009, A&A, 508, 751
Silich, S., & Tenorio-Tagle, G. 2017, MNRAS, 465, 1375
Silich, S., Tenorio-Tagle, G., & Muñoz-Tuñón, C. 2003, ApJ, 590, 791
Silich, S., Tenorio-Tagle, G., & Rodríguez-González, A. 2004, ApJ, 610, 226
Smartt, S. J. 2015, PASA, 32, e016
Szécsi, D. 2017a, CoSka, 47, 108
Szécsi, D. 2017b, PoS(MULTIF2017)065, arXiv:1710.05655
Szécsi, D., Langer, N., Yoon, S.-C., et al. 2015, A&A, 581, A15
Szécsi, D., Mackey, J., & Langer, N. 2018, A&A, 612, A55
Tenorio-Tagle, G., Silich, S., Martínez-González, S., et al. 2013, ApJ, 778, 159
Tenorio-Tagle, G., Silich, S., Rodríguez-González, A., & Muñoz-Tuñón, C. 2005, ApJ, 620, 217
Tenorio-Tagle, G., Wünsch, R., Silich, S., & Palouš, J. 2007, ApJ, 658, 1196
The LIGO Scientific Collaboration, the Virgo Collaboration, Abbott, B. P., et al. 2017, PhRvL, 118, 221101
Ventura, P., Carini, R., & D'Antona, F. 2011, MNRAS, 415, 3865
Vesperini, E., McMillan, S. L. W., D'Antona, F., & D'Ercole, A. 2010, ApJL, 718, L112
Vigna-Gómez, A., Neijssel, C. J., Stevenson, S., et al. 2018, MNRAS, 481, 4009
Vink, J., de Koter, A., & Lamers, H. 2000, A&A, 362, 295
Vink, J. S. 2018, A&A, 615, A119
Vink, J. S., de Koter, A., & Lamers, H. J. G. L. M. 1999, A&A, 350, 181
Woosley, S. E., Blinnikov, S., & Heger, A. 2007, Natur, 450, 390
Wünsch, R., Palouš, J., Tenorio-Tagle, G., & Ehlerová, S. 2017, ApJ, 835, 60
Wünsch, R., Silich, S., Palouš, J., Tenorio-Tagle, G., & Muñoz-Tuñón, C. 2011, ApJ, 740, 75
Wünsch, R., Tenorio-Tagle, G., Palouš, J., & Silich, S. 2008, ApJ, 683, 683
Yong, D., Grundahl, F., Lambert, D. L., Nissen, P. E., & Shetrone, M. D. 2003, A&A, 402, 985
Yoon, S.-C., Dierks, A., & Langer, N. 2012, A&A, 542, A113
Yoon, S.-C., Langer, N., & Norman, C. 2006, A&A, 460, 199
Zhang, Z.-Y., Romano, D., Ivison, R. J., Papadopoulos, P. P., & Matteucci, F. 2018, Natur, 558, 260

Astronomy & Astrophysics

Supergiants and their shells in young globular clusters

Dorottya Szécsi[1,2], Jonathan Mackey[3,4,5], and Norbert Langer[5]

[1] Astronomical Institute of the Czech Academy of Sciences, Fričova 298, 25165 Ondřejov, Czech Republic
   e-mail: dorottya.szecsi@gmail.com
[2] Institute of Gravitational Wave Astronomy and School of Physics and Astronomy, University of Birmingham, Edgbaston, Birmingham B15 2TT, UK
[3] Dublin Institute for Advanced Studies, School of Cosmic Physics, 31 Fitzwilliam Place, Dublin 2, Ireland
[4] Physikalisches Institut, Universität zu Köln, Zülpicher Straße 77, 50937 Köln, Germany
[5] Argelander-Institut für Astronomie der Universität Bonn, Auf dem Hügel 71, 53121 Bonn, Germany

Received 3 July 2017 / Accepted 10 November 2017

ABSTRACT

Context. Anomalous surface abundances are observed in a fraction of the low-mass stars of Galactic globular clusters, that may originate from hot-hydrogen-burning products ejected by a previous generation of massive stars.
Aims. We aim to present and investigate a scenario in which the second generation of polluted low-mass stars can form in shells around cool supergiant stars within a young globular cluster.
Methods. Simulations of low-metallicity massive stars ($M_i \sim 150-600\ M_\odot$) show that both core-hydrogen-burning cool supergiants and hot ionizing stellar sources are expected to be present simultaneously in young globular clusters. Under these conditions, photoionization-confined shells form around the supergiants. We have simulated such a shell, investigated its stability and analysed its composition.
Results. We find that the shell is gravitationally unstable on a timescale that is shorter than the lifetime of the supergiant, and the Bonnor-Ebert mass of the overdense regions is low enough to allow star formation. Since the low-mass stellar generation formed in this shell is made up of the material lost from the supergiant, its composition necessarily reflects the composition of the supergiant wind. We show that the wind contains hot-hydrogen-burning products, and that the shell-stars therefore have very similar abundance anomalies that are observed in the second generation stars of globular clusters. Considering the mass-budget required for the second generation star-formation, we offer two solutions. Either a top-heavy initial mass function is needed with an index of -1.71 to -2.07. Alternatively, we suggest the shell-stars to have a truncated mass distribution, and solve the mass budget problem by justifiably accounting for only a fraction of the first generation.
Conclusions. Star-forming shells around cool supergiants could form the second generation of low-mass stars in Galactic globular clusters. Even without forming a photoionizaton-confined shell, the cool supergiant stars predicted at low-metallicity could contribute to the pollution of the interstellar medium of the cluster from which the second generation was born. Thus, the cool supergiant stars should be regarded as important contributors to the evolution of globular clusters.

Key words. supergiants – globular clusters: general – circumstellar matter – stars: formation – stars: abundances – radiative transfer

1. Introduction

Globular clusters (GC) are found in the halo of the Milky Way orbiting around the Galactic core. They are generally composed of old, low-mass stars bound together by gravity. The composition of these stars may vary between clusters, but in average, GCs have subsolar metallicity (Z; Gratton et al. 2004; Harris 2010). GCs are under intensive investigation for many reasons. Their stars are so old that they constrain the minimum age of the Universe. Additionally, their stars are both coeval and equidistant, thereby providing natural laboratories for stellar evolution.

One of the most intriguing open questions concerning GCs is the so-called abundance anomalies (Yong et al. 2003; Da Costa et al. 2013). Light element abundances such as O and Na anti-correlate with each other: if O is depleted in a star, then Na is enhanced. The same is observed for the proton-capture isotopes of Mg and Al: if Mg is depleted in a star, then Al is enhanced. Moreover, with the Al-abundance increasing, the ratio of the ^{24}Mg isotope to the total Mg is decreasing, the ^{25}Mg is slightly decreasing and the ^{26}Mg is considerably increasing in the observed GC stars. This is consistent with the interpretation

that one generation of stars has been polluted by nuclear burning products produced at very high temperatures ($>6 \cdot 10^7$ K, Ventura et al. 2011). The nucleosynthetic processes that can increase Na and Al while destroying O and Mg (as well as creating the Mg-isotopic ratios observed) are the Ne-Na chain and the Mg-Al chain (Burbidge et al. 1957), respectively. These burning chains are side-reactions of the CNO-cycle, the main hydrogen-burning process in massive stars. Consequently, there must have been at least one population of massive (and/or intermediate-mass) stars born in the early epochs of the GC's life. These massive stars are already dead, but their nuclear imprint is what we observe today as anomalous abundance patterns in the second generation of low-mass stars. The question is then: how did the pollution happen, that is, how did massive stars lose the amount of nuclear-processed material, and how did this material end up in some of the low-mass stars?

According to the most commonly accepted explanation, the interstellar medium (ISM) had been polluted by hydrogen-burning products from massive stars, and the second generation of stars were born from the polluted ISM (Decressin et al. 2007; D'Ercole et al. 2008). Alternatively, low-mass stars could accrete

the ISM during a long pre-main sequence phase (Bastian et al. 2013). In both cases, an astrophysical source – a polluter – is needed. This source, a population of massive or intermediate-mass stars, should only produce hydrogen-burning products (including helium), since no traces of helium burning products or supernova ejecta are observed. Additionally, the polluter should eject the material slowly enough for it to stay inside the gravitational potential well of the GC. This condition excludes fast winds of massive OB stars or Wolf-Rayet stars unless the fast winds are shocked and can cool efficiently before leaving the cluster (cf. Wünsch et al. 2017).

Several astrophysical scenarios were proposed that fulfill the conditions above. Asymptotic giant branch stars could eject their hot bottom burning products (Ventura et al. 2001; D'Ercole et al. 2008). Fast rotating massive stars that are close to the breakup rotation could eject core burning products (Decressin et al. 2007; Tailo et al. 2015). Supermassive (10 000 $M_\odot$) stars could pollute through continuum driven stellar wind (Denissenkov & Hartwick 2014). In addition, massive binary systems could pollute via non-conservative mass transfer (de Mink et al. 2009).

Here we propose a new scenario: low mass stars could be born in photoionization-confined shells around cool supergiant (SG) stars in the young globular clusters, as shown in Fig. 1. Szécsi et al. (2015b) simulated very massive (80–300 $M_\odot$) and long-living SGs. These long-living SGs are predicted only to exist at low-Z, because at solar composition the strong mass-loss removes their envelopes and turns them into Wolf–Rayet stars before reaching the SG branch. Moreover, the very massive, metal-poor SGs form *before* the hydrogen is exhausted in the core (this is due to envelope inflation, cf. Sanyal et al. 2015). Core-hydrogen-burning cool supergiants spend 0.1–0.3 Myr in the SG branch. During this time, they lose a large amount of mass (up to several hundred $M_\odot$ in the case of a 600 $M_\odot$ star, as we show below). This mass lost in the SG wind has undergone nuclear burning and shows similar abundance variations to those observed in GC stars.

Photoionization-confined shells can be present around cool supergiants at the interface of ionized and neutral material, as shown by Mackey et al. (2014). The shell can contain as much as 35% of the mass lost in the stellar wind. The main condition for forming a photoionization-confined shell is that the SG has a cool and slow wind and is surrounded by strong sources of Lyman-continuum radiation. These conditions may have been fulfilled at the time when Galactic globular clusters were born. Evolutionary simulations of low-Z massive stars by Szécsi et al. (2015b) predict that both supergiant stars and compact hot stars develop at the same time. The latter are fast rotating, hot and luminous massive stars that emit a huge number of Lyman-continuum photons. The slowly rotating stars, on the other hand, evolve to be cool red or yellow SGs. Thus, the condition required by Mackey et al. (2014) about SGs and ionizing sources close to each other may have been common in the first few million years of a GC's life. Consequently, photoionization-confined shells could form there, too.

This work is organized as follows. In Sect. 2, we present the evolution of the models that become core-hydrogen-burning cool SG stars, and discuss the composition of their winds. In Sect. 3, we introduce the star-forming supergiant shell scenario, and show that in the environment of the young globular clusters, it is possible to form low-mass stars in a supergiant shell from the material ejected by the SG's wind. In Sect. 4, we discuss the mass budget of our scenario, as well as the amount of helium predicted in the second generation. In Sect. 5, we summarize the work.
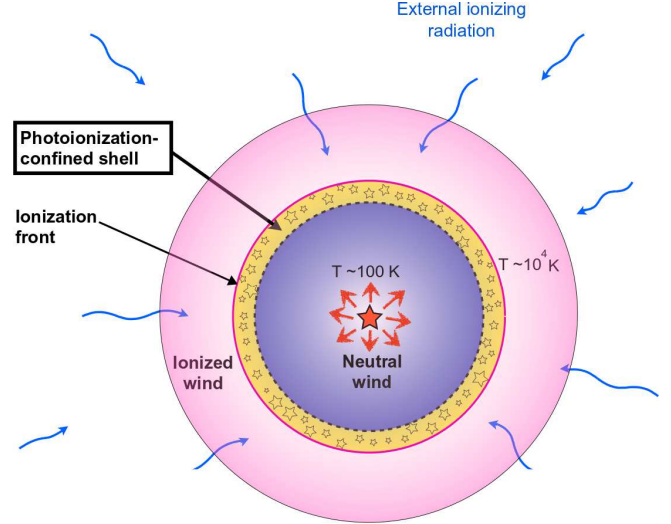
Fig. 1. Photoionization-confined shell around a cool supergiant star. The second generation of low-mass stars are formed in the shell. This scenario could be common in the first few million years of the early globular clusters, explaining the pollution of the second generation. This simple drawing serves to present the original idea; as for the nominal values of our model, the shell forms at $r \approx 0.02$ pc from the central star (cf. our simulation of a shell in Fig. 7). The central supergiant itself has a stellar radius of ~5000 $R_\odot$; that is, the supergiant is 170 times smaller in radial dimension than the sphere of the shell. (This figure is derived from Fig. 1 of Mackey et al. 2014.)

2. Supergiants in young GCs

2.1. The evolution of core-hydrogen-burning cool SGs

The first generation of stars in the young GCs almost certainly contained massive stars. We see massive stars forming in young massive clusters (YMC) today (Longmore et al. 2014). YMCs are theoretically similar to the young GCs and are thought to become GC-like objects eventually (e.g. Brodie & Strader 2006; Mucciarelli et al. 2014; Andersen et al. 2017).

The massive stars of this first generation must have had the same metallicity that we observe today in the low-mass GC stars. The metallicity distribution of GCs in the Galaxy is shown in Fig. 2. It is a broad and bi-modal distribution with a large peak at [Fe/H] ~ −1.4 and a smaller peak at ~−0.6 (cf. Gratton et al. 2004; Brodie & Strader 2006; Harris et al. 2006; Harris 2010; Forbes & Bridges 2010). While there is recent evidence that a few of the high-metallicity GCs seem to harbor multiple generations too (Schiavon et al. 2017), here we only consider low-metallicity GCs that are in the large peak, that is between [Fe/H] = −1.0 to −2.0, because the abundance anomalies seem to be consistently present in almost all of them (Gratton et al. 2004).

We use the low-metallicity ([Fe/H] = −1.7, corresponding to 0.02 $Z_\odot$) massive star simulations of Szécsi et al. (2015b) to model the young GC environment and the first generation of massive and very massive stars. However, Szécsi et al. (2015b) do not use an α-enhanced mixture (as suggested for GC stars by Decressin et al. 2007, see their Table 3), but a mixture suitable for dwarf galaxies. Therefore, when comparing to observations (in Figs. 4–6), the initial O, Na, Mg, and Al abundance of our models are scaled to the following abundance ratios: [O/Fe]$_{\rm first}$ = 0.4, [Na/Fe]$_{\rm first}$ = −0.4, [Mg/Fe]$_{\rm first}$ = 0.6, [Al/Fe]$_{\rm first}$ = 0.2, approximately matching the observed composition of the first generation of GC stars.
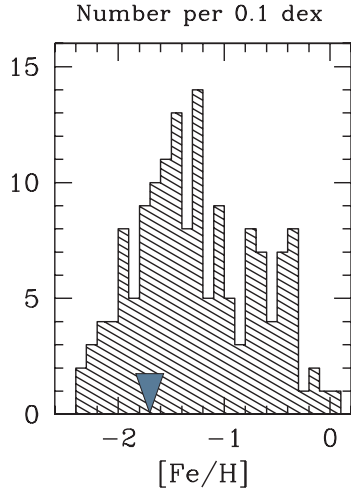
Fig. 2. Number of GCs at a given metallicity. The figure is taken from Harris (2010), and shows the distribution of 157 GCs with measured [Fe/H] value. We apply a metallicity of [Fe/H] = −1.7 (marked in the figure) to model the first generation of massive stars in GCs.
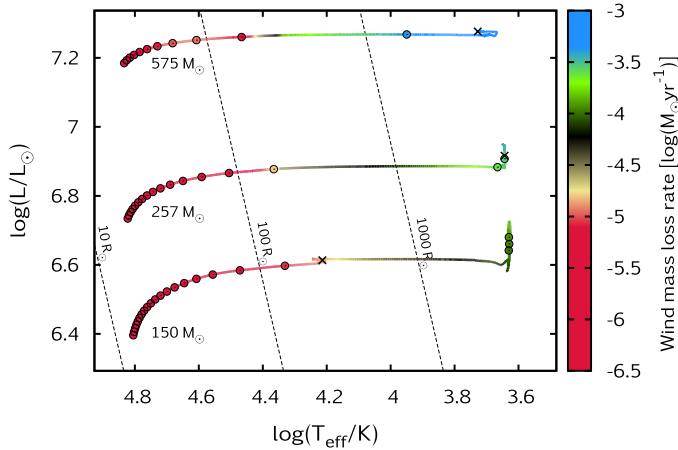

Fig. 3. Hertzsprung–Russell diagram of three low-Z evolutionary models that become core-hydrogen-burning SG stars with initial masses of 150, 257, and 575 $M_\odot$ and initial rotational velocity of 100 km s^{-1}. Dots in the tracks mark every 10^5 years of evolution. Crosses mark the end of the core-hydrogen-burning phase; in case of the model with 575 $M_\odot$, the end of the computation. Theoretical mass-loss rates are colour coded, and dashed lines indicate the radial size of the stars on the diagram.

Massive stars at low Z evolve differently from those at $Z_\odot$. Simulations of Szécsi et al. (2015b) predict different evolutionary paths and, consequently, new types of objects present in low-Z environments. One of the predictions at low Z are the core-hydrogen-burning cool supergiant stars. These objects start their evolution as O-type stars but, during their main-sequence phase, they expand due to envelope inflation (Sanyal et al. 2015) and become cool SG stars while still burning hydrogen in their cores. The cool supergiants in general have a convective envelope because of their low ($<10^4$ K) surface temperature. Envelope convection mixes nuclear products from the burning regions (core or shell) to the surface. Thus, the wind of the cool SG stars contains the products of nuclear burning that is happening in the deeper regions of these stars. In case of core-hydrogen-burning cool supergiants, the nuclear burning products in the wind are, necessarily, hot-hydrogen-burning products.

Core-hydrogen-burning cool SGs with low metallicity (0.02 $Z_\odot$) are predicted at masses higher than $M_{\rm ini} \gtrsim 80\ M_\odot$.
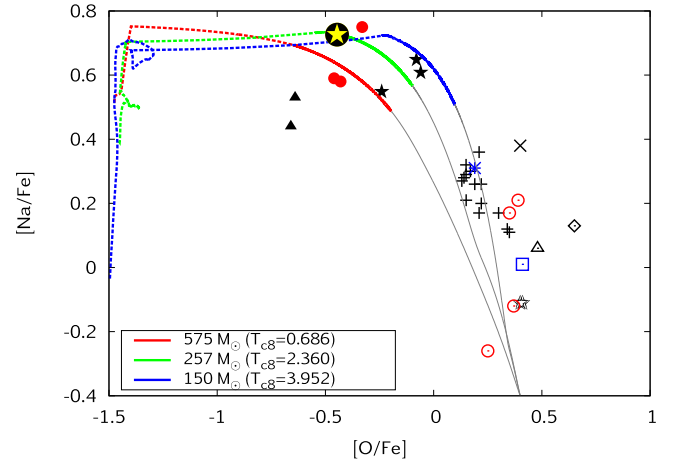
Fig. 4. Theoretical predictions of the wind composition (surface Na abundance as a function of the surface O abundance, in solar Fe units) of three stellar models that become core-hydrogen-burning SGs are plotted with lines. The grey part of the lines correspond to surface compositions at $T_{\rm eff} > 10^4$ K (i.e. the evolution before reaching the SG branch), while the coloured part of the lines show surface composition at $T_{\rm eff} < 10^4$ K (i.e. on the SG branch). When the lines become dashed, they represent the composition of the envelope in the last computed model (i.e. deeper layers that could still be lost if the mass-loss rate was higher than assumed here). The evolutionary calculations ended at the core temperatures, $T_{\rm c8}$, given in the legend (units in 10^8 K). The black-yellow star-symbol corresponds to the composition for the simulation presented in Sect. 3.5. Observational data of the surface composition of GC stars (ω Cen red, NGC 6752 black and M 4 blue) are plotted with dots of different colours and shapes, following Yong et al. (2003), Da Costa et al. (2013) and Denissenkov & Hartwick (2014). Open symbols mark the "primordial" population of stars, that is, those without pollution. Filled symbols mark the "extremely" polluted population of stars. Crosses mark the "intermediate" population stars, that is, those with some but not extreme pollution. For details of the observations and the properties of these categories, we refer to Yong et al. (2003) and Da Costa et al. (2013).

They stay on the SG branch and burn hydrogen for a relatively long time (in some cases, as long as 0.3 Myr, which corresponds to 15% of their main sequence lifetimes). These objects have a contribution to the chemical evolution of their environments. Such a star could eject several tens, or hundreds, of $M_\odot$ through stellar wind mass-loss, the composition of which material being different from that of the circumstellar gas.

We simulate the cool supergiant phase by applying the mass-loss rate prescription by Nieuwenhuijzen & de Jager (1990), which is a parametrized version of that by de Jager et al. (1988). The latter has been shown by Mauron & Josselin (2011) to be still applicable in the light of new observations of red supergiants. A metallicity-dependence of the wind is implemented as $\dot{M} \sim Z^{0.85}$ according to Vink et al. (2001). Thus, the mass-loss recipe we use:

$$\log \frac{\dot{M}}{M_\odot {\rm yr}^{-1}} = 1.42 \log(L/L_\odot) + 0.16 \log(M/M_\odot)$$
$$+ 0.81 \log(R/R_\odot) - 15 \log(9.6310)$$
$$+ 0.85 \log(Z_{\rm ini}/Z_\odot) \qquad (1)$$

This formula is in accordance with the results of Mauron & Josselin (2011) who find that the metallicity exponent should be between 0.5 and 1. However, it is important to note that this prescription is based on red SG stars with masses between 8–25 $M_\odot$. Since there is no mass-loss rate observed for SG stars with masses of 150–600 $M_\odot$, we extrapolate Eq. (1) up

to these masses, pointing out that this approach involves large uncertainties.

Figure 3 shows the Hertzsprung–Russell diagram of three evolutionary models that become core-hydrogen-burning SG stars towards the end of their main-sequence evolution. The models were taken from Szécsi et al. (2015b), except for the most massive one ($M_{ini} = 575$ $M_\odot$) which was computed for this work. Our simulation of the model with $M_{ini} = 575$ $M_\odot$ was carried out until the central helium mass-fraction was 0.81, that is, before the end of core hydrogen-burning. We estimate that until core-hydrogen exhaustion, this model needs about 0.28 Myr of further evolution, thus the total time it spends as a core-hydrogen-burning cool SG is 0.37 Myr. Based on its main-sequence lifetime of 1.56 Myr and the general trend that massive stars spend 90% of their total life on the main-sequence and 10% on the post-main-sequence, we expect a post-main-sequence lifetime of ∼0.17 Myr. The mass loss in the SG phase can be as high as 10^{-3} $M_\odot$ yr^{-1}. It is expected that with this high mass-loss, the model loses its whole envelope during its post-main-sequence lifetime. But even if all its hydrogen-rich layers are lost, it will stay cool. According to Köhler et al. (2015, their Fig. 19) the zero-age main-sequence (ZAMS) of pure helium-stars bends towards that of hydrogen-rich stars, crossing it over at ∼300 $M_\odot$ in the case of models with subsolar (SMC and LMC) composition. Although the exact mass where the crossover of the two ZAMS-lines happens at our sub-SMC metallicity needs to be investigated in the future, the model with $M_{ini} = 575$ $M_\odot$ (and a total mass of 491 $M_\odot$ at the end of our simulation) is most probably above it. Therefore, we do not expect this model to become a hot Wolf–Rayet star after its envelope is lost, but instead to stay cool, and become a helium-rich SG during the remaining evolution.

The model with $M_{ini} = 257$ $M_\odot$ from Szécsi et al. (2015b) was followed during its post-main-sequence evolution. Our simulation stops when the central helium mass fraction has decreased to 0.73 during core *helium*-burning. The model spends 0.26 Myr as a core-hydrogen-burning cool SG (with a radius of ∼5000 $R_\odot$ ∼3.5 · 10^{14} cm), and is expected to spend a total of ∼0.25 Myr as a core-helium-burning object. The mass-loss rate is $2.9 \cdot 10^{-4}$ $M_\odot$ yr^{-1} (i.e. −3.5 on a logarithmic scale) in the last computed model. Supposing that this mass-loss rate stays constant until the end of its post-main-sequence lifetime, this model will end up having only 140 $M_\odot$. It remains an open question if this model, having lost its hydrogen-rich envelope, would stay cool or would become a hot Wolf–Rayet star. To decide, one would need either to follow the rest of its evolution, or to establish a mass-limit where the helium-ZAMS and the hydrogen-ZAMS cross. Since these tasks would require improvements of the code and creating a dense grid of high-mass models, they fall outside of the scope of current work. However, given all the uncertainties concerning the mass-loss rates of actual supergiant stars at this mass, it may be that the model never even loses its envelope because the real mass-loss rate is lower than assumed here.

The model with $M_{ini} = 150$ $M_\odot$ has finished core-helium-burning in our simulation. It spends 0.07 Myr as a core-hydrogen-burning cool SG (during which time its surface does not become cooler than 19 000 K; its largest radius is 182 $R_\odot$) and another 0.30 Myr as a core-*helium*-burning red supergiant (with a surface temperature of ∼4250 K and a radius of ∼4000 $R_\odot$). It has a final mass of 118 $M_\odot$, and the mass-loss rate in the last computed model is $8.0 \cdot 10^{-5}$ $M_\odot$ yr^{-1}. Since core-helium-burning is finished in this model, we know its final surface temperature, as well as its envelope composition: it is

a red supergiant at the end of its life, and it has an envelope of about 25 $M_\odot$ which is composed of 49.02% hydrogen, 50.96% helium, and 0.02% metals. Thus, we know for sure that it stays cool until the end of its life, whereas we could not be sure for the two more massive models discussed above. Moreover, we find no helium-burning side-products at its surface. The reason for this is that the size of the convective core during helium-burning is smaller than that during hydrogen-burning, and the convective envelope of the red supergiant never reaches the layers of the helium-burning. It only mixes the ashes from core-hydrogen-burning and, during the post-main-sequence phase, shell-hydrogen-burning to the surface. As the observed composition of GC stars show no traces of helium-burning products either, we suggest that this SG model, having finished its post-main-sequence evolution while ejecting about 30 $M_\odot$ of material polluted with hot-hydrogen-burning products, is a potential source of the pollution in the young GCs.

2.2. Composition of the SG wind

Core-hydrogen-burning cool SGs have a convective envelope that mixes the hydrogen-burning products from the interior to the surface. The strong stellar wind then removes the surface layers. To calculate the composition of the ejecta, we need to sum over the surface composition of the evolutionary models. Figure 4 shows the surface Na abundance as a function of the surface O abundance of the three models presented above (in Fig. 3). During their SG phase, the surface composition of our models cover the area where the most extremely polluted population of GC stars are found. This means that if low-mass stars form from the material lost by the SG directly (i.e. without mixing the ejecta with pristine gas), this second generation of low-mass stars would be observed as part of the extremely polluted population (cf. Sect. 3.5). In case, however, if the material lost via the slow SG wind is mixed with non-polluted gas, the second generation of low-mass stars could possibly reflect the composition of the so-called intermediate population (i.e. those stars that show some traces of pollution, compared to a not-polluted, primordial population, as explained by Da Costa et al. 2013).

Since the mass-loss rates of our models are uncertain, it is worth investigating how a higher mass-loss rate would influence the ejecta composition. Therefore, we also plotted the composition of the envelope in the last model in Fig. 4. With a higher mass-loss rate (or, in the case of the two most massive models, during the remaining evolutionary time), deeper layers could be lost in the wind, contributing to the extremely polluted generation with very low [O/Fe] (<−1) and very high [Na/Fe] (∼0.7). Deep inside the envelope, the Na abundance drops suddenly because the high temperature ($\gtrsim 0.8 \cdot 10^8$ K) destroys the Na.

The Mg-Al surface abundances of our models are shown in Fig. 5. The surface Mg and Al abundances cover only a small fraction of all the observed variations in these elements. However, losing deeper layers of the envelope could explain the whole observed ranges of Mg and Al variations. When it comes to Mg, it is not only the sum of all three Mg-isotopes that is measured, but the ratios of them as well (Yong et al. 2003, 2006; Da Costa et al. 2013). Figure 6 shows the observed isotopic ratios of Mg as a function of the Al-abundance. As mentioned above, our models can reproduce the most extreme Al-abundance values observed in the case where deeper layers of the models are lost. In these deep layers, the Mg-isotopes also follow the observed trend: ^{24}Mg is decreasing, ^{25}Mg is slightly decreasing, and ^{26}Mg is considerably increasing compared to their values at the surface.
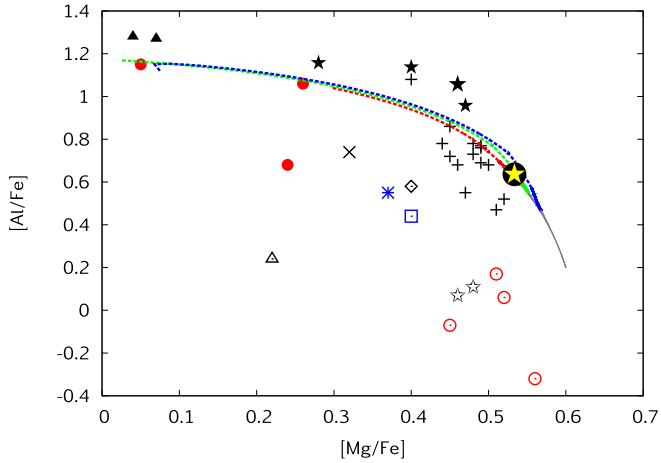
Fig. 5. The same as Fig. 4 but for Mg and Al.

Due to the high core temperatures, the Mg-Al chain is very effective in our cool SG models. This is a clear advantage of our scenario: for example, neither the fast rotating star scenario nor the massive binary scenario can reach the required spread in Al and Mg, or reproduce the extreme ratios of the Mg-isotopes, unless the reaction rate of the Mg-Al chain is artificially increased (Decressin et al. 2007; de Mink et al. 2009).

From the comparison of our models' composition with the observed light-element abundances, we conclude that cool SG stars are promising candidates for the astrophysical source that pollutes the second generation of GC stars. Their strong, slow winds can enrich the interstellar material of the cluster with hot-hydrogen-burning products; the light-element abundances in their envelopes correspond to the most extreme pollution observed. If the stellar wind mixes with the pristine gas of the cluster (as assumed for all other scenarios, such as the asymptotic giant branch star, the fast rotating star and the massive binary scenarios, Bastian et al. 2015), this mixture can form stars with all of the observed abundance spreads. Thus, cool SGs should be considered as potential contributors of the general pollution of GCs.

However, here we discuss our cool SG models' role not in the general pollution of the interstellar medium of GCs, but in the context of another star-forming process: low-mass star formation in a photoionization-confined shell around the cool SGs. To predict the composition of the SG-ejecta and thus the composition of the second generation of low-mass stars, we need to sum over the surface composition of the SG evolutionary models. We come back to this issue in Sect. 3.5. In the following, we introduce the concept of the star-forming SG shell.

3. Starformation in the shell

3.1. Conditions in young GCs

Apart from the core-hydrogen-burning cool SGs, another important prediction by Szécsi et al. (2015b) is that the fast rotating massive stars become hot, compact and bright for their whole lifetime. These objects, called Transparent Wind UV-Intense (TWUIN) stars, have similar surface properties to those of Wolf–Rayet stars, but differ in that their stellar winds are optically thin (see also Szécsi et al. 2015a; Szécsi 2017b, for further discussions of these objects). TWUIN stars produce a huge amount of ionizing radiation during their lifetimes. According to Szécsi et al. (2015b), TWUIN stars have a Lyman-continuum luminosity of

$Q_0 \approx 10^{50} - 10^{51}$ s^{-1}. A SG located 0.5 pc from such a star is therefore exposed to an ionizing photon flux, F_γ, between 3.3×10^{12} cm^{-2} s^{-1} and 3.3×10^{13} cm^{-2} s^{-1}. In a dense cluster it is possible for the separation to be even smaller, leading to potentially even more extreme irradiating fluxes.

Following Szécsi et al. (2015b), we suppose that ∼20% of all massive stars rotate faster than required for quasi-homogeneous evolution, that is, TWUIN-star formation (This ratio is supported by the rotational velocity distribution of massive stars in the Small Magellanic Cloud observed by Mokiem et al. 2006). Thus, we have a population of massive stars in a young globular cluster where ∼80% of stars evolve towards the supergiant branch while ∼20% stay hot and emit ionizing radiation.

Supposing that the ionizing-radiation field of the TWUIN stars is isotropic, the wind structure of the SG stars changes significantly: their winds are photoionized from the outside in. At the interface between ionized and neutral material, a dense, spherical shell developes, if the wind is sufficiently slow. This region is called the photoionization-confined shell.

3.2. Photoionizaton-confined shells around cool SGs

Mackey et al. (2014) developed the photoionization-confined shell model to explain the static shell observed around Betelgeuse, a nearby red SG star. According to their calculations, pressure from the photoionized wind generates a standing shock in the neutral part of the wind and forms an almost static, photoionization-confined shell. The shell traps up to 35% of all mass lost during the red SG phase, confining this gas close to the central object until its final supernova explosion.

We carried out simulations of a shell around a low-Z very massive SG star that undergoes core hydrogen burning. We use the PION code with spherical symmetry (Mackey 2012) to simulate an evolving stellar wind that is photoionized by external radiation. The source of the ionizing radiation are the fast-rotating TWUIN stars, creating an isotopic radiation field that surrounds the SG star. The simulations follow Mackey et al. (2014) except that we include stellar evolution and we use non-equilibrium heating and cooling rates for the gas thermal physics (as in Mackey et al. 2015). The stellar wind flows through the inner boundary of the grid with properties taken from the model with $M_{\rm ini} = 257\ M_\odot$ of Szécsi et al. (2015b, also see Sect. 2.1). This evolutionary model has an initial rotational velocity of 100 km s^{-1} and mass loss in the SG phase of about $10^{-3.5}\ M_\odot$ yr^{-1}.

The wind is initially cold (200 K; this has no effect on the results because the wind is highly supersonic). The wind velocity is calculated from the escape velocity following Eldridge et al. (2006), except that we set the SG wind velocity to be $v_\infty = 0.1 v_{\rm esc}$ for $T_{\rm eff} < 4500$ K. The above modification gives a minimum value of $v_\infty \approx 12$ km s^{-1}. The simulations are run with a total metallicity of 0.0002 and surface abundance mass fractions $X = 0.5$ and $Y = 0.4998$, similar to the surface abundances in the low-Z stellar model (Szécsi et al. 2015b). The wind is exposed to an ionizing photon flux of $F_\gamma = 10^{13}$ cm^{-2} s^{-1} (cf. Sect. 3.1) in the calculations presented here.

The formation of the shell in the simulation depends on the thermal physics of the shocked wind (which must be able to cool into a dense and cold layer); this is rather uncertain because we have no constraints on dust formation in such low-metallicity SGs. We use atomic line cooling (Wolfire et al. 2003) as implemented in Mackey et al. (2013), scaled to the metallicity of the stellar wind.
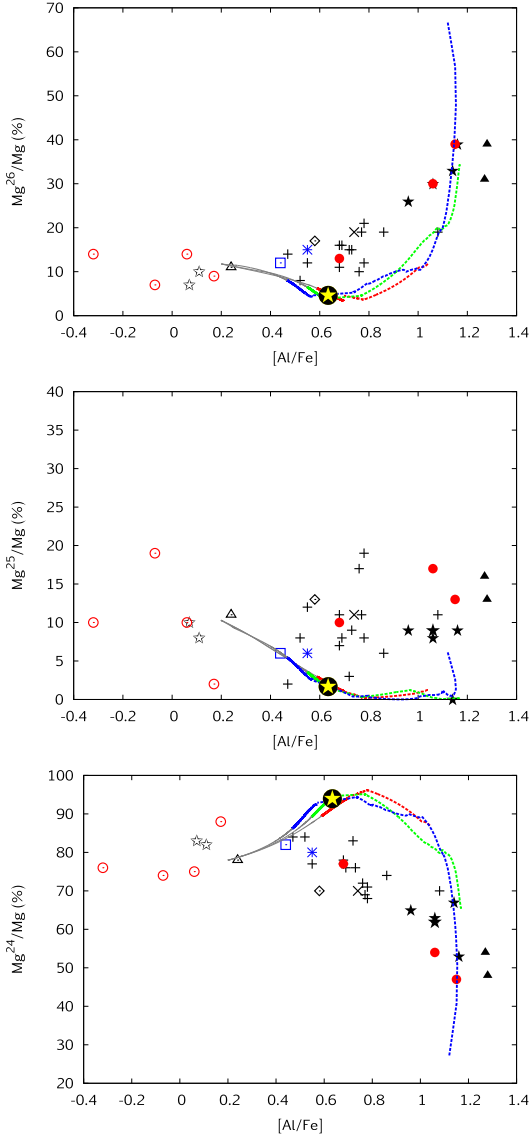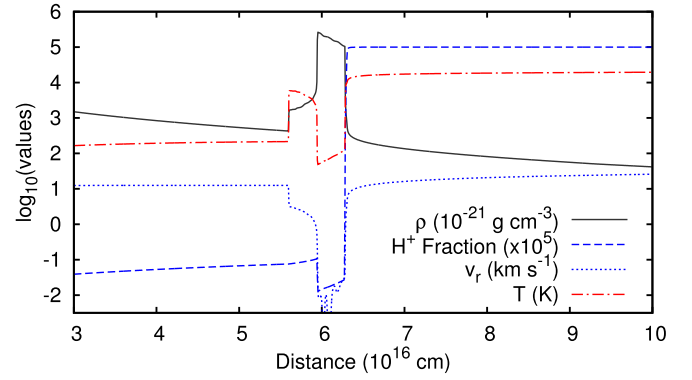
Fig. 7. Density, temperature, velocity, and ionization fraction for the simulation of the photoionizaton-confined shell around a core hydrogen burning supergiant with initial mass of 257 $M_\odot$. The snapshot is taken at the end of the stellar evolution calculation, when the star has an age of 1.88 Myr, at which time the shell mass is 14 $M_\odot$.

3.3. Gravitational instability in the shell

For the second generation of low mass stars to form in the photoionization-confined shell, the shell should be gravitationally unstable. To show that the shell in our simulation is indeed gravitationally unstable against perturbations, we follow Elmegreen (1998, see their Eqs. (2.12)–(2.14)) who describes the stability of a shocked sheet of gas (see also Doroshkevich et al. 1980; Vishniac 1983). The dispersion relation (Eq. (2.13)) gives the condition that perturbations with wavelength λ are unstable ($\omega^2 > 0$) if

$$\lambda \geq \frac{c^2}{G\sigma} = \frac{P}{G\sigma\rho} \tag{2}$$

where c is the isothermal sound speed defined by $c^2 \equiv P/\rho$ (P being the thermal pressure and ρ the density), and σ is the column density through the shell. This condition needs to be fulfilled by the shell in order to become gravitationally unstable. We define $\lambda_{\min}$ to be the wavelength at which this inequality is an equality.

In our simulation, the shell thickness is $l = 0.36 \times 10^{16}$ cm, density is $\rho = 2.65 \times 10^{-16}$ g cm^{-3}, and pressure is $P = 5.89 \times 10^{-7}$ dyne cm^{-2}. For this shell, the above condition gives a perturbation wavelength $\lambda_{\min} = 3.4 \times 10^{16}$ cm.

An overdense region should have a diameter of $\lambda/2$. For our spherical shells, we should restrict $\lambda/2$ to be significantly less than the radius of curvature, so that the unstable part of the shell looks more like a flat sheet than a sphere. The shell is at radius $\sim 6.2 \times 10^{16}$ cm (0.02 pc). The angular size of the overdense region is thus $\lambda_{\min}/2R_{\rm sh} = 1.7/6/2 \approx 0.3$ which is much less than one radian (about 16°), so curvature effects are relatively small. Figure 8 shows that $\lambda_{\min}/2R_{\rm sh} \approx 0.33$ at the end of the simulation, similar to the estimate above.

The Bonnor-Ebert mass for this dense region is

$$M_{\rm BE} = 1.18 \frac{c^4}{P^{1/2}G^{3/2}} = 0.2 \ M_\odot, \tag{3}$$

meaning that if the dense region contains more mass than this, it would collapse to a protostar. The mass of the dense region depends on its geometry, but with a density of $\rho = 2.65 \times 10^{-16}$ g cm^{-3} and a length scale of $\lambda/2 \approx 1.7 \times 10^{16}$ cm, it is around 2–3 $M_\odot$. We see from Fig. 8 that the shell contains a mass $M_{\rm sh} \approx 50 M_{\rm BE}$ at the end of the simulation.

Fig. 6. The same as Fig. 5 but for the isotopes of Mg.

Figure 7 shows the structure of the shell. The shell formed at a radius $r \approx 0.02$ pc (6×10^{16} cm) from the supergiant (recall that the radius of the stellar model itself is 3.4×10^{14} cm, see Sect. 2.1) and shows the classic structure of a radiative shock: (i) an initial density jump at the shock of a factor of approximately four with associated jumps in temperature and velocity according to the Rankine–Hugoniot jump conditions; (ii) a cooling region where the temperature decreases with r, the density increases, and the velocity decreases; and (iii) a cold dense layer. The cold layer is bounded on the outside by the ionization front, at which radius the stellar wind is heated to $\approx 12\,000$ K. A thermally driven wind accelerates outwards from the ionization front. We find that at the metallicity of the SG, the atomic cooling simulation produces a shell with density $\rho \approx 2 \times 10^{-16}$ g cm^{-3} and temperature $T \approx 50$ K.

The shell mass, $M_{\rm shell}$, is plotted as a function of time in Fig. 8. It grows to $M_{\rm shell} \approx 14\ M_\odot$ by the end of the simulation. The Bonner-Ebert mass (i.e. the mass limit of the overdense region, above which the material collapses into a proto-star), $M_{\rm BE}$, and the minimum unstable wavelength $\lambda_{\min}$ are also plotted in Fig. 8. They are discussed in the next section.
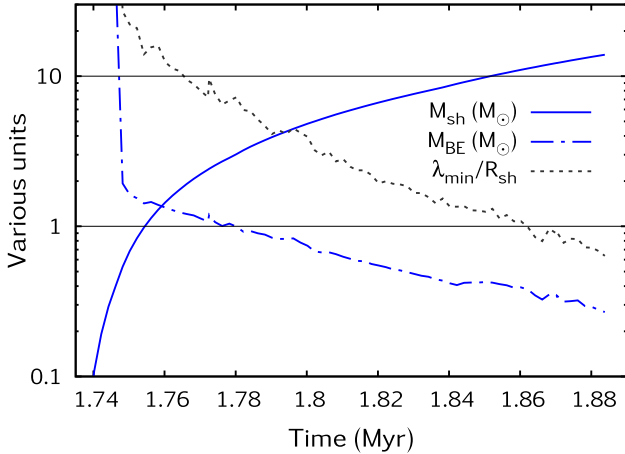
Fig. 8. Shell mass, M_{sh}, as a function of time since the star's birth (solid blue line), compared to the Bonner-Ebert mass M_{BE} at the densest point in the shell (dot-dashed blue line). The dashed black line shows the minimum unstable wavelength in units of the shell radius.

The stability analysis shows that the shell does not become unstable until it contains $\geq 20\,M_{BE}$ because the mass is distributed in a shell and not in a spherical cloud. We conclude therefore, that the thermodynamic conditions in the shell allow for gravitational instability, and that potentially many low mass stars may form from a single shell.

3.4. Forming the second generation of stars in the shell

Even if gravitational instabilities develop in the shell, the proto-stars should have been formed before the shell evaporates. This means that the growth timescale of the perturbation should be less than a few times 10^5 years (cf. lifetimes of SG stars in our simulation, Sect. 2.1). Using Eqs. (2.12) and (2.14) from Elmegreen (1998), we get 3100 and 2.2×10^4 years, respectively. These timescales are indeed significantly shorter than the life of the SG star with shell.

Once gravitational instability sets in, the collapse timescale is very short because the shell already has a very high density, much larger than dense cores in molecular clouds (Tóth & Kiss 2007; Tóth et al. 2014). Three-dimensional simulations are required to follow the gravitational collapse, so we cannot predict the final masses of the stars that will form. They may be larger than M_{BE} because the shell is constantly replenished from the cool SG's mass-loss, and this could accrete onto collapsing cores.

It is highly unlikely, however, that this star-formation channel would have a typical initial mass function. It will rather be dominated by stars with less than one solar mass, and the probability of forming massive stars is expected to be extremely small. On the other hand, we also do not expect very low-mass stars since our simulation predicts a typical mass of $0.2\,M_{\odot}$ for proto-stars, and they are probably still accreting.

Star formation could be a bursty process if gravitational instability sets in at the same time everywhere in the shell (i.e. if the shell is homogeneous), or more continuous if the shell is asymmetric and/or clumpy. In either case, star formation does not destroy the shell, but rather makes space for further gas accumulation and subsequent collapse to form more stars. After the shell begins to collapse, its gaseous mass (excluding protostars) is determined by the addition of new material from the stellar wind of the cool SG, balanced by the collapse of shell material to form new stars, plus accretion of shell material onto existing

protostars. The addition of new material is about 35% of the cool SG's mass-loss rate, so $\sim 10^{-4}\,M_{\odot}\,yr^{-1}$. Accretion rates onto low-mass protostars are typically $10^{-7}\,M_{\odot}\,yr^{-1}$ (Hartmann & Kenyon 1996), and so this is unlikely to affect the shell mass because the shell can only form ≈ 10–50 protostars at any one time (recall, it becomes unstable when its mass is $\gtrsim 10\,M_{\odot}$). The reservoir of gas available to form new stars is therefore determined by the mass-loss rate of the cool SG and the rate at which new protostars are condensing out of the shell.

This means that star formation in the shell is expected to be a more or less continuous (but stochastic) process. After the shell has formed and grown to become unstable, some bits of it collapse at different times. But in the meantime, the shell-material is constantly replenished by the SG wind. Thus, an equilibrium develops between mass added to the shell and mass lost through star formation.

3.5. Composition of the stars in the shell

The low-mass stars formed in the shell necessarily reflect the composition of the SG wind which is polluted by hot-hydrogen-burning products. To compute the composition of the shell-stars, we assume that the wind that leaves the SG star goes directly into the shell, and that the material inside the shell is homogeneously mixed. We take into account that the shell only traps a certain amount of the wind-mass (as follows from the hydrodynamical simulations of its structure presented in Fig. 8), and thus sum over the wind composition.

Figures 4 and 5 show the composition of a star formed inside the shell simulated around the $M_{ini} = 257\,M_{\odot}$ supergiant. The abundances of Na and O of the shell-stars are compatible with the surface composition observed in the extremely polluted population. The abundances of Mg and Al of our shell stars are compatible with the intermediate population. To fit more extreme abundances of Mg and Al, deeper layers of the SG star should be lost (represented in Fig. 5). This could still happen during the post-main-sequence evolution of the SG model which would last for an additional 0.17 Myr (not simulated). The shell stars have a helium mass fraction of $Y_{sh} = 0.48$. We discuss the issue of the observed helium abundance of GC stars in Sect. 4.4.

4. Discussion
4.1. Mass budget

Any scenarios that aim to explain the abundance anomalies observed in GCs need to account for the mass that is contained in the first as well as in the second generation of stars. The three most popular of the polluter sources (asymptotic giant branch stars, fast rotating stars, massive binaries), when only one of them is taken into consideration, fail to explain the amount of stellar mass that we observe with polluted composition. These scenarios suppose that the polluted material stays inside the gravitational potential well of the cluster, preferably accumulating near the centre. There the polluted material mixes with the pristine material and forms the second stellar generation. This would explain why we observe not just the primordial and extreme abundances but everything in between (see the observations in Figs. 4 and 5). But for a second generation to be as numerous as the first generation, one needs much more polluted material than one of these sources can provide (de Mink et al. 2009). Therefore, it is possible that more then one pollution source is present, or even that all the suggested sources contribute (Bastian et al. 2013).

The mass budget constraint in its simplest form is the following: the second generation that is born inside the shell should contain as much (50:50) mass as the first generation of low-mass stars born normally (The ratio 50:50 is applicable for the GCs with average mass, but there is evidence that higher-mass clusters have a higher fraction of second generation stars, see Sect. 4.2).

4.1.1. Classical IMF

To investigate the mass budget of our starforming shell scenario, we follow the discussion of de Mink et al. (2009). Namely, we apply an initial mass function (IMF) between 0.1–1000 $M_\odot$ to represent the first generation of stars, as follows (Salpeter 1955; Kroupa 2001):

$$N(m) = \begin{cases} 0.29 \cdot m^{-1.3}, & \text{if } 0.1 < m < 0.5 \\ 0.14 \cdot m^{-2.3}, & \text{if } 0.5 < m < 1000. \end{cases} \quad (4)$$

We take the low-mass stars in the first, unpolluted generation to be between 0.1–0.8 $M_\odot$, that is, the mass of stars observed in GCs today (see de Mink et al. 2009). As for the shell-forming SGs in the first generation, we argue that our models are representative for them in the mass range of 80–1000 $M_\odot$. This argument is justified because (1) mass-loss rates in this mass range are high enough for massive shells to form (cf. Sect. 4.3) and because (2) models in this mass range are expected to become core-hydrogen-burning SG stars (cf. Sect. 2.1). Additionally, we assume here that the second generation of shell-stars also form between 0.1–0.8 $M_\odot$, following the mass-distribution of the unpolluted first generation of low-mass stars. We discuss the consequences of *not* assuming this in Sect. 4.7.

Equation (4) predicts that the first generation of low-mass stars represent 35% of the total stellar mass initially present in the cluster. Thus to fulfil the mass budget constraint, the second generation should also account for the same, 35% of the total mass. Unfortunately, the mass of the SG stars represent only 10% of the total. If it would be lost through the wind and incorporated into the second generation in the shell with an efficiency of $\xi = 100\%$ (which is clearly a very weak constraint not only because it would require an unreasonably high mass-loss rate but also because we expect ~20% of all massive stars to be hot TWUIN stars, see Sect. 3.1), this is still far from the 35% we aim to account for.

4.1.2. Top-heavy IMF

One simple way around this issue is to assume a top-heavy IMF, which has indeed been favoured for massive clusters recently (Ciardi et al. 2003; Dabringhausen et al. 2009). For example, Decressin et al. (2010) suggests a flat IMF with index -1.55 (instead of -2.3 as in Eq. (4)) to make their fast rotating star scenario work. Our SG shell scenario, however, can work with less extreme values. Assuming that the massive component of the IMF has an index of -2.07 (instead of -2.3), the first generation low-mass stars (0.1–0.8 $M_\odot$) represent 23% of the stellar mass initially present in the cluster, while the SG stars (80–1000 $M_\odot$) also represent 23%, satisfying the weak constraint mentioned at the end of Sect. 4.1.1.

A strong constraint should take into account: (1) only ~40% of the SG mass is lost in the wind; (2) the shell contains only ~35% of the wind mass; and (3) only ~80% of massive stars evolve towards the supergiant branch (the rest are the TWUIN stars responsible for the ionization). Thus, the mass contained in SG stars will be converted into low-mass stars with an efficiency

of $\xi \approx 40\% \times 35\% \times 80\% \approx 12\%$. With this efficiency, an IMF index of -1.71 is needed, which translates to 7% of the total mass in first generation low-mass stars (i.e. 0.1–0.8 $M_\odot$), and 55% of the total mass in massive stars (i.e. 80–1000 $M_\odot$). The mass budget problem is then solved because from this 55%, only $55\% \times \xi \approx 7\%$ will be converted into the second generation of low-mass stars.

However, we may not need this strong constraint, since the ratio of the material trapped in the SG shell should be higher than 35%, which is the nominal value in our simulation. Thus the efficiency, ξ, of converting SG mass into shell-stars may be significantly higher than 12%. The reason for this is that, according to the speculation at the end of Sect. 3.3, the shell may retain more wind material than the nominal value since the proto-stars are constantly accreting. Since accretion is not included into our shell-simulation, we cannot properly quantify that at this point. Nonetheless, the weak and the strong constraints presented above correspond to IMF indices of -2.07 and -1.71, respectively, so we conclude that the index required for our scenario to work should be somewhere between these two values.

4.1.3. On the number of stars in the cluster and in the shell

We give an order of magnitude estimate of the number of stars present in a typical GC where SG shells are forming the second generation. To do this, we assume an average GC with total mass of 10^5 $M_\odot$ and with an IMF index -1.71. This IMF allocates 7% of the total mass into first generation stars between 0.1–0.8 $M_\odot$, and 55% into SG stars between 80–1000 $M_\odot$ (while the rest has no mass-contribution to this particular scenario). The mass of stars in the second generation (i.e. formed from shells around SGs) also represents 7%.

We take 257 $M_\odot$ to be the representative mass for the massive regime (that is, the initial mass of the SG model around which our simulation was carried out); and we take 0.2 $M_\odot$ to be the representative average mass for both the first generation low-mass stars and the second generation of shell-stars. This value, 0.2 $M_\odot$, is the Bonnor-Ebert mass of the objects in our simulation presented in Sect. 3.3, so it may depend on the mass and geometry of the shell and, therefore, on the mass of the SG.

With these assumptions, the first generation of low-mass stars consist of 35 000 stars, and so does the second generation. Besides, the first generation must have contained 214 stars in the massive regime. From these, 171 should evolve to be supergiants and have shells, and 43 should be hot TWUIN stars. Note however that there are much more ionizing sources than that, since fast rotating models in the mass range of 9–80 $M_\odot$ also predict TWUIN stars (Szécsi et al. 2015b).

To form 35 000 second-generation stars, all 171 supergiants have to form ~200 low-mass stars of 0.2 $M_\odot$ out of its wind material. One may recall from Sect. 3.3 that the structure of our simulated shell facilitates the formation of only 50 protostars of this mass at any given time, and that the protostars condensing out of the shell make space for further gas accumulation and subsequent collapses. Thus, from the mass budget constraints it follows that the shell in our simulation should undergo around three to four subsequent events of gravitational collapse.

We say subsequent collapses, but we are not suggesting that the shell will form, then everywhere collapse into stars, then reform and re-collapse, and repeat again. What we suggest is that the shell will form, grow to become unstable, and then there will be stars forming out of cloud material all the time. We do not expect it to be an episodic process, but rather a continuous one, resulting in ~3–4 times 50 protostars at the end.

4.2. On very massive stars and very massive globular clusters

A crucial assumption of the star-forming-shell scenario is the presence of very massive stars in the young cluster. Very massive ($>100\ M_\odot$) stars are theorized to form either via accretion (i.e. the same process that creates lower mass stars) or collision (in extremely dense regions, Krumholz et al. 2014). Therefore, it is not unreasonable to hypothesize stars as massive as this born in the young GCs. For example, Denissenkov & Hartwick (2014) assumed stars with $10^4\ M_\odot$ to give a possible explanation for the GC abundance anomalies.

Statistically, to find very massive stars in a star-forming region in significant number, either the mass of the region has to be large or the IMF has to be very top-heavy – or both. In Sect. 4.1.3 we apply a top-heavy IMF of index −1.71 (coming from the strong constraint presented in Sect. 4.1) and an average GC mass of $10^5\ M_\odot$ (which results in 171 SGs of the nominal mass 257 $M_\odot$). However, some GCs are significantly more massive than that. For example, the mass of ω Cen is $4 \cdot 10^6\ M_\odot$.

It has been suggested that the fraction of enriched stars (and in general, the complexity of the multiple population phenomenon) correlates with cluster mass (Carretta et al. 2010; Piotto et al. 2015; Milone et al. 2017). To account for this, we computed the IMF index not only for a 50:50 ratio of second vs. first generation, but also for a 70:30 ratio (as in some high mass clusters) and a for a 90:10 ratio (as in the highest mass clusters such as e.g. NGC 2808). In the case of a 70:30 ratio, an IMF index of −1.6 is needed to fulfill the strong constraint in our starforming shell scenario; while in the case of a 90:10 ratio, −1.4 is needed. So we conclude that if – for some reason – the IMF gets more top-heavy with cluster mass, our scenario may work to explain even the most massive clusters. But this argument also applies to all other self-enrichment scenarios involving massive stars, so it is not a distinguishing feature of our scenario.

It is so far unclear if the same mechanism forms all Galactic GCs. There is evidence that the low-metallicity GCs in the outer halo have been accreted from neighbouring dwarf galaxies, while the high-metallicity GCs in the inner halo have been formed in situ (Brodie & Strader 2006; Forbes & Bridges 2010). Some of the most massive GCs, ω Cen amongst them, possibly used to be dwarf galaxies (Schiavon et al. 2017). In short, the formation of globular clusters is a complex problem that may require several theoretical scenarios to work together; our scenario may be one of them.

4.3. Supergiants at lower masses

We presented SG models with initial masses between 150–575 $M_\odot$, and considered them representative for the mass range of 80–1000 $M_\odot$ when talking about the mass budget in Sect. 4.1. The reasons for not including SG models with lower masses (9–80 $M_\odot$) into our analysis, are the following.

First, their mass-loss is too low to form shells around them. We recall from Sect. 2.1 that the model around which we simulated the shell, has a mass-loss rate of −3.5 [log $M_\odot$ yr^{-1}]. Our computations of SG models with 70, 43, and 26 $M_\odot$ show that they have mass-loss rates of −4.6, −5.2, and −5.9, respectively. The shells around them will not be massive enough for the second generation of stars to form: it takes a long time to build up a solar mass in the shell, let alone tens of solar masses, if $\log(\dot{M}) \sim -5$. The second problem is geometric. The shell will be closer to the star, and so have smaller volume and less physical space in which to grow.

We cannot exclude, however, that the wind material of these lower-mass SG stars will be expelled into the cluster. There, it might be able to cool later on and – possibly diluted with some pristine gas – make new stars. Since these lower-mass SG stars are more likely to form, and thus would dominate over the very massive stars even with a top-heavy IMF, it is an important question to investigate their contribution to the cluster's chemical evolution. A detailed analysis of this scenario will be performed in another work. Our preliminary results nonetheless show that models below 80 $M_\odot$ evolve to the SG branch only during their core-helium burning phase. Their surface Na&O composition reflects the primordial or intermediate population (as defined in Fig. 4), but not the extreme one. As for the Mg & Al anticorrelation, they show some minor variation only in Al, but no variation in Mg.

Recently, Schiavon et al. (2017) implied that, at a fixed metallicity, some GCs show variation in Mg and some not. In particular, they detected 23 giant stars in some high-Z and low-Z GCs (situated in the inner Galaxy), and found no clear anticorrelation between Al and Mg. Instead, they report a substantial spread in the abundance of Al and a smaller spread in Mg; while they also admit that the their sample is too small for this to be statistically significant. Nonetheless, this is an interesting finding from our point of view, especially when we talk about lower-mass SGs with <80 $M_\odot$. As we see only minor variation in Al and no variation in Mg, we speculate that – without quantifying their contribution at this point – the presence of SG stars with <80 $M_\odot$ in young clusters may help us to explain why some GCs show variation in Mg and some not.

4.4. Helium spread in different clusters

In some globular clusters, there are extremely helium-rich stars. For example, ~15% of the stars in NGC 2808 show helium abundance of $Y \sim 0.4$, as inferred from their multiple main sequences (Piotto et al. 2007; D'Antona & Ventura 2007), as well as from spectroscopic measurements (Marino et al. 2014). Other GCs, however, have less extreme helium variations (Bastian et al. 2015; Dotter et al. 2015).

The most extreme values cannot be reproduced by asymptotic giant branch stars (Karakas et al. 2006). All the other polluter sources (massive binaries, fast rotating stars, supermassive stars) have a general problem reproducing the required light element variations when the helium spread is a constraint, as shown by Bastian et al. (2015). The reason for this is that the Ne-Na and Mg-Al chains are side-processes of the CNO-cycle – therefore, together with their burning products a significant amount of helium must be produced as well.

Our simulated shell-stars behave the same way as other massive polluters. Their surface composition (represented by the black-yellow symbol in Figs. 4 and 5) contains helium: $Y_{\rm sh} = 0.48$. Therefore, they can also only explain the pollution in Na-O and Mg-Al together with a high helium abundance, similar to other scenarios that involve massive stars.

This issue is generic, as both the Ne-Na chain and the Mg-Al chain are side reactions of hot hydrogen-burning (Bastian et al. 2015; Lochhaas & Thompson 2017). Hydrogen burns into helium; therefore, whatever nuclear change occurs in the Na, O, Mg, and Al abundances due to these chains, it will be accompanied by a change in helium abundance, unless we find a mechanism that separates Na, O, Mg, and Al from helium either inside the star or in the interstellar material.

4.5. Dynamical interactions

4.5.1. Collisions of cluster members and shell

Here we discuss issues about collisions of a random cluster star with a shell around a SG: how often may these collisions happen, and what consequences they may have.

Globular clusters have central densities $\gtrsim 10^3\ M_\odot\ pc^{-3}$ and typical stellar mass $0.8\ M_\odot$ (Portegies Zwart et al. 2010) corresponding to a number density, $n_\star \gtrsim 10^3\ pc^{-3}$. They also have internal velocity dispersion, $\sigma_v \approx 1$–$10\ km\ s^{-1}$ (Harris 1996). The collision time, t_{coll}, of one of their stars with a shell around a SG, with shell radius $R_{sh} \approx 0.02\ pc$, can be derived from Eq. (26) of Portegies Zwart et al. (2010) as follows:

$$t_{coll} \approx 0.16\ Myr \left(\frac{n_\star}{10^3\ pc^{-3}}\right)^{-1} \left(\frac{\sigma_v}{5\ km\ s^{-1}}\right)^{-1} \left(\frac{R_{sh}}{0.02\ pc}\right)^{-2}. \quad (5)$$

According to this simple, order-of-magnitude estimate, on the order of one star will pass through the cool SG shell during its existence (it lasts $\sim 10^5$ years).

However, central densities of *young* GCs might have been higher than assumed in Eq. (5). One argument for this is that YMCs, thought to be analogous to young GCs, have central densities much higher than observed today in GCs. A well-known example of a resolved YMC is the Arches cluster with central density of $10^5\ M_\odot\ pc^{-3}$ (Portegies Zwart et al. 2010). Another argument is that the mass may be segregated (i.e. stars with masses greater than a given value are found to be more centrally concentrated than the average stellar mass) leading to a higher central density. Additionally, gravitational focusing (i.e. enhanced probability that two stars will collide due to their mutual gravitational attraction) may play a role.

If the central stellar density is higher than assumed in Eq. (5), this means two things. First, this would lead to more (potentially destructive) collisions. In such a dense environment as the Arches cluster, the estimated collision time is two orders of magnitudes higher than in Eq. (5). Second, the ionizing sources would be closer to the SGs if the central density is higher. Thus, the ionizing flux would be larger and the shells would be more compact. This would decrease the probability of a collision, balancing the first effect.

Whether the interaction with a star of low-mass would enhance or inhibit star formation in the SG shell is not clear, and would require complex simulations to model accurately. If, on the other hand, the star were massive with a strong wind and large Lyman-continuum luminosity, then it would have a strong disruptive effect on the shell. This may be happening to the wind of the red supergiant W26 in Westerlund 1 (Mackey et al. 2015). The probability of a massive star passing through a cool SG shell is small, however, because even the top-heavy mass function prefers low-mass objects (cf. the discussion on the number of stars in Sect. 4.1).

Finally, we point out that even if the shells are destroyed by collision, their material may sink into the cluster core. It is possible that, independently of the formation of SG shells, the material in the cluster core is constantly forming stars, as supposed by many other scenarios (cf. Bastian et al. 2015). Our supergiants are therefore expected, even with their shells destroyed, to contribute to the chemical evolution of the young cluster by expelling polluted gas into the intracluster medium.

4.5.2. The probability of falling into the SG

Once the second generation of stars form in the shell, they are no longer subject to the radiation pressure from the central SG.

The radial velocity of the shell-stars is therefore quite small. But it is not zero. In Galactic star formation, the clouds and the dense cores have velocity dispersions larger than the sound speed, attributed to supersonic turbulence (Mac Low & Klessen 2004). The shell around the SG will be the same, and so we expect that the dense cores that collapse to form stars will have non-radial velocities that are at least comparable to the local sound speed, and probably larger.

While detailed star-formation simulations and N-body dynamics calculations would be required to address this problem, we can present a simple estimation here to demonstrate our point. For T = 70 K, the sound speed is about $0.6\ km\ s^{-1}$. For a 250 $M_\odot$ supergiant, and a shell at 6.0×10^{16} cm from the star, the escape velocity is $3.3\ km\ s^{-1}$ and the circular velocity is $2.4\ km\ s^{-1}$. This means that the random non-radial motions are, on average, >25% of the circular orbital velocity, and so the shell stars will be on elliptical orbits.

The probability of actually falling into the supergiant is thus very small when simply considering orbits. It is not obvious whether N-body interactions between the many protostars in the shell would eject stars into the cluster and/or increase the likelihood of collision with the central supergiant, and we cannot make predictions at this stage.

4.6. On high-metallicity clusters and future plans

Our work focuses on low-metallicity since the majority of GCs with abundance anomalies are between [Fe/H] = −2.0 and −1.0. We suspect that our model of star-formation in shells will hardly work at high-metallicity. As shown by the models of Brott et al. (2011) and Köhler et al. (2015), massive stars with LMC metallicity do indeed experience envelope inflation above 40 $M_\odot$. However, the very massive ones ($\gtrsim 150\ M_\odot$) do not become cool supergiants because their mass-loss is very high and so they become hot Wolf–Rayet stars instead. We do not expect shells to form around these hot stars. As for the LMC models between 40–150 $M_\odot$, they do evolve to the supergiants branch. So they may form shells, although it is beyond the scope of the present work to simulate such a shell and analyse its stability.

The fact that multiple populations have not been found in nearby super star clusters to date (Mucciarelli et al. 2014) may mean, in the context of our scenario, that either (1) SG shells are not stable at high-metallicity, or (2) they do not create (too many) new stars, or even (3) that the composition of the new stars is indistinguishable from that of the old ones. Indeed, our preliminary investigation of the LMC models shows that they have lower core temperatures than their low-Z counterparts, and so the Mg-Al chain is not effective in them. Thus, even if the second generation is formed in a high-metallicity cluster, we do not expect them to show significant Mg/Al variations. As for the other elements, the variations of Na/O in the winds of the LMC models are present, but more moderate than in our low-metallicity models.

On the other hand, some of the higher-metallicity GCs also have multiple populations (as observed by e.g. Schiavon et al. 2017). This however does not mean that the same scenario produces the multiple populations at all metallicities. As mentioned in Sect. 4.2, we do not expect that the complex problem of GC formation would be solved by one simple scenario. Indeed, both our low-Z models and the LMC models can be applied in another scenario, in which the mass lost in winds from massive stars can later cool in the cluster core and form new stars (cf. Sect. 4.3).

Detailed investigation of both sets of models and their wind composition, as well as the possible ways their strong wind may

influence the chemical and hydrodynamical evolution of their clusters, are planned in the future.

Indeed, the metallicity-dependence of our scenario, along with that of other scenarios in the literature, should be investigated. Some observations (such as the compilation of photometric results from the HST UV survey by Milone et al. 2017, which is mainly tracing N-abundance variations) imply that there is no clear relation between the fraction of stars in each population and the metallicity of the host cluster. From the modelling point of view, we can say the following about metallicities between our models and the LMC models. Sanyal et al. (2017) showed that we can expect core-hydrogen-burning SG stars with the composition of the Small Magellanic Cloud (SMC) with luminosities above $10^6 \, L_\odot$. Thus, those GCs that have well-studied multiple populations near SMC metallicity (e.g. 47 Tuc or M71 with [Fe/H] ~ -0.7) may be explained with our scenario too. The fact that we currently do not see any luminous SG stars in the SMC is not surprizing, given the IMF, short lifetime of these stars, and low starformation rate in the SMC.

4.7. Proposing another solution for the mass budget: a non-classical IMF for the second generation

Discussing the mass budget in Sect. 4.1 and after, we assumed that the mass-distribution of the shell-stars is the same as that of the first generation of low-mass stars between 0.1–0.8 $M_\odot$, and showed that we need a top-heavy IMF for our shell-scenario to work under this assumption. We did this because it helps to compare our scenario to others, such as the fast rotating stars or the massive binary polluters. However, there is another way around the mass budget problem – one that is unique to our scenario.

Observationally, it is not excluded that all GC stars with $M < 0.6 M_\odot$ are first generation stars (the abundances are always determined near the turn-off, i.e. at 0.8 $M_\odot$). Other scenarios usually do not account for this, as this would make their mass budget solution even more speculative. Indeed, if star formation happens out of the interstellar material in the cluster centre, it is already hard to justify why the second generation only harbours stars below 0.8 $M_\odot$ and nothing above (as done, for example, in de Mink et al. 2009). It would be even more difficult to explain why the IMF would be truncated at both the high and the low ends. Or why, for that matter, the form of the distribution would not follow the classical power-law observed everywhere in the Universe.

In our shell-scenario however, the mode of star formation is so unusual that the IMF must be quite irregular. Apart from massive stars being justifiably excluded on quite robust grounds, it is not clear whether or not the minimum mass could be even larger than the Bonnor-Ebert mass (0.2 $M_\odot$, as quoted in Eq. (3)). After all, the proto-stars may be still accreting some more mass from the shell.

So for us, it is fathomable to account for a first generation well above 0.2 $M_\odot$, the lower limit depending on the accretion rates of the proto-stars. As an example, if the range to account for was only between 0.6–0.8 $M_\odot$, then the stars represent 7% of the total cluster mass (following the classical IMF in Eq. (4)). SGs represent 10%, but their material is inserted into the second generation of shell-stars with an ill-established efficiency ξ. This efficiency was taken to be 100% in the weak case in Sect. 4.1.1 and 12% in the strong case in Sect. 4.1.2, but we expect its realistic value to be somewhere between. Supposing for example that $\xi = 70\%$, the mass budget is solved with having a first generation as numerous (50:50) as the second generation

(10% $\times \xi$ = 7%). (With ξ =100%, we get a 60:40 ratio of first vs. second generation, cf. Sect. 4.2.)

Furthermore, we have no reason to suppose that the form of the mass distribution of the second generation is identical to that of the first generation. It certainly needs further investigations (possibly, 3D simulations of star formation in a spherical shell) to know more about its supposed mathematical form, but in the most optimistic case where all second generation stars form with 0.6 $M_\odot$, the efficiency of inserting SG mass into shell-stars can be as low as $\xi = 40\%$ to solve the mass budget with a second generation as numerous as the first (50:50). We can also explain very massive clusters where the ratio is more extreme, cf. Sect. 4.2, if we suppose larger ξ values.

We recall from Sect. 4.1.2 that ξ depends on three astrophysical effects: the mass loss rate of very massive SGs, the amount of material captured in the shell, and the ratio of TWUIN stars vs. SG stars. All three are poorly constrained at this point, so it is quite conceivable that their interplay adds up to $\xi \gtrsim 40\%$.

Note that in these considerations, the mass distribution of the *first* generation of stars (both massive and low-mass) follows the classical (not top-heavy) IMF given in Eq. (4). Solving the mass budget problem this way – having a justifiably irregular IMF for the *second* generation – is a unique feature of our starforming supergiant shell scenario.

4.8. Uncertainties of the star-forming shell scenario

From the point of view of observations, there is some uncertainty as to whether these massive and cool supergiants with low-metallicity actually exist in nature. This will be addressed in the near future by infrared observations of a larger sample of low-metallicity galaxies by the James Webb Space Telescope. From a theoretical point of view, the physics of these stars with inflated envelopes is quite uncertain, and it is undergoing intensive investigation at the moment (Sanyal et al. 2015, 2017). Additionally, as mentioned in Sect. 2.1, the mass-loss prescription we use involves an extrapolation beyond the mass range where it has been measured.

The process of star formation in a shell is considered rather delicate. It requires several astrophysical effects to combine: that sufficiently dense and long-lived photoionization-confined shells form around very massive SG stars isotropically, so that gravitational instability could occur and lead to the formation of a second generation of stars. As for the mass budget, either the IMF of the cluster should have an index between -1.71 and -2.07 (as explained in Sect. 4.1 – also note that the upper limit for the first generation, 0.8 $M_\odot$ is rather arbitrary), or the second generation should have a non-classical IMF, truncated at both the high and the low end. Additionally, massive stars in this cluster should have a broad rotational velocity distribution, because the TWUIN stars that produce the ionizing radiation are fast rotators. Under these conditions, the star-forming shell scenario could potentially produce a second population of stars with the observed abundance variations, and with a similar total mass to that of the first generation of low-mass stars.

4.9. Supergiants may end up as massive black holes in globular clusters

With the direct detection of merging black holes via their gravitational wave radiation (Abbott et al. 2016a,b; Bagoly et al. 2016; The LIGO Scientific Collaboration et al. 2017; Szécsi 2017a), many authors suggested globular clusters as the host of these black holes (Rodriguez et al. 2015; Antonini et al. 2016;

Belczynski et al. 2016; Askar et al. 2017). In this section, we discuss the final fate and remnants of our supergiant models.

The cores of very massive stellar models at low-Z undergo pair-instability (Burbidge et al. 1957; Langer 1991; Heger et al. 2003; Langer et al. 2007; Yoon et al. 2012; Kozyreva et al. 2014). This instability makes the core collapse during oxygen burning, that is, before an iron-core could form. Above a helium-core mass of $\sim 133\ M_\odot$, the collapse directly leads to black hole formation. Below this mass, however, it leads to a pair-instability supernova (Heger & Woosley 2002).

From the three supergiant models presented in the context of the star-forming supergiant shell scenario, the most massive two models (with $M_{ini} = 575\ M_\odot$ and $M_{ini} = 257\ M_\odot$) are predicted to form black holes without a supernova explosion (Szécsi 2016). The masses of these black holes are expected to be above $140\ M_\odot$, depending on the strength of the mass-loss (discussed in Sect. 2.1). They will thus contribute to the black hole population of their globular clusters.

The model with $M_{ini} = 150\ M_\odot$ on the other hand, which has a final mass of $118\ M_\odot$, is predicted to explode as a pair-instability supernova (Szécsi 2016). The explosion of the SG star may disrupt the shell, but leave the majority of the proto-stars intact. The supenova ejecta is probably too energetic to stay in the cluster's potential well (Lee et al. 2009), so it may not pollute the second generation of stars (cf. however Wünsch et al. 2017).

5. Conclusions

We propose star-forming shells around cool supergiants as a possible site to form the second generation of low-mass stars in Galactic globular clusters at low-metallicity. Photoionizaton-confined shells around core-hydrogen-burning cool supergiant stars may have been common in the young GCs. We simulate such a shell and find that it is dense enough to become gravitationally unstable. The new generation of low mass stars that would be formed in the shells should have an initial composition reflecting that of the supergiant's stellar wind, i.e. polluted by hot-hydrogen-burning products.

We summarize the most important ingredients of our star-forming shell scenario below.

1. *Low-metallicity supergiant models.* We present state-of-the-art stellar models of low-metallicity supergiants. At this low-metallicity (comparable to the metallicity of globular clusters), our models spend several hundreds of thousands of years on the supergiant branch already during their core-hydrogen-burning phase. They also stay on the supergiant branch during their remaining evolution.

2. *Slow, but strong stellar wind.* The supergiant models lose a significant amount of their material in their winds. Since the winds are slow, the material likely stays inside the young globular cluster.

3. *Hot-hydrogen burning.* In our models of very massive supergiants, the two nuclear burning cylces (Ne-Na chain and Mg-Al chain) that are responsible for the anticorrelation (of O vs. Na and Mg vs. Al, respectively) are effective.

4. *Convective envelope even during hydrogen-burning.* Although the burning processes take place in the core during the core-hydrogen-burning phase, the ashes are mixed between the core and the surface due to the large convective envelope of the supergiant. The composition of the stellar wind is, therefore, enhanced in Na and Al, while depleted of O and Mg.

5. *Presence of ionizing sources (TWUIN stars).* We point out that in a population of low-Z massive stars with a broad rotational velocity distribution, the fastest rotating stars will evolve quasi-homogeneously. This chemically homogeneous evolution is responsible for the creation of hot, luminous objects with intense ionizing ratiation, the so-called Transparent Wind UV-Intense stars. We suppose that the radiation field of TWUIN stars is approximately isotropic in the young globular cluster.

6. *Photoionization-confined shells.* Where the neutral, cool stellar wind of the supergiants meet the ionized, hot region of the cluster environment, photoionization-confined shells may form. We simulate such a photoionization-confined shell around one of our supergiant models. The shell has a density of 2×10^{-16} g cm^{-3} and temperature of ~ 50 K.

We analyse the stability of the photoionization-confined shell in our simulation, and find that it is gravitationally unstable on a timescale much shorter than the lifetime of the supergiant. The Bonnor-Ebert mass of the overdense regions is low enough to allow star formation. The mass distribution of the new stars is unknown, but we certainly expect the majority of them to be above $0.2\ M_\odot$ and below $1\ M_\odot$. It is unlikely that massive stars would form because of the geometry of this particular star-forming region.

We show that the composition of a star formed in the photoionization-confined shell is comparable to the observed composition of old, low-mass stars in the most extremely polluted population in globular clusters. We match the abundances of O, Na, Al, and Mg, as well as the isotopes of ^{24}Mg, ^{25}Mg, and ^{26}Mg. We emphasize that the very high masses of our supergiant models naturally explain the Mg isotope observations, with which some of the alternative scenarios (fast rotating star scenario and the massive binary scenario) clearly struggle. Our scenario also only works in metal-poor environments however, and cannot apply to the most metal-rich clusters.

Our simulated shell-stars have a high surface helium mass fraction of $Y_{sh} = 0.48$. We find that low-metallicity supergiants behave the same way as other massive polluters when it comes to helium: they can also only explain the spread in Na & O and Mg & Al together with a high helium abundance. But this issue is generic, as both the Ne-Na chain and the Mg-Al chain are side reactions of hot hydrogen-burning (Bastian et al. 2015; Lochhaas & Thompson 2017).

To fulfill the mass-budget constraint, we offer two possibilities. One possibility is that we apply a top-heavy initial mass function with an index being somewhere between -1.71 and -2.07. These values are less restrictive than those required for some of the other scenarios; for example the supermassive stars with $10^4\ M_\odot$ of Denissenkov & Hartwick (2014) or the fast rotating stars of Decressin et al. (2007). Another possibility is to use a non-classical IMF for the second generation of stars in the shell. We argued that both massive stars and very low-mass stars are justifiably excluded from this second generation, making possible for us to solve the mass budget by accounting only for a fraction of the first generation low-mass stars.

We emphasize that even if the shells are destroyed for example by collision, the corresponding gas may sink into the cluster core and lead to star formation there. Thus, supergiant shells should be considered possible contributors to the chemical evolution of globular clusters.

If the conditions do not facilitate the formation of a photoionization-confined shell (e.g. because the ionizing radiation field is too weak), the supergiant stellar models presented here should still be considered. Their winds are slow, strong and enhanced by ashes of hot-hydrogen burning. Therefore, our low-Z supergiant models should be taken into account when

one is assessing all the possible sources of pollution in young globular clusters.

Although there are some uncertainties necessarily associated with our proposed scenario of star-forming shells around cool supergiant stars, it shows strong potential for explaining at least some of the second generation of stars with anomalous abundances in GCs – especially the more extreme cases. Our calculations presented here show that the cool supergiant scenario, both with or without a photoionization-confined shell, deserves serious consideration alongside other, more established scenarios, and should be investigated in more detail in the future.

References

Abbott, B. P., Abbott, R., Abbott, T. D., et al. 2016a, Phys. Rev. Lett., 116, 061102

Abbott, B. P., Abbott, R., Abbott, T. D., et al. 2016b, ApJ, 818, L22

Andersen, M., Gennaro, M., Brandner, W., et al. 2017, A&A, 606, A22

Antonini, F., Chatterjee, S., Rodriguez, C. L., et al. 2016, ApJ, 816, 65

Askar, A., Szkudlarek, M., Gondek-Rosińska, D., Giersz, M., & Bulik, T. 2017, MNRAS, 464, L36

Bagoly, Z., Szécsi, D., Balázs, L. G., et al. 2016, A&A, 593, L10

Bastian, N., Lamers, H., de Mink, S. E., et al. 2013, MNRAS, 436, 2398

Bastian, N., Cabrera-Ziri, I., & Salaris, M. 2015, MNRAS, 449, 3333

Belczynski, K., Holz, D. E., Bulik, T., & O'Shaughnessy, R. 2016, Nature, 534, 512

Brodie, J. P., & Strader, J. 2006, ARA&A, 44, 193

Brott, I., de Mink, S. E., Cantiello, M., et al. 2011, A&A, 530, A115

Burbidge, E. M., Burbidge, G. R., Fowler, W. A., & Hoyle, F. 1957, Rev. Mod. Phys., 29, 547

Carretta, E., Bragaglia, A., Gratton, R. G., et al. 2010, A&A, 516, A55

Ciardi, B., Ferrara, A., & White, S. D. M. 2003, MNRAS, 344, L7

Da Costa, G. S., Norris, J. E., & Yong, D. 2013, ApJ, 769, 8

Dabringhausen, J., Kroupa, P., & Baumgardt, H. 2009, MNRAS, 394, 1529

D'Antona, F., & Ventura, P. 2007, MNRAS, 379, 1431

de Jager, C., Nieuwenhuijzen, H., & van der Hucht, K. A. 1988, A&AS, 72, 259

de Mink, S. E., Pols, O. R., Langer, N., & Izzard, R. G. 2009, A&A, 507, L1

Decressin, T., Meynet, G., Charbonnel, C., Prantzos, N., & Ekström, S. 2007, A&A, 464, 1029

Decressin, T., Baumgardt, H., Charbonnel, C., & Kroupa, P. 2010, A&A, 516, A73

Denissenkov, P., & Hartwick, F. 2014, MNRAS, 437

D'Ercole, A., Vesperini, E., D'Antona, F., McMillan, S. L. W., & Recchi, S. 2008, MNRAS, 391, 825

Doroshkevich, A. G., Kotok, E. V., Poliudov, A. N., et al. 1980, MNRAS, 192, 321

Dotter, A., Ferguson, J. W., Conroy, C., et al. 2015, MNRAS, 446, 1641

Eldridge, J. J., Genet, F., Daigne, F., & Mochkovitch, R. 2006, MNRAS, 367, 186

Elmegreen, B. G. 1998, in Origins, ed. C. E. Woodward, J. M. Shull, & H. A. Thronson, Jr., ASP Conf. Ser., 148, 150

Forbes, D. A., & Bridges, T. 2010, MNRAS, 404, 1203

Gratton, R. G., Sneden, C., & Carretta, E. 2004, ARA&A, 42, 385

Harris, W. E. 1996, AJ, 112, 1487

Harris, W. E. 2010, Arxiv e-prints [arXiv:1012.3224]

Harris, W. E., Whitmore, B. C., Karakla, D., et al. 2006, ApJ, 636, 90

Hartmann, L., & Kenyon, S. J. 1996, ARA&A, 34, 207

Heger, A., & Woosley, S. E. 2002, ApJ, 567, 532

Heger, A., Fryer, C. L., Woosley, S. E., Langer, N., & Hartmann, D. H. 2003, ApJ, 591, 288

Karakas, A. I., Fenner, Y., Sills, A., Campbell, S. W., & Lattanzio, J. C. 2006, ApJ, 652, 1240

Köhler, K., Langer, N., de Koter, A., et al. 2015, A&A, 573, A71

Kozyreva, A., Blinnikov, S., Langer, N., & Yoon, S.-C. 2014, A&A, 565, A70

Kroupa, P. 2001, MNRAS, 322, 231

Krumholz, M. R., Bate, M. R., Arce, H. G., et al. 2014, Protostars and Planets VI, 243

Langer, N. 1991, A&A, 252, 669

Langer, N., Norman, C. A., de Koter, A., et al. 2007, A&A, 475, L19

Lee, J.-W., Kang, Y.-W., Lee, J., & Lee, Y.-W. 2009, Nature, 462, 480

Lochhaas, C., & Thompson, T. A. 2017, MNRAS, 470, 977

Longmore, S. N., Kruijssen, J. M. D., Bastian, N., et al. 2014, Protostars and Planets VI, 291

Mac Low, M.-M., & Klessen, R. S. 2004, Rev. Mod. Phys., 76, 125

Mackey, J. 2012, A&A, 539, A147

Mackey, J., Langer, N., & Gvaramadze, V. V. 2013, MNRAS, 436, 859

Mackey, J., Mohamed, S., Gvaramadze, V. V., et al. 2014, Nature, 512, 282

Mackey, J., Castro, N., Fossati, L., & Langer, N. 2015, A&A, 582, A24

Marino, A. F., Milone, A. P., Przybilla, N., et al. 2014, MNRAS, 437, 1609

Mauron, N., & Josselin, E. 2011, A&A, 526, A156

Milone, A. P., Piotto, G., Renzini, A., et al. 2017, MNRAS, 464, 3636

Mokiem, M. R., de Koter, A., Evans, C. J., et al. 2006, A&A, 456, 1131

Mucciarelli, A., Dalessandro, E., Ferraro, F. R., Origlia, L., & Lanzoni, B. 2014, ApJ, 793, L6

Nieuwenhuijzen, H., & de Jager, C. 1990, A&A, 231, 134

Piotto, G., Bedin, L. R., Anderson, J., et al. 2007, ApJ, 661, L53

Piotto, G., Milone, A. P., Bedin, L. R., et al. 2015, AJ, 149, 91

Portegies Zwart, S. F., McMillan, S. L. W., & Gieles, M. 2010, ARA&A, 48, 431

Rodriguez, C. L., Morscher, M., Pattabiraman, B., et al. 2015, Phys. Rev. Lett., 115, 051101

Salpeter, E. 1955, ApJ, 121, 161

Sanyal, D., Grassitelli, L., Langer, N., & Bestenlehner, J. M. 2015, A&A, 580, A20

Sanyal, D., Langer, N., Szécsi, D., Yoon, S.-C., & Grassitelli, L. 2017, A&A, 597, A71

Schiavon, R. P., Johnson, J. A., Frinchaboy, P. M., et al. 2017, MNRAS, 466, 1010

Szécsi, D. 2016, Ph.D. Thesis, Mathematisch-Naturwissenschaftlichen Fakultät der Universität Bonn, Germany

Szécsi, D. 2017a, Contributions of the Astronomical Observatory Skalnate Pleso, 47, 108

Szécsi, D. 2017b, Arxiv e-prints [arXiv:1710.05655]

Szécsi, D., Langer, N., Sanyal, D., et al. 2015a, in Wolf-Rayet Stars: Proc. of an International Workshop held in Potsdam, Germany, 1–5 June 2015, ed. W.-R. Hamann, A. Sander, & H. Todt (Universitätsverlag Potsdam), 189

Szécsi, D., Langer, N., Yoon, S.-C., et al. 2015b, A&A, 581, A15

Tailo, M., D'Antona, F., Vesperini, E., et al. 2015, Nature, 523, 318

The LIGO Scientific Collaboration, the Virgo Collaboration, Abbott, B. P., et al. 2017, Phys. Rev. Lett., 118, 221101

Tóth, L. V. & Kiss, Z. T. 2007, IAU Symp., 237, 124

Tóth, L. V., Marton, G., Zahorecz, S., et al. 2014, PASJ, 66, 17

Ventura, P., D'Antona, F., Mazzitelli, I., & Gratton, R. G. 2001, ApJ, 550, L65

Ventura, P., Carini, R., & D'Antona, F. 2011, MNRAS, 415, 3865

Vink, J., de Koter, A., & Lamers, H. 2001, A&A, 369, 574

Vishniac, E. T. 1983, ApJ, 274, 152

Wolfire, M. G., McKee, C. F., Hollenbach, D., & Tielens, A. G. G. M. 2003, ApJ, 587, 278

Wünsch, R., Palouš, J., Tenorio-Tagle, G., & Ehlerová, S. 2017, ApJ, 835, 60

Yong, D., Aoki, W., & Lambert, D. L. 2006, ApJ, 638, 1018

Yong, D., Grundahl, F., Lambert, D. L., Nissen, P. E., & Shetrone, M. D. 2003, A&A, 402, 985

Yoon, S.-C., Dierks, A., & Langer, N. 2012, A&A, 542, A113

Low-metallicity massive single stars with rotation

II. Predicting spectra and spectral classes of chemically homogeneously evolving stars

B. Kubátová[1], D. Szécsi[1,2], A. A. C. Sander[3,4], J. Kubát[1], F. Tramper[5,9], J. Krtička[6], C. Kehrig[7], W.-R. Hamann[3],
R. Hainich[3], and T. Shenar[8]

[1] Astronomický ústav, Akademie věd České republiky, Fričova 298, 251 65 Ondřejov, Czech Republic
   e-mail: `brankica.kubatova@asu.cas.cz`
[2] School of Physics and Astronomy and Institute of Gravitational Wave Astronomy, University of Birmingham, Edgbaston,
   Birmingham B15 2TT, UK
[3] Institut für Physik und Astronomie, Universität Potsdam, Karl-Liebknecht-Str. 24/25, 14476 Potsdam, Germany
[4] Armagh Observatory and Planetarium, College Hill, Armagh BT61 9DG, UK
[5] European Space Astronomy Centre (ESA/ESAC), Operations Department, 28692 Villanueva de la Cañada, Madrid, Spain
[6] Ústav teoretické fyziky a astrofyziky, Masarykova univerzita, Kotlářská 267/2, 611 37 Brno, Czech Republic
[7] Instituto de Astrofísica de Andalucía (IAA/CSIC), Glorieta de la Astronomía s/n Aptdo. 3004, 18080 Granada, Spain
[8] Institute of Astrophysics, KU Leuven, Celestijnenlaan 200 D, 3001 Leuven, Belgium
[9] Institute for Astronomy, Astrophysics, Space Applications & Remote Sensing, National Observatory of Athens, Vas. Pavlou and I.
   Metaxa, Penteli 15236, Greece

ABSTRACT

Context. Metal-poor massive stars are assumed to be progenitors of certain supernovae, gamma-ray bursts, and compact object mergers that might contribute to the early epochs of the Universe with their strong ionizing radiation. However, this assumption remains mainly theoretical because individual spectroscopic observations of such objects have rarely been carried out below the metallicity of the Small Magellanic Cloud.

Aims. Here we explore the predictions of the state-of-the-art theories of stellar evolution combined with those of stellar atmospheres about a certain type of metal-poor ($0.02\,Z_\odot$) hot massive stars, the chemically homogeneously evolving stars that we call Transparent Wind Ultraviolet INtense (TWUIN) stars.

Methods. We computed synthetic spectra corresponding to a broad range in masses ($20-130\,M_\odot$) and covering several evolutionary phases from the zero-age main-sequence up to the core helium-burning stage. We investigated the influence of mass loss and wind clumping on spectral appearance and classified the spectra according to the Morgan-Keenan (MK) system.

Results. We find that TWUIN stars show almost no emission lines during most of their core hydrogen-burning lifetimes. Most metal lines are completely absent, including nitrogen. During their core helium-burning stage, lines switch to emission, and even some metal lines (oxygen and carbon, but still almost no nitrogen) are detected. Mass loss and clumping play a significant role in line formation in later evolutionary phases, particularly during core helium-burning. Most of our spectra are classified as an early-O type giant or supergiant, and we find Wolf–Rayet stars of type WO in the core helium-burning phase.

Conclusions. An extremely hot, early-O type star observed in a low-metallicity galaxy could be the result of chemically homogeneous evolution and might therefore be the progenitor of a long-duration gamma-ray burst or a type Ic supernova. TWUIN stars may play an important role in reionizing the Universe because they are hot without showing prominent emission lines during most of their lifetime.

Key words. stars: massive – stars: winds, outflows – stars: rotation – galaxies: dwarf – radiative transfer

1. Introduction

Low-metallicity massive stars are essential building blocks of the Universe. Not only do these objects play a role in cosmology by contributing to the chemical evolution of the early Universe and the reionization history (e.g., Abel et al. 2002; Yoshida et al. 2007; Sobral et al. 2015; Matthee et al. 2018), they may also influence the structure of low-metallicity dwarf galaxies in the local Universe (e.g., Tolstoy et al. 2009; Annibali et al. 2013; Weisz et al. 2014). Moreover, they may lead to spectacular explosive phenomena such as supernovae (e.g., Quimby et al. 2011; Inserra et al. 2013; Lunnan et al. 2013), gamma-ray bursts (e.g., Levesque et al. 2010; Modjaz et al. 2011; Vergani et al.

2015), and possibly even gravitational wave-emitting mergers (e.g., Abbott et al. 2016, 2017). The details of all these processes, however, are still veiled by many uncertainties because low-metallicity ($<0.2\,Z_\odot$) massive stars have rarely been analyzed by quantitative spectroscopy as individual objects: the instrumentation necessary to obtain the required data quality has only recently become available. Individual spectral analyses of massive stars have been published only down to $0.1\,Z_\odot$, such as one Wolf–Rayet (WR) star of type WO in the galaxy IC 1613 (Tramper et al. 2013) and several hot stars in the galaxies IC 1613, WLM, and NGC 3109 (e.g., Tramper et al. 2011, 2014; Herrero et al. 2012; Garcia et al. 2014; Bouret et al. 2015; Camacho et al. 2016). Additionally, massive stars have been

studied in the Small Magellanic Cloud (SMC) at $Z_{SMC} \sim 0.2\,Z_\odot$, including 10 red supergiants (Davies et al. 2015), 12 WR stars (Hainich et al. 2015; Massey et al. 2015; Shenar et al. 2016), and a few hundred O-type stars (Lamb et al. 2016).

At metallicities below $0.1\,Z_\odot$, however, no direct spectroscopic observations of individual massive stars have been reported so far. Although such stars might have been contributing to our Galaxy's chemical composition in the past (specifically in globular clusters, see, e.g., Szécsi et al. 2018; Szécsi & Wünsch 2019), they no longer exist in our Galaxy. Even if the second generation of stars in the early Universe was indeed composed of many massive and very massive stars (e.g., Choudhury & Ferrara 2007; Ma et al. 2017), our observing capacities are not sufficient to look that far for individual objects.

Even in local star-forming dwarf galaxies it is hard to resolve massive stars individually because they are embedded in dense and gaseous OB associations (Shirazi & Brinchmann 2012; Kehrig et al. 2013). However, we may be able to find indirect traces of their existence, such as the total amount of ionizing photons emitted by them, or the integrated emission lines of their WR stars (Kehrig et al. 2015; Szécsi et al. 2015a,b). Future observing campaigns may even provide us with a census of massive stars in metal-poor dwarf galaxies such as Sextant A ($\sim1/7\,Z_\odot$, McConnachie 2012) or I Zwicky 18 ($\sim1/40\,Z_\odot$, Kehrig et al. 2016).

In this paper, we focus on a certain exotic type of low-metallicity massive stars: those that are fast rotating and evolve chemically homogeneously. Szécsi et al. (2015b, hereafter Paper I) called their core hydrogen-burning (CHB) phases TWUIN stars; the term stands for Transparent Wind UltraViolet INtense. These stars were so named because they were predicted to have weak, optically thin stellar winds while being hot, and thus emitting most of their radiation in the UV band (for more details, see Szécsi et al. 2015a,b; Szécsi 2016, 2017a,b). TWUIN stars have extensively been investigated from an evolutionary point of view, mainly as a means to explain cosmic explosions and mergers. They were referred to as "stars with chemically homogeneous evolution" and "fast-rotating He-stars" by Yoon & Langer (2005) and Yoon et al. (2006), who showed that they may be applied as single-star progenitors of long-duration gamma-ray bursts and supernovae of type Ib/c. They were referred to as "stars that evolve chemically homogeneously" by Brott et al. (2011), who presented such single-star models with SMC metallicity. They were referred to as "the quasi-chemically homogeneous massive stars" by Cantiello et al. (2007), who created such models to account for long-duration gamma-ray bursts, this time through binary interaction at Z_{SMC}. They were referred to as "Wolf–Rayet stars in disguise" by de Mink et al. (2009), who showed that such binaries may finally form a double black-hole system. The latter hypothesis was further elaborated on by de Mink & Mandel (2016) and Mandel & de Mink (2016), as well as by Marchant et al. (2016, 2017), to provide progenitor channels to gravitational-wave emission. In particular, Marchant et al. (2016) found that chemically homogeneous stars at $\sim0.02\,Z_\odot$ (indeed what we call TWUIN stars here), when in a close binary, predict the highest rate of double black-hole mergers compared to other metallicities.

All these authors were mainly concerned with either the inner structure or the final fate of these stars, but rarely with their appearance. Theorists sometimes called them simply WR stars (e.g., Cui et al. 2018) because their surface composition and temperature, as predicted by the evolutionary models, are similar to those of observed WR stars. However, to determine whether they are in fact WR stars from an observational point of view (i.e., if they show broad and bright emission lines in the optical region), their spectral appearance needs to be known. A pioneer study in this direction was recently carried out by Hainich et al. (2018).

This is the second paper of a series. In Paper I we presented stellar evolutionary computations of TWUIN stars (see Sects. 6 and also 10.4) during the CHB phase, while some of these models were followed over the core helium-burning (CHeB) phase in Szécsi (2016, see Chapter 4 of the thesis). In the current paper, we now simulate the atmospheres and spectra of chemically homogeneously evolving stars of different masses and cover their whole evolution. We use the the Potsdam Wolf-Rayet (PoWR) stellar atmosphere code to compute the synthetic spectra. The initial metallicity of the evolutionary models based on which the synthetic spectra are created is $0.02\,Z_\odot$. The choice of this particular metallicity value is motivated by the fact that binary models of this metallicity have been successfully applied in the context of double compact object progenitors (e.g., Marchant et al. 2016) as well as other explosive phenomena (see the review of Szécsi 2017b), and that such stars might be found in some local dwarf galaxies (Szécsi et al. 2015a). We explore the expected observable characteristics of these stars, classify them accordingly, and provide the spectral features that can be used to guide targeted observing campaigns. The predicted spectra are later applied to create a synthetic population to be compared to observational properties of low-metallicity dwarf galaxies in a next part of this series.

This paper is organized as follows: In Sect. 2 we give an overview of the stellar evolutionary model sequences used in this work. In Sect. 3 we present the stellar atmosphere and wind models. In particular, stellar parameters and chemical composition are summarized in Sect. 3.1, while the wind properties are described in Sect. 3.1. In Sect. 4 we provide synthetic spectra of chemically homogeneously evolving stars. The effects of mass loss and wind clumping on line formation are presented in Sects. 4.2 and 4.3, respectively. Classifications of the model spectra are presented in Sect. 5. In Sect. 6 we discus the validity of the models and suggest future research directions. Finally, a summary is given in Sect. 7. All the calculated spectra are available in Appendix B.

2. Stellar evolutionary model sequences

Single stellar evolutionary sequences of low-metallicity ($Z \sim 0.02\,Z_\odot$ or [Fe/H] $= -1.7$), fast-rotating massive stars were computed in Paper I for the CHB phase. The sequences were created using the Bonn evolutionary code (BEC). For the details of the code and the initial parameters of the computations, we refer to Paper I and references therein. Because we are also interested in further hydrogen-free evolution, we rely on the work of Szécsi (2016), who continued the computation of these sequences during CHeB until helium exhaustion in the core. To represent different evolutionary stages with spectra, we use three chemically homogeneously evolving sequences: those with initial masses M_{ini} of $20\,M_\odot$, $59\,M_\odot$, and $131\,M_\odot$, and initial rotational velocities of $450\,\mathrm{km\,s^{-1}}$, $300\,\mathrm{km\,s^{-1}}$, and $600\,\mathrm{km\,s^{-1}}$, respectively. These three tracks are shown in Fig. 1.

All three evolutionary sequences are computed assuming initial fast rotation, which is inherited from the 15 models that we compute spectra for. Their rotational velocities are in the range of $400-1000\,\mathrm{km\,s^{-1}}$ (see Table 1), which is still not close the critical rotational limit of these massive stars ($\sim0.4-0.6\,v_{crit}$). Therefore, we do not expect these stars to form a decretion disk. Additionally, although these velocities may seem extremely high, a very similar evolution is found at lower rotational rates
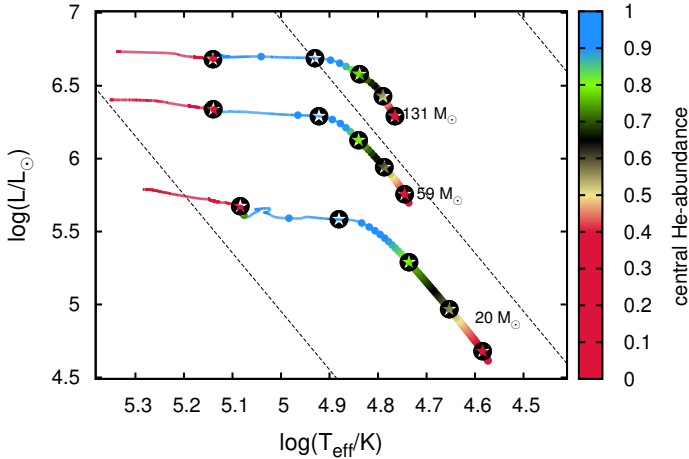
Fig. 1. HR diagram of our models (black symbols) and their corresponding evolutionary sequences. The sequences are taken from Paper I and Szécsi (2016). Initial masses are labeled, showing where the tracks start their evolution, proceeding toward the hot side of the diagram. Colors show the central helium mass fraction, and dots represent every 10^5 years of evolution. Dashed lines mark equiradial lines with 1, 10, and $100\,R_\odot$ from left to right. The black symbols represent the models for which we computed synthetic spectra. From right to left: black symbols correspond to evolutionary phases with surface helium mass fractions of 0.28, 0.5, 0.75, and 0.98, and the fifth symbol on the very left corresponds to a central helium mass fraction of 0.5, i.e., the middle of the CHeB phase.

as well. For example, the model with $M_{\rm ini} = 131\,M_\odot$ rotates with about $800–900\,{\rm km\,s}^{-1}$ in the first part of its CHB lifetime, and the model rotating only with $450\,{\rm km\,s}^{-1}$ in this phase evolves in almost exactly the same way (cf. Fig. 4 in Paper I). As discussed in Sect. 10.4 of Paper I, it is expected that about 20% of all massive stars at this metallicity evolve chemically homogeneously because of their fast rotation; indeed, observations down to $Z_{\rm SMC}$ suggest that stellar rotation increases with lower metallicity (Mokiem et al. 2006; Martayan et al. 2007).

To simulate the wind structure and spectra, we chose four models for each track: those with a surface helium mass fraction, $Y_{\rm S}$, of 0.28, 0.5, 0.75, and 0.98, as well as one model per track for the CHeB phase, as shown in Fig. 1 (note the color coding in the figure showing the central helium mass fraction, $Y_{\rm C}$, of the model sequences, which reflects the evolutionary stage) and in Table 1.

2.1. Mass loss applied to the evolutionary sequences

Mass loss of massive stars may influence their evolution significantly even at this low metallicity (see Paper I). The sequences were computed assuming a prescription for radiation-driven mass loss of hot O-type stars (Vink et al. 2000, 2001) providing the mass-loss rate $\dot{M}$ as a function of initial metal abundance $Z_{\rm ini}$ (given in units of solar metallicity $Z_\odot$) and further stellar parameters:

$$\log \frac{\dot{M}}{M_\odot/{\rm yr}} = -6.7 + 2.2 \log\left(L_*/10^5\right) - 1.3 \log\left(M_*/30\right)$$
$$- 1.2 \log\left(\frac{v_\infty/v_{\rm esc}}{2.0}\right) + 0.9 \log\left(T_{\rm eff}/40\,000\right)$$
$$- 10.9 \left[\log\left(T_{\rm eff}/40\,000\right)\right]^2 + 0.85 \log(Z_{\rm ini}/Z_\odot), \tag{1}$$

where $\dot{M}$ is in units of $M_\odot/{\rm yr}$, stellar effective temperature $T_{\rm eff}$ is in units of Kelvin, stellar mass M_* and luminosity L_* are

in solar units; the ratio of the terminal velocity v_∞ and escape velocity $v_{\rm esc}$ are taken as $v_\infty/v_{\rm esc} = 2.6$ for the evolutionary models because they all are above the bistability jump (Lamers et al. 1995; Vink et al. 2000). This formula was applied when $Y_{\rm S}$ was lower than 0.55, which is true for every first two models of our three evolutionary sequences (i.e., the T-1, T-2, T-6, T-7, T-11, and T-12 models, cf. Table 1). Because the models evolve chemically homogeneously, the surface abundances are very close to those in the core, $Y_{\rm S} \sim Y_{\rm C}$.

A different prescription was assumed for phases when $Y_{\rm S} > 0.7$, which applies for WR stars,

$$\log \frac{\dot{M}}{M_\odot/{\rm yr}} = 1.5 \log \frac{L_*}{L_\odot} - 2.85 X_{\rm S} - 12.95 + 0.85 \log \frac{Z_{\rm ini}}{Z_\odot}, \tag{2}$$

used for models T-3, T-4, T-8, T-9, T-13, and T-14. Here $X_{\rm S}$ is the surface hydrogen mass fraction. This expression follows from Eq. (2) in Hamann et al. (1995), but has been reduced by a factor of 10, as suggested by Yoon et al. (2006). The reduction by 10 gives a mass-loss rate comparable to the commonly adopted rate reported by Nugis & Lamers (2000; see Fig. 1 in Yoon 2015). For the dependence on $X_{\rm S}$, see the steepness of the fit in Fig. 7 of Hamann et al. (1995).

During the whole CHeB phase, the WR-type prescription of Eq. (2) was applied everywhere (models T-5, T-10, and T-15).

2.2. Uncertainties in the mass-loss prediction

Many uncertainties are associated with this treatment of the wind mass loss. For example, the prescription in Eq. (2) includes a metallicity dependence of $\dot{M} \sim Z_{\rm ini}^{0.85}$ following Vink et al. (2001). In reality, however, the dependence may be weaker than this (i.e., real winds are stronger than assumed), as suggested by theoretical calculations for classic WR stars in Vink & de Koter (2005) and Eldridge & Vink (2006). Conversely, observations of WN stars carried out by Hainich et al. (2015) found a stronger dependence (i.e., real winds are weaker than assumed). It seems therefore that the question of the metallicity dependence of WR winds remains to be settled.

Additionally, WN stars and WC stars may well be different from each other when it comes to wind mass loss; and both are quite different from the CHB phase of our chemically homogeneously evolving models (when they are TWUIN stars). Still, the reason in Paper I for using a mass-loss rate prescription based on observations of WR stars to simulate TWUIN stellar evolution was that in terms of surface composition and temperature, WR stars are the objects that are most similar to TWUIN stars. We provide suggestions for future research directions to establish the wind properties of TWUIN stars (both observationally and theoretically) in Sects. 6.3 and 6.4.

To account for all these uncertainties, we created two versions for every model. One has a nominal mass-loss rate as implemented in the evolutionary models, that is, according to Eqs. (1) and (2). The other has a reduced value that is a factor 100 lower than the nominal value. Choosing a factor of 100 is motivated by the work of Hainich et al. (2015), who found a steeper metallicity-dependence of WR winds. This is to say that using the mass-loss prescription given by Eq. (11) of Hainich et al. (2015), we obtained mass-loss rates that were similar to our reduced values; see Table 2. We refer to the nominal value as "higher", which means in the context of our study that it is the higher value of the two. By testing these two rather extreme values, we account for uncertainties in the mass-loss predictions of these stars.

Table 1. Main parameters of the 15 model stars.

M_{ini} $(M_\odot)$	Label	$\log T_{eff}$ (K)	$\log L_*$ $(L_\odot)$	$\log \dot{M}$ $(M_\odot/yr)$	Y_S	Y_C	C	O	N	R_* $(R_\odot)$	M_* $(M_\odot)$	$\log g$ (cm/s^2)	v_{rot} $(km\,s^{-1})$
20	0.28 (T-1)	4.58	4.68	-8.48	0.28	0.34	5.47×10^{-6}	3.55×10^{-5}	9.12×10^{-5}	4.93	20.0	4.35	695
20	0.50 (T-2)	4.65	4.97	-7.80	0.50	0.55	1.61×10^{-6}	2.88×10^{-6}	1.24×10^{-4}	5.01	20.0	4.34	675
20	0.75 (T-3)	4.74	5.29	-6.89	0.75	0.78	2.13×10^{-6}	2.25×10^{-6}	1.24×10^{-4}	4.95	19.8	4.35	650
20	0.98 (T-4)	4.88	5.58	-5.77	0.98	1.00	3.54×10^{-6}	1.59×10^{-6}	1.23×10^{-4}	3.58	19.2	4.61	702
20	CHeB (T-5)	5.08	5.67	-5.49	0.84	0.10*	1.36×10^{-1}	2.13×10^{-2}	5.89×10^{-3}	1.55	16.8	5.28	994
59	0.28 (T-6)	4.74	5.75	-7.00	0.28	0.36	8.26×10^{-6}	4.00×10^{-5}	8.40×10^{-5}	8.14	58.9	4.39	421
59	0.50 (T-7)	4.79	5.94	-6.70	0.50	0.57	2.27×10^{-6}	3.07×10^{-6}	1.23×10^{-4}	8.31	58.7	4.37	428
59	0.75 (T-8)	4.84	6.13	-5.82	0.75	0.79	2.52×10^{-6}	1.94×10^{-6}	1.24×10^{-4}	8.08	58.3	4.39	422
59	0.98 (T-9)	4.92	6.29	-4.92	0.98	1.00	3.94×10^{-6}	1.44×10^{-6}	1.23×10^{-4}	6.68	55.3	4.53	404
59	CHeB (T-10)	5.14	6.34	-4.70	0.68	0.10*	2.41×10^{-1}	7.31×10^{-2}	3.65×10^{-3}	2.60	49.4	5.30	755
131	0.28 (T-11)	4.76	6.29	-6.17	0.28	0.30	3.34×10^{-6}	1.06×10^{-5}	1.15×10^{-4}	13.71	130.8	4.28	905
131	0.50 (T-12)	4.79	6.42	-5.89	0.50	0.52	2.33×10^{-6}	2.06×10^{-6}	1.24×10^{-4}	14.26	129.9	4.24	925
131	0.75 (T-13)	4.84	6.57	-4.96	0.75	0.76	2.71×10^{-6}	1.28×10^{-6}	1.24×10^{-4}	13.63	126.8	4.27	820
131	0.98 (T-14)	4.93	6.69	-4.27	0.98	0.99	4.07×10^{-6}	1.39×10^{-6}	1.23×10^{-4}	10.18	112.5	4.47	520
131	CHeB (T-15)	5.14	6.68	-4.23	0.56	0.10*	3.19×10^{-1}	1.23×10^{-1}	3.79×10^{-4}	3.82	93.3	5.24	587

Notes. An asterisk marks models that are undergoing CHeB (i.e., post-main-sequence evolution). $\log \dot{M}$ refers to our nominal ("higher") mass-loss rate. The columns C, N, and O show surface mass fractions of carbon, nitrogen, and oxygen, respectively. We computed four synthetic spectra for each model in this table, corresponding to two different values of mass-loss rates (nominal and reduced) and clumping factors ($D = 1$ and 10).

Table 2. Mass-loss rate values applied in the synthetic spectra computations, compared to those that Hainich et al. (2015) would predict for the same stars.

M_{ini}	Label	$\log \dot{M}_h$ $(M_\odot/yr)$	$\log \dot{M}_r$ $(M_\odot/yr)$	$\log \dot{M}_{Hainich}$ $(M_\odot/yr)$
20	T-1 (0.28)	-8.48	-10.48	-10.77
20	T-2 (0.50)	-7.80	-9.80	-10.39
20	T-3 (0.75)	-6.89	-8.89	-8.68
20	T-4 (0.98)	-5.77	-7.77	-7.99
20	T-5 (pMS)	-5.50	-7.50	-8.17
59	T-5 (0.28)	-7.00	-9.00	-9.29
59	T-6 (0.50)	-6.70	-8.70	-8.29
59	T-7 (0.75)	-5.82	-7.82	-7.52
59	T-8 (0.98)	-4.92	-6.92	-7.00
59	T-10 (pMS)	-4.70	-6.70	-7.50
131	T-11 (0.28)	-6.17	-8.17	-8.53
131	T-12 (0.5)	-5.89	-7.89	-8.04
131	T-13 (0.75)	-4.96	-6.96	-9.10
131	T-14 (0.98)	-4.27	-6.27	-7.80
131	T-15 (pMS)	-4.23	-6.23	-7.27

Notes. $\log \dot{M}_r$ means the reduced mass-loss rate, and $\log \dot{M}_h$ the "higher", i.e., the nominal rate as applied in the evolutionary sequences in Paper 1 (i.e., computed using our Eqs. (1) or (2)).

3. Stellar atmosphere and wind models

To calculate the synthetic spectra and to obtain the stratification of wind parameters, a proper modeling of the static and expanding atmosphere is required. We calculated stellar spectra by means of the Potsdam Wolf-Rayet (PoWR) atmosphere code. Because the PoWR code treats both quasi-static (i.e., photospheric) and expanding layers (i.e., wind) of the stellar atmosphere consistently, it is applicable to most types of hot stars.

The PoWR code solves the non-local thermal equilibirum (non-LTE) radiative transfer in a spherically expanding atmosphere with a stationary mass outflow. A consistent solution for the radiation field and the population numbers is obtained iteratively by solving the equations of statistical equilibrium and radiative transfer in the comoving frame (Mihalas 1978; Hubeny & Mihalas 2014). After an atmosphere model is converged, the synthetic spectrum is calculated by a formal integration along emerging rays.

To ensure energy conservation in the expanding atmosphere, the temperature stratification is updated iteratively using the electron thermal balance method (Kubát et al. 1999) and a generalized form of the so-called Unsöld-Lucy method, which assumes radiative equilibrium (Hamann & Gräfener 2003). In the comoving frame calculations during the non-LTE iteration, the line profiles are assumed to be Gaussians with a constant Doppler broadening velocity v_D, which accounts for broadening due to thermal and microturbulent velocities. In this work we use $v_D = 100\,km\,s^{-1}$. All spectra correspond to being seen edge-on, that is, the lines are fully broadened by rotation.

After the model iteration converged and all population numbers are established, the emergent spectrum is finally calculated in the observer's frame, using a refined set of atomic data (e.g., with multiplet splitting) and accounting in detail for thermal, microturbulent, and pressure broadening of the lines. Detailed information on the assumptions and numerical methods used in the code can be found in Gräfener et al. (2002), Hamann & Gräfener (2003, 2004), and Sander et al. (2015).

3.1. Stellar parameters and chemical composition

Fundamental stellar parameters required as input for PoWR model atmosphere calculations are the stellar temperature T_*, the stellar mass M_*, and the stellar luminosity L_*. These were adopted from the stellar evolutionary model sequences (see Table 1), assuming that the hydrostatic surface temperature T_{eff} of the BEC evolutionary models coincides with T_*. With given L_* and T_*, the stellar radius R_* was calculated via Stefan-Boltzmann's law

$$L_* = 4\pi\sigma_{SB}R_*^2 T_*^4, \tag{3}$$

where σ_{SB} is the Stefan-Boltzmann constant. In the PoWR code the temperature T_* is an effective temperature at the radius R_*, which is defined at the Rosseland continuum optical depth $\tau_{max} = 20$. The outer atmosphere (i.e., wind) boundary is

set to $1000\,R_*$ with the exception of the models for $M_{\rm ini} = 20\,M_\odot$, where $100\,R_*$ is already sufficient. Further details about the method of model atmosphere calculations can be found in Sander et al. (2015).

Detailed model atoms of all relevant elements are taken into account. Line blanketing is considered with the iron-group elements treated in the super-level approach, accounting not only for Fe, but also for Sc, Ti, V, Cr, Mn, Co, and Ni (see Gräfener et al. 2002, for details). The abundances of H, He, C, N, O, Ne, Mg, Al, Si, and Fe are adopted from the stellar evolutionary model sequences. The additional elements such as P, S, Cl, Ar, K, and Cl, which are not considered in the stellar evolutionary models but are used in the PoWR model atmosphere calculations, are also considered in a minimum-level approach to account for their potential contributions to the wind driving. The additional elements have abundances of $Z_\odot/50$. For iron group elements we consider the ionization stages from ɪ up to xvɪɪ to ensure that all sources that significantly contribute to opacity are taken into account. Higher ionization stages of Fe are important especially for the CHeB stages of the considered stars.

3.2. Wind properties

Because we consider objects that were predicted only theoretically and have never been observed, there exist no observational constraints on their wind properties so far. Within the frame of model consistency, there is therefore some freedom in adopting atmospheric and wind parameters.

Mass-loss rates. With specified $\dot{M}$ in the PoWR code, the density stratification $\rho(r)$ in the wind is calculated via the continuity equation given as

$$\dot{M} = 4\pi r^2 \, v(r) \, \rho(r). \tag{4}$$

To be consistent with stellar evolutionary models that provide the basis for our spectral models, we decided to apply the same mass-loss rate values as in these models. We note that these values were assumed in the evolutionary models based on prescribed recipes (see Sect. 2.1) and are not predicted by the models. To test the effect of mass loss on the emergent spectra, we therefore supplemented our work by another set of models: one model calculated with a mass-loss rate that is hundred times lower than in the original set (see Table 2 and Sect. 2.1). This enables us to roughly estimate uncertainties of our emergent radiation prediction due to uncertainties in the choice of mass-loss rates.

Velocity. The adopted velocity field in the PoWR models consists of two parts. A hydrostatic part where gravity is balanced by gas and radiation pressure, and a wind part where the outward pressure exceeds gravity and therefore the matter is accelerated. To properly account for the velocity field in the inner part of the wind, the quasi-hydrostatic part of the atmosphere is calculated self-consistently to fulfill the hydrostatic equation. Computing hydrodynamically consistent stellar atmosphere models this way is a new approach, recently implemented in the PoWR code (see Sander et al. 2015). In the wind domain (i.e., the supersonic part), the velocity field is prescribed by the so-called β-law (see, e.g., Lamers & Cassinelli 1999) as

$$v(r) = v_\infty \left(1 - \frac{R_*}{r}\right)^\beta, \tag{5}$$

where v_∞ is the wind terminal velocity and β a parameter describing the steepness of the velocity law.

Since there exist no predictions (neither theory based nor observation implied) about the velocity field of TWUIN stars, we adopted only schematic parameters. For β we assumed values of 0.8 or 1.0. This choice was motivated by the fact that the typical value of the β parameter for massive stars ranges between 0.6 and 2.0 (see, e.g., Puls et al. 2008). For the terminal wind velocity v_∞, we assumed the same value for all models, that is, $v_\infty = 1000\,{\rm km\,s^{-1}}$. This is a reasonable estimate, since in the simplified relation between terminal and escape velocities ($v_\infty/v_{\rm esc} = 2.6$) used in mass-loss rate prescriptions, the ratio $v_\infty/v_{\rm esc}$ decreases significantly when a rapid stellar rotation is accounted for (Friend & Abbott 1986). In Sect. 6.2 we discuss possible ways to improve the assumptions about v_∞ in the future.

Clumping. Because clumping is another wind property that influences the emergent spectra, we also calculated an additional set of models assuming clumping in the wind. This enabled us to estimate the influence of clumping on our prediction of the emergent radiation.

Wind inhomogeneities are treated in the microclumping approximation (see Hamann & Koesterke 1998), which means that all clumps are assumed to be optically thin. The density in clumps is enhanced by a clumping factor $D = 1/f_{\rm V}$, where $f_{\rm V}$ is a fraction of volume occupied by clumps (i.e., volume filling factor). The inter-clump medium is assumed to be void. For models in which clumping was assumed, we also allowed the clumping factor to depend on radius. We implemented clumping stratification with

$$f_{\rm V}(r) = f_{\rm V,\infty} + (1 - f_{\rm V,\infty}) \exp\left(-\frac{\tau_{\rm cl}}{\tau_{\rm Ross}(r)}\right), \tag{6}$$

where $f_{\rm V,\infty} = D_\infty^{-1}$, D_∞ denotes the maximum clumping value, and $\tau_{\rm cl}$ is a free parameter denoting a characteristic Rosseland optical depth for the clumping "onset" (for more details, see Sander et al. 2017). In all models with a depth-dependent clumping stratification, we used $\tau_{\rm cl} = 2/3$.

4. Spectral models

To explore the spectral appearance of chemically homogeneously evolving stars, we computed four sets of atmosphere models with three different $M_{\rm ini}$ (20, 59, and 131 $M_\odot$) for five different evolutionary stages defined by $Y_{\rm S}$ (0.25, 0.5, 0.75, 0.98, and CHeB). The models of the CHeB evolutionary phase have no hydrogen, and their $Y_{\rm S}$ abundances are given in Table 1. The four sets of models consist of two sets with different values of a mass-loss rate and two sets with different values of a clumping factor. We created 60 models in total.

To calculate the line profiles, we took into account line broadening for all lines, accounting for radiation damping, pressure broadening, and rotational broadening. For the latter, we used the same value of the rotational velocity $v_{\rm rot}$ as in stellar evolutionary models. The influence of rotation on line formation is usually accounted for by performing a flux-convolution with a rotation profile. However, this may not be valid in the case of expanding atmospheres. Therefore, we used an option in the PoWR code that accounts for rotation with a 3D integration scheme of the formal integral, assuming that the corotation radius is same as the radius of the star (for more details, see Shenar et al. 2014). The mass-loss rates and rotational velocities used in the calculations are given in Table 1.

The continuum spectral energy distributions (SEDs) of all models are shown in Fig. 2. The maximum emission is found in the far- and extreme ultra-violet (UV) region. With increasing
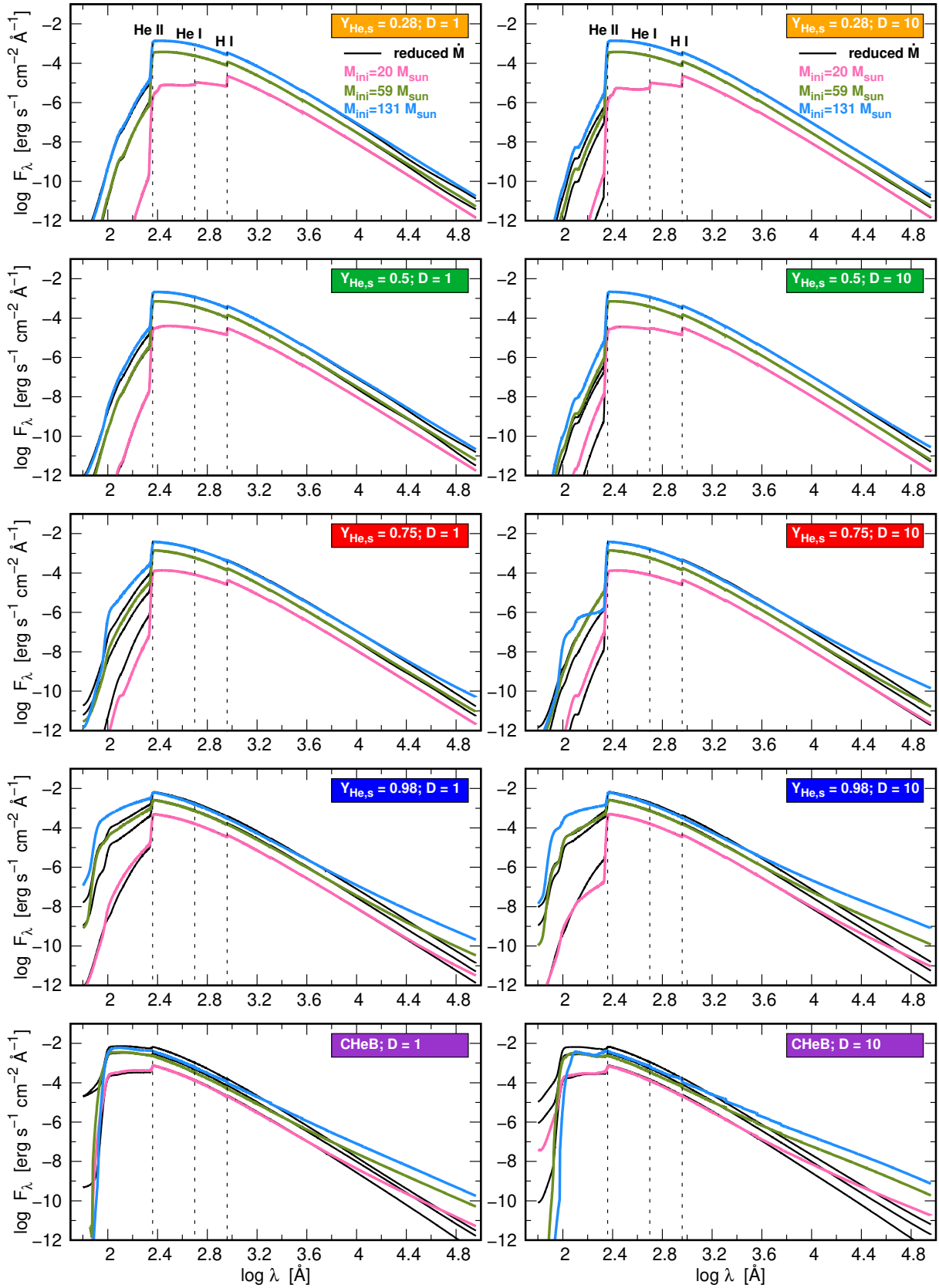
Fig. 2. Spectral energy distribution (continuum) of chemically homogeneously evolving stars in different evolutionary stages as marked in the colored boxes in each panel. *Left panels*: provide the continuum SED of the models calculated with a smooth ($D = 1$) wind, while the right panels depict the same for the clumped ($D = 10$) wind assumption. The colored lines correspond to the models with specific M_{ini} (denoted in the *top panels*) and calculated assuming the same (nominal) mass-loss rate as given in Table 1. For each colored line, a black line also represents the SED of the model for the same star in the same evolutionary stages with the same clumping factor D, but assuming a mass-loss rate 100 times lower. For better visibility of the differences between the SEDs in the CHeB phase, see Fig. B1.

M_{ini}, the luminosity and thus the resulting flux also increases. With the exception of the $20\,M_\odot$ model at the first evolutionary stage, the flux maximum is always close to the He II ionization edge. The SEDs also reveal that for all three mass branches, the amount of emitted far- and extreme UV ionizing radiation increases more and more during the evolution of the stars. This is a direct consequence of the chemically homogeneous evolution where T_{eff} most of the time increases monotonically.

Decreasing the mass-loss rates has no significant influence on the emitted radiation during most of the CHB phases. Only small differences in the emitted fluxes can be seen at wavelengths shorter than 227 Å and longer than 10 000 Å (see the differences between the colored and black lines in the left panels of Fig. 2). The same conclusion can be drawn for the clumped wind models with $D = 10$ (see the differences between the colored and black lines in the right panels of Fig. 2). These differences are higher and more visible in the evolutionary stages shortly before the end of CHB phase and in the CHeB phase (see the differences between the colored and black lines in the left and right panels with blue and purple boxes in Fig. 2).

The differences in the emitted fluxes between models calculated for smooth and clumped wind are very small and present mostly at the wavelengths shorter than 227 Å, regardless of the adopted $\dot{M}$. Small differences between SEDs are also found at wavelengths longer than 10 000 Å for models in the later stages, assuming higher $\dot{M}$ (see the differences between the black and colored lines in the left panels with higher $\dot{M}$ and in the right panels with reduced $\dot{M}$ in Fig. B2).

The SEDs reveal that the radiation with frequencies higher than the H I, He I, and He II ionization limits increase both with the initial mass and during the evolution of the stars. More massive and more evolved stars emit more ionizing flux. The consequences of ionizing fluxes of chemically homogeneously evolving stars and their application will be discussed in a subsequent paper (Szécsi et al., in prep.).

4.1. Description of spectral features

To discuss the detailed spectral features, we analyzed the normalized spectra. The optical range is depicted in Figs. 3 and 4, and the spectra in the UV and infrared (IR) regions of each model are plotted in Figs. B3–B6.

The spectra calculated with mass-loss rates taken from stellar evolution calculations and assuming a smooth wind in earlier evolutionary phases with CHB show most lines in absorption (see the colored lines in Fig. 3). These lines turn into emission in the CHeB phase, during which these stars have no hydrogen in the atmosphere (see the colored lines in the top panel in Fig. 4). This trend is also visible in the UV and IR spectra (see also the colored lines in Figs. B3 and B5 and in the top panels in Figs. B4 and B6). The spectra of these stars do not typically show any P Cygni line profiles. This is somewhat surprising, but is most likely related to the low Z of these stars.

Synthetic spectra of models with $Y_S = 0.25$ and $Y_S = 0.5$, regardless of their initial mass, show almost exclusively absorption lines in most of the spectral regions, except for the emission line N IV $\lambda7123$ Å in the optical range (see the pink line in the panel with the green box in Fig. 3); and very weak blending lines He II $\lambda1.86\,\mu$m and He I $\lambda1.88\,\mu$m in the IR range (see the purple and green lines in the panels with the orange and green boxes in Fig. B5).

When the stars reach the evolutionary stage with $Y_S = 0.75$, some additional emission lines appear in the spectra of the higher-mass models ($M_{ini} = 59\,M_\odot$ and $131\,M_\odot$). For instance, the helium emission line He II $\lambda4686$ Å and the hydrogen emission line Hα $\lambda6563$ Å can be found in the optical spectra (see the green and blue lines in the panel with the red box in Fig. 3). In the UV spectral region, the helium emission line He II $\lambda1641$ Å and the nitrogen line N V $\lambda1239$ Å can be found (see the colored line in the panel with the red box in Fig. B3). In the IR part of the spectra, additional He II emission lines (e.g., He II $1.01\,\mu$m and He II $1.16\,\mu$m) can be found only in the spectra of the highest-mass model (i.e., $M_{ini} = 131\,M_\odot$, see the blue line in the panel with the red box in Fig. B5). The model with $M_{ini} = 20\,M_\odot$ does not show any sign of emission lines in this evolutionary phase. Even the emission line N IV $\lambda7123$ Å disappears.

At the evolutionary stage with $Y_S = 0.98$, that is to say, shortly before the end of CHB, synthetic spectra of the higher-mass models with $M_{ini} = 59\,M_\odot$ and $131\,M_\odot$ show more intense emission lines. In addition to the emission lines they had in the previous evolutionary phases, more He II lines in all spectral regions are now in emission (see the colored lines in the panels with the blue boxes in Fig. 3, and in Figs. B3 and B5). In the UV spectral region, a hydrogen line Lα $\lambda1216$ Å appears in emission. This line would probably be masked by interstellar absorption when observed in the local Universe; but at high redshift, provided that a sufficiently massive population of chemically homogeneously evolving stars are present, it may indeed be identifiable in the host galaxy spectra.

In addition, other He II lines as well as metal lines of C IV and O VI appear (see the colored lines in the panel with the blue box in Fig. B3). Of the N V lines, only N V $\lambda4606$ Å is detected in in absorption, every other nitrogen line is completely absent. In the IR spectral regions, more He II lines are now seen in emission (see the colored lines in the panel with the blue box in Fig. B5). Lines that were in emission in the previous evolutionary phase now become much stronger. The spectra with $M_{ini} = 20\,M_\odot$ also show these emission lines at this evolutionary stage.

The strongest emission line in the optical spectra up to this evolutionary stage is the He II $\lambda4686$ Å line. The flux in the line center corresponds up to about twice that of the continuum (see zoom of the optical spectra in the upper panels in Fig. 5). Another strong line in the optical spectrum is a blend of He II $\lambda6560$ Å and hydrogen Hα (see zoom of the optical spectra in the lower panels in Fig. 5). The strongest line in the UV spectra is He II $\lambda1640$ Å, while in the IR, we find the strongest line to be He II $\lambda1.01\,\mu$m and He II $\lambda1.86\,\mu$m.

At the CHeB stage, all models show almost only emission lines. These are much stronger than any emission line in the preceding CHB phases. In addition to the He II lines, more metal lines of C and O begin to appear (see the colored lines in the upper panels in Fig. 4 and Figs. B4 and B6). N lines are again completely absent, except for Ni v $\lambda4606$ Å, but it is very weak. The strongest lines in the optical spectrum in this evolutionary phase are the oxygen doublet O VI $\lambda\lambda3811, 3834$ Å, the carbon line C IV $\lambda4657$ Å blended with He II $\lambda4686$ Å, and C IV $\lambda7724$ Å. Additionally, other lines are also strong, for instance, O VI $\lambda4499$ Å, O VI $\lambda5288$ Å, and O VI $\lambda6191$ Å. In the UV region the strongest lines are O VI $\lambda1032$ Å and the doublet line C IV $\lambda\lambda1548, 1551$ Å, but also O VI $\lambda1125$ Å, O VI $\lambda2070$ Å, and He II $\lambda1641$ Å. In the IR region the strongest lines are O VI $\lambda1.08\,\mu$m, O VI $\lambda1.46\,\mu$m, and O VI $\lambda1.92\,\mu$m.

We infer that chemically homogeneously evolving stars in early evolutionary phases show spectral features that are typical of weak and optically thin winds. Thus the term TWUIN star
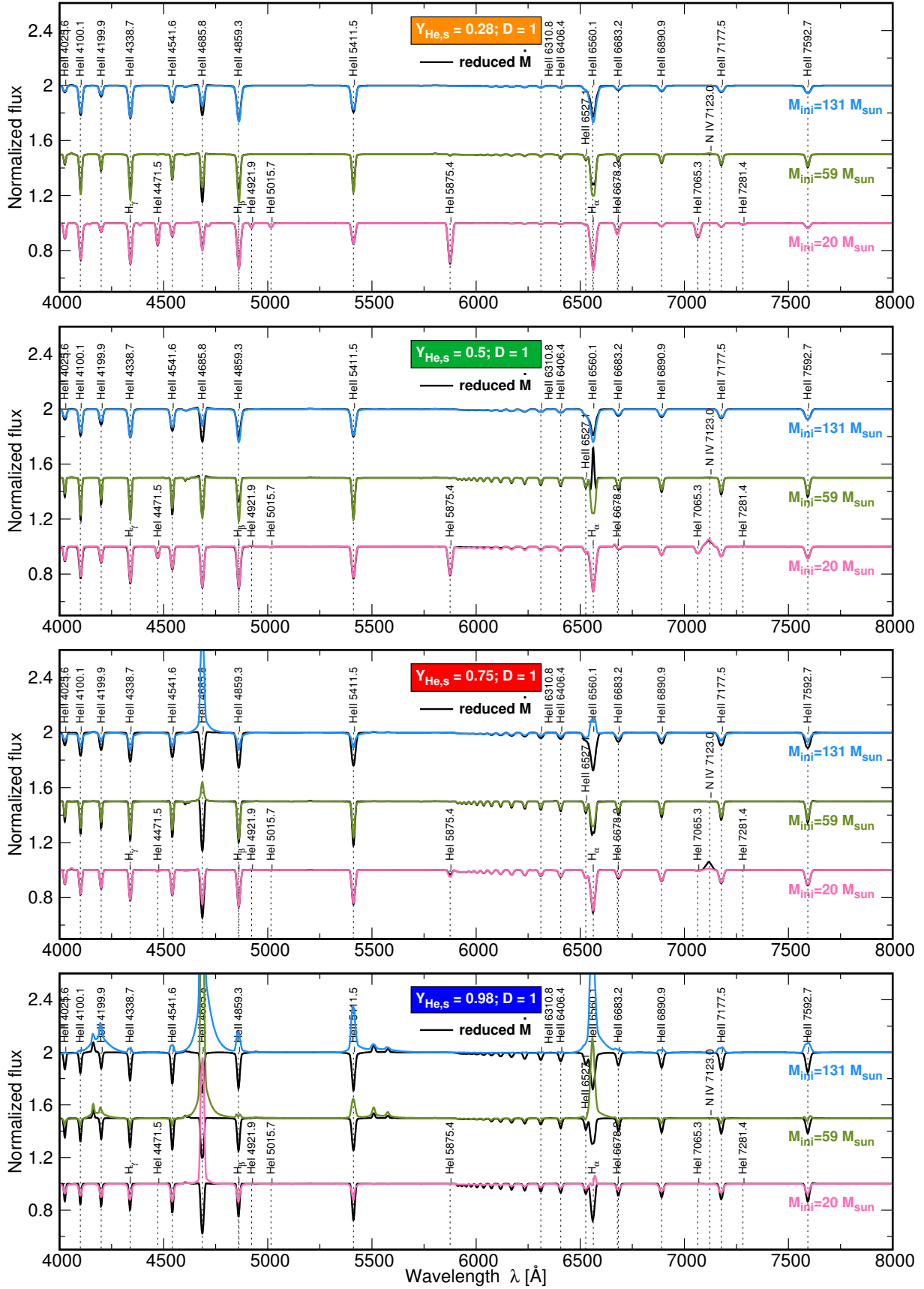
Fig. 3. PoWR spectra in the optical region of TWUIN stars with different $M_{\rm ini}$ (see labels on the right sides of the panels) and in different CHB evolutionary phases marked by the value $Y_{\rm S}$ in the colored boxes. The colored lines correspond to the models calculated with mass-loss rates as given in Table 1. The black lines correspond to the models of the same stars in the same evolutionary stages, but calculated with mass-loss rates 100 times lower (i.e., reduced $\dot{M}$). In all cases, the spectra correspond to smooth ($D = 1$) wind models.
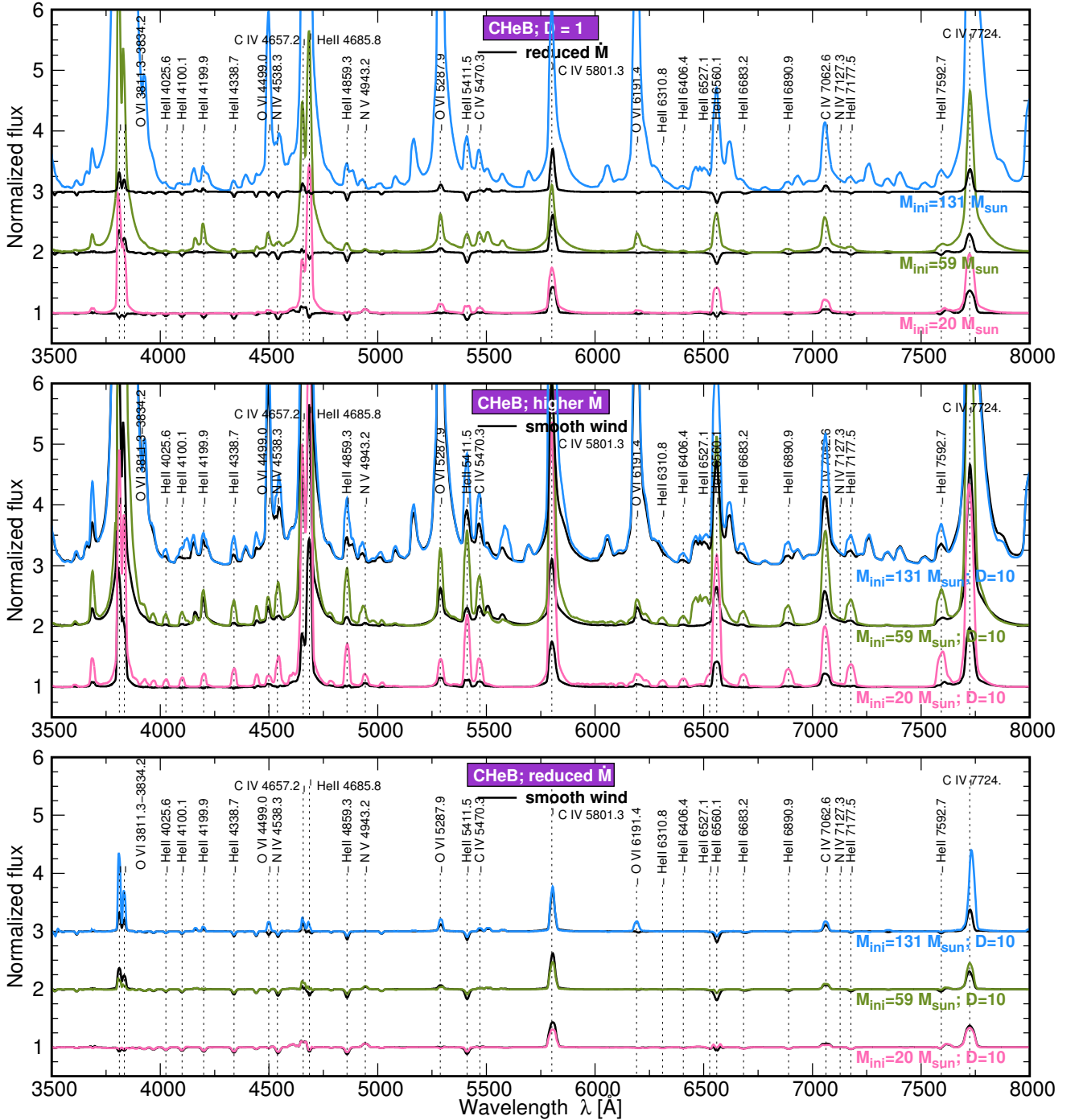
Fig. 4. *Top panel*: same as Fig. 3, but for the CHeB evolutionary phase with Y_S as given in Table 1. *Middle and lowest panels*: same as the top panel, but for clumped wind (i.e., $D = 10$) with nominal (i.e., higher) $\dot{M}$ (*middle panel*) and reduced $\dot{M}$ (*lowest panel*); black lines correspond to the model with smooth wind assumption.

indeed applies to them. In the later evolutionary phases, however, these stars begin to exhibit spectral features that are common for stars with strong and optically thick winds. These features are typical of WR stars.

Table 3 lists the optical depths of the winds of our individual PoWR models. We defined them as the layers with a wind velocity of $v > 0.1\,\mathrm{km\,s^{-1}}$. This is in line with the definition from Eq. (14) in Langer (1989) that we applied in Paper I, but it no longer explicitly relies on the β-law, although this law is implicitly used in the atmosphere models. We list two different optical depth scales in Table 3: τ_{Thom}, which includes only the Thomson

electron scattering, thereby allowing a direct comparison with the estimates made without a detailed atmosphere calculation in Paper I, while τ_{Ross} is the Rosseland mean optical depth that includes all lines and continuum opacity, which is an even more meaningful quantity for identifying optically thick regimes. We marked models with a wind optical depth of $\tau < 1$ in both scales as TWUIN stars.

We find that all models with a reduced mass-loss rate (regardless of clumping) belong to TWUIN stars (i.e., they have a transparent wind), even in their CHeB stages. Models with nominal mass-loss rates and clumping develop an optically thick
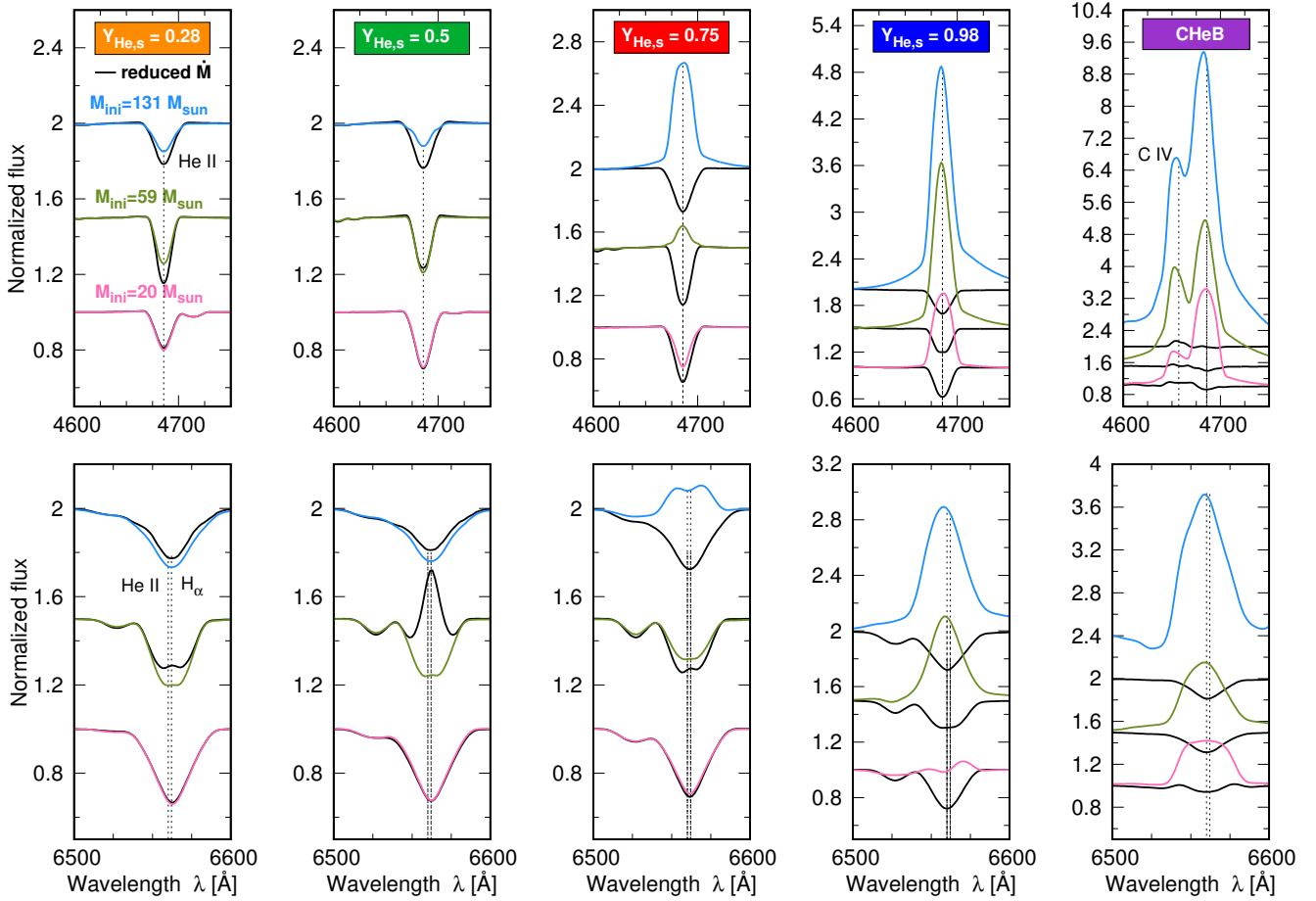
Fig. 5. Same as Fig. 3, but zooming in on the He II $\lambda 4686$ Å line (*upper panels*) and Hα line blended with He II $\lambda 6560$ Å line (*lower panels*). In the CHeB evolutionary phase, the C IV $\lambda 4657$ Å line appears.

wind in their CHeB stages after they experienced the TWUIN phase during their CHB stages. Additionally, the models with high M_{ini} (i.e., M_{ini} = 59 and 131) have optically thick winds even in stages just before the CHeB phase (i.e., with 0.98% of He). From this we can conclude that throughout most of their lifetimes, chemically homogeneously evolving stars at low Z that emit most of their radiation in the UV (see Sect. 6.1.1) have a transparent wind, or in other words, they are TWUIN stars. However, the existence of several optically thick lines or continua in a part of the wind is not excluded. All this is a consequence of the adopted $\dot{M}$ prescriptions in the calculations, as we discuss in the following section.

4.2. Effect of mass loss

To study the effect of mass-loss rates on the synthetic spectra, we calculated a set of models with mass-loss rates that are 100 times lower than used in the stellar evolution calculations. The other parameters remained unchanged. These models are plotted as black lines in Figs. 3, and 5, and in the top panels of Figs. 4, but also in Figs. B3, and B5, and in the top panels of Figs. B4 and B6.

Models with lower mass-loss rate yield mostly absorption-line spectra during the CHB evolutionary phases. They show only negligible emission features (see the black lines in Fig. 3 and Figs. B3 and B5). Lowering the mass-loss rate affects the strength of the lines. While those few lines that are in emission become less intense, for most of the lines that are already

in absorption using the lower mass-loss rates, the absorption becomes even deeper. This illustrates that even pure absorption lines can be filled up by wind emission when applying higher $\dot{M}$. A more prominent effect of the same origin is the change in some lines from emission to absorption (see the differences between the colored and black lines in Fig. 3 and Figs. B3 and B5).

However, some absorption lines calculated with lower mass-loss rate become less pronounced than what is expected as a general influence of lowering mass loss. A more prominent effect of the same origin (i.e., absorption lines switch to emission) can be seen, for instance, in He II $\lambda 6560$ Å blended with Hα (see the first and second lower panels from the left in Fig. 5) and He II $\lambda 1.09\,\mu$m, He II $\lambda 1.28\,\mu$m, He II $\lambda 1.88\,\mu$m, and He II $\lambda 1.88\,\mu$m blended with H I lines (see the upper two panels with orange and green boxes in Fig. B5). The reason is that for the models with a higher percentage of hydrogen (more than 50%), the He II lines that are in absorption are blended with hydrogen emission lines, which are stronger. The combination of the He II absorption line and H I emission lines results in the effect we described above. For more evolved models (i.e., those that have much less or no helium at the surface), this effect is not visible.

The low mass-loss spectra of less evolved TWUIN stars (with Y_S = 0.28 and Y_S = 0.5) regardless of their mass do not show any significant differences from their high mass-loss counterparts except for the effect we described above. Thus we can conclude that in early evolutionary stages, the assumptions about mass loss in stellar evolutionary computations has a negli-

Table 3. Wind optical depths from our PoWR models.

D	$\dot{M}$	M_{ini}	Label	τ_{Thom}	τ_{Ross}	TWUIN
		20	T-1 (0.28)	0.001	0.001	Yes
		20	T-2 (0.50)	0.002	0.002	Yes
		20	T-3 (0.75)	0.015	0.016	Yes
		20	T-4 (0.98)	0.222	0.235	Yes
		20	T-5 (pMS)	0.914	1.112	No
		59	T-6 (0.28)	0.015	0.016	Yes
		59	T-7 (0.50)	0.024	0.025	Yes
1	Higher	59	T-8 (0.75)	0.149	0.157	Yes
		59	T-9 (0.98)	3.740	4.613	No
		59	T-10 (pMS)	4.456	5.748	No
		131	T-11 (0.28)	0.059	0.062	Yes
		131	T-12 (0.50)	0.090	0.094	Yes
		131	T-13 (0.75)	0.589	0.622	Yes
		131	T-14 (0.98)	3.460	3.848	No
		131	T-15 (pMS)	8.401	10.804	No
		20	T-1 (0.28)	0.000	0.000	Yes
		20	T-2 (0.50)	0.000	0.000	Yes
		20	T-3 (0.75)	0.000	0.000	Yes
		20	T-4 (0.98)	0.002	0.002	Yes
		20	T-5 (pMS)	0.009	0.009	Yes
		59	T-6 (0.28)	0.037	0.041	Yes
		59	T-7 (0.50)	0.000	0.000	Yes
1	Reduced	59	T-8 (0.75)	0.002	0.002	Yes
		59	T-9 (0.98)	0.037	0.041	Yes
		59	T-10 (pMS)	0.048	0.054	Yes
		131	T-11 (0.28)	0.001	0.001	Yes
		131	T-12 (0.50)	0.001	0.001	Yes
		131	T-13 (0.75)	0.007	0.007	Yes
		131	T-14 (0.98)	0.034	0.036	Yes
		131	T-15 (pMS)	0.093	0.102	Yes
		20	T-1 (0.28)	0.001	0.001	Yes
		20	T-2 (0.50)	0.002	0.002	Yes
		20	T-3 (0.75)	0.015	0.016	Yes
		20	T-4 (0.98)	0.225	0.256	Yes
		20	T-5 (pMS)	0.926	1.054	No
		59	T-6 (0.28)	0.014	0.015	Yes
		59	T-7 (0.50)	0.026	0.028	Yes
10	Higher	59	T-8 (0.75)	0.142	0.157	Yes
		59	T-9 (0.98)	1.153	1.198	No
		59	T-10 (pMS)	4.329	5.471	No
		131	T-11 (0.28)	0.057	0.061	Yes
		131	T-12 (0.50)	0.088	0.095	Yes
		131	T-13 (0.75)	0.649	0.673	Yes
		131	T-14 (0.98)	3.536	3.863	No
		131	T-15 (pMS)	8.447	10.776	No
		20	T-1 (0.28)	0.000	0.000	Yes
		20	T-2 (0.50)	0.000	0.000	Yes
		20	T-3 (0.75)	0.000	0.000	Yes
		20	T-4 (0.98)	0.002	0.002	Yes
		20	T-5 (pMS)	0.009	0.009	Yes
		59	T-6 (0.28)	0.000	0.000	Yes
		59	T-7 (0.50)	0.000	0.000	Yes
10	Reduced	59	T-8 (0.75)	0.002	0.002	Yes
		59	T-9 (0.98)	0.015	0.015	Yes
		59	T-10 (pMS)	0.042	0.047	Yes
		131	T-11 (0.28)	0.001	0.001	Yes
		131	T-12 (0.50)	0.001	0.001	Yes
		131	T-13 (0.75)	0.007	0.008	Yes
		131	T-14 (0.98)	0.035	0.037	Yes
		131	T-15 (pMS)	0.087	0.194	Yes

Notes. τ_{Thom} only includes electron scattering, while τ_{Ross} includes all lines and continuum opacity. Models with $\tau < 1$ in the wind in both of the τ scales are marked as TWUIN stars. Values of $\tau < 0.001$ are listed as zero.

gible effect and would not lead to predicting different observable spectra.

At the evolutionary stage $Y_S = 0.75$, the spectra with $M_{ini} = 59$ and $131\,M_\odot$ show changes in some optical lines (e.g., He II at $\lambda 4686\,\text{Å}$ and $\lambda 6560\,\text{Å}$) from emission to absorption with decreasing mass-loss rate, while those with $M_{ini} = 20\,M_\odot$ still do not show any significant difference in their spectra (see the panel with the red box in Fig. 3). A similar effect is seen in the UV and IR regions (see the panels with the red boxes in Figs. B3 and B5).

The fact that chemically homogeneously evolving stars in early evolutionary stages have weak and transparent winds is in accordance with previous studies such as Paper I. There the authors were motivated to introduce the class of TWUIN stars.

For stars in the evolutionary stage $Y_S = 0.98$, the effect of the mass loss on the spectra is more pronounced. These spectra show a few very weak emission lines, such as He II at $\lambda 4200\,\text{Å}$ and He II $\lambda 5412\,\text{Å}$ (see the panel with the blue box in Fig. 3). In the UV and IR spectral regions, the effect of a decreasing mass-loss rate is also visible (see the panels with the blue boxes in Figs. B3 and B5). The spectra with $20\,M_\odot$ show the same spectral features as more massive stars in previous evolutionary stages.

The most pronounced differences appear for the latest evolutionary stage. Models with CHeB show a strong dependence on the applied mass-loss rate, particularly for the stars with $M_{ini} = 59$ and $131\,M_\odot$ (see the top panel in Fig. 4 and Figs. B4 and B6). These more evolved stars have a strong and thick wind with our default prescription, and thus decreasing the mass-loss rates has an enormous influence on the resulting spectra. While the nominal mass loss produces very strong and broad emission features, the reduced one produces much less pronounced emission lines, if any. We therefore conclude that while varying the mass-loss rates in the early evolutionary phases has no significant effect on the spectral appearance of these TWUIN stars, proper mass-loss rates for the more evolved stages where the models start to show WR-features are of uttermost importance.

4.3. Effect of clumping

From observations and theoretical considerations, we know that winds of almost all massive stars are inhomogeneous (e.g., Hamann et al. 2008; Puls et al. 2008). The absence of direct observations of chemically homogeneously evolving (TWUIN) stars also means that we do not have any observational constraint on clumping. However, we can check how wind inhomogeneities may influence the spectral appearance from a purely theoretical point of view. Using a different clumping factor D, here we study how much the spectral appearance changes when all other parameters are kept the same.

For our two sets of models, the set with the mass-loss rates as used in the stellar evolutionary models (higher $\dot{M}$) and the other set with mass-loss rates 100 times lower (reduced $\dot{M}$), we calculated spectra with clumping factors $D = 1$ (corresponding to a smooth wind) and $D = 10$ assuming a clumping onset in the wind.

For the models with higher mass-loss rates, the general influence of clumping on the spectral appearance is a reduction of absorption. The lines that are in emission in the smooth wind models are made much stronger by clumping. Some lines even switch from absorption to emission, for instance, the He II $\lambda 1641\,\text{Å}$, $\lambda 4686\,\text{Å}$, $\lambda 5412\,\text{Å}$ lines and He II $\lambda 6560\,\text{Å}$ line blended with the hydrogen Hα $\lambda 6563\,\text{Å}$ line (see Fig. 6 and also Figs. B8 and B10).

For the models with reduced mass-loss rates, spectra during the CHB phases stay almost unchanged when clumping is taken
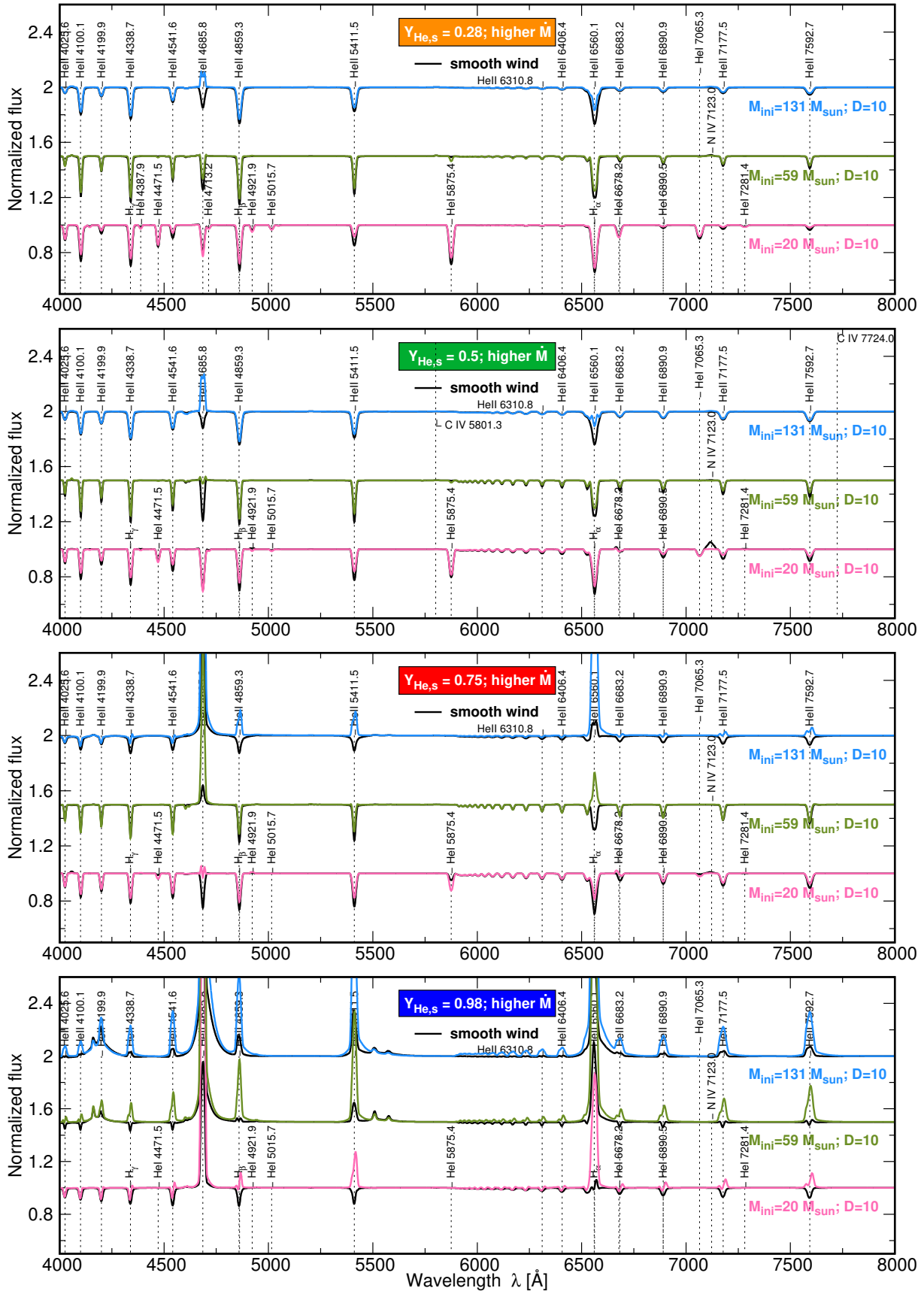
Fig. 6. PoWR spectra in the optical region of TWUIN stars with different $M_{\rm ini}$ (see labels on the right side of the panels) and in different CHB evolutionary phases marked by the value $Y_{\rm S}$ in the colored boxes. The mass-loss rates are taken from the stellar evolutionary calculations (i.e., higher $\dot{M}$). Colored lines correspond to the clumped wind models (i.e., $D = 10$), while the black lines correspond to the smooth wind.
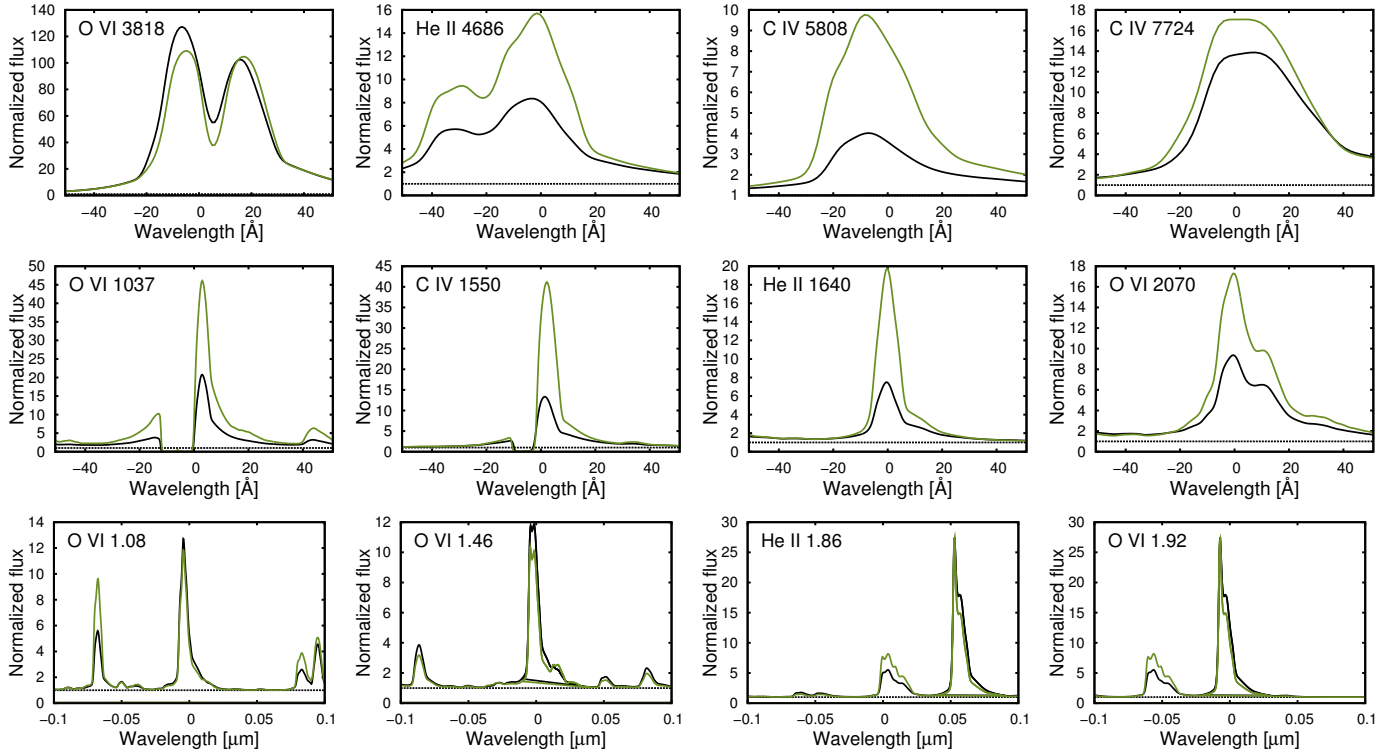
Fig. 7. Influence of clumping on the line strength. Emission lines in the optical (*upper panels*), the UV (*middle panels*), and the IR (*lower panels*) regions of the model with $M_{ini} = 131\,M_\odot$ in the CHeB evolutionary phase (mass-loss rate of $\log(\dot{M}/M_\odot/\text{yr} = -4.23)$). X-axis is centered around the wavelength indicated by the key legend (e.g., He II 4686 means He II $\lambda 4686\,\text{Å}$). Green lines corresponds to clumped wind models with $D = 10$, and black lines to smooth wind models with $D = 1$.

into account (see the comparison between the colored and black lines in Figs. B7, B9, and B11). This effect is reasonable because with reduced mass-loss rates the wind becomes weaker, less dense, and more transparent. Hence, introducing clumping contributes very little to the changes in optical properties of the wind.

The influence of clumping on spectral appearance is as expected. Models with the same $\dot{M}\sqrt{D}$ give similar spectra (at least the same equivalent width of the recombination lines). Therefore, if we increase clumping with the same $\dot{M}$, the spectra react as if we had increased $\dot{M}$. If $\dot{M}$ is low enough not to affect the recombination lines very much, we do not see much difference, which is why the low-$\dot{M}$ models do not show much difference.

The importance of clumping is more pronounced in the CHeB phase. In this stage, the winds become stronger and denser, and the contribution of clumping to the line formation becomes important. The models for CHeB stars with higher mass-loss rates show very pronounced emission lines, which become even stronger when clumping is taken into account, as shown in Fig. 7. With clumping, the dense wind becomes more transparent, and thus more radiation can escape and contribute to the line strength (see the middle panels in Fig. 4). However, the models with reduced mass-loss rates remain, even in this evolutionary stage, almost unchanged when clumping is taken into account (see the lowest panel in Fig. 4). A similar effect is seen in the UV and IR regions (see the middle and lowest panels in Figs. B4 and B6).

5. Spectral classification

We classified our model spectra according to the commonly used Morgan–Keenan spectroscopic classification scheme. We give a detailed description of this classification scheme in the context

of hot massive stars in Appendix A. We report our findings summarized in Table 4, and discuss some details below.

5.1. TWUIN stars are very hot O stars

Most of our spectra that show almost no emission lines, that is, the stellar models that have been designated as TWUIN stars in Paper I, are assigned to class O 4 or earlier. This means that they are very early O-type giants or supergiants because the logarithm of the ratio of He I $\lambda 4473\,\text{Å}$ to He II $\lambda 4543\,\text{Å}$, which is being smaller than -0.6, causes them to belong at least to type O 4 (Mathys 1988), and in the absence of nitrogen lines, we cannot distinguish between earlier classes (as done, e.g., in Walborn et al. 2002). The ratio of these helium lines is usually around -1.5 or lower. All we can safely say for these stars therefore is that they are of class O 4 or earlier.

Luminosity classes for the spectra that are consistent with classes earlier than O 4 type (marked as <O 4 in Table 4) are defined based on the nature of the He II $\lambda 4686\,\text{Å}$ line. If it is found in emission, the spectrum is classified as a supergiant (i.e., luminosity class I). If it is found in weak absorption (i.e., the logarithm of the absolute value of the equivalent width is lower than 2.7, cf. Mathys 1988), the spectrum is classified as a giant (i.e., luminosity class III), and if it is strongly in absorption, a dwarf (i.e., luminosity class V).

We find late-O type stars, that is, O 5 to O 9.5, only among the lowest mass models (with $M_{ini} = 20\,M_\odot$). As for their luminosity classes, we applied two criteria: one for those earlier than O 8, as explained above, and another for those between O 8.5−O 9.5 (cf. Appendix A). This other criterion is provided by Conti & Alschuler (1971) and is based on the equivalent width ratio of the lines Si IV $\lambda 4090\,\text{Å}$ and He I $\lambda 4143\,\text{Å}$ (but

Table 4. Spectral classification of our stellar models.

M_{ini}	Label	$D = 1$		$D = 10$	
		Reduced $\dot{M}$	Nominal/higher $\dot{M}$	Reduced $\dot{M}$	Nominal/higher $\dot{M}$
20	T-1 (0.28)	O 8.5 V	O 8.5 V	O 9.5 V	O 9 V
20	T-2 (0.5)	O 5.5 III	O 6 III	O 7 III	O 7 III
20	T-3 (0.75)	<O 4 III	<O 4 III	<O 4 III	O 5 I
20	T-4 (0.98)	O 4 III	<O 4 I	<O 4 III	O 4 I
20	T-5 (pMS)	WO 2 [−]	WO 1	WO 2 [−]	WO 1 [WO 3]
59	T-6 (0.28)	<O 4 III	<O 4 III	<O 4 III	<O 4 III
59	T-7 (0.5)	<O 4 III	<O 4 III	<O 4 III	<O 4 I
59	T-8 (0.75)	O 4 III	<O 4 I	<O 4 III	<O 4 I
59	T-9 (0.98)	<O 4 III	<O 4 I	<O 4 III	[WO 2 or WO 1]
59	T-10 (pMS)	WO 1 [WO 3]	WO 1	WO 1 [WO 3]	WO 1
131	T-11 (0.28)	O 4 III	<O 4 III	<O 4 III	<O 4 I
131	T-12 (0.5)	O 4 III	<O 4 III	<O 4 III	<O 4 I
131	T-13 (0.75)	<O 4 III	<O 4 I	O 4 III	<O 4 I
131	T-14 (0.98)	<O 4 III	O 4 I	<O 4 III	WO 4 [WO 2 or WO 1]
131	T-15 (pMS)	WO 1 [WO 3]	WO 1	WO 1 [WO 3]	WO 1

Notes. TWUIN stars (i.e., CHB objects) are typically assigned to some O-type subclass; a "<" sign indicates that a model is consistent with earlier classes as well. For WR stars, the spectrum may be consistent with more than one subclass; we give the secondary classification (as defined in Table 3 of Crowther & Hadfield 2006) in square brackets. See also the text and Appendix A.

see also Martins 2018). With this, our spectra of a 20 $M_\odot$ star are assigned to dwarf (V) at the ZAMS and to giant (III) in the middle of the MS phase. However, this distinction seems to be an artifact of using two different criteria for those earlier and later than O 8. As Fig. 1 and Table 1 attest, the radius of the 20 $M_\odot$ model does not change significantly between the phases $Y_S = 0.28$ and $Y_S = 0.5$. The luminosity does change, however, showing that the conventional nomenclature associated with luminosity classes (giant, dwarf, etc.) may not always be very meaningful in accounting for the radial size of a star.

We did not find any of our spectra to be consistent with the O f subclass (Crowther et al. 1995; Crowther & Walborn 2011) because the defining feature of this subclass, the line N III λ4640 Å, is completely absent in all our spectra. The O f subclass practically means that the star has a fairly strong wind; therefore galactic early-type stars tend to have it. It is not surprising, however, that our low-metallicity stars with weak winds do not show this feature.

Some of our <O 4 stars are really hot. Tramper et al. (2014) investigated ten low-metallicity (down to 0.1 $Z_\odot$) O-type stars and found the hottest to be $T_{\mathrm{eff}} = 45$ kK, while our hottest O-type object has $T_{\mathrm{eff}} = 85$ kK. The detection of a very hot, early-O type star at low metallicity without an IR-excess would therefore mean that this source is a strong candidate for a star resulting from chemically homogeneous evolution. We refer to our Sect. 6.1, where we compare one of our <O 4 type spectra to a regular O-type stellar spectra from the literature.

5.2. TWUIN stars turn into Wolf–Rayet stars in the CHeB phase

The term Wolf–Rayet stars refers to a spectral class, based on broad and bright emission lines that are observed in the optical region. As briefly described in Sect. 1, authors working on stellar evolution sometimes refer to objects that are hot and (more or less) hydrogen-deficient as WR stars as well. From an evolutionary point of view, the surface of a massive star can become hydrogen-poor because of the (partial) loss of the hydrogen-rich envelope either by Roche-lobe overflow (a scenario originally

suggested by Paczyński 1967), or by stellar winds (Conti 1975). A third option that can lead to a hydrogen-deficient surface composition is internal mixing (e.g., due to rotation, as in the present work). Nonetheless, the fact that a stellar model surface is hydrogen poor does not necessarily mean that its wind is optically thick (as shown in Sect. 6 of Paper). It does not mean either that broad emission lines develop (as shown by our CHB spectra), although this may occur (as shown by our CHeB spectra). Below we discuss the spectral classes of the latter case.

All our spectra of the CHeB phase show features typical for WR stars of the WO type: strong C IV λ5808 Å, O V λ5590 Å, and O VI λ3818 Å in emission. We classify these objects according to criteria in Table 3 of Crowther et al. (1998). There are two main criteria, a primary and a secondary. We find that these two sometimes do not provide the same class. In this case, we mention the secondary classification in square brackets in our Table 4.

We find that nitrogen lines are almost completely absent. The line N V λ4606 Å is sometimes present, most of the time in absorption. When it is in emission, its equivalent width never increases above 0.3 Å, which means that it is very weak. Other lines typical for WN stars (Smith et al. 1996) such as N III λ4640 Å and N IV λ4057 Å, are not found in any of our spectra. The almost complete absence of N-lines may make a future observer consider such a star to be some other type, certainly not WN.

Thus we conclude that after first producing very hot early-O type stars during the CHB phase, chemically homogeneous evolution leads to WO type stars during the CHeB phase. We recall that the CHeB lifetime is about 10% as long as the CHB lifetime. Therefore, in a population of chemically homogeneously evolving stars, we expect to find ten times more hot early-O stars than WO stars.

6. Discussion

6.1. Comparison to synthetic spectra from the literature

6.1.1. O-type spectra

We compared one of our absorption line spectra to a typical O-type spectra in the literature. In particular, we compared

our model labeled T-8 in Table 1 (with clumping and nominal mass-loss rate), and a model spectrum of an O 3 star taken from the PoWR SMC OB model grid (see Hainich et al. 2019) database[1] (see Fig. 8) corresponding to the composition of the SMC ($Z_{SMC} \sim 0.2\,M_\odot$). The parameters of the SMC O 3 model are $T_{eff} = 50\,kK$, $\log(L_*/L_\odot) = 5.52$, $\log(\dot{M}/M_\odot/yr) = -5.9$, $\log(g\,cm^{-1}\,s^{-2}) = 4.4$, and $D = 10$. We note that the main differences between the two models are (i) the metallicity (ours is about ten times lower, but the He abundance is almost the same) and (ii) the surface temperature (ours is 69 kK). An effect of smoothing and broadening the lines due to fast rotation is taken into account (see Sect. 4) for both models assuming the same rotational velocity, which corresponds to the T-8 model (see Table 1).

From comparing the SEDs of both stars placed at the same distance of 10 pc (see the top panel in Fig. 8) we can infer that the amount of emitted far- and extreme UV ionizing radiation increases particularly at shorter wavelengths (around the H I ionization edge). This is consistent with the fact that our model has a higher surface temperature. Another effect that may lead to higher UV flux is that there is less line blanketing at low metallicity, therefore less flux is redistributed to longer wavelengths.

For the spectral features, we can infer the following. In the optical region, the SMC O 3 spectrum shows the C IV $\lambda\lambda 5801, 5812\,Å$ lines, while in the TWUIN T-8 model, we do not find any metal lines. In the UV region, the SMC O 3 spectra also show very strong metal lines (e.g., the doublet O VI $\lambda\lambda 1032, 1038\,Å$, the doublet N V $\lambda\lambda 1239, 1243\,Å$, O V $\lambda 1371\,Å$, and the doublet N IV $\lambda\lambda 1548, 1551\,Å$) that are not present in the TWUIN T-8 model spectra. This is expected because the TWUIN star models have very low metallicity.

He II lines are in very strong emission in the TWUIN T-8 model spectra (e.g., He II $\lambda 1641\,Å$, He II $\lambda 4687\,Å$, and He II $\lambda 6562\,Å$), while in the SMC O 3 spectra, these lines are in absorption. This is consistent with the fact that the TWUIN model has a high surface helium abundance ($Y_S \sim 0.5$). On the other hand, He I lines are not present in the TWUIN T-7 model spectra, while in SMC O 3, they are visible (see the He I $\lambda 5877\,Å$, He I $\lambda 7065\,Å$, and He I $\lambda 3888\,Å$ lines in Fig. 8).

6.1.2. WO-type spectra

We compared our emission line spectra to a typical WO-type spectra from the literature. Comparing our models to a WO star model was difficult because no analyses of observations of WO stars exist with the metallicity we study here, and, consequently, no models exist either. For somewhat higher metallicities such as Z_{SMC}, very few models have ever been calculated. Here we used a model from Shenar et al. (2016), which was applied for the analysis of the SMC binary star AB 8 with the following model parameters: $T_{eff} = 141\,kK$, $\log(L_*/L_\odot) = 6.15$, $\log(\dot{M}/M_\odot/yr) = -4.8$, $v_\infty = 3700\,km\,s^{-1}$, $\log g(cm^{-1}\,s^{-2}) = 5.4$, and $D = 40$. These parameters are similar to those of our T-10 model (see Table 1) with clumping and nominal mass-loss rate.

The comparison is shown in Fig. 9. For both models rotation is taken into account assuming the same rotational velocity, which corresponds to the T-10 model (see Table 1). The T-10 model is somewhat more luminous. Both models have the same beta (i.e., $\beta = 1$), and similar mass-loss rates and

$\log g$. The mass-loss rates of both models are relatively high, but we do expect the Z-dependency to drop for WO stars because their atmospheres are enriched with fusion products that are not related to the initial metallicity, and these products contribute to the driving of their winds. Moreover, the WO star in the SMC seems to be much more luminous than the Galactic WO stars, which increase their mass-loss rate compared to other WO stars.

The main differences between the two models are (i) the surface temperature (ours is 138 kK), (ii) the terminal velocity (ours is 1000 km s^{-1}), (iii) the clumping factor (ours is 10), and (iv) the metallicity and element ratios (see the mass fractions in Table 1). The mass-fraction of the WO 4 model are He = 0.399, C = 3×10^{-1}, O = 3×10^{-1}, and Fe = 6×10^{-4}. In the WO 4 model, N was not included, while in the T-10 model it is. For both models, H is not included. The T-10 model has about twice as much, somewhat less C, by more than two orders of magnitude less O, and by more than one order of magnitude fewer iron group elements.

The difference in SED (see the top panel in Fig. 9) can be attributed to the different Fe abundances in the models. The Fe abundance in the WO star model is more than an order of magnitude higher than in our T-10 model, causing substantial absorption and re-emission of UV photons in the visual part (line blanketing). The difference in the spectral line shapes can mainly be attributed to differences in v_∞, which is more than a factor three larger in the WO model. Finally, the large differences in the strength of some spectral lines is a result of differences in two things: the abundances, and the so-called "transformed radii" R_t, which represent an integrated emission measure in the wind (see Eq. (1) in Hamann et al. 2006). The SMC WO model has a higher R_t value, and hence overall weaker spectral lines. Although the spectra of these models differ significantly, they do predict similar lines to appear in the spectrum.

To conclude, the different environment and formation history of chemically homogeneously evolving stars could mean that they appear somewhat different than the SMC WO component at their evolved phases. Their exact appearance would depend on parameters such as the terminal velocity, which was fixed in our study. Regardless of this uncertainty, however, we find that so-called TWUIN stars appear as WO stars in their evolved phases.

6.2. Validity of our model assumptions

Our wind models and emergent spectra are theoretical predictions based on current knowledge of stellar evolution and stellar wind modeling. However, they are also subject to several assumptions.

The radial wind velocities in our models were assumed to follow the β-law in Eq. (5). Although there exist several calculations of the wind velocity law that take into account acceleration of matter by scattered and absorbed radiation either in an approximate way using force multipliers (e.g., Castor et al. 1975; Abbott 1980; Pauldrach et al. 1986) or in a more exact way using detailed radiative transfer (e.g., Abbott 1982; Gräfener & Hamann 2005; Pauldrach et al. 2012; Krtička & Kubát 2010, 2017; Sander et al. 2017), the β-velocity law became a standard assumption in modeling stellar wind spectra. Using a free parameter β allows finding a velocity law that fits the observations best, regardless of the consistency of such a result. As discussed by Krtička et al. (2011), the β-velocity law is a good approximation to consistent hydrodynamical calculations, but a better and more exact fit can be obtained using Legendre polynomials. In any case, using the β-velocity law is a reasonable first approximation.

---

[1] http://www.astro.physik.uni-potsdam.de/~wrh/PoWR/SMC-OB-II/
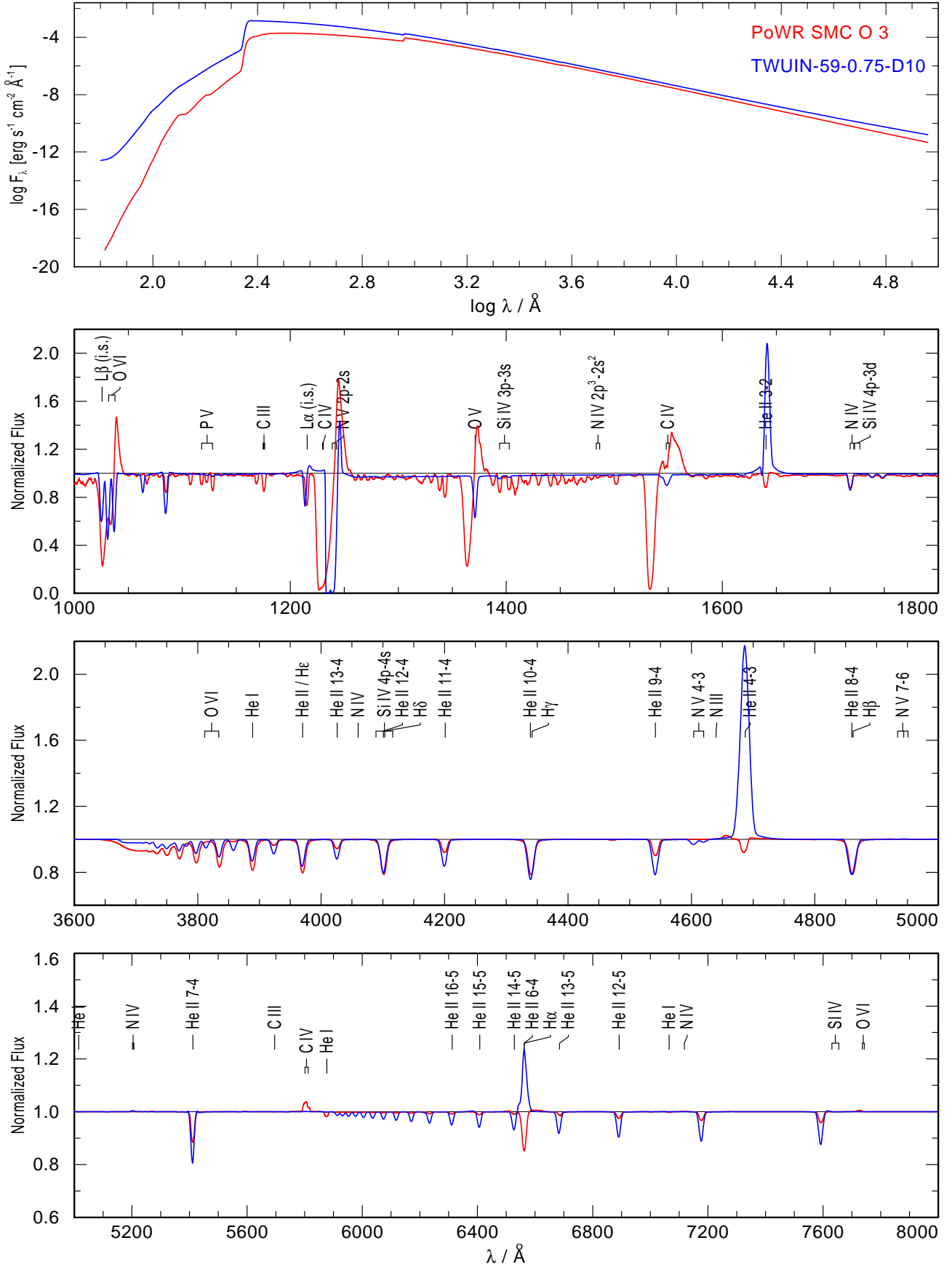
Fig. 8. Comparison of one of our representative O 3 III spectra (i.e., the TWUIN T-8 model, see Table 1) to an O 3 synthetic star from the literature. Both stars are placed at the same distance of 10 pc. An effect of line broadening due to fast rotation is taken into account, as described in Sect. 4 assuming the same rotational velocity, which corresponds to the T-8 model. See Sect. 6.1 for more details.
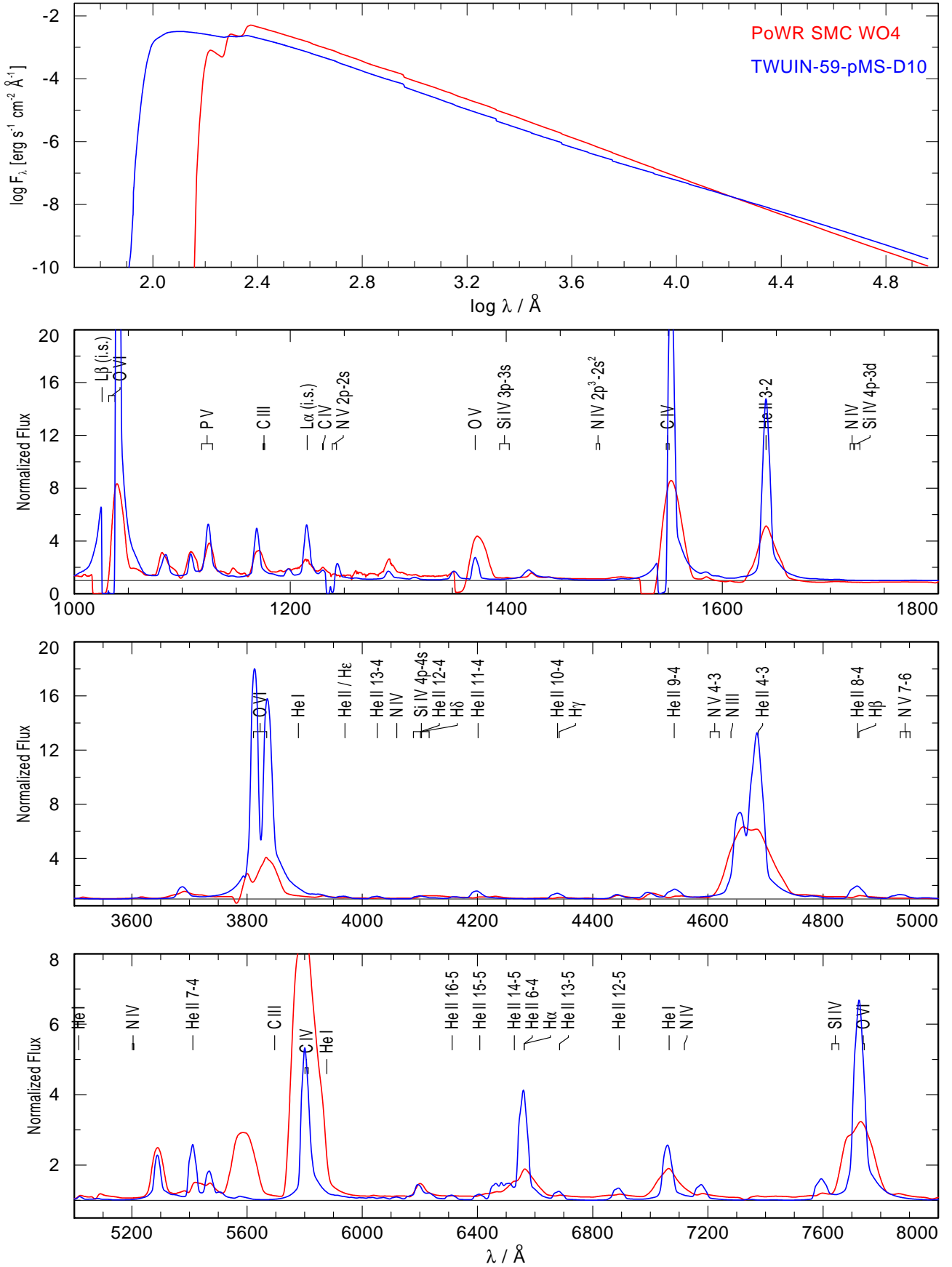
Fig. 9. Same as Fig. 8, but comparing our WO 1 spectra (i.e., TWUIN T-10 model, see Table 1) to an SMC WO 4 synthetic spectrum from Shenar et al. (2016).

We also had to assume a mass-loss rate. This was done by taking the mass-loss rates that were assumed in the stellar evolutionary models. As explained in Sect. 2.1, the evolutionary models assumed a mass-loss rate following certain recipes. The recipe of Vink et al. (2000, 2001) in Eq. (1) was derived from atmosphere simulations that used a detailed treatment of a full line list for a fixed velocity law. The recipe of Hamann et al. (1995) given in Eq. (2) was, on the other hand, based on observed spectra of WR stars. Nonetheless, these prescriptions may not be valid for TWUIN stars. To ensure that we understand the consequences of using them anyway, we therefore tested the effect of decreasing the mass loss by 100, to be consistent with the findings of Hainich et al. (2015, cf. our Table 2). The results of this test in the context of line formation was reported in Sect. 4.2.

As chemically homogeneously evolving stars are generally fast rotators (~0.6 $v_{\rm crit}$), this may have some as yet unexplored effect on their wind structures (Owocki et al. 1996). However, this would require detailed hydrodynamical calculations in at least 2D, which are beyond the scope of this paper. We accounted for the spectral imprint of fast rotation by performing a flux convolution of the emergent spectrum with a rotation profile.

Here we only studied the spectra of single stars, but a large fraction of massive stars are born in close binary systems and thus undergo interaction with a companion during the evolution at some point (e.g., Paczyński 1967; Sana et al. 2012; Götberg et al. 2017). However, the ratio of binary stars versus single stars is unknown at the metallicity we study, and it may be quite different from the Galactic case (e.g., because the stability of the collapsing star-forming cloud may be influenced by its metallicity). For example, TWUIN stars in a close binary orbit have been suggested to be the stellar progenitors of compact object mergers, explaining the origin of gravitational waves (Marchant et al. 2016, 2017). How such an interaction with a companion influences the spectral appearance remains to be studied.

6.3. Future research on TWUIN stars – theory

Taking the same mass-loss rate as was assumed when computing the evolution makes our spectral predictions consistent with evolutionary models. However, in the absence of actual observations of TWUIN stars, the question is whether such a star can have a wind at all. Testing this can be done similarly to how it was done by Krtička & Kubát (2014) for the case of winds with non-solar CNO abundances. Although this test is computationally expensive and goes beyond the scope of this work, here we summarize the basic idea, as well as the results we may expect from such a test, as a motivation for future work.

As described, we assumed that the wind structure of all TWUIN stars can be described by a β-law (e.g., Puls et al. 2008), motivated by hydrodynamical consistent calculations for Galactic WN stars, for example (Gräfener & Hamann 2008). Additionally, we assumed input parameters (β, v_∞) that are typical for hot massive O-type stars and WR stars at $0.2 \ldots 1\,Z_\odot$. All this may not hold for extremely low-metallicity environments; and the issue is further complicated by the observed steep metallicity dependence of the mass loss found by Hainich et al. (2015) as well as by the so-called "weak wind problem" (see, e.g., Martins et al. 2005; Marcolino et al. 2009; Huenemoerder et al. 2012).

One way to validate the assumptions we used in this work would be hydrodynamical simulations of the wind and its structure. This has been done for Galactic massive O stars in Krtička & Kubát (2017) and for a few WR stars in Gräfener & Hamann (2008). Although expensive, such simula-

tions for the models presented in this work could provide essential information on how valid our spectrum predictions are.

For example, if atmosphere models based on hydrodynamic simulations point to different values for β, $\dot{M}$, or v_∞, this will influence the predicted line strengths in our spectra and thus lead to assigning different spectral classes for these stars. The models may even show that the β-law as such is not applicable at all in this regime or that these stars, at least during some parts of their evolution, might not have winds at all. Thus, future studies in this direction are sorely needed.

As for metallicity, here we only applied one set of stellar evolutionary models, all computed with $Z_{\rm ini} = 0.02\,Z_\odot$. However, chemically homogeneous evolution is predicted to occur at various sub-solar metallicities (see, e.g., Brott et al. 2011). Although its prevalence is expected to be larger at lower metallicity (see Sect. 10.4 of Paper 1), it is nonetheless an important future research direction to study the spectra of chemically homogeneously evolving stars up to at least $Z_{\rm SMC}$.

6.4. Future research on TWUIN stars – observations

It is essential to obtain observational samples of metal-poor massive stars to test our theories. Ideally, we would need an extensive spectral catalog of about 50–100 massive stars at metallicities lower than $0.1\,Z_\odot$. This task seems challenging, but not at all impossible with the most modern observing facilities and the next-generation telescopes coming up. For example, ESO's MUSE spectrograph can take optical spectra of several dozen massive stars in local-group galaxies (Castro et al. 2018), while systematic studies of these spectra (including spectral classification and determination of mass-loss rates) could be made with advanced tools (e.g., Hillier & Miller 1998; Puls et al. 2005; Gustafsson et al. 2008; Kamann et al. 2013; Tramper et al. 2013; Ramachandran et al. 2018).

Until we obtain a comprehensive census of individual massive stars at low metallicity, we may compare our predictions to observed populations of massive stars. Such a comparison of our model predictions to unresolved observed features of massive star populations in the dwarf galaxy I Zwicky 18 (Kehrig et al. 2015, 2016) is planned in a subsequent work.

Another interesting application of our spectra might be made in the context of the reionization history of the Universe. It has been suggested that massive stars, and especially chemically homogeneous evolution, may be important for this process (e.g., Eldridge & Stanway 2012), as WR-like emission bumps are often not found in the spectra of high-redshift galaxies. We note that our spectral models suggests that TWUIN stars are indeed not expected to show prominent emission lines because their winds are rather weak. Thus, these stars' contribution to the reionization epoch should also be investigated in the future.

7. Summary and conclusions

We studied the spectral appearance of chemically homogeneously evolving stars, as predicted by evolutionary model sequences of fast-rotating massive single stars with low metallicity. To compute the spectra, we employed the NLTE model stellar atmosphere and stellar wind code PoWR. We predicted detailed spectra for selected stars from three evolutionary models: those with initial masses $20\,M_\odot$, $59\,M_\odot$, and $131\,M_\odot$. Various evolutionary stages were studied (comprising the CHB and CHeB phases). The stellar parameters effective temperature, luminosity, mass, and chemical composition were taken from the evolutionary models. Wind

models and their spectra were calculated for fixed values of the terminal velocity and velocity law. We tested the influence of two of the most uncertain assumptions in stellar wind modeling, mass-loss rate and clumping. The model spectra were classified according to the Morgan–Keenan spectroscopic classification scheme. Our main findings are summarized below.

- Our models in early evolutionary phases have weak and optically thin winds, while in later phases, these stars exhibit stronger and optically thick winds. This is consistent with earlier studies (see Paper I, which established that in the early phases, these objects should be called TWUIN stars), and is a consequence of the adopted $\dot{M}$ prescription. When adopting a reduced mass-loss rate, we find only a few weak emission lines in the spectra even in the most evolved phases.

- The maximum of the emitted radiation is in the far- and extreme UV region. The emitted radiation in the He II continuum increases both with M_{ini} and the evolutionary status, later stages having higher emissions. The total emitted flux is not very sensitive to variations of either the mass-loss rate or clumping.

- In earlier evolutionary phases with 50% of hydrogen or more in the atmosphere, most of our spectra, regardless of their M_{ini}, almost exclusively show absorption lines. This is true for the whole spectral region. More emission lines start to appear in later evolutionary phases, shortly before the end of the CHB phase. In the CHeB phase almost all lines are found in emission. In particular, the helium emission lines are strong and very characteristic for evolved stars. Their line strengths increase with higher helium abundance.

- Our models predict that lower mass-loss rates than those adopted from the evolutionary calculations have a negligible effect on the emergent spectra of the TWUIN star models in early evolutionary phases. More pronounced influence on spectral appearance is seen in later evolutionary phases with more helium in the atmosphere, especially in the CHeB phase.

- The assumed clumped wind has no significant influence on the predicted TWUIN spectra in earlier evolutionary phases. The spectra of higher-mass models in later evolutionary phases are, on the other hand, sensitive to clumping. Reducing the mass-loss rate cancels out this sensitivity, however, that is, model spectra with reduced mass-loss rates remain almost unchanged when a clumped wind is assumed, even in late evolutionary phases.

- Our TWUIN model spectra are assigned to spectral class O 4 or earlier. Nitrogen lines are almost completely absent. TWUIN O-type stars are predicted to be much hotter than the O-type stars that have been observed spectroscopically so far (down to $0.1\,Z_{\odot}$). Thus, the detection of a very hot star without almost any metal lines but with strong He II emission lines that is consistent with some very early-O type giant or supergiant would be a strong candidate for a star resulting from chemically homogeneous evolution.

- In later evolutionary phases, most of our model spectra are assigned to the WO-type spectral class. Nitrogen lines are almost completely absent in this late phase as well. Thus, chemically homogeneous evolution first leads to very hot early-type O stars (TWUIN stars) and then, for the last $\lesssim 10\%$ of the evolution, to Wolf–Rayet stars of type WO.

- The fact that chemically homogeneously evolving stars only develop emission lines during their CHeB phase, but have only absorption lines during their long lived CHB phase (when they are TWUIN stars), suggests that these stars may have contributed to the reionization of the Universe.

Observations of high-redshift galaxies typically show that an intensive ionizing source is present that produces almost no WR-like emission bumps in the galactic spectra. Some populations of TWUIN stars may be this source.

Single stars with chemically homogeneous evolution may be the progenitors of long-duration gamma-ray bursts and type Ic supernovae, as shown, for example, by Yoon et al. (2006) and Szécsi (2016, Chapter 4). In a close binary system, they may lead to two compact objects that eventually merge, giving rise to detectable gravitational wave emission (Marchant et al. 2016, 2017). Our choice of metallicity was indeed motivated by the fact that at this metallicity, binary models predict a high rate of gravitational-wave-emitting mergers.

Our test with the two mass-loss rate values indicates that even if the mass-loss rate turns out to be much lower than what is applied in the evolutionary models during the CHB phase, and indeed even if some of these stars turn out not to have winds at all, our conclusions about the absorption-like spectra will remain the same. In the CHeB phase, the mass-loss rate plays an important role; we suggest carrying out hydrodynamic simulations of the wind structure for these stars, to enable constraining their mass-loss rates and thereby to investigate their spectral appearance further.

As a result of the lack of spectroscopic observations of individual massive stars with metallicity below $0.1\,Z_{\odot}$, we were unable to compare our spectra with observations of any stars that may be of similar nature. The main purpose of our work is indeed to motivate future observing campaigns aiming at low-metallicity star-forming galaxies such as Sextant A or I Zwicky 18.

References

Abbott, D. C. 1980, ApJ, 242, 1183
Abbott, D. C. 1982, ApJ, 259, 282
Abbott, B. P., Abbott, R., Abbott, T. D., et al. 2016, ApJ, 818, L22
Abbott, B. P., Abbott, R., Abbott, T. D., et al. 2017, Phys. Rev. Lett., 118, 221101
Abel, T., Bryan, G., & Norman, M. 2002, Science, 295, 93
Annibali, F., Cignoni, M., Tosi, M., et al. 2013, AJ, 146, 144
Bouret, J.-C., Lanz, T., Hillier, D. J., et al. 2015, MNRAS, 449, 1545
Brott, I., de Mink, S. E., Cantiello, M., et al. 2011, A&A, 530, A115
Camacho, I., Garcia, M., Herrero, A., & Simón-Díaz, S. 2016, A&A, 585, A82
Cantiello, M., Yoon, S.-C., Langer, N., & Livio, M. 2007, A&A, 465, L29
Castor, J. I., Abbott, D. C., & Klein, R. I. 1975, ApJ, 195, 157
Castro, N., Crowther, P. A., Evans, C. J., et al. 2018, A&A, 614, A147
Choudhury, T. R., & Ferrara, A. 2007, MNRAS, 380, L6
Conti, P. S. 1975, Mem. Soc. Roy. Sci. Liege, 9, 193
Conti, P. S., & Alschuler, W. R. 1971, ApJ, 170, 325
Conti, P. S., & Frost, S. A. 1977, ApJ, 212, 728
Conti, P. S., & Leep, E. M. 1974, ApJ, 193, 113
Crowther, P. A., & Hadfield, L. J. 2006, A&A, 449, 711
Crowther, P. A., & Walborn, N. R. 2011, MNRAS, 416, 1311
Crowther, P. A., Hillier, D. J., & Smith, L. J. 1995, A&A, 293, 172
Crowther, P. A., De Marco, O., & Barlow, M. J. 1998, MNRAS, 296, 367
Cui, Z., Wang, Z., Zhu, C., et al. 2018, PASP, 130, 084202
Davies, B., Kudritzki, R.-P., Gazak, Z., et al. 2015, ApJ, 806, 21
de Mink, S. E., & Mandel, I. 2016, MNRAS, 460, 3545
de Mink, S. E., Cantiello, M., Langer, N., et al. 2009, A&A, 497, 243
Eldridge, J. J., & Vink, J. S. 2006, A&A, 452, 295
Eldridge, J. J., & Stanway, E. R. 2012, MNRAS, 419, 479

Friend, D. B., & Abbott, D. C. 1986, ApJ, 311, 701
Garcia, M., Herrero, A., Najarro, F., Lennon, D. J., & Urbaneja, M. A. 2014, ApJ, 788, 64
Götberg, Y., de Mink, S. E., & Groh, J. H. 2017, A&A, 608, A11
Gräfener, G., & Hamann, W.-R. 2005, A&A, 432, 633
Gräfener, G., & Hamann, W.-R. 2008, A&A, 482, 945
Gräfener, G., Koesterke, L., & Hamann, W.-R. 2002, A&A, 387, 244
Gustafsson, B., Edvardsson, B., Eriksson, K., et al. 2008, A&A, 486, 951
Hainich, R., Pasemann, D., Todt, H., et al. 2015, A&A, 581, A21
Hainich, R., Oskinova, L. M., Shenar, T., et al. 2018, A&A, 609, A94
Hainich, R., Ramachandran, V., Shenar, T., et al. 2019, A&A, 621, A85
Hamann, W.-R., & Gräfener, G. 2003, A&A, 410, 993
Hamann, W.-R., & Gräfener, G. 2004, A&A, 427, 697
Hamann, W.-R., & Koesterke, L. 1998, A&A, 335, 1003
Hamann, W.-R., Koesterke, L., & Wessolowski, U. 1995, A&A, 299, 151
Hamann, W.-R., Gräfener, G., & Liermann, A. 2006, A&A, 457, 1015
Hamann, W. R., Feldmeier, A., & Oskinova, L. M. 2008, Clumping in Hot-star Winds
Herrero, A., Garcia, M., Puls, J., et al. 2012, A&A, 543, A85
Hillier, D. J., & Miller, D. L. 1998, ApJ, 496, 407
Hubeny, I., & Mihalas, D. 2014, Theory of Stellar Atmospheres (Princeton: Princeton University Press)
Huenemoerder, D. P., Oskinova, L. M., Ignace, R., et al. 2012, ApJ, 756, L34
Inserra, C., Pastorello, A., Turatto, M., et al. 2013, A&A, 555, A142
Kamann, S., Wisotzki, L., & Roth, M. M. 2013, A&A, 549, A71
Kehrig, C., Pérez-Montero, E., Vílchez, J. M., et al. 2013, MNRAS, 432, 2731
Kehrig, C., Vílchez, J. M., Pérez-Montero, E., et al. 2015, ApJ, 801, L28
Kehrig, C., Vílchez, J. M., Pérez-Montero, E., et al. 2016, MNRAS, 459, 2992
Krtička, J., & Kubát, J. 2010, A&A, 519, A50
Krtička, J., & Kubát, J. 2014, A&A, 567, A63
Krtička, J., & Kubát, J. 2017, A&A, 606, A31
Krtička, J., Owocki, S. P., & Meynet, G. 2011, A&A, 527, A84
Kubát, J., Puls, J., & Pauldrach, A. W. A. 1999, A&A, 341, 587
Lamb, J. B., Oey, M. S., Segura-Cox, D. M., et al. 2016, ApJ, 817, 113
Lamers, H. J. G. L. M., Snow, T. P., & Lindholm, D. M. 1995, ApJ, 455, 269
Lamers, H., & Cassinelli, J. 1999, Introduction to Stellar Winds (Cambridge University Press)
Langer, N. 1989, A&A, 210, 93
Levesque, E. M., Kewley, L. J., Berger, E., & Zahid, H. J. 2010, AJ, 140, 1557
Lunnan, R., Chornock, R., Berger, E., et al. 2013, ApJ, 771, 97
Ma, Q., Maio, U., Ciardi, B., & Salvaterra, R. 2017, MNRAS, 472, 3532
Mandel, I., & de Mink, S. E. 2016, MNRAS, 458, 2634
Marchant, P., Langer, N., Podsiadlowski, P., Tauris, T. M., & Moriya, T. J. 2016, A&A, 588, A50
Marchant, P., Langer, N., Podsiadlowski, P., et al. 2017, A&A, 604, A55
Marcolino, W. L. F., Bouret, J.-C., Martins, F., et al. 2009, A&A, 498, 837
Martayan, C., Frémat, Y., Hubert, A.-M., et al. 2007, A&A, 462, 683
Martins, F. 2018, A&A, 616, A135
Martins, F., Schaerer, D., Hillier, D. J., et al. 2005, A&A, 441, 735
Massey, P., Neugent, K. F., & Morrell, N. 2015, ApJ, 807, 81
Mathys, G. 1988, A&AS, 76, 427
Matthee, J., Sobral, D., Gronke, M., et al. 2018, A&A, 619, A136
McConnachie, A. W. 2012, AJ, 144, 4
Mihalas, D. 1978, Stellar Atmospheres, 2nd ed. (San Francisco: W. H. Freeman and Co.)
Modjaz, M., Kewley, L., Bloom, J. S., et al. 2011, ApJ, 731, L4
Mokiem, M. R., de Koter, A., Evans, C. J., et al. 2006, A&A, 456, 1131
Nugis, T., & Lamers, H. 2000, A&A, 360, 227
Owocki, S. P., Cranmer, S. R., & Gayley, K. G. 1996, ApJ, 472, L115
Paczyński, B. 1967, Acta Astron., 17, 355
Pauldrach, A., Puls, J., & Kudritzki, R. P. 1986, A&A, 164, 86
Pauldrach, A. W. A., Vanbeveren, D., & Hoffmann, T. L. 2012, A&A, 538, A75
Puls, J., Urbaneja, M. A., Venero, R., et al. 2005, A&A, 435, 669
Puls, J., Vink, J., & Najarro, F. 2008, A&ARv, 16, 209
Quimby, R. M., Kulkarni, S. R., Kasliwal, M. M., et al. 2011, Nature, 474, 487
Ramachandran, V., Hamann, W.-R., Hainich, R., et al. 2018, A&A, 615, A40
Sana, H., de Mink, S. E., de Koter, A., et al. 2012, Science, 337, 444
Sander, A., Shenar, T., Hainich, R., et al. 2015, A&A, 577, A13
Sander, A. A. C., Hamann, W.-R., Todt, H., Hainich, R., & Shenar, T. 2017, A&A, 603, A86
Shenar, T., Hamann, W.-R., & Todt, H. 2014, A&A, 562, A118
Shenar, T., Hainich, R., Todt, H., et al. 2016, A&A, 591, A22
Shirazi, M., & Brinchmann, J. 2012, MNRAS, 421, 1043
Smith, L. F., Shara, M. M., & Moffat, A. F. J. 1996, MNRAS, 281, 163
Sobral, D., Matthee, J., Darvish, B., et al. 2015, ApJ, 808, 139
Szécsi, D. 2016, PhD Thesis, Mathematisch-Naturwissenschaftlichen Fakultät der Universität Bonn
Szécsi, D. 2017a, Contributions of the Astronomical Observatory Skalnate Pleso, 47, 108
Szécsi, D. 2017b, Proceedings of Science PoS(MULTIF2017)065
Szécsi, D., & Wünsch, R. 2019, ApJ, 871, 20
Szécsi, D., Langer, N., Sanyal, D., et al. 2015a, in Proceedings of Wolf-Rayet Stars Workshop, Potsdam, Germany, eds. W. R. Hamann, A. Sander, & H. Todt, 189
Szécsi, D., Langer, N., Yoon, S.-C., et al. 2015b, A&A, 581, A15
Szécsi, D., Mackey, J., & Langer, N. 2018, A&A, 612, A55
Tolstoy, E., Hill, V., & Tosi, M. 2009, ARA&A, 47, 371
Tramper, F., Sana, H., de Koter, A., & Kaper, L. 2011, ApJ, 741, L8
Tramper, F., Gräfener, G., Hartoog, O. E., et al. 2013, A&A, 559, A72
Tramper, F., Sana, H., de Koter, A., Kaper, L., & Ramírez-Agudelo, O. H. 2014, A&A, 572, A36
Vergani, S. D., Salvaterra, R., Japelj, J., et al. 2015, A&A, 581, A102
Vink, J., & de Koter, A. 2005, A&A, 442, 587
Vink, J., de Koter, A., & Lamers, H. 2000, A&A, 362, 295
Vink, J., de Koter, A., & Lamers, H. 2001, A&A, 369, 574
Walborn, N. R., Howarth, I. D., Lennon, D. J., et al. 2002, AJ, 123, 2754
Weisz, D. R., Dolphin, A. E., Skillman, E. D., et al. 2014, ApJ, 789, 147
Yoon, S.-C. 2015, PASA, 32, 15
Yoon, S.-C., & Langer, N. 2005, A&A, 443, 643
Yoon, S.-C., Langer, N., & Norman, C. 2006, A&A, 460, 199
Yoshida, N., Oh, S. P., Kitayama, T., & Hernquist, L. 2007, ApJ, 663, 687

Appendix A: Spectral classification

The Morgan–Keenan spectroscopic classification scheme is based on comparing the strengths of certain lines. That is, if the ratio of two given lines falls into an (observationally predefined) regime, the star is assigned to a certain class. For example, if the ratio of the lines He I λ4473 Å to He II λ4543 Å falls between 0.2 and 0.1, the spectra is classified as type O 8.

The line strength is usually measured by the equivalent width of the line. Typically in the literature, the ratio of two lines is expressed as the logarithm[2] of the ratio of their equivalent widths[3], that is, $\log_{10}(EW_{\text{line1}}/EW_{\text{line2}})$.

For O-type stars, the work of Mathys (1988), who in turn relied on the works done by Conti & Alschuler (1971), Conti & Leep (1974), and Conti & Frost (1977), comprehensively defines subclasses. They take into account the ratio of He I λ4473 Å to He II λ4543 Å when the spectral subclasses between type O 3 (early) to O 9.7 (late) are defined; the classification scheme we base our work on is given in Table III of Mathys (1988). Walborn et al. (2002) updated this scheme for the earliest types, introducing type O 2; however, they used the ratio of certain nitrogen lines, which are absent from our spectra. Additionally, in paragraph 6 of Sect. 4.2 of Mathys (1988), for instance, O f subclasses are defined on the basis of the N III λ4640 Å line; this line is also absent from our spectra.

For luminosity classes of O-type stars, we classify everything with He II λ4686 Å in emission as a supergiant (i.e., luminosity class I). For dwarfs (class V) and giants (class III), on the other hand, Mathys (1988) suggested the following approach: For spectral types earlier than O 8.5 (i.e., types between O 3–O 8), he used the line strength of He II λ4686 Å to distinguish between luminosity classes. His criterion is given in paragraph 4 of his Sect. 4.2: if strongly in absorption, meaning log |EW| > 2.7, it is of class V (note the absolute values). If only weakly in absorption, it is of class III. For spectral types O 8.5 and later, he uses the sum of the logarithm of two lines, He I λ4388 Å and He II λ4686 Å. However, we found that in our spectra both of these lines are too weak, so even their sum is not an applicable criterion. Instead, we relied on Conti & Alschuler (1971) for these late spectral types, who used the equivalent width ratios of Si IV λ4090 Å to He I λ4143 Å with a criterion given in their Table 5.

For WR stars, we have to distinguish between so-called nitrogen-sequence WR stars (type WN) on the one hand, and carbon- and oxygen-sequence WR stars (WC and WO) on the other.

WN stars are typical in that they have strong nitrogen emission lines, in particular, N III λ4640 Å and Ni IV λ4059 Å (Crowther et al. 1995; Smith et al. 1996; Crowther & Walborn 2011). Moreover, He II λ4686 Å is in emission in their spectra. There is a comprehensive set of criteria for WN classification in Table 4a of Smith et al. (1996). According to this table, we find no WN stars amongst our spectra.

A quantitative classification of WC and WO stars was done by Crowther et al. (1998). In their Table 3, equivalent width ratios of certain carbon- and oxygen-lines are used to distinguish between classes from WC 11 to WC 4, and also from WO 4 to WO 1. We rely on this system to classify those spectra that have strong emission features in carbon and oxygen. We note, however, that the line C III λ5696 Å, which is used to distinguish between WC type subclasses, is completely absent from our spectra, leading us to classify all our emission line spectra into type WO.

---

[2]   When we talk about logarithm, we always mean $\log_{10}$ unless specified otherwise.

[3]   The equivalent width ratio is sometimes denoted as $\log_{10} W_\lambda$ in the literature. We caution that this notation is contradictory, as also the equivalent width itself is commonly denoted by $\log_{10} W_\lambda$.
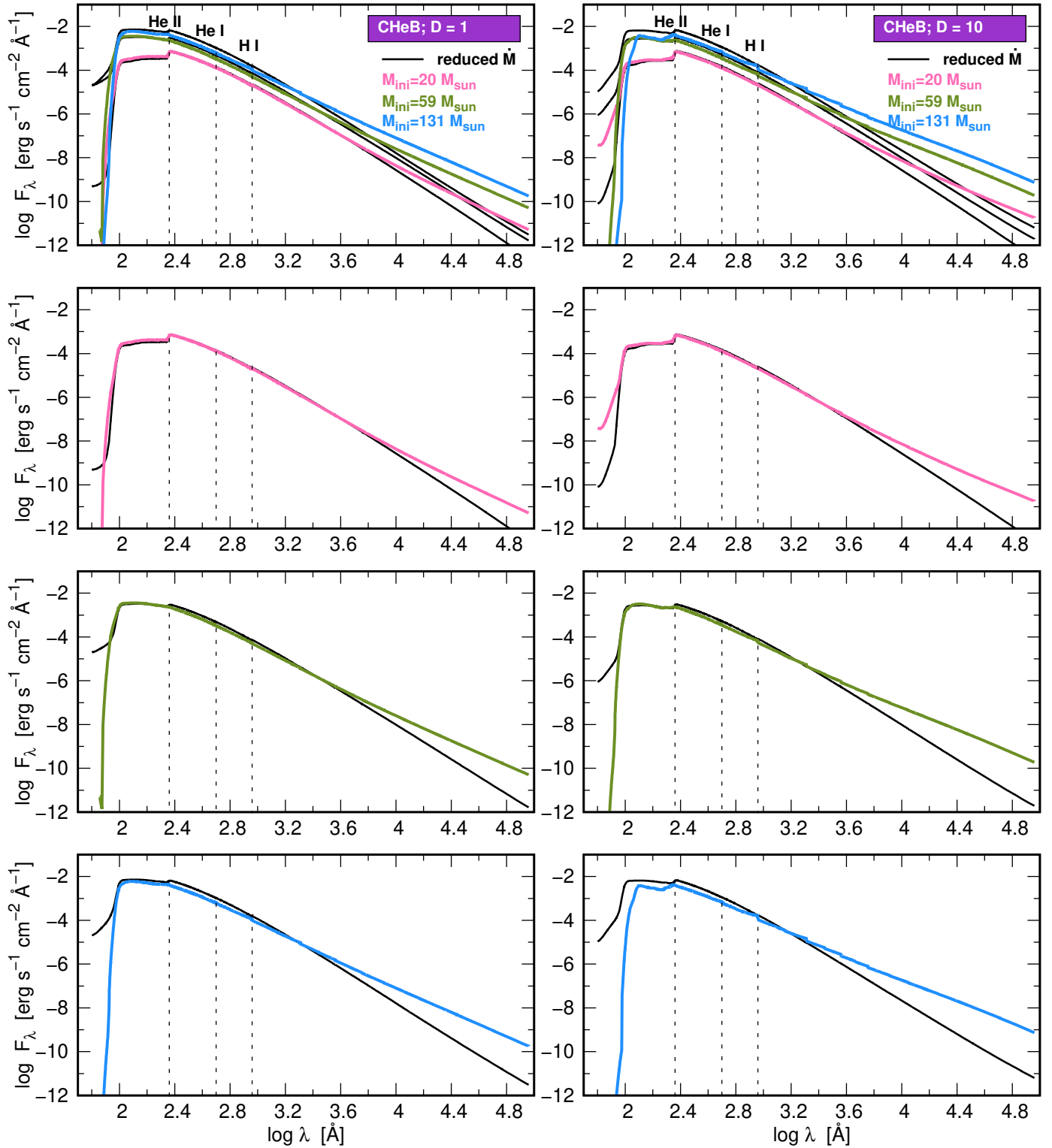
Appendix B: Spectral models of TWUIN stars

Fig. B1. Same as Fig. 2, but only for CHeB evolutionary phase.
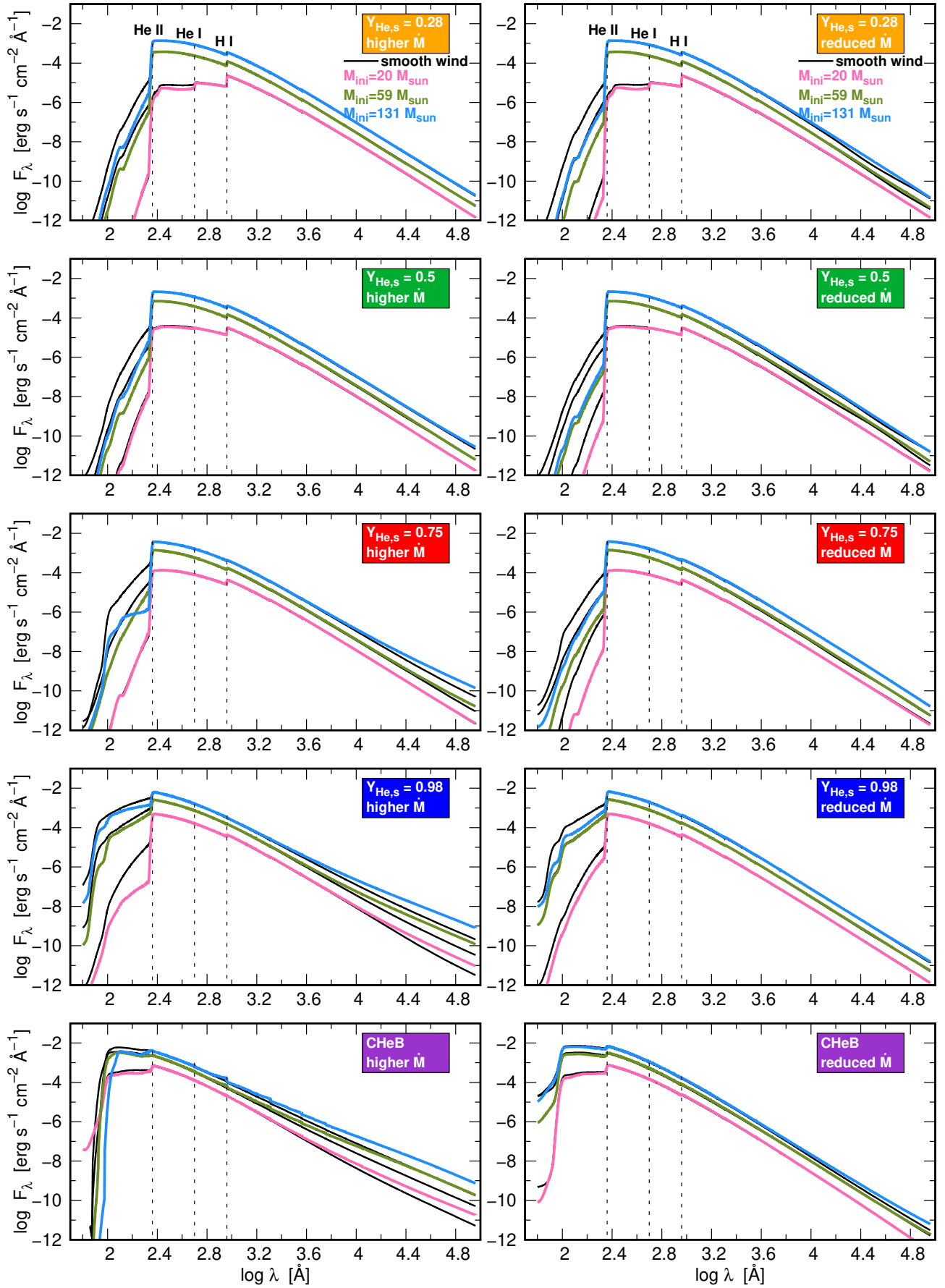
Fig. B2. Same as Fig. 2, but differences between SEDs are shown for smooth (black lines) and clumped (colored lines) wind models for higher (*left panels*) and reduced (*right panels*) mass-loss rate $\dot{M}$.
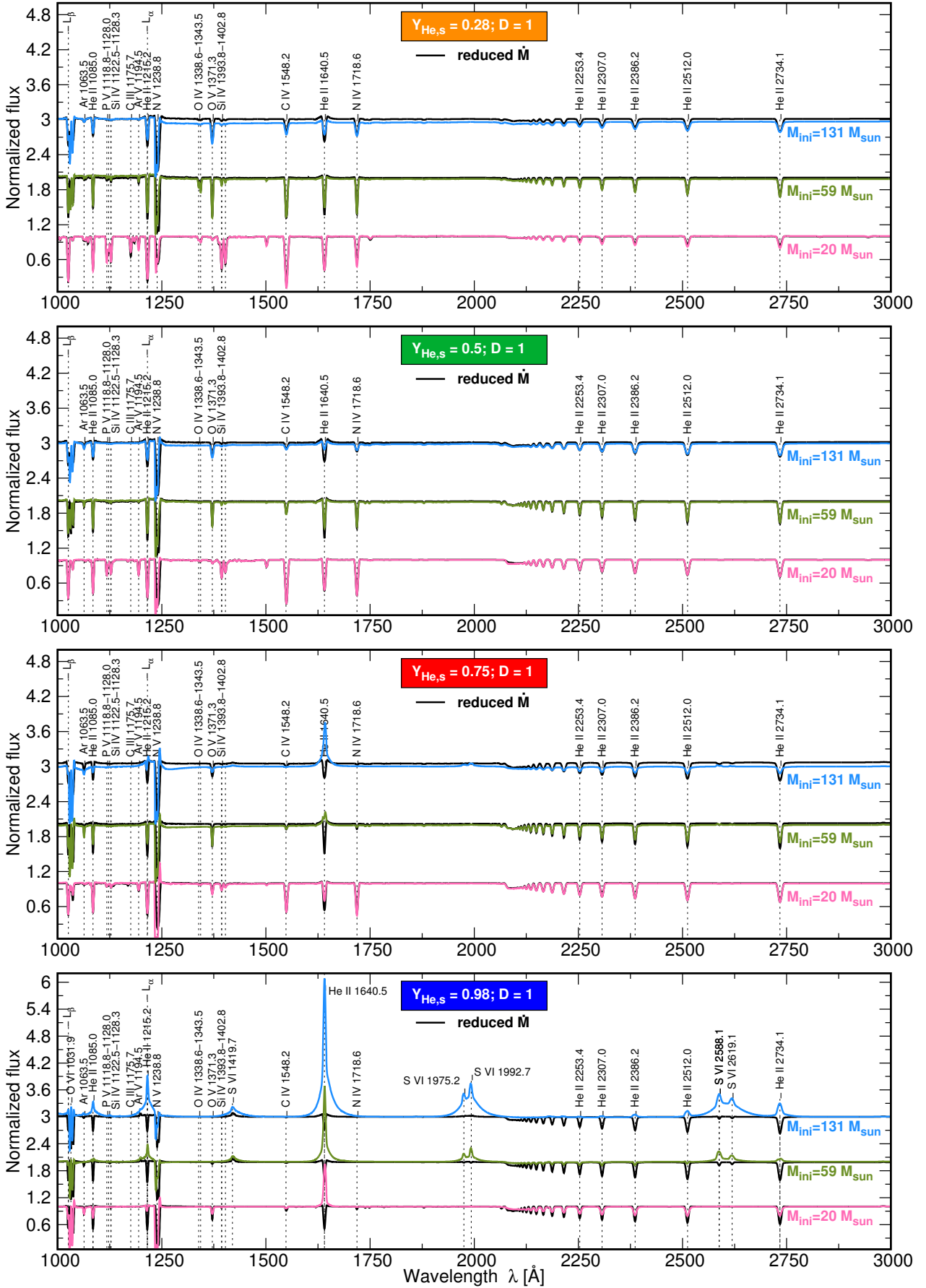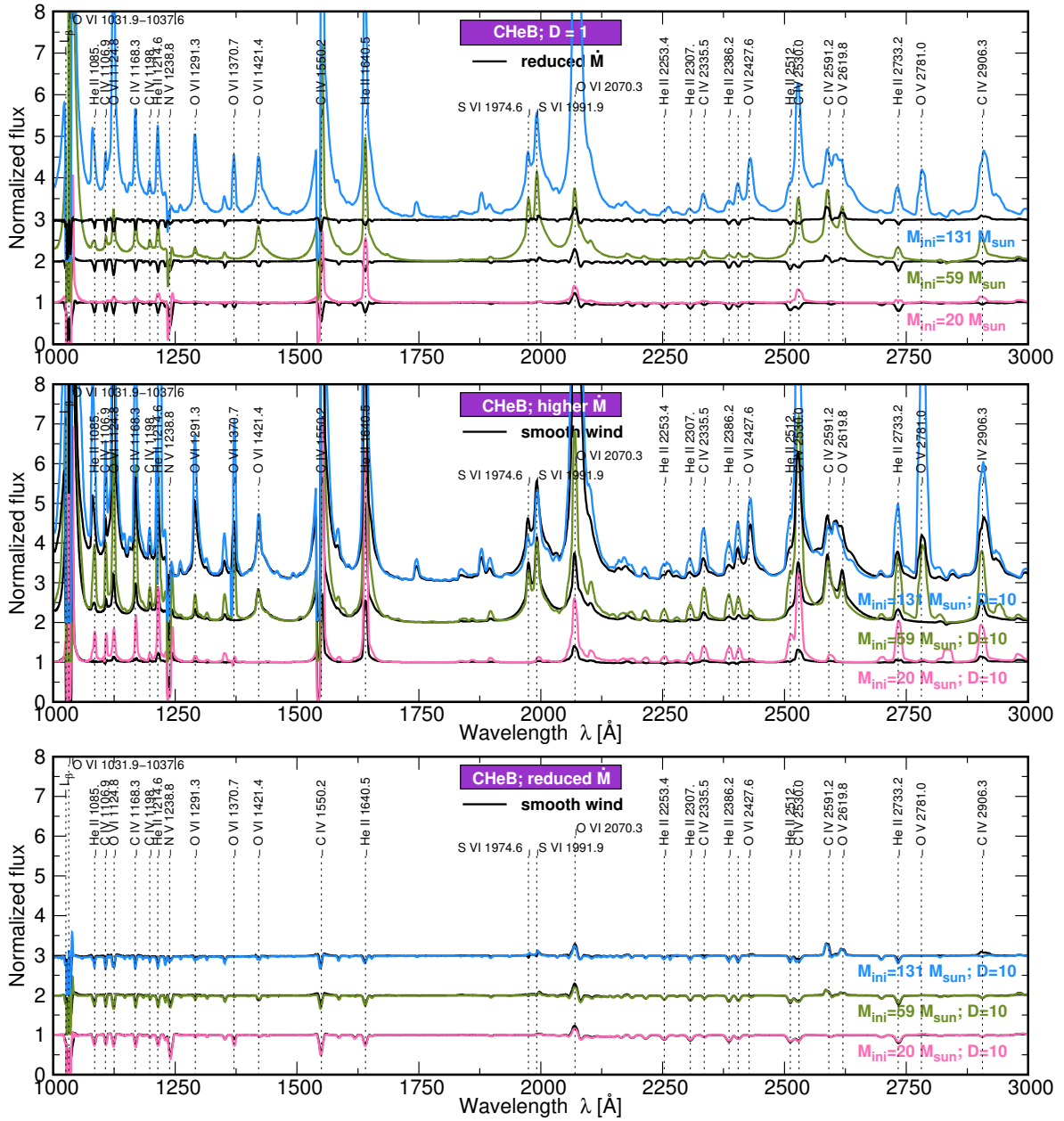
Fig. B3. Same as Fig. 3, but in the UV region.
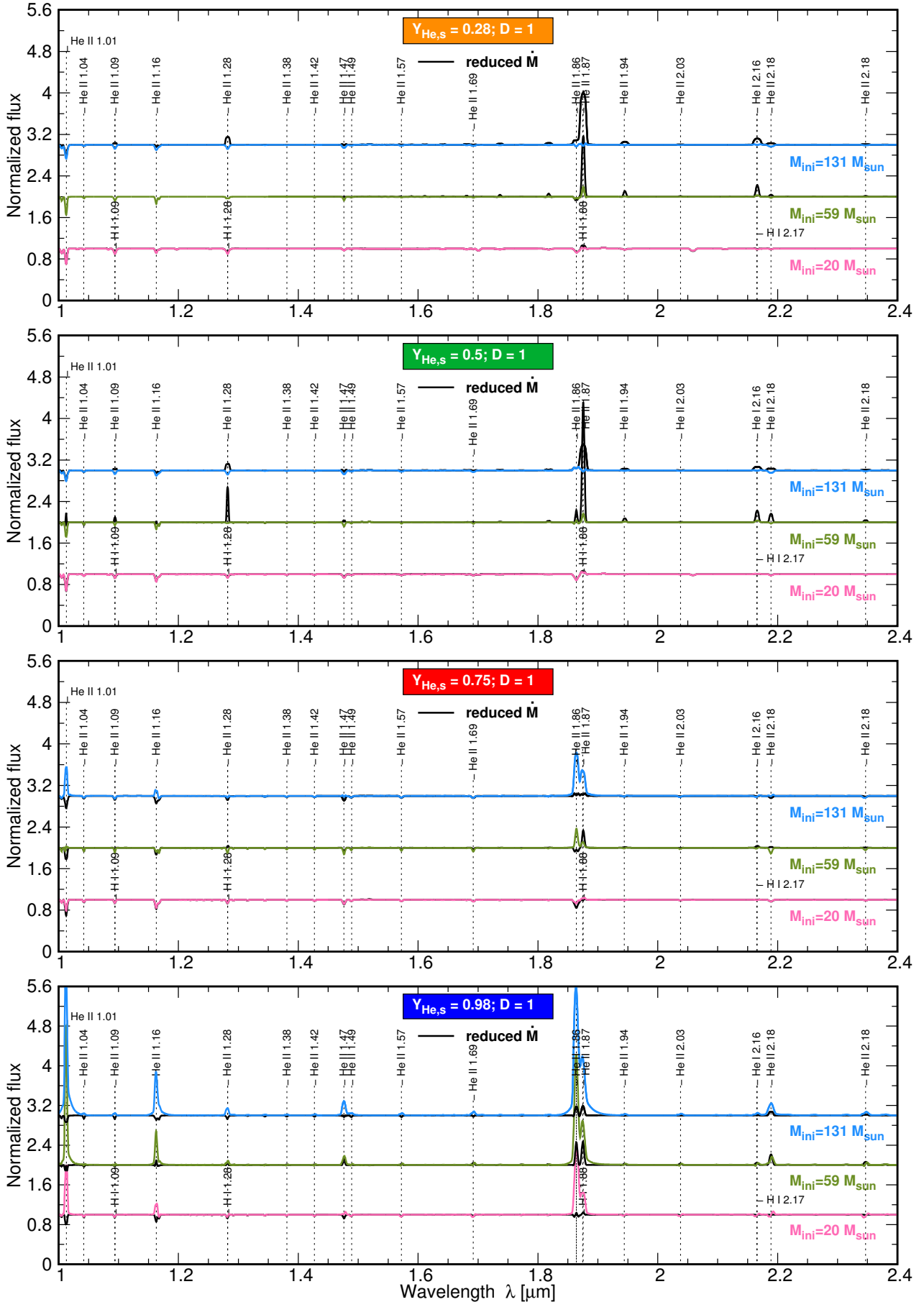
Fig. B4. Same as Fig. 4, but in the UV region.
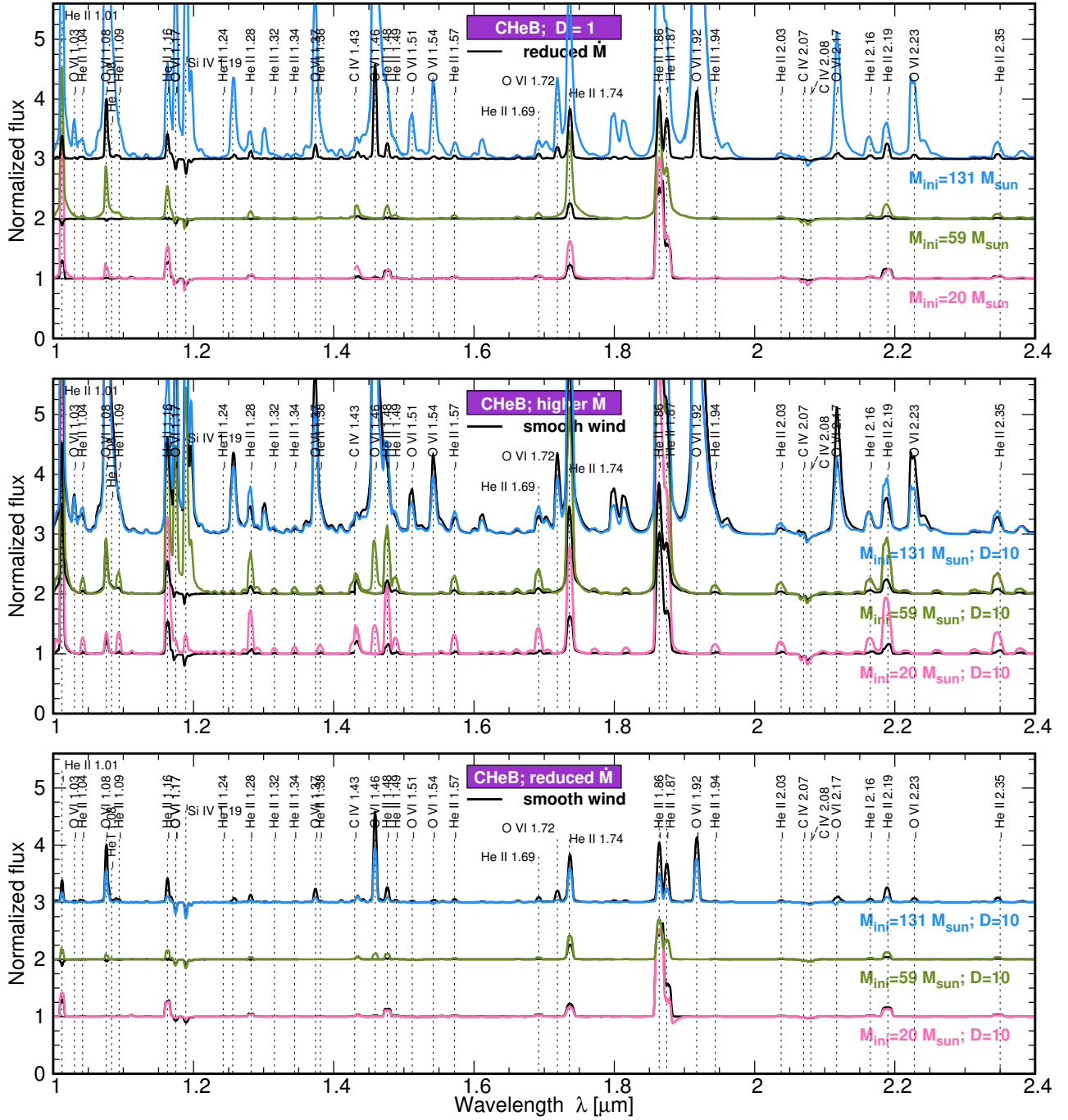
Fig. B5. Same as Fig. 3, but in the IR region.

Fig. B6. Same as Fig. 4, but in the IR region.
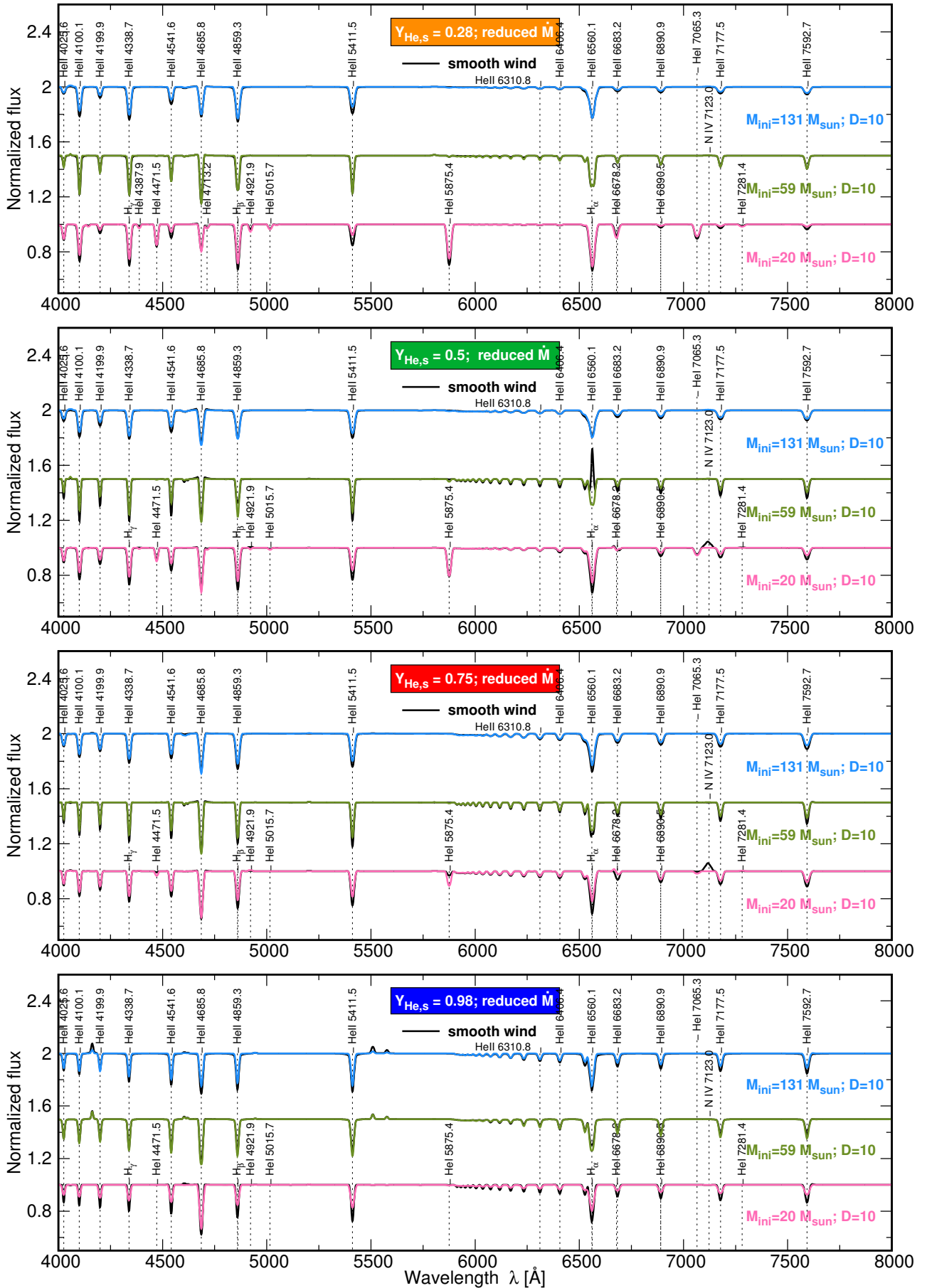
Fig. B7. Same as Fig. 6, but assuming a mass-loss rate hundred times lower than nominal (i.e. higher) value.
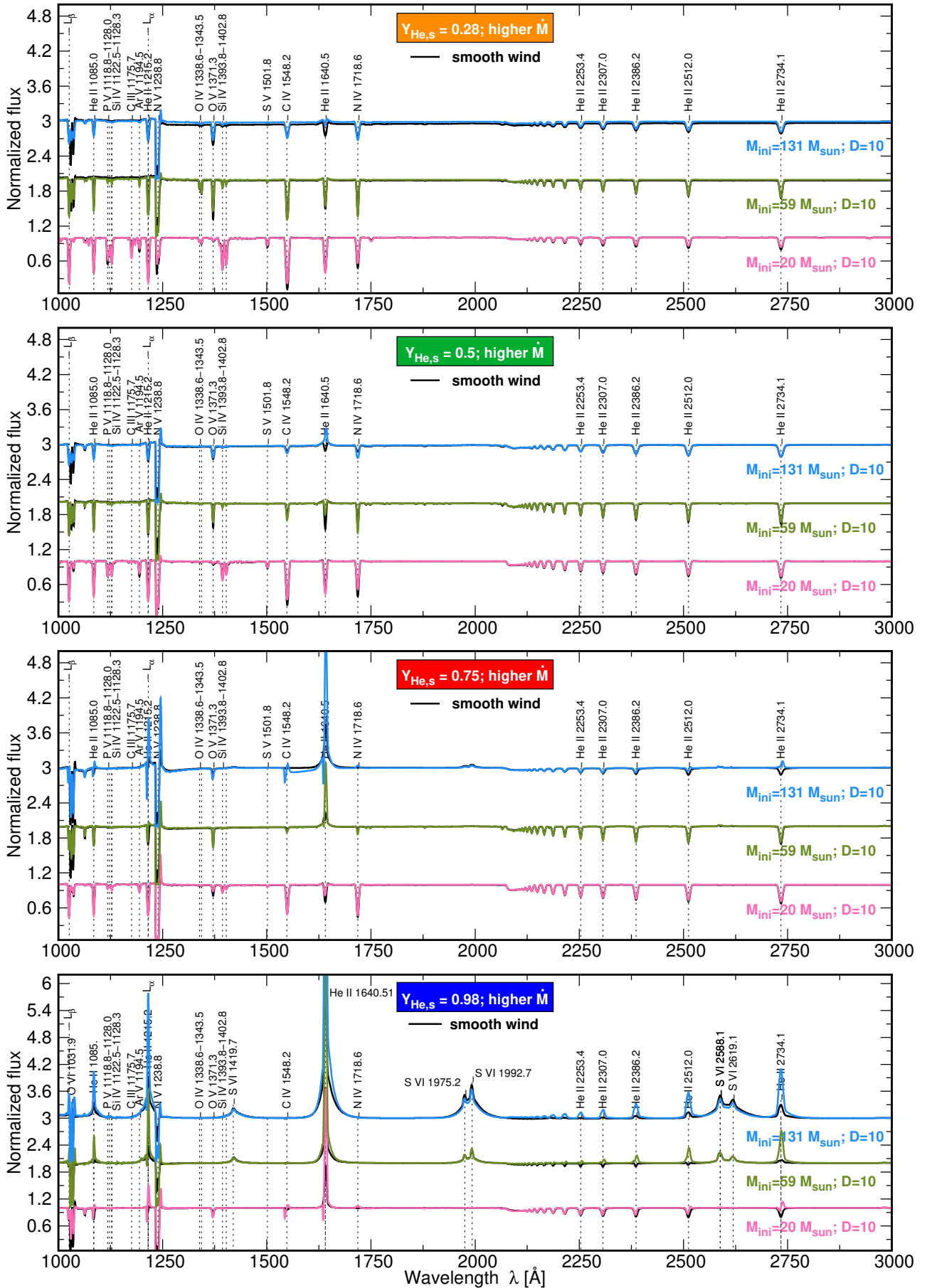
Fig. B8. Same as Fig. 6, but in the UV region.
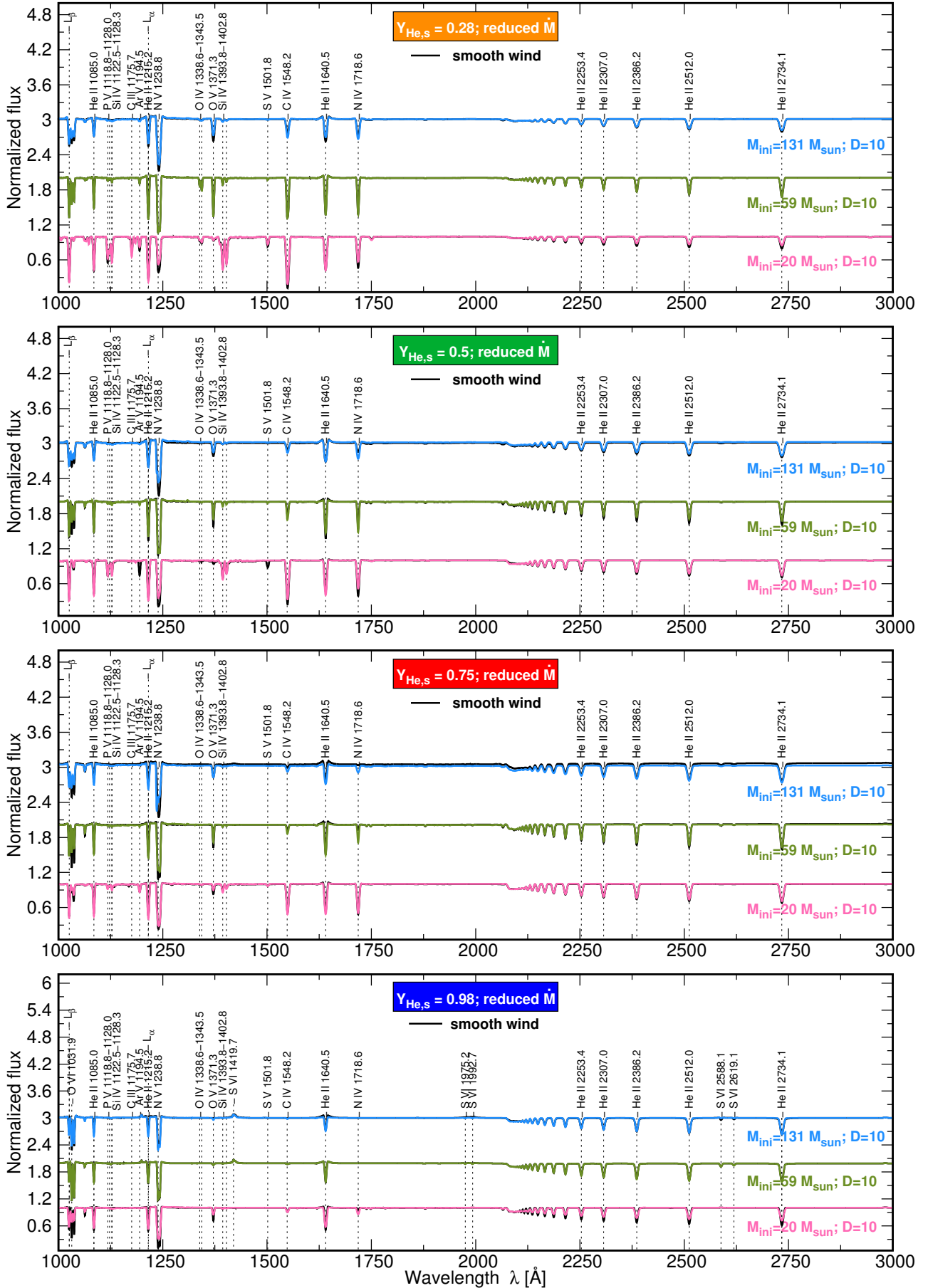
Fig. B9. Same as Fig. B7, but in the UV region.
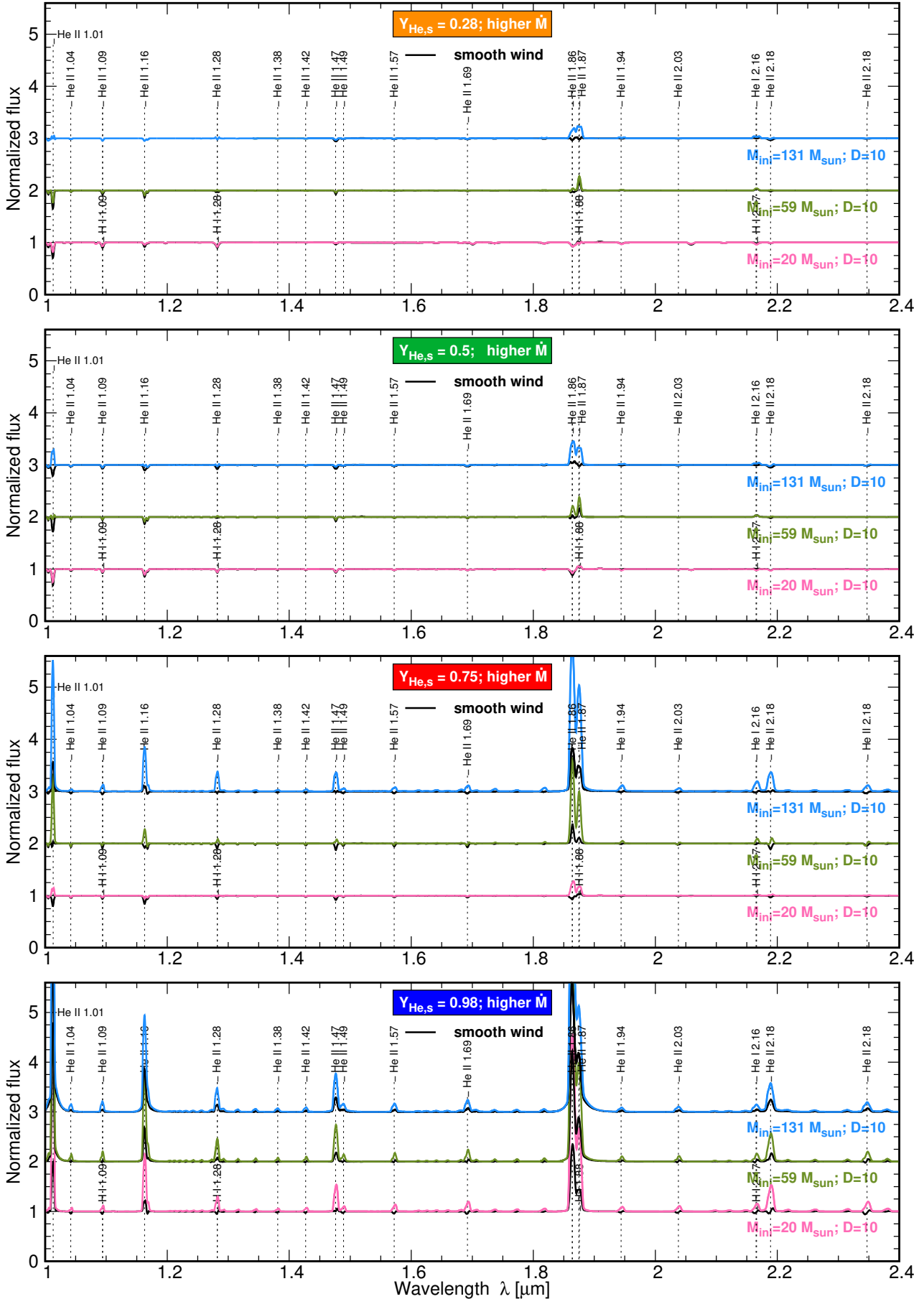
Fig. B10. Same as Fig. 6, but in the IR region.
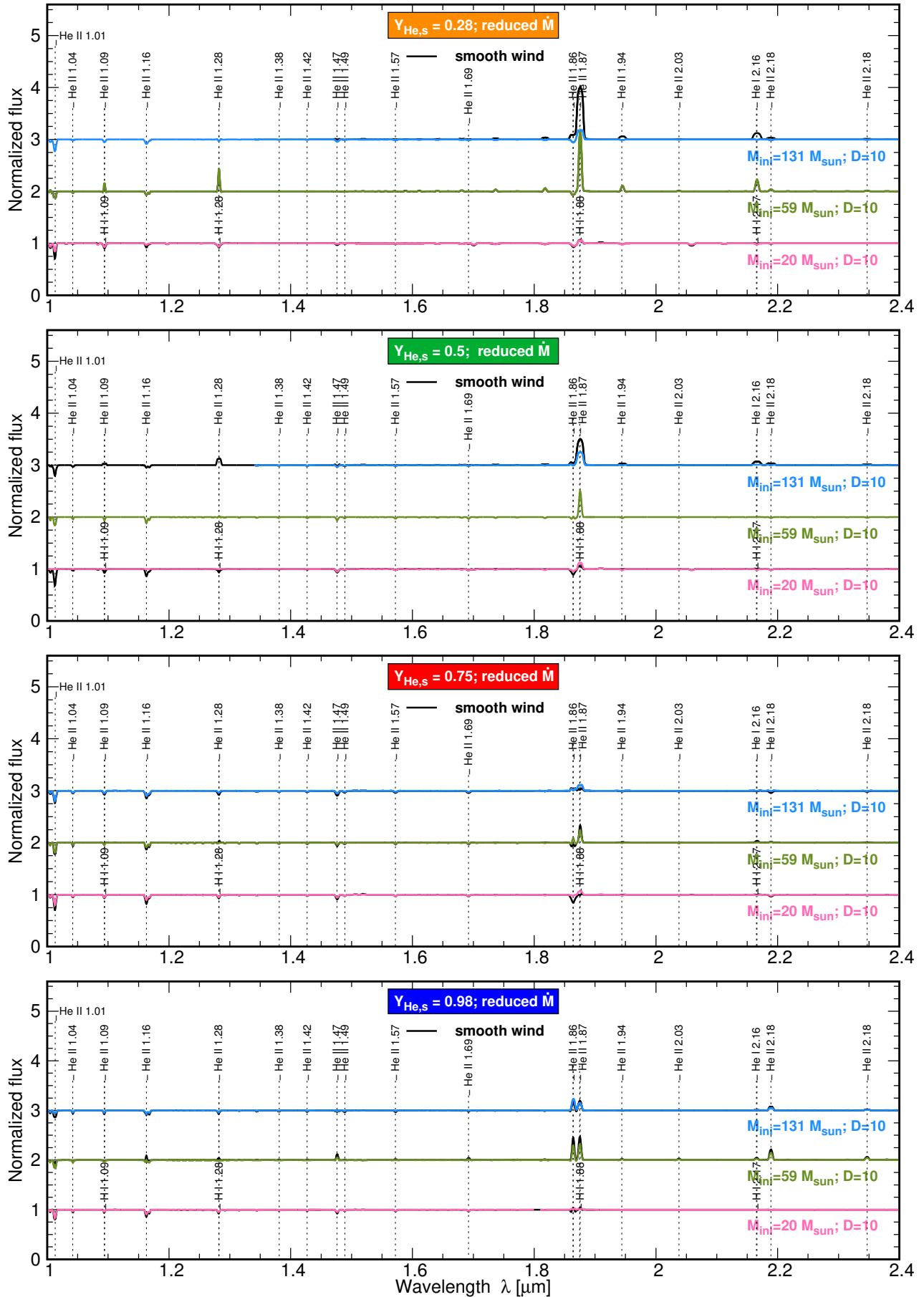
Fig. B11. Same as Fig. B7, but in the IR region.

Direction dependent background fitting for the *Fermi* GBM data

D. Szécsi[1,2,3], Z. Bagoly[1,4], J. Kóbori[1], I. Horváth[4], and L. G. Balázs[1,2]

[1] Eötvös University, 1053 Budapest, Hungary
 e-mail: zsolt.bagoly@elte.hu
[2] MTA CSFK Konkoly Observatory, 1121 Budapest, Hungary,
[3] Argelander-Institute für Astronomie der Universität Bonn, 53121 Bonn, Germany
[4] Bolyai Military University, 1581 Budapest, Hungary

ABSTRACT

Context. We present a method for determining the background of the gamma-ray bursts (GRBs) of the *Fermi* Gamma-ray Burst Monitor (GBM) using the satellite positional information and a physical model. Since the polynomial fitting method typically used for GRBs is generally only indicative of the background over relatively short timescales, this method is particularly useful in the cases of long GRBs or those that have autonomous repoint request (ARR) and a background with much variability on short timescales.
Aims. Modern space instruments, like *Fermi*, have some specific motion to survey the sky and catch gamma-ray bursts in the most effective way. However, GBM bursts sometimes have highly varying backgrounds (with or without ARR), and modelling them with a polynomial function of time is not efficient – one needs more complex, *Fermi*-specific methods. This article presents a new direction dependent background fitting method and shows how it can be used for filtering the lightcurves.
Methods. First, we investigate how the celestial position of the satellite may have influence on the background and define three underlying variables with physical meaning: celestial distance of the burst and the detector's orientation, the contribution of the Sun and the contribution of the Earth. Then, we use multi-dimensional general least square fitting and Akaike model selection criterion for the background fitting of the GBM lightcurves. Eight bursts are presented as examples, of which we computed the duration using background fitted cumulative lightcurves.
Results. We give a direction dependent background fitting (DDBF) method for separating the motion effects from the real data and calculate the duration (T_{90}, T_{50}, and confidence intervals) of the nine example bursts, from which two resulted an ARR. We also summarize the features of our method and compare it qualitatively with the official GBM Catalogue.
Conclusions. Our background filtering method uses a model based on the physical information of the satellite position. Therefore, it has many advantages compared to previous methods. It can fit long background intervals, remove all the features caused by the rocking behaviour of the satellite, and search for long emissions or not-triggered events. Furthermore, many parts of the fitting have now been automatised, and the method has been shown to work for both sky survey mode and ARR mode data. Future work will provide a burst catalogue with DDBF.

Key words. gamma-ray burst: general – methods: data analysis – instrumentation: detectors – gamma rays: diffuse background

1. Introduction

NASA's *Fermi* Gamma-ray Space Telescope has an orbit of altitude ~565 km and period of ~96 min. It carries two main instruments on board. The Large Area Telescope's (LAT) energy range (20 MeV−300 GeV) overlaps the energy range of the Gamma-ray Burst Monitor (GBM, 8 keV−40 MeV). GBM consists of two types of detectors: 12 sodium iodide (NaI) and 2 bismuth germanate-oxide (BGO) detectors (Meegan et al. 2009).

The primary observation mode of *Fermi* is sky survey mode. This enables the LAT to monitor the sky systematically, whilst maintaining an uniform exposure. In this mode, the entire sky is observed for ~30 min per 2 orbits. If a sufficiently bright GRB is detected by GBM, an autonomous repoint request (ARR) may be issued. This will cause the satellite to slew, so that the burst's coordinates (calculated by the GBM) stay within the field of view of the LAT for ~2 h (Fitzpatrick et al. 2011). However, this repositioning right after the trigger results in rapid and high background rate variations of the GBM lightcurves – sometimes even during the burst, which is the most important time of the observation. Therefore, it is crucial to have a filtering method, which is capable of correcting for the background variations caused by the ARR.

To date, GBM has triggered on 1000 GRBs (GCN 2013), (Fermi-Timeline-Posting 2013). Only a small fraction (~70 GRBs) resulted an ARR (Paciesas 2013, priv. comm.). The relatively low rate of ARR's is due to the GBM trigger that has to meet certain criteria (such as high peak flux) before an ARR occurs. When we started to analyse GRBs detected by GBM, we found that several non-ARR bursts have a background variation of the same order of magnitude as the burst itself. As we will show, one can find connection between these background rates and the actual position and orientation of the satellite. Therefore it is necessary to use the directional information to filter the background not only for ARR but also for many non-ARR cases.

Here, we present the effect of the slew and how it is represented in the measured data of the GBM. We summarize why the usual background subtraction methods are inefficient in most cases, especially for the long bursts, as seen in Sect. 2. Then, we introduce variables based on the position of the satellite related to the Earth and the Sun (Sect. 3) and use them with the time variable to fit a general multi-dimensional linear function to the background (Sect. 4). Our method is called direction dependent background fitting (DDBF).
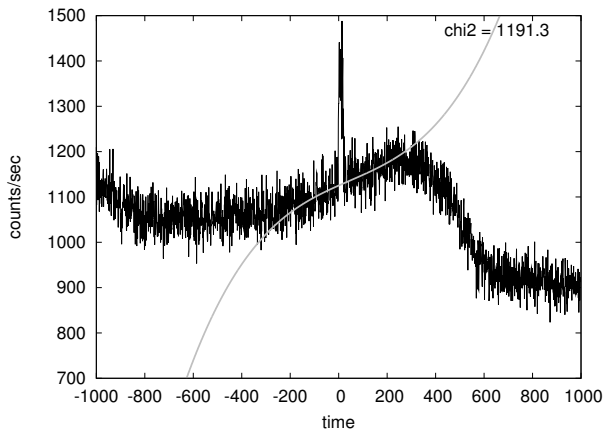
Fig. 1. Lightcurve of the *Fermi* burst 091030.613 measured by the 3rd GBM-detector without any background filtering with 1-s bins. The grey line is a fitted polynomial function of time of order 3 for the ranges of [−200;−20] and [38;200] s, which does not seem to be a correct model for this whole background. Reduced chi-square statistics are given in the top right corner (Szécsi et al. 2012a).

We also present examples where we compute the duration (T_{90} and T_{50}) from our background-filtered lightcurves and show that the DDBF method can be used for both the Sky Survey and ARR observations (Sect. 5). Confidence levels and a comparison to the GBM catalogue are given in Sect. 6.

2. Difficulties with the *Fermi* background

2.1. Lightcurves with unpredictably varying background

The lightcurve for GBM trigger 091030.613 is shown in Fig. 1 in the energy range ~11–980 keV. This burst did not result in an ARR (GCN 2013). We decided to use the sum of the channels except for the highest and lowest, where the detector's efficiency drops, so the signal is statistically stronger. Since we are only interested in the duration information of the bursts, we use the high time resolution data (CTIME, see Sect. 3 for the detailed description) and sum of the channels. We note that, however, the analysis can be done using either different channels or the high spectral resolution data files (CSPEC), so spectral information can be obtained (see Szécsi et al. 2012b).

In Fig. 1, the burst is clearly visible above the background, but the background is varying so rapidly and to such an extent that one can question the usefulness of fitting and subtracting a simple polynomial function of order 3 (grey line in Fig. 1). This situation is typical in the case of *Fermi*, as can be seen in the examples in Sect. 5.2. Especially when a long burst occurs, the background rate can change too quickly for analyses without some knowledge about the satellite position and the gamma sources on the sky. In the following, we are investigating for possible background sources. We will see that one can find a correspondence between the gamma background and the celestial orientation of the satellite. Furthermore, both the Sun and the Earth limb have a contribution, given that they move in and out of the field of view because of the rocking motion of the satellite. Based on these physical conditions, we are constructing a background model and a fitting algorithm, both of which give us a more effective method for filtering the motion effects. Since the method is based on the actual directional information of the satellite, it is possible to analyse bursts for which an ARR was issued.

2.2. Previous methods

In the BATSE era, it was sufficient to fit a low-order polynomial in the function of time for most cases. It was because BATSE has had a fixed orientation and has not been able to change it during a burst. As a result, sources moving in and out of the field of view could not play an important role on a shorter timescale, and all the backgrounds could be subtracted by fitting a time-dependent low-order (up to 3) polynomial (Koshut et al. 1996; Sakamoto et al. 2008; Varga et al. 2005).

In the *Fermi* era, this situation has however fundamentally changed. To present this on our example above, we fitted a simple 3rd-order polynomial function of time shown with a grey line in Fig. 1. The fitting was done by using only a selected short time interval around the burst, which is a common method of the BATSE era. This fit may be sufficient around the burst prompt emission, but is sufficient only there. It is clear that the background cannot be well modelled with this simple function over a long timescale. Moreover, an incidental longtime emission would be overlooked.

Fitting higher order polynomials of time could be suggested. We rule out this solution because of two reasons. First, these fittings show polynomial instabilities in the burst interval, as we have seen it in our early experiments; namely, we got high order, low amplitude oscillations of these fittings during the interval of the burst. Second, we wanted to take into consideration that the main cause of the complicated background is well known (namely the rocking motion of the satellite). Indeed, we use physically defined underlying variables, as we will show in Sect. 4, and with them, we fit higher order multidimensional functions. As a conclusion, time-dependent polynomial fittings may have been sufficient for the BATSE data but *Fermi*-data cannot be analysed that way due to the rapid motion of the satellite: we need a *Fermi* specific method.

Such a method was presented by Fitzpatrick et al. (2011). They estimated the background successfully with the rates from adjacent days, when the satellite was at the same geographical coordinates. This solution is only applicable when the satellite is in sky survey mode and cannot be used if an ARR occurred. If an ARR is accepted, this technique cannot be employed.

3. Investigation of possible background sources

3.1. Orientation of NaI detectors

As we mentioned above, *Fermi* uses a complex algorithm to optimize the observation of the gamma-ray sky. In sky survey mode, the satellite rocks around the zenith within ±50°, and the pointing alternates between the northern and southern hemispheres each orbit (Meegan et al. 2009; Fitzpatrick et al. 2011).

The set-up of the instruments on-board is well known from the literature (Meegan et al. 2009). The 12 NaI detectors are placed in such a way that the entire unocculted sky is observable with them at the same time, as seen in Fig. 2. *Fermi* has a proper coordinate system, whose Z axis is given by the LAT main axis. From now on, we only analyse the data of the NaI detectors; the BGO detectors will be considered in a future work.

The *Fermi* data set is available from the web for the GBM's 12 NaI detectors[1]. The positional information of the spacecraft is contained in the LAT data (called Spacecraft Data[2]). The GBM

---

[1] The High Energy Astrophysics Science Archive Research Center (HEASARC): legacy.gsfc.nasa.gov

[2] LAT Photon, Event, and Spacecraft Data Query: http://Fermi.gsfc.nasa.gov/cgi-bin/ssc/LAT/LATDataQuery.cgi
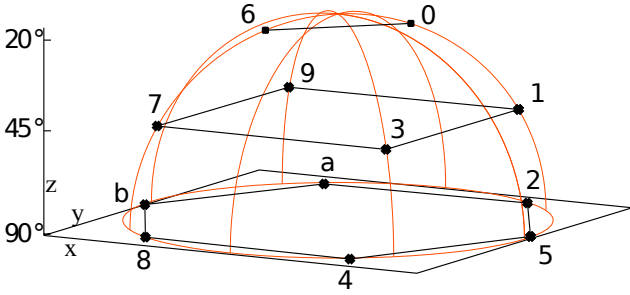
Fig. 2. Setup of the 12 NaI detectors of GBM given in the Spacecraft Coordinates (see Meegan et al. 2009). The zenith angle of the detectors in degrees is marked. This design is built in order to cover the whole visible part of the sky with the GBM. (The figure is based on Table 1. of Meegan et al. 2009. Notations "a" and "b" mean the 10th and 11th NaI detectors, respectively.)
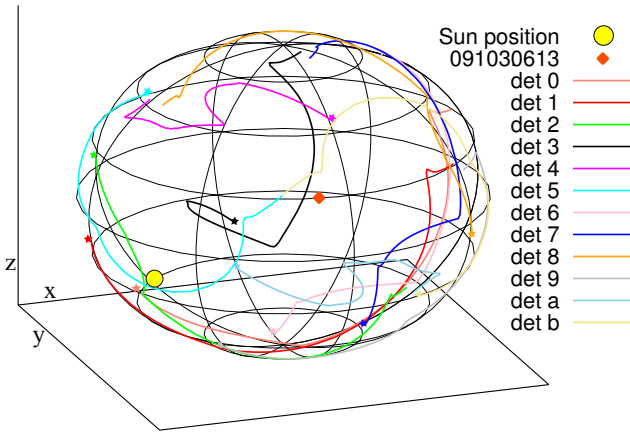

Fig. 3. Orientation of the 12 NaI detectors on the sky (in the second equatorial system), during the pre- and post-1000 s around the burst 091030.613. To show the direction with time, we marked the starting points of every line with a small star. The Sun's position is marked with big sphere. The burst position is marked with diamond.

data, which we use in our analysis (called CTIME), are available at 8 energy channels with 0.064-s and 0.256-s resolution (for triggered and non-triggered mode, respectively). The position data is available in 30-s resolution.

The 30-s Spacecraft Data were evenly proportioned to 0.256-s and 0.064-s bins using linear interpolation, to correspond to the CTIME data of non-triggered and triggered mode, respectively. We created a 3D-plot from this data using the known orientation of the 12 NaI detectors given in the Spacecraft coordinate system. Figure 3 shows the detectors' orientation (path) on the sky during the pre- and post-1000 s around the trigger of 091030.613 (lightcurve was shown in Fig. 1).

The catalogue location for the GRB is shown with a diamond ($\alpha = 260.72°$, $\delta = 22.67°$, see Paciesas et al. 2012). Since we wanted to know the position of the detectors on the sky, we needed to transform the proper coordinate system of the *Fermi* shown in Fig. 2 to the general (second) equatorial system, since the burst's position was given in the latter. In addition, we plot the celestial angle between the 3rd detector (black line in Fig. 3) and the burst 091030.613 (marked with a diamond in Fig. 3) against time in Fig. 4.

At this point, we have to mention the effect of the NaI detectors' characteristics. Figure 12 from Meegan et al. (2009) shows the angular dependence of a NaI detector effective area: the angular response for the flat crystal is approximately cosine. For
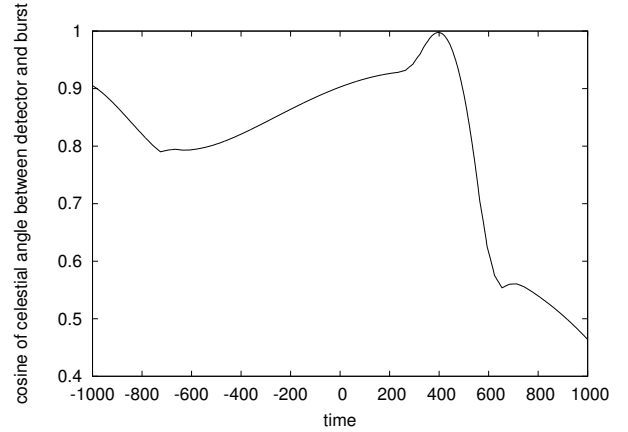

Fig. 4. Celestial distance of the 3rd GBM detector and the *Fermi*-burst 091030.613 as a function of time. It is worth comparing this figure to Fig. 1.

this reason, we define our first underlying variable as the *cosine* of the celestial angle between the detector and the burst (as it is shown in Fig. 4). We will find further underlying variables in Sects. 3.2 and 3.3.

However, the NaI characteristics are also energy dependent: The dependence of the transmissivity on the angle of incidence is more important at higher than at lower energies. Furthermore, a detector has two small sensitivity peaks around −150 and 150 degrees, which means that they can detect photons coming under the plane of the crystal. We consider these features by allowing higher orders when performing the fits seen in Sect. 4.

If we compare Figs. 4 to 1, it is clear that the unpredictable variation in the background is connected to the orientation of the detector in question. We can also examine other bursts (see Sect. 5.2. for more examples). However, we cannot state a clear relation between the angle and the lightcurve.

3.2. Earth

The satellite's *Z* axis (the direction of the LAT) is pointing to the opposite direction of the Earth, when it is possible. Due to the rocking behavior, GBM detectors' orientation are, however, towards the Earth-limb from time to time.

The Earth-limb is notable from the board of *Fermi*. At an altitude of ∼565 km, it corresponds to an aperture of ∼134° when fully in the FoV. Therefore, we have to consider the effect of the Earth-limb when analysing the data of the GBM detectors. There are terrestrial gamma-ray flashes (brief bursts of gamma-radiation that are thought to be associated with lightning in the upper atmosphere); furthermore, gamma-rays of the GRB's scatter on the atmosphere. The main contributor in our background model is the latter. Terrestrial gamma-ray flashes have a duration of only tens of milliseconds (Briggs et al. 2010) and are too short to have a significant effect.

We presume therefore that the detected background also depends on how much sky the Earth-limb shields from the detector's FoV. To measure this, we define the *Earth-occulted sky rate* as the rate of the Earth-covered sky correlated to the size of the FoV. As *Fermi* has a proper motion, the Earth-occulted sky rate is a function of time, satellite position, and orientation. Based on spherical geometrical computations given in Appendix A, we can get the Earth-occulted sky rate as a function of the aperture of the Earth-limb and the maximum altitude of the Earth seen
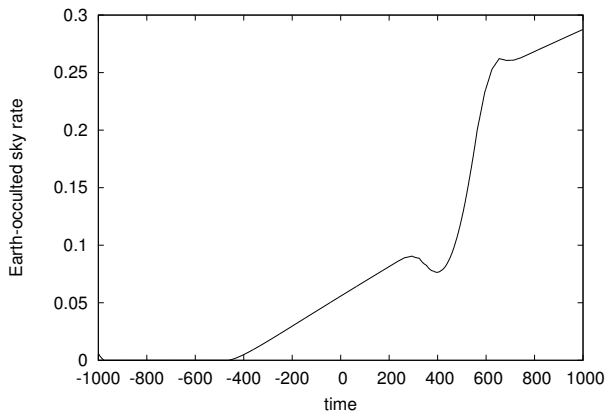
Fig. 5. Earth-occulted sky rate for the 3rd GBM detector as a function of time during the GRB 091030.613. (The Earth-occulted sky rate is zero, if the Earth-limb is out of the FoV.)
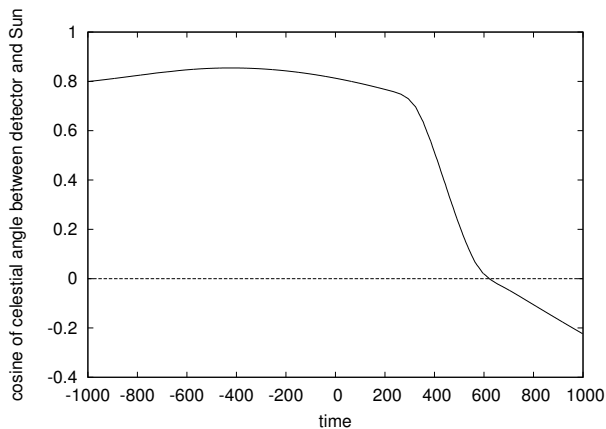

Fig. 6. Celestial distance of the 3rd GBM detector and the Sun as a function of time during the GRB 091030.613. The dashed line shows the 0 level (under this the Sun and the detector close in an angle larger than 90°). It is worth comparing this figure to Fig. 1.

from the *Fermi*. The Earth-occulted sky rate is plotted in Fig. 5 as a function of time.

We can see the same effect like above: there is some noticeable connection between the lightcurve in Fig. 1 and the Earth-occulted sky rate in Fig. 5.

3.3. Sun

One of the main contributors of the gamma-ray sky is the Sun. Flares and other eruptive solar events produce gamma rays in addition to those created by cosmic rays striking the Suns gas. If we are looking for a complete model of the background, we need to consider the contribution of the Sun as well.

The Sun's position is known from ephemeris tables for the day of the burst. We do not need more precise data than one day, because the time interval around the burst is only 2000 s in our analysis, and the position of the Sun does not change significantly during that time.

We compute the celestial distance (i.e. the angle) between the detector's direction and the Sun's position. This parameter is shown in Fig. 6. The Sun's position is also shown in the Fig. 3 with a yellow circle.

Comparing Figs. 1 to 6, one can see a connection between them. It is interesting to take notice of the fact that when the Sun's angle is larger then 90° (the cosine is lower that 0) around 600 s, the background rate in Fig. 1 drops. It shows a further correspondence of the background and the direction of the satellite towards to the Sun.

3.4. Other gamma sources

It is known today that the gamma-ray sky is not dark (Ackermann et al. 2012). Apart from the gamma-ray bursts, the terrestrial flashes, and the Sun's activity, there are also additional gamma-ray sources. Some examples include the gamma-rays produced when cosmic rays collide with gas in the Milky Way and the contribution from individual galactic sources, such as pulsars and other transient sources. As an extragalactic counterpart, we see collective radiation from galaxies that we are not detecting directly and gamma-rays from jets of active galaxies.

All this gamma-background has to be paid respect to. Rather than consider each contributing source individually, we introduce them into our model by allowing higher order terms when constructing the basis function of the general least square problem in Sects. 4.1 and 4.2. Furthermore, we use the method of singular value decomposition and Akaike model selection described in Sects. 4.3 and 4.4 for choosing the contributing ones, since the net effect of all these sources is hard to compute at every second.

4. Background subtraction

In Sect. 3, we have found three variables, which contribute to the variation in the background (see Figs. 4–6). They may help extend the polynomials of time that are only usable in some short intervals around the bursts. These three variables contain physical information of the background, because they are suggested by the actual position and orientation of the satellite.

However, we cannot quantify the contribution from the various sources at any given time. As we know that they have an influence on the background, we can fit a theoretical function of these physical underlying variables. Therefore, we fit and subtract the background using the three defined variables (burst position, Sun, and Earth) and the time variable, on a higher degree.

At this point, the following question may arise: why is the burst location needed? If a curve contains no burst for sure, there is no sense of using the burst position as an underlying variable. In that case, we would probably need to use only the Sun and the Earth (maybe implement the position of some other gamma-sources as well).

The reason why we use the burst position when there is a burst in the data is that the burst itself is a gamma source. Of course, it does not produce gamma photons at a constant level, but transiently. It is possible, nevertheless, that a not yet identified long emission would be enhanced (or weakened) because the satellite moved toward (or away of) the burst. To analyse (or sometimes even detect) emission coming from the astrophysical source outside of the main burst interval, it is needed to identify the fluctuations of the background rate caused by the change in the distance between the detector and the burst.

Next, we summarize the method of general least square for multidimensional fits, the algorithm of singular value decomposition, its numerical solution, and the Akaike model selection criterion for choosing the best model. Since we use underlying variables, which are calculated based on the actual direction and

orientation of the satellite, we call this method direction dependent background fitting (DDBF).

4.1. General least square

For simplifying the explanation, we will use the following notation:

y_i = counts per bin;

$x_i^{(1)}$ = celestial distance between burst and detector orientation (Fig. 4);

$x_i^{(2)}$ = celestial distance between Sun and detector orientation (Fig. 6);

$x_i^{(3)}$ = rate of the Earth-uncovered sky (Fig. 5);

$x_i^{(4)}$ = time.

We have a set of datapoints $(\boldsymbol{x}_i, y_i)$, where the components of $\boldsymbol{x}_i$ are $\boldsymbol{x}_i = (x_i^{(1)}, x_i^{(2)}, x_i^{(3)}, x_i^{(4)})$, while $i = 1 \ldots N$.

We use the general least square method (Press et al. 1992) for a multidimensional fit (since $\boldsymbol{x}_i$ has more than one component). The theoretical value of $y(\boldsymbol{x}_i)$ can be expressed with functions of $\boldsymbol{x}_i$, known as the *basis functions* $X_k(\boldsymbol{x}_i)$:

$$y(\boldsymbol{x}_i) = \Sigma_{k=1}^{M} a_k X_k(\boldsymbol{x}_i), \tag{1}$$

where the weights a_k are the model parameters that we need to estimate from the data ($k = 1 \ldots M$). Note that the basis functions $X_k(\boldsymbol{x}_i)$ can be nonlinear functions of $\boldsymbol{x}_i$ (this is why the method is called generalized), but the model depends only linearly on its parameters a_k.

The maximum likelihood estimate of the model parameters a_k is obtained by minimizing the quantity

$$\chi^2 = \Sigma_{i=1}^{N} \left(\frac{y_i - \Sigma_{k=1}^{M} a_k X_k(\boldsymbol{x}_i)}{\sigma_i} \right)^2, \tag{2}$$

which is known as the chi-square statistics or chi-square function.

One can write the chi-square function in a matrix equation form as well. For that, it is useful for defining the *design matrix* $\mathbf{A}$ ($N \times M$, $N \geq M$) of the fitting problem. Since the measured values of the dependent variable do not enter the design matrix, we may also define the vector $\boldsymbol{b}$. The components of $\mathbf{A}$ and $\boldsymbol{b}$ are defined to be the following:

$$A_{ij} = \frac{X_j(\boldsymbol{x}_i)}{\sigma_i}, \qquad b_i = \frac{y_i}{\sigma_i}. \tag{3}$$

From now, we set $\sigma_i = \text{const.}$

In terms of the design matrix $\mathbf{A}$ and the vector $\boldsymbol{b}$, the chi-square function can be written as

$$\chi^2 = (\mathbf{A} \cdot \boldsymbol{a} - \boldsymbol{b})^2, \tag{4}$$

and we need an $\boldsymbol{a}$ that minimizes this function, so the derivatives of χ^2 with respect of the components of $[\boldsymbol{a}]_k = a_k$ are zeros. That leads us to the equation for $\boldsymbol{a}$:

$$\boldsymbol{a} = (\mathbf{A}^{\mathrm{T}}\mathbf{A})^{-1}\mathbf{A}^{\mathrm{T}}\boldsymbol{b}, \tag{5}$$

where $\mathbf{A}^{\mathrm{T}}$ means the transpose of $\mathbf{A}$, and the expression $(\mathbf{A}^{\mathrm{T}}\mathbf{A})^{-1}\mathbf{A}^{\mathrm{T}}$ are called *generalized inverse* or *pseudoinverse* of $\mathbf{A}$. The best technique of computing pseudoinverse is based on *singular value decomposition* (SVD), which we describe in Sect. 4.3. We first specify the general method written above for the case of the *Fermi* GBM lightcurves in the following section.
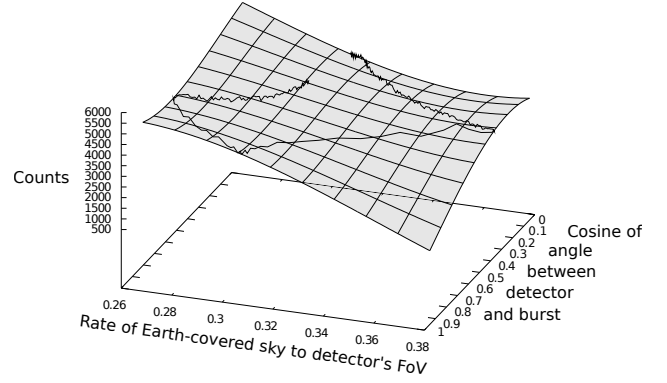

Fig. 7. The 2-dimensional hypersurface of a 3rd degree fitting to a *Fermi* lightcurve is shown. The fitted variables ($x_i^{(1)}$, $x_i^{(3)}$) are along the horizontal axes, while vertical axis represents the counts of the lightcurve y_i (shown by the black curve on the fitted grey plane).

4.2. Multidimensional fit

Equation (1) describes a hypersurface, and it is a generalization of fitting a straight line to the data. Very simple backgrounds may be fitted well with first degree hypersurface (hyperplane) of the four variables described as $\boldsymbol{x}_i = (x_i^{(1)}, x_i^{(2)}, x_i^{(3)}, x_i^{(4)})$:

$$y(\boldsymbol{x}_i) = a_1 \cdot x_i^{(1)} + a_2 \cdot x_i^{(2)} + a_3 \cdot x_i^{(3)} + a_4 \cdot x_i^{(4)}, \tag{6}$$

where the basis functions are $X_l(\boldsymbol{x}_i) = x_i^{(l)}$, respectively, and the design matrix simply consists of the components of $\boldsymbol{x}_i$ with $A_{ij} = x_i^{(j)}$.

For the most complicated *Fermi* backgrounds, higher degree of the variables are needed, however. One can illustrate the lightcurve data y_i and the fitted hypersurface $y(\boldsymbol{x}_i)$ using the two variables $x_i^{(1)}$ and $x_i^{(3)}$, which are both of 3rd degree on a 3D plot, as seen in Fig. 7. The design matrix of this problem is

$$\mathbf{A} = \begin{pmatrix} x_1^{(1)} & (x_1^{(1)})^2 & x_1^{(3)} & (x_1^{(3)})^2 & x_1^{(1)} \cdot x_1^{(3)} & 1 \\ x_2^{(1)} & (x_2^{(1)})^2 & x_2^{(3)} & (x_2^{(3)})^2 & x_2^{(1)} \cdot x_2^{(3)} & 1 \\ \ldots & & & & & \\ x_N^{(1)} & (x_N^{(1)})^2 & x_N^{(3)} & (x_N^{(3)})^2 & x_N^{(1)} \cdot x_N^{(3)} & 1 \end{pmatrix}. \tag{7}$$

Since we would like to have a method for all the cases of *Fermi*-bursts (whether it is simple, complicated, non-ARR, or ARR), we define our model to be comprehensive. Let us have $y(\boldsymbol{x}_i)$ as the function of $\boldsymbol{x}_i = (x_i^{(1)}, x_i^{(2)}, x_i^{(3)}, x_i^{(4)})$ of order 3, so the basis functions $X_k(\boldsymbol{x}_i)$ (and columns of the design matrix) consist of every possible products of the components $x_i^{(l)}$ up to order 3. That means that we have $M = k_{\max} = 35$ basis functions and $a_1, a_2 \ldots a_{35}$ as free parameters. We are sure that we do not need so many free parameters to describe a simple background, and although a complicated or ARR background may require more free parameters, 35 is too much in every practical case. Therefore, we decrease the number of free parameters using SVD in the next section.

4.3. Singular value decomposition

In Sect. 4.1, we showed that the least square problem can be solved by computing the pseudoinverse of the design matrix $\mathbf{A}$. For this purpose, we used Singular Value Decomposition (SVD),

since SVD is robust and very stable numerically (Long 2005; Press et al. 1992).

The SVD takes an $N \times M$ matrix $\mathbf{A}$ and factors it into $\mathbf{A} = \mathbf{U}\mathbf{S}\mathbf{V}^{\mathrm{T}}$. In this expression, U and V are $N \times N$ and $M \times M$ orthogonal matrices, respectively, and S is an $N \times M$ diagonal matrix. The columns of $\mathbf{U}$ and V are the eigenvectors of $\mathbf{A}\mathbf{A}^{\mathrm{T}}$ and $\mathbf{A}^{\mathrm{T}}\mathbf{A}$, respectively. Furthermore, S contains the square roots of the eigenvalues of $\mathbf{A}\mathbf{A}^{\mathrm{T}}$ and $\mathbf{A}^{\mathrm{T}}\mathbf{A}$ (both have the same eigenvalues, but different eigenvectors). These eigenvalues (diagonal elements in S) are called the *singular values*, s_i.

In overdetermined cases ($N \geq M$), the last $N - M$ singular values, however, are zeros, so we may consider only U as an $N \times M$ matrix, V as an $M \times M$ matrix, and S as $M \times M$ (it is called *economic* SVD).

If U and V enter the SVD decomposition of $\mathbf{A}$ as described above, one can show easily (using the orthogonalithy of U and V) that the pseudoinverse of $\mathbf{A}$ can be obtained as

$$pinv(\mathbf{A}) = (\mathbf{A}^{\mathrm{T}}\mathbf{A})^{-1}\mathbf{A}^{\mathrm{T}} = \mathbf{V}\mathbf{S}^{-1}\mathbf{U}^{\mathrm{T}}. \qquad (8)$$

SVD is implemented in several numerical software. In our work, we used OCTAVE's SVD function[3], known as the svd, and pseudoinversion function, known as the pinv (Long 2005).

Computing the pseudoinverse, we need the reciprocal of the singular values in the diagonals of S^{-1}, and there is a problem with this. The size of a singular value tells you exactly how much influence the corresponding rows and columns of U and V have over the original matrix $\mathbf{A}$. We can find the exact value of $\mathbf{A}$ by multiplying $\mathbf{U}\mathbf{S}\mathbf{V}^{\mathrm{T}}$. If we, however, remove (for example) the last columns of U and V and the final singular value, we are removing the least important data. If we then multiplied these simpler matrices, we would only get an approximation to $\mathbf{A}$ but one which still contains all but the most insignificant information. This means that SVD allows us to identify linear combinations of variables that do not contribute much to reducing the chi-square function of our data set.

The singular values are usually arranged in the order of size with the first being the largest and most significant. The corresponding columns of U and V are therefore also arranged in importance. If a singular value is tiny, very little of the corresponding rows and columns get added into the matrix $\mathbf{A}$ when it is reconstructed by SVD. If we compute the pseudoinverse of $\mathbf{A}$, the reciprocals of the tiny and not important singular values will be unreasonably huge and enhance the numerical roundoff errors as well.

This problem can be solved defining a *limit* value, below which reciprocals of singular values are set to zero. It means that the resulted matrix is an approximation of the real pseudoinverse, but we only omit information of the less interest.

With Eq. (1), we can define models of any number of variables and of arbitrary degree. In our case, we define models with four underlying variables of degree 3. Therefore, we have $M = 35$ free fitting parameters, as described above in Sect. 4.2. We do not know how many and which ones of these parameters have real importance in the variation in the background, but SVD can give us the answer trivially: pseudoinverse should be done by omitting the singular values which do not contribute so much.

The only question that remains is where this limit should be when singular values are not so important. We find an answer to that question in Sect. 4.4 using model selection criteria.

4.4. Model selection

Model selection is usually based on some information criterion. We use the Akaike information criterion (AIC) method to distinguish between different models to the data (Akaike 1974). However, we note here that AIC has to be used with caution, especially in the most complicated cases of backgrounds (see examples in Sect. 5.2).

We first assume that we have M models so that the kth model has k free parameters ($k = 1...M$). When the deviations of the observed values from the model are normally and independently distributed, every model has a value AIC_k so that

$$\mathrm{AIC}_k = N \cdot \log \frac{RSS_k}{N} + 2 \cdot k, \qquad (9)$$

where RSS_k is the residual sum of squares from the estimated model ($RSS = \Sigma_{i=1}^{N}(y_i - y(\boldsymbol{x}_i, k))^2$), N is the sample size, and k is the number of free parameters to be estimated. The first term of Eq. (9) measures the *goodness of fit* (discrepancy between observed values and the values expected under the model in question), the second term penalizes the free parameters. Given any two estimated models, the model with the lower value of AIC_k is the one to be preferred. Given many models, the one with lowest AIC_k will be the best choice: It has as many free parameters as needed but not more. Note that we do not use AIC for deciding how good the fit is but only for choosing one model over the another. The goodness of fit is given by the chi-square statistics defined by Eq. (2).

So far, we defined a complex model with 35 free parameters and, therefore, the design matrix $\mathbf{A}$ has 35 singular values (see Sect. 4.2). However, we know that we can omit some of the tiny singular values when computing the pseudoinverse of $\mathbf{A}$ – the ones, which are not necessary to the best fit of the gamma background. Thus, we take a loop over the pseudoinverse operation and decrease the omitted number (that is, increase the used number) of singular values in every step. Furthermore, we also compute the AIC_k in every step with k being the number of singular values not omitted. In that way, the number of singular values, which minimize the AIC_k as a function of k will be the best choice when calculating the pseudoinverse, so we get the most useful estimation of the model parameters $\boldsymbol{a}$ (let us remember that singular values are sorted in decreasing order, so the last and not important ones will be penalized by the second term of AIC).

At this point, we return to the *Fermi*'s GRB 091030.613 presented in Sects. 2 and 3 and follow the method of general least square, as described above. We compute AIC_k for every $k = 1...35$. This function is shown in Fig. 8.

Based on the AIC, the model with 14 singular values is the best choice. We present the result of the fitting with this model in Sect. 5.

4.5. Features of DDBF

One cornerstone of the fitting algorithm DDBF described above is the definition of the boundaries that decide the interval of the burst and the intervals of the background. In this work, we follow the common method of using user-selected time intervals (Paciesas et al. 2012).

Unlike in Paciesas et al. (2012), usage of the position data gives us the possibility of fitting the whole background of the CTIME file instead of selecting two or three small fractions around the burst. This notable feature has two important consequences.
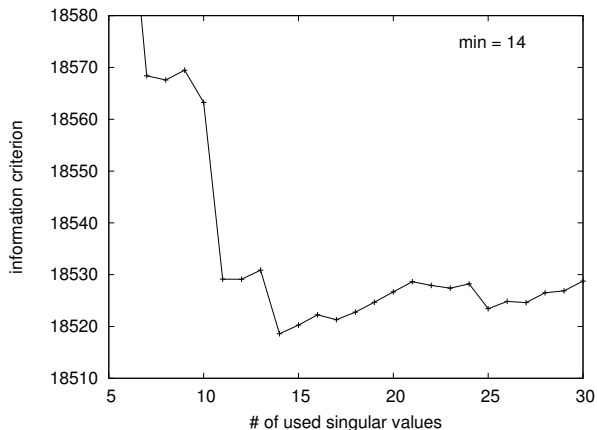
Fig. 8. Akaike information criterion for model selection. Model with 14 singular values is selected. (First and last five singular values are usually too high, so we do not show them.)

Fig. 9. Fitted background of the lightcurve of the *Fermi* burst 091030.613 measured by the 3rd GBM detector. Fitting was done by DDBF method (Szécsi et al. 2012a,c), using 14 non-zero singular values according to AIC. Reduced chi-square statistics is shown in the top right corner.

Fig. 10. Cumulative lightcurve of the *Fermi* burst 091030.613 by the 3rd GBM detector. Horizontal lines are drawn at 0% and 100% of total cumulated counts; dots mark every 5%. (Model with 14 singular values was selected, as seen in Fig. 8.)

First, the user has to select only the two boundaries before and after the burst; the other boundaries of the background intervals are inherently at the beginning and at end of the CTIME datafile. This reduces the error factor put into the DDBF method by the user compared to the method of Paciesas et al. (2012).

Second, one can easily detect a possible long emission coming from the astrophysical source. Since this emission has nothing to do with the direction and orientation of the satellite, the signal consequently has to be present in the lightcurve after the background filtering. (The opposite is also true: a signal after the burst could be considered a long emission when the user defines two short background intervals, although it was caused by the motion of the satellite. One example for this case is presented in Sect. 5.2.2.)

In the case of the GRB 091030.613, we used a burst-interval between -20 and $38\,\text{s}$ before and after the burst, respectively (see Sect. 5, Fig. 9). This means that the data of this time interval were omitted when fitting to the background. Other than that, the whole CTIME lightcurve were fitted.

It is one of our future plans to create a self-consistent method, which can automatically define these intervals based on a self-consistent iteration algorithm, so the user's presence would be unnecessary and the method would be totally automatic.

5. Results

5.1. Direction dependent fit and T_{90} for GRB 091030.613

In this section, we present the result of the DDBF for the GRB 091030.613 (the one that we showed in Fig. 1 and noted that there are difficulties with its background fitting).

The DDBF method is a good alternative for the polynomial fitting of time for two reasons. First, the background model consists of astrometric computations of astrophysical objects, and the fitting variables have physical meanings. This property is missing when one uses simple polynomial fitting of time; however, *Fermi*'s complex motion prefers to have a more detailed model for the background sources.

Second, using the polynomial fitting of time, one has to define two short time intervals before and after the burst, which can be well described by a polynomial function (see Sect. 4.5). Usually, these intervals have to be short enough and defined precisely to get a correct fit. DDBF can fit all the 2000-s data of the
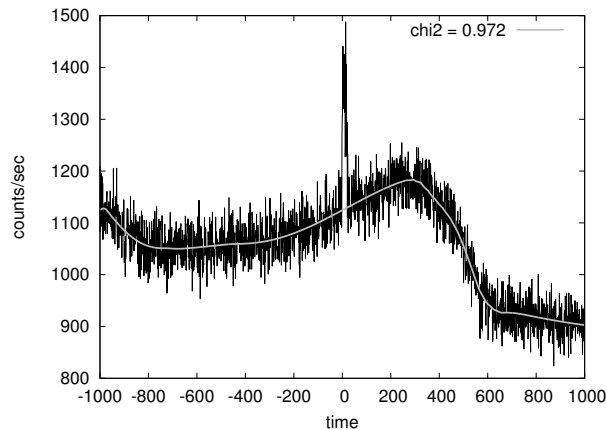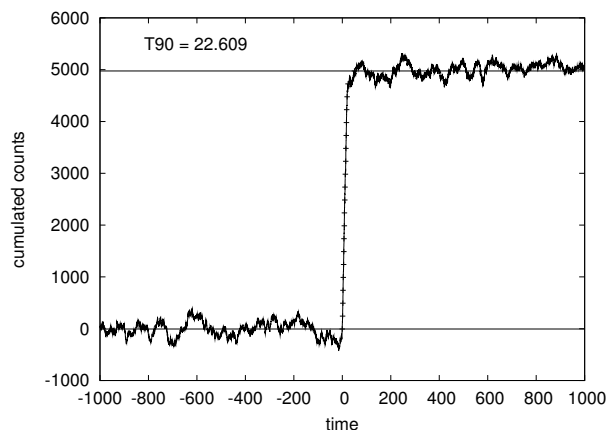
CTIME (and CSPEC) files. Therefore, we are also able to study long emissions or precursors.

Figure 10 shows the cumulative lightcurve from which we computed the durations (Szécsi et al. 2012b). Horizontal lines were computed by averaging the cumulated background levels before and after the burst: These are the levels of 0% and 100% of total cumulated counts.

We note that these levels were selected by the user for the *Fermi* GBM Catalogue. Since they only fitted some short intervals around the burst using time-dependent polynomials, this step could not been automatised (Paciesas et al. 2012). With DDBF, however, we fit all the 2000 s of the CTIME file (except for the burst in the middle) using direction dependent underlying variables. Our method gives us cumulative lightcurves, where the resulting levels are tightly distributed around a constant value, and therefore, the automation (calculating the average of the levels) is possible.

Between the levels of 0% and 100%, 19 equally heightened points mark every 5% of their cumulated counts (the first and last are fixed where the lightcurves step over and below the levels

before and after). T_{90} is computed by subtracting the value corresponding to 5% from the value corresponding to 95%.

The *Fermi* GBM Catalogue reports $T_{90}^{cat} = 19.200 \pm 0.871$ s. Our result is $T_{90} = 22.609^{+13.518}_{-4.522}$ s. We always give confidence intervals instead of error bars with the T_{90} values, since the DDBF method is complicated: the error estimation needs further considerations. See Sect. 6 for details.

This result does not depend on the spectrum or the detector response matrix, because we summed up the channels of the CTIME files. However, the DDBF can be used for every channel separately (as it was done in Szécsi et al. 2012b) and can also be used with CSPEC data to obtain spectral information.

5.2. Examples

We began with the observation that many of *Fermi* bursts (even in non-ARR cases) have a varying background corresponding to the actual direction of the satellite. Thus, our idea was to use this directional information in the filtering algorithm. We created a method, which is able to separate this background from the lightcurves. Now, we want to demonstrate the effectiveness of our method, so we present examples here, with each having an extreme background.

These examples were purposely chosen to demonstrate how powerful DDBF can be and to give an overall impression about the cases for which it can be used in and the advantages and the difficulties it carries. Two of the examples below are ARR bursts (Sects. 5.2.5 and 5.2.7). In general, we would like to draw attention to the connection between the direction dependent underlying variables and the variability features of the lightcurve: the correlation between them are undeniable in every single case (even in no-ARR cases).

In each example, we present figures of the original lightcurves for one of the triggered detectors, summarizing the counts of the effective range of channels of CTIME file. On these lightcurves, we plot the fitted theoretical background with a solid line and the reduced chi-square statistics in the top right corner. Then, we show the *absolute value* of the direction dependent underlying variables (in one graph), and the AIC_k as a function of used singular values.

As a final result, we show the cumulative lightcurves, which we used to compute the T_{90} values. We also give the preliminary T_{90}^{pre} from the gamma-ray coordinates network (GCN 2013), and the T_{90}^{cat} from the catalogue computed and published by the GBM team (Paciesas et al. 2012). We give confidence intervals of the computed T_{90}s (and T_{50}s as well). The description of how these confidence intervals were computed is in Sect. 6.

It is important to note, however, that only long GRBs were analysed here. The reason of this is that short bursts usually are not influenced by the fast motions of the satellite. During one short burst, the background does not change so much that DDBF should be used. Furthermore, short bursts are better analysed using the time tagged events (TTE) data type instead of CTIME (and CSPEC), and therefore, they are not presented here.

Since we want to present how effective our method is, we show the detector having the highest background variability without filtering in every case. However, it is possible to combine the same analysis for a number of bright detectors for each burst to reduce the error. It will be a part of a future work to create a catalogue of the durations of the *Fermi* bursts using DDBF, in which we will use more than one detector's data. Here, we present the method with only one triggered detector for each case.
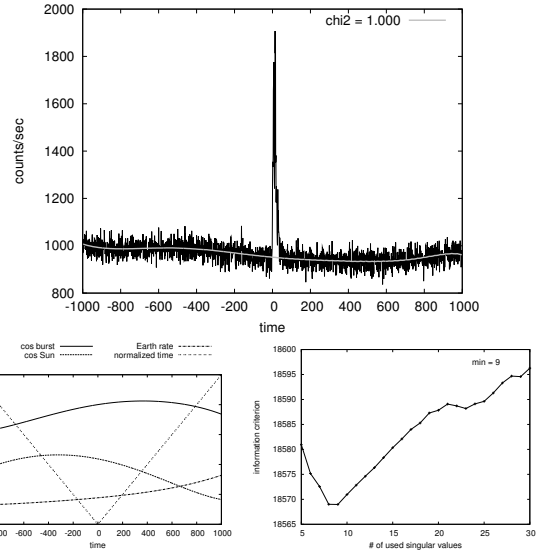
Fig. 11. *Top*: lightcurve of the *Fermi* GRB 090102.122 as measured by the triggered GBM detector "a" and the fitted background with a grey line. Burst interval (s): [−5:35]. *Bottom left*: underlying variables (absolute values). See Sect. 3. *Bottom right*: Akaike information criterion. See Sect. 4.4.
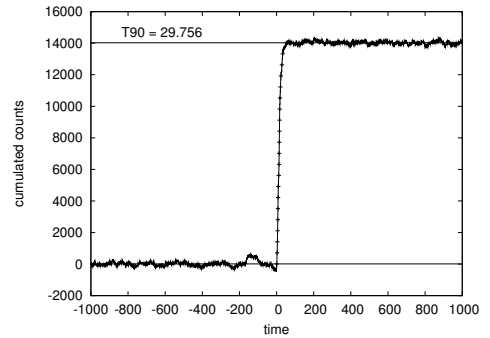

Fig. 12. Cumulative lightcurve of GRB 090102.122. Horizontal lines are drawn at 0% and 100% of total cumulated counts; dots mark every 5%.

5.2.1. GRB 090102.122

GRB 090102.122 is an example where no fast motion was carried out, and therefore, no high background rate variation is taken place. This burst had no ARR. The lightcurve is simple in the sense that a time dependent polynomial function could possibly be used to fit it properly. However, we present DDBF results only to show that the method works in these simple cases as well. The AIC chose 9 singular values, and one can see in the information criterion plot that more values than this are punished by the AIC: Too many free parameters would cause the fitted curve to have unnecessary loops fitted to the noise of the background. The *Fermi* catalogue reports $T_{90}^{cat} = 26.624 \pm 0.810$ s (Paciesas et al. 2012). Detector "a" was analysed here.

Around −150 s in the lightcurve, there is a peak, which cannot be explained by the physical underlying variables. This causes a little hump in the cumulative lightcurve in Fig. 12. (Furthermore, the same peak can be seen in the lightcurves of the other triggered detector.) It is out of the scope of this article to decide whether it is a pre-burst or another instrumental effect, however, we emphasize again that DDBF can also

be used for finding pre-bursts or long emissions. We measured $T_{90} = 29.756^{+2.971}_{-1.198}$ s.

5.2.2. GRB 090113.778

The *Fermi* catalogue reports $T^{cat}_{90} = 17.408 \pm 3.238$ s ([Paciesas et al. 2012](#)) and this is a no-ARR case. Detector "0" was analysed here ([Szécsi et al. 2012c](#)). This lightcurve in Fig. 23 has some extra counts around 400 and 600 s. Both of them can be explained with the variation in the underlying variables: around 400 s, the Earth limb was out of the FoV and then it came back and peaked at 600 s until the Sun's position changed significantly. Both of these could cause the extra counts. The best chosen model with 12 singular values could fit these peaks (see the big and small loops in the fitted lightcurve at 400 and 600 s). Since the underlying variables are based on the motion of the satellite, it follows that these two peaks are probably not astrophysical effects. They do not come from the GRB but from the combined effect of the background sources in the surroundings: the Earth and the Sun. It is important to note that a statement like that could not be made using the traditional method of polynomial fitting of time.

After the background subtraction, the cumulative lightcurve (Fig. 14) is noisy because this burst was not so intense with only ~1800 counts, while other examples have 10 000−20 000 counts. Our result is $T_{90} = 19.679^{+10.883}_{-6.421}$ s.

5.2.3. GRB 090618.353

The *Fermi* catalogue reports $T^{cat}_{90} = 112.386 \pm 1.086$ s ([Paciesas et al. 2012](#)). No ARR was taken.

The data from detector "7" were analysed here. Nevertheless, we should note that detector "4" has so many counts that almost any kind of background model seems to be good enough to compute T_{90} when using detector "4". We still choose to present detector "7" here, because we can show our method working in a more complicated case.

Now we may be used to the fact that quickly varying underlying variables (which correspond to fast motion of the satellite) cause a quick change in the lightcurve background at the same time. This burst had no ARR, but the satellite started to rotate according to the fast change of the underlying variables after the trigger. At this point, the lightcurve is changing more quickly than before. The fitted grey line (chi-square statistics are 1.009) pursue this change, and results in a duration of $T_{90} = 103.338^{+3.842}_{-6.725}$ s.

5.2.4. GRB 090828.099

GRB 090828.099 was detected by the GBM on 28 August 2009 at 02:22:48.20 UT ([GCN 2013](#), 9844). The first GBM catalogue reported $T^{cat}_{90} = 68.417 \pm 3.167$ s ([Paciesas et al. 2012](#)). This is a non-ARR case. The data from detector "5" was analysed here.

The AIC gives us the model with 7 singular values. This is also a simple background. Only the first 300−400 s are influenced by the fast motion, but DDBF could filter this effect. The duration computed with the DDBF is $T_{90} = 63.608^{+1.467}_{-1.652}$ s.

5.2.5. GRB 091024.372 and .380

This case deserves attention because an ARR was caused by this burst. The GBM was triggered twice on GRB 091024: the first time at 08:55:58.47 UT (GRB 091024.372) and the second time at 09:06:29.36 UT (GRB 091024.380). The GCN 10114
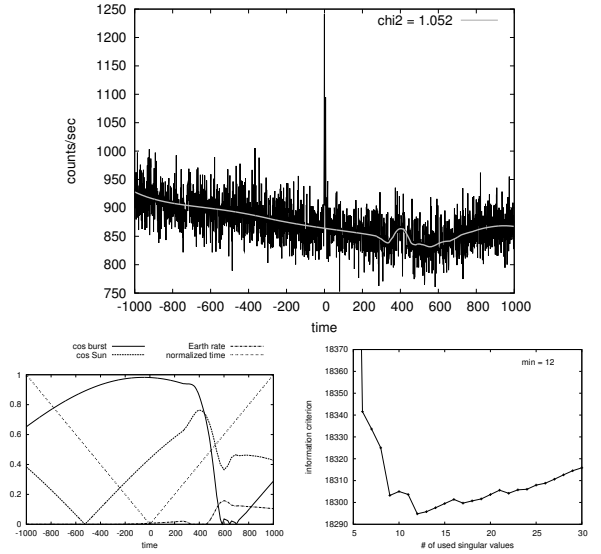

Fig. 13. *Top*: lightcurve of the *Fermi* GRB 090113.778 as measured by the triggered GBM detector 0' and the fitted background with a grey line. Burst interval: [−20:40]. *Bottom left*: underlying variables (absolute values). See Sect. 3. *Bottom right*: Akaike information criterion. See Sect. 4.4.
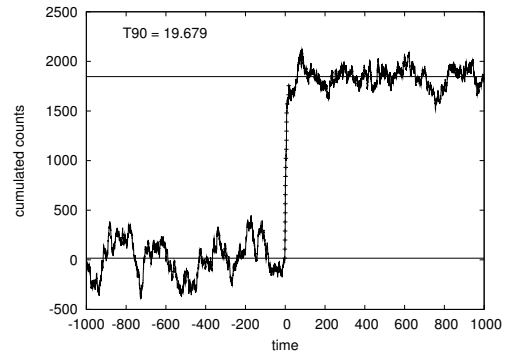

Fig. 14. Cumulative lightcurve of GRB 090113.778. Horizontal lines are drawn at 0% and 100% of total cumulated counts; dots mark every 5%.

reports: *"This burst was detected by Swift and the Fermi Gamma-ray Burst Monitor with a first emission interval lasting ~50 s and a second emission interval starting ~630 s after trigger and lasting more than 400 s. The spacecraft performed a repointing maneuver for this burst which resulted in pointed observation for 5 h starting ~350 s after* [the second] *trigger."* ([GCN 2013](#), 10114).

Additionally, [Gruber et al. (2011)](#) performed a detailed analysis of this burst and its optical afterglow. Here, we show DDBF duration results separately for the two triggers. Further investigation is needed to analyse the total ~1020 s of this extreme long burst as a whole with DDBF. This will be provided in a future work.

Figure 19 shows the CTIME data of the first trigger (.372) using the triggered detector "8". The second burst episode after 630 s can also be recognized in the lightcurve by the naked eye (however, the satellite changed its position at the time of this second trigger, so this emission looks less intensive here in detector "8"). On the other hand, one can notice that the underlying variables do not show any variability at this time interval. Qualitatively this means that something is happening there
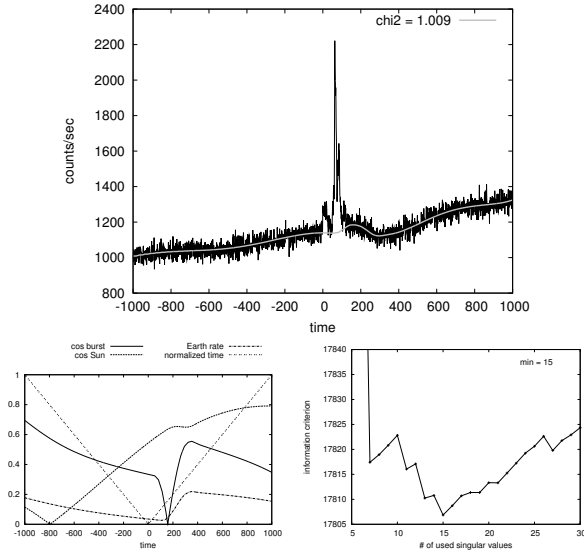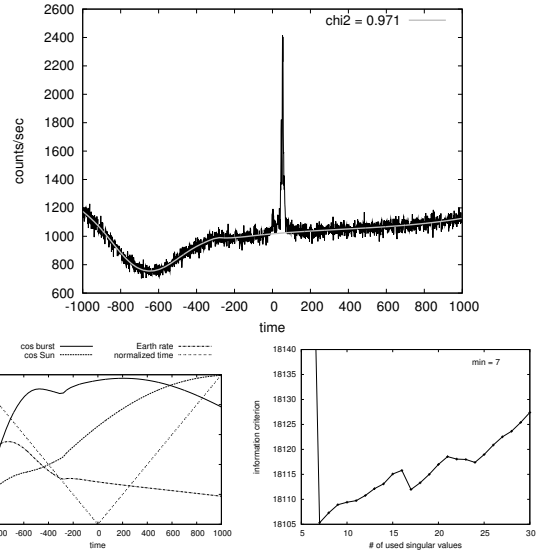
Fig. 15. *Top*: lightcurve of the *Fermi* GRB 090618.353 as measured by the triggered GBM detector "7" and the fitted background with a grey line. Burst interval: [−20:130]. *Bottom left*: underlying variables (absolute values). See Sect. 3. *Bottom right*: Akaike information criterion. See Sect. 4.4.
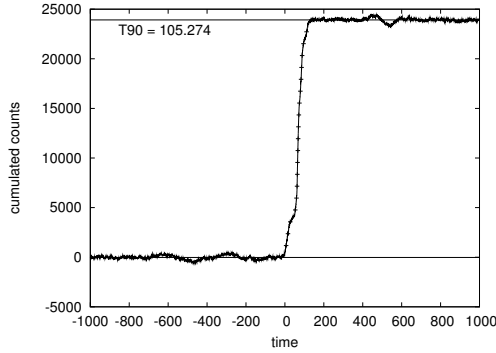

Fig. 17. *Top*: lightcurve of the *Fermi* GRB 090828.099 as measured by the triggered GBM detector "5" and the fitted background with a grey line. Burst interval: [−10:80]. *Bottom left*: underlying variables (absolute values). See Sect. 3. *Bottom right*: Akaike information criterion. See Sect. 4.4.

Fig. 16. Cumulative lightcurve of GRB 090618.353. Horizontal lines are drawn at 0% and 100% of total cumulated counts; dots mark every 5%.
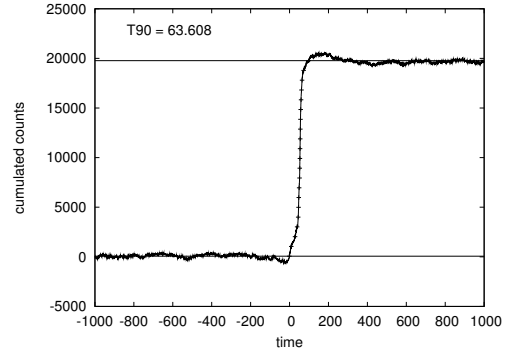
Fig. 18. Cumulative lightcurve of GRB 090828.099. Horizontal lines are drawn at 0% and 100% of total cumulated counts; dots mark every 5%.

which is not coming from our modelled sources (Earth or Sun). This can be shown more quantitatively, if one considers that another local minimum can be seen at 15 which are close to the global minimum at 20, which AIC determines for this fit. Here the models with too many free parameters considered the second burst as a background noise and tried to filter it with these polynomial loops. Indeed, the fitted curve shows several loops, especially at the interval of the second burst.

We can draw two lessons from all of this. First, one has to use AIC with caution. Sometimes, the preferred singular value is not the one AIC gives, if there is another one close enough. In the case of the first emission (.372), there are no loops on the fitted curve, when one uses only 15 singular values (the second local minimum of the AIC). Fortunately, the final T_{90} result does not change much (less than 1% in this case). Second, one needs to pay more attention to too many singular values (we would say more than 20, based on our other examples), especially if there is an additional local minimum in AIC close to the chosen one. This can mean that something is happening that cannot be well modelled and may be an astrophysical process. We already mentioned that DDBF can be used to detect long emissions: this

is clearly such a case. Our final result for the first emission (.372) is $T_{90} = 100.013^{+7.908}_{-4.156}$ s.

The second burst emission is after 630 s in Fig. 19. As we already mentioned, this second emission resulted a second trigger from the GBM (.380), which is shown in Fig. 21 using the data of the triggered detector "9". Here, the first trigger is visible at −630 s. However, it is less intensive, since detector "9" was not triggered with the first emission.

This second burst was so long (GBM Catalogue reported $T_{90}^{cat} = 450.569$ s, Paciesas et al. 2012) that we needed to reconsider the best model given by AIC. The minimum of AIC as a function of the used singular values is at 11, but this model has a large polynomial loop in the burst interval and is, therefore, useless. Although this is understandable, longer burst intervals lead to shorter fitted backgrounds (and thus, a large amount of information can be lost), it implies that the information criterion has to be used with caution, especially in extreme cases. In this case, we chose the model with 7 singular values. This model fits the background considerably well according to our experience, and is supported by the information criterion: the smallest local minimum is at 7.
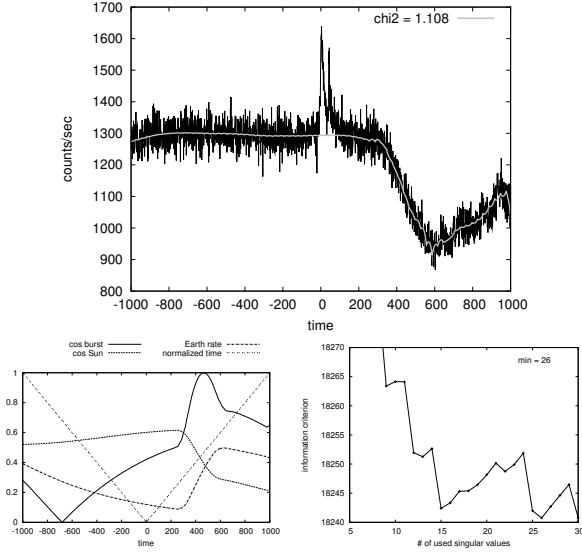
Fig. 19. *Top*: lightcurve of the *Fermi* GRB 091024.372 as measured by the triggered GBM detector "8" and the fitted background with a grey line. Burst interval: [−19:119]. *Bottom left*: underlying variables (absolute values). See Sect. 3. *Bottom right*: Akaike information criterion. See Sect. 4.4.
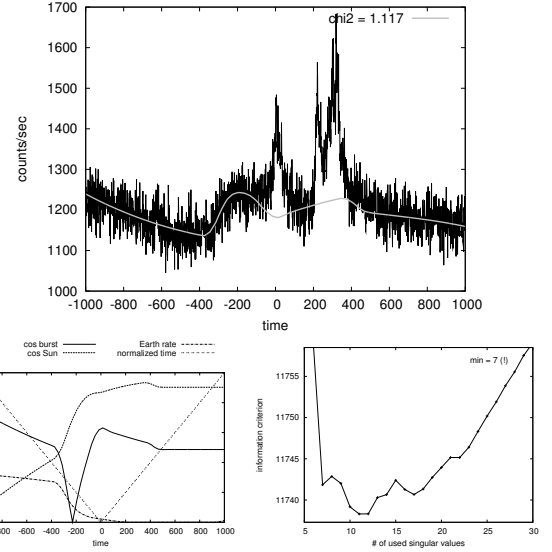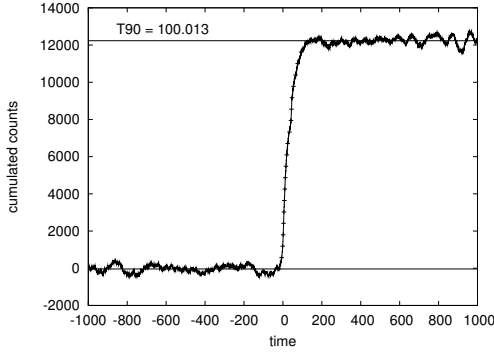

Fig. 20. Cumulative lightcurve of GRB 091024.372. Horizontal lines are drawn at 0% and 100% of total cumulated counts; dots mark every 5%.
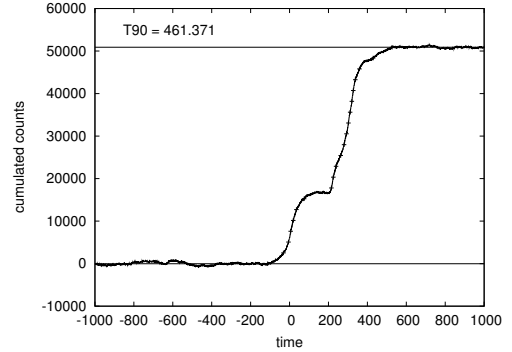
The ARR was issued at 09:12:14.28 UT, ~970 s after the first trigger (.372) and ~350 s after the second trigger (.380) (Gruber et al. 2011). A small change in the underlying variables at 350 s in Fig. 21 can be seen, but the ARR slew was not too large, since the source was already at 15 degrees from the LAT boresight. Nonetheless, the effect of the ARR is represented by the fitted model, as seen by the small knot of the grey line at 350−400 s in Fig. 21. As for the cumulative lightcurve in Fig. 22, the first emission at −630 s is present with a non-significant sign, otherwise our result of $T_{90} = 461.371^{+48.575}_{-71.535}$ s agrees with the GBM Catalogue.

5.2.6. GRB 100130.777

The *Fermi* GRB 100130B was detected by the GBM on 10 January 2010 at 18:38:35.46 UT. The GBM GRB Catalogue presented $T_{90}^{\text{cat}} = 86.018 \pm 6.988$ s (Paciesas et al. 2012). We analyse the data of triggered NaI detector "8" using DDBF.

Although the background does not change extremely during the ~80 s of the burst, it is a good example to present the contribution of the celestial position of the satellite to the actual level

Fig. 21. *Top*: lightcurve of the *Fermi* GRB 091024.380 as measured by the triggered GBM detector "9" and the fitted background with a grey line. Burst interval: [−200:600]. *Bottom left*: underlying variables (absolute values). See Sect. 3. *Bottom right*: Akaike information criterion, the smallest local minimum of 7 singular values is used here. See Sect. 4.4.

Fig. 22. Cumulative lightcurve of GRB 091024.380. Horizontal lines are drawn at 0% and 100% of total cumulated counts; dots mark every 5%.

of the background. If one takes a look at Fig. 23, one can see that the variation in the lightcurve has a connection to the variation in the underlying variables.

AIC gives us a best model of 17 singular values. After the background subtraction, the cumulative lightcurve (Fig. 24) gives us $T_{90} = 87.725^{+5.311}_{-4.911}$ s. For error estimation, see Sect. 6.

5.2.7. GRB 100414.097

This GRB also had an ARR event. Quoting the GCN report 10595: *"at 02:20:21.99 UT on 14 April 2010, the Fermi Gamma-Ray Burst Monitor triggered and located GRB 100414A. The Fermi Observatory executed a maneuver following this trigger and tracked the burst location for the next 5 h, subject to Earth-angle constraints."* (GCN 2013, 10595).

In this case, we chose to analyse a non-triggered detector (detector "5"). Because this burst was so intensive and bright, the triggered detectors show totally negligible background rate variations compared to the brightness of the burst. Since we want to demonstrate that our method works in very complicated cases
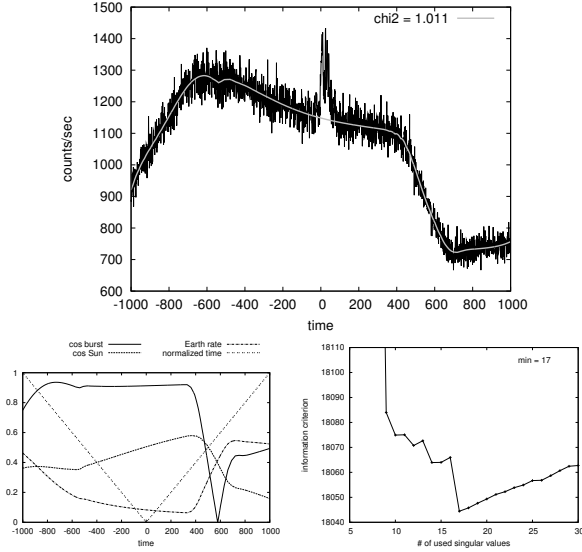
Fig. 23. *Top*: lightcurve of the *Fermi* GRB 100130.777 as measured by the triggered GBM detector "8" and the fitted background with a grey line. Burst interval: [−30:90]. *Bottom left*: underlying variables (absolute values). See Sect. 3. *Bottom right*: Akaike information criterion. See Sect. 4.4.
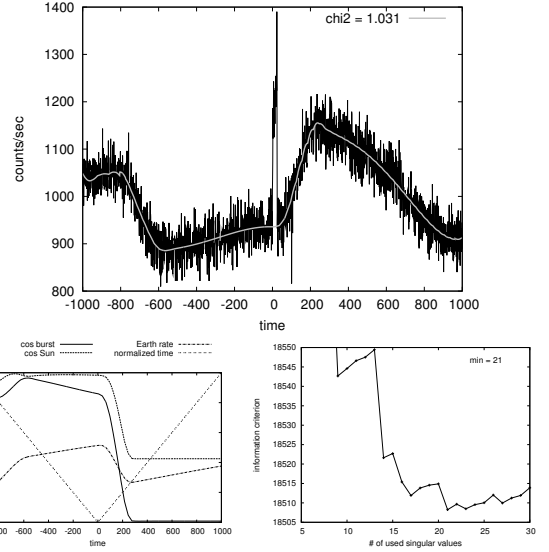

Fig. 25. *Top*: lightcurve of the *Fermi* GRB 100414.097 as measured by the non-triggered GBM detector "5" and the fitted background with a grey line. Burst interval: [−20:30]. *Bottom left*: underlying variables (absolute values). See Sect. 3. *Bottom right*: Akaike information criterion. See Sect. 4.4.
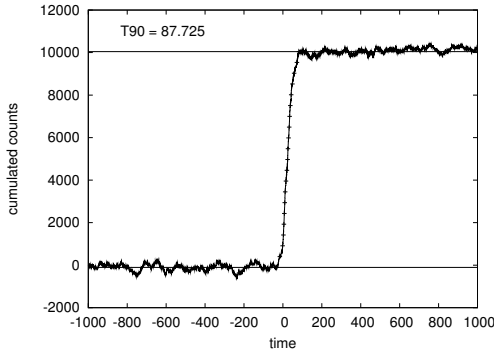

Fig. 24. Cumulative lightcurve of GRB 100130.777. Horizontal lines are drawn at 0% and 100% of total cumulated counts; dots mark every 5%.
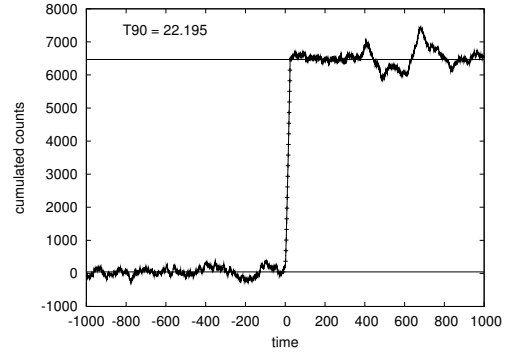

Fig. 26. Cumulative lightcurve of GRB 100414.097. Horizontal lines are drawn at 0% and 100% of total cumulated counts; dots mark every 5%.

as well, we analyse a lower signal-to-noise detector. Evidently, DDBF can also fit the data of the bright triggered detectors well.

The GBM Catalogue reports a duration of $T_{90} = 26.497 \pm 2.073$ s. According to the GCN 10594 and 10610, this burst also triggered the LAT and the *Suzaku Wide-band All-sky Monitor (WAM)* (GCN 2013, 10594, 10610).

As we already mentioned above, singular values that are too high ($\gtrsim 20$) deserve attention. In this case, the AIC chose 21 singular values. This 21 singular value model describes the background well. The only exception is the extra count rate around 600 s, which is also clearly noticeable in the cumulative lightcurve. More detailed analysis of the spectral features of this event are needed to determine if this event is caused by the burst or not. Given that there were additional observations by the LAT and by the Suzaku WAM which do not report long emission, we expect that this was a local event at the GBM caused by cosmic rays or another possible transient source, which could be filtered by using different energy channels. Our result is $T_{90} = 22.195^{+2.149}_{-1.421}$ s.

6. Confidence intervals

The DDBF method described above is too complicated to give a simple expression for the error of T_{90} using general rules of error propagation. We therefore decided to give confidence intervals corresponding to 68% (approximately 1σ level). For this, we use Monte Carlo (MC) simulations. We simulate the data with Poisson noise: assuming that counts are given by a Poisson process, we exchange our input data to one coming from a random Poisson distribution. In the case of a Poisson distribution, which is parametrised by the mean rate (λ), the expected value is given by λ. We therefore replace each datapoint with a value drawn from a Poisson distribution with a mean equal to the datapoint in question.

DDBF was repeated for 1000 MC simulated data. The distribution of the Poisson-modified T_{90} and T_{50} values are shown in Figs. 27 and 28 for GRB 091030.613, respectively.

Figure 27 shows two significant peaks around 22 and 47 s. The first peak at 22 s corresponds to the measured T_{90} value. However, the measured T_{90} value is systematically longer in some cases of the Poisson noise simulation, because this burst has a little pulse around 47 s (see Figs. 9 and 10), and T_{90} is

Table 1. Final T_{90} and T_{50} results.

Burst	Sing.v.	T_{90} (s)	Conf. int. (s)		T_{90}^{cat} (s)	T_{50} (s)	Conf. int. (s)		T_{50}^{cat} (s)
090102.122	9	29.756	+2.971	−1.198	26.624 ± 0.810	10.859	+0.531	−0.556	9.728 ± 0.572
090113.778	12	19.679	+10.883	−6.421	17.408 ± 3.238	6.408	+0.498	−0.344	6.141 ± 1.446
090618.353	15	103.338	+3.842	−6.725	112.386 ± 1.086	22.827	+2.201	−1.530	23.808 ± 0.572
090828.099	7	63.608	+1.467	−1.652	68.417 ± 3.167	11.100	+0.198	−0.194	10.752 ± 0.320
091024.372	26	100.013	+7.908	−4.156	93.954 ± 5.221	41.896	+2.987	−1.731	39.937 ± 1.056
091024.380	7	461.371	+48.575	−71.535	450.569 ± 2.360	283.202	+7.360	−65.306	100.610 ± 0.923
091030.613	14	22.609	+13.518	−4.522	19.200 ± 0.871	10.770	+0.388	−0.424	9.472 ± 0.345
100414.097	21	22.195	+2.149	−1.421	26.497 ± 2.073	11.468	+0.549	−0.906	13.248 ± 0.272
100130.777	17	87.725	+5.311	−4.911	86.018 ± 6.988	30.829	+1.317	−1.928	34.049 ± 1.493

Notes. Final T_{90} and T_{50} results, confidence intervals (see Sect. 6 and Szécsi et al. 2012c), and the number of singular values (Sect. 4.3) found with Akaike information criterion (Sect. 4.4) for the bursts analysed in this paper (Sect. 5). We also show the duration value of T_{90}^{cat} and T_{50}^{cat} of the GBM Catalogue (Paciesas et al. 2012) for comparison (Sect. 6.1).
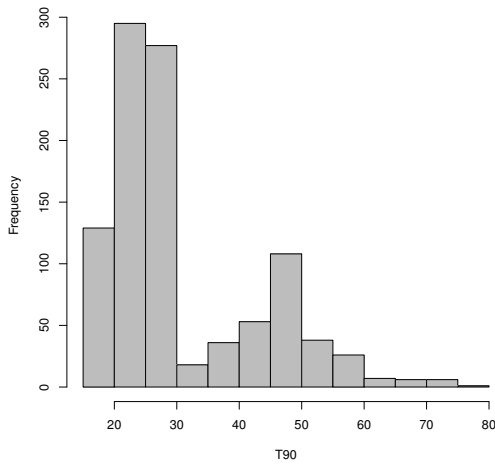
Fig. 27. Distibution of the T_{90} obtained from the MC simulated data for *Fermi* burst 091030.613 (Szécsi et al. 2012c).
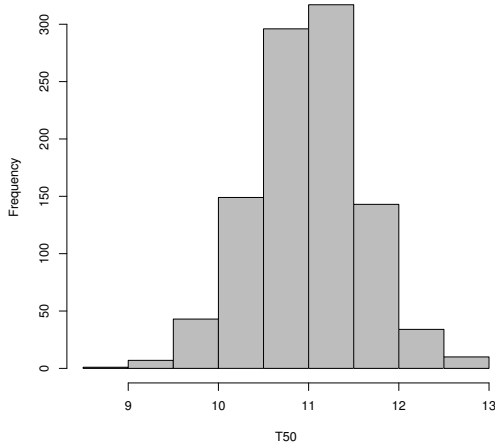
Fig. 28. Distibution of the T_{50} obtained from the MC simulated data for the *Fermi* burst 091030.613 (Szécsi et al. 2012c).

sensitive for this kind of uncertainties. In Fig. 28., there is, how-ever, no sign of this second peak: T_{50} is more robust and less likely to be influenced by these fluctuations (Szécsi et al. 2012c).

Final results of T_{90}s and T_{50}s with confidence intervals are given in Table 1 for the bursts mentioned in Sect. 5.2.

6.1. Comparison with the Fermi GBM Catalogue

In Table 1, we also show the T_{90}^{cat}s and T_{50}^{cat}s of the *Fermi* GBM Catalogue (Paciesas et al. 2012) for comparison.

At this point, we need to give some notes about the differ-ences between the method of the Catalogue and DDBF. First of all, we only used one detector when we measured the duration, whilst the Catalogue used the sum of the brightest detectors.

On the other hand, there are further differences between the Catalogue's method and the DDBF. As we mentioned in Sect. 5, our method solved the problem of automatizing the identification of the 0% and 100% levels of cumulated counts, so the user do not need to define them by hand. This disposes of one possible error source.

Additionally, using direction dependent variables produced the possibility of fitting the whole CTIME background (only the burst has to be taken off in the middle). This reduces the error of the user selected background intervals and, on the other hand, makes the automatic detection of a long emission possible. See Sect. 4.5. for more details.

With respect to the error estimation of the Catalogue, they followed the method developed for the BATSE data by Koshut et al. (1996), which uses the variance of the 0% and 100% levels of cumulated counts as a basis for the error estimates (Paciesas et al. 2012). We decided to avoid this method (as we avoid the use of time-dependent polynomial methods developed for the BATSE, as seen in Sect. 2), and give an alternative solution with Monte Carlo simulation of the data in Sect. 6. This choice is based on our belief that the DDBF is too complicated, and using the error estimation of Koshut et al. (1996) would underestimate the real error of our method.

Furthermore, we give different higher and lower confi-dence intervals. In our experience, many bursts show different amounts of uncertainties at the starting point than at the fin-ishing point. One demonstrative example is the T_{90} value of GRB 091030.613: the MC modified distribution in Fig. 27 is clearly not symmetric. Therefore, it would be an oversimplifica-tion to give only one value as an error bar or confidence interval. For more examples, see Szécsi et al. (2012c).

Given all of these facts, it follows that a comparison with the *Fermi* GBM Catalogue data is not meaningful in a quan-titative sense at the moment. It is currently under way to pro-cess all *Fermi* bursts with DDBF and publish an alternative cat-alogue, in which we will use the combined data of the detectors. Unfortunately, we cannot say anything about the robustness of

our method until we finish processing a significant number of bursts. Once it is done, we will provide an overall statistical comparison between the two dataset together with our catalogue.

7. Summary and conclusion

Since the commonly used background filtering methods are not efficient for many cases of the *Fermi*, we developed a new technique based on the motion and orientation of the satellite known as the the direction dependent background fitting (DDBF) method.

The DDBF technique considers the position of the burst, the Sun and the Earth. Based on this information on position, we computed physically meaningful underlying variables and fitted a four dimensional hypersurface on the background. Singular value decomposition and AIC were used to reduce the number of free parameters. More research may be required to find a more suitable model dimension reducing criterion.

The background model was subtracted from the measured data, resulting in background-free lightcurves. These lightcurves can be used to perform statistical surveys. We showed the efficiency of our DDBF method computing durations of some very complicated cases. We also calculated confidence intervals for our duration values corresponding to 1σ level.

We summarized some of the main differences between DDBF and the background estimation method of the GBM Catalogue and decided not to give a quantitative comparison at this point. Our plan is to process the combined data of the detectors with DDBF for every *Fermi* burst and produce an alternative catalogue. This future work will also contain the statistically relevant comparison of the official GBM Catalogue and the DDFB Catalogue which has yet to come.

The DDBF method has the advantage of considering only variables with physical meanings and it fits all the 2000 s CTIME data well as opposed to the currently used method. These features are indeed necessary when analysing long GRBs, where motion effects can influence the background rate in a very extreme way. Therefore, not only Sky Survey but also ARR mode GRB's can be analysed, and possible long emission can be detected.

Furthermore, there seems to be no reason why DDBF could not be used for other sources than GRBs. The method only considers the background levels before and after the event; therefore, the event itself has no influence to the resulted background model, even if it is very bright. Nevertheless, the duration can play a role in its applicability. Events that are comparably long to the 2000 s data file could be problematic. The DDBF is not necessary for short events, as the effects of the motion of the spacecraft are negligible: one may use the time dependent polynomial fitting for short GRBs. However, DDBF is able to discover long emissions or prebursts, as we have shown in Sect. 5.2. Therefore, DDBF could be used to verify the final result in the case of short bursts as well.

In summary, celestial position plays an important role in the *Fermi* data set. If one wants to filter the background more efficiently and in a physically more comprehensible way, one has to use this information. Utilizing this principle, we have created the DDBF method. In future work, DDBF will be used to create a catalogue of the durations of the *Fermi* GBM GRBs.

Appendix A: Earth in the FoV

In Sect. 3.2, we defined one of the underlying variables as the Earth-occulted sky rate – i.e., the Earth-uncovered sky correlated to the size of the detector's field of view (FoV). Here, we present the computations.

Let us have R as the radius of Earth and h as the altitude of the satellite. (The actual h during the burst is known from the LAT spacecraft data file.) The aperture σ of the cone constituted by the Earth-limb seen from the board of satellite is

$$\sigma = a\sin\frac{R}{R+h}. \tag{A.1}$$

Angular dependence of the detector effective area is assumed to be constant, so the FoV of one GBM detector is 2π sterad. However, more precise calculations could be done knowing the real characteristics (Meegan et al. 2009).

When the Earth-limb is totally in the FoV, the Earth-covered area is computed by integrating on a spherical surface as follows,

$$\Omega_{\text{total}}(\sigma) = \int_0^{2\pi} \int_0^{\sigma} \sin\theta \, d\theta \, d\phi = 2\pi\left(1 - \cos\sigma\right). \tag{A.2}$$

Equation (A.2) means the solid angle of a cone of aperture σ.

If only a fraction of the Earth-limb is in the FoV, then $\Omega = \Omega(\sigma, \rho)$ is smaller then Ω_{total} and is a function of the maximum altitude of the Earth-limb ρ as well. In this case, we have to separate the area in the FoV to two parts, which are marked with light grey and dark grey in Fig. A.1.
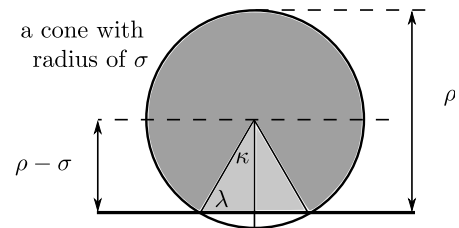

Fig. A.1. Earth limb seen onboard from the *Fermi*. Detector can only see the coloured parts above the solid horizontal black line.

We can calculate the dark grey surface the same way as above. Using $2\pi - 2\kappa$, instead of 2π when integrating with respect to ϕ, we find that

$$\Omega_{\text{darkgrey}}(\sigma, \rho) = 2(\pi - \kappa)\left(1 - \cos\sigma\right), \tag{A.3}$$

where κ is a function of ρ and σ. It is easy to see that the light grey triangle in Fig. A.1 is a spherical triangle, since its every side is a geodetic curve. Therefore, κ can be calculated from the Napiers pentagon:

$$\kappa = a\cos\left(\frac{\tan(\rho - \sigma)}{\tan\sigma}\right). \tag{A.4}$$

Then, we calculate the light grey surface. The area of a spherical triangle is given by the Girard formule:

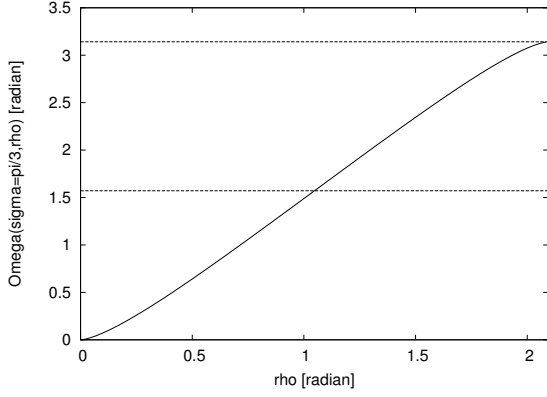$$\Omega_{\text{lightgrey}}(\sigma, \rho) = -\pi + 2\kappa + 2\lambda, \tag{A.5}$$

where $\lambda = \mathrm{acos}\left(\cos\left(\rho - \sigma\right)\sin\kappa\right)$ from the Napiers pentagon.

Thus, the surface above the black line is the sum of the light grey and dark grey parts:

$$
\begin{aligned}
\Omega^{\sigma<\rho}(\sigma,\rho) \;=\; & 2\left[\pi - \mathrm{acos}\left(\frac{\tan\left(\rho-\sigma\right)}{\tan\sigma}\right)\right](1 - \cos\sigma) \\
& -\pi + 2\mathrm{acos}\left(\frac{\tan\left(\rho-\sigma\right)}{\tan\sigma}\right) \\
& + 2\mathrm{acos}\left(\cos\left(\rho-\sigma\right)\cdot\sin\mathrm{acos}\frac{\tan\left(\rho-\sigma\right)}{\tan\sigma}\right). \quad \text{(A.6)}
\end{aligned}
$$

Equation (A.6) has to be modified a little bit when $\rho < \sigma$: in this case, the horizontal solid black line is *over* the half of the circle, and the light grey triangle has to be *subtracted* from the integral calculated from (A.2) with 2κ instead of 2π:

$$
\begin{aligned}
\Omega^{\rho<\sigma}(\sigma,\rho) \;=\; & 2\left[\mathrm{acos}\left(\frac{\tan\left(\sigma-\rho\right)}{\tan\sigma}\right)\right][1 - \cos\sigma] + \pi \\
& -2\mathrm{acos}\left(\frac{\tan\left(\sigma-\rho\right)}{\tan\sigma}\right) \\
& -2\mathrm{acos}\left(\cos\left(\sigma-\rho\right)\cdot\sin\mathrm{acos}\left(\frac{\tan\left(\sigma-\rho\right)}{\tan\sigma}\right)\right). \quad \text{(A.7)}
\end{aligned}
$$

We plot Eqs. (A.6) and (A.7) as a function of ρ for $\sigma = \pi/3$, as seen in Fig. A.2. Equations (A.6) and (A.7) give us Eq. (A.2), when $\rho = 2\sigma$, and have no meaning when $\rho < \sigma$ or $\rho > 2\sigma$. Therefore, we define an underlying variable $x^{(3)}$ (called the Earth-occulted sky rate, see Sects. 3.2 and 4.1) the following way:

$$
x^{(3)} = \begin{cases}
0, & \text{if } \rho \leq 0; \\
\dfrac{\Omega^{\rho<\sigma}(\sigma,\rho)}{2\pi}, & \text{if } 0 < \rho \leq \sigma; \\
\dfrac{\Omega^{\sigma<\rho}(\sigma,\rho)}{2\pi}, & \text{if } \sigma < \rho < 2\sigma; \\
\dfrac{\Omega_{\text{total}}(\sigma)}{2\pi}, & \text{if } 2\sigma \leq \rho.
\end{cases}
\quad \text{(A.8)}
$$

Note that we divided by 2π because we assumed that FoV of the detector is 2π sterad. In that way, we get the rate of the Earth-limb to the FoV. We computed expression (A.8) for every second of the lightcurve and use it as an underlying variable in Sect. 3.2.

References

Ackermann, M., Ajello, M., Atwood, W. B., et al. 2012, ApJ, 750, 3
Akaike, H. 1974, IEEE Transactions on Automatic Control, 19, 716
Briggs, M. S., Fishman, G. J., Connaughton, V., et al. 2010, JGR, 115, 7323
Fermi-Timeline-Posting 2013, Fermi Science Support Center, http://fermi.gsfc.nasa.gov/ssc/observations/timeline/posting/arr/
Fitzpatrick, G., et al. 2011, Fermi Symposium Proc., eConf C110509
GCN 2013, The Gamma Ray Coordinates Network, gcn.gsfc.nasa.gov
Gruber, D., Krühler, T., Foley, S., et al. 2011, A&A, 528, A15
Koshut, T., Paciesas, W., Kouveliotou, C., et al. 1996, ApJ, 463, 570
Long, P. 2005, Introduction to Octave, Department of Engineering, University of Cambridge
Meegan, C., Lichti, G., Bhat, P. N., et al. 2009, ApJ, 702, 791
Paciesas, W. S., Meegan, C. A., von Kienlin, A., et al. 2012, 199, 18
Press, W. H., Teukolsky, S. A., Vetterling, W. T., & Flannerty, B. P. 1992, Numerical Recipes in C: The Art of Scientific Computing (New York: Cambridge University Press)
Sakamoto, T., Barthelmy, S. D., Barbier, L., et al. 2008, ApJS, 175, 179
Szécsi, D., Bagoly, Z., Horváth, I., et al. 2012a, Acta Polytech., 52, 43
Szécsi, D., Bagoly, Z., Balázs, L. G., Veres, P., & Kóbori, J. 2012b, Proc. of Fermi/Swift GRB Conference, Munich, PoS(GRB 2012)051
Szécsi, D., Bagoly, Z., Kóbori, J., et al. 2012c, Fermi Symposium Proc., eConf C121028 [arXiv:1303.3141]
Varga, B., Horváth, I., & Balázs, L. G. 2005, Il Nuovo Cimento C, 28, 861

GUIDING MOTION

....

Institute of Astronomy
....

Nicolaus Copernicus University
....

ul. Gagarina 11, 87-100 Toruń, Poland
....

(name and address of institution conferring the post-doctoral degree of habilitated doctor, in charge of the procedure)

through:

The Council of Scientific Excellence
pl. Defilad 1
00-901 Warsaw
(Palace of Science and Culture, 24th floor, room 2401)

Dr. Dorottya Szécsi
....

(name of applicant)

Institute of Astronomy, Nicolaus Copernicus University
....

(name of employer/academic institution unit)

Application

dated ... 28 June 2023 ....

re.: commencement of the procedure for the conferment of the post-doctoral degree of doctor habilitated in the field of ... natural sciences ....
in the following discipline .... astronomy ....

Scientific achievement which entitles the applicant to commence the procedure for the conferment of the post-doctoral degree of doctor habilitated

Role of Gravitational-Wave Progenitors in the Universe
....

Pursuant to art. 221 para 10 of the Higher Education and Science Act dated 20 July 2018 (Polish Journal of Laws of 2018 item 1668, as amended) I hereby kindly request that the habilitation commission pass a resolution on the conferment of the post-doctoral degree of doctor habilitated in ~~secret~~/**open** voting*[1]

---

[1] * Delete if not applicable

I was advised of the following:

The President of the Scientific Council of Excellence with its registered office in Warsaw (pl. Defilad 1, 24th floor, 00-901 Warsaw) is the Administrator of personal data collected under the procedure for the conferment of the post-doctoral degree of doctor habilitated.

Contact us via e-mail: kancelaria@rdn.gov.pl , phone 22 656 60 98 or personally at our office. Personal data shall be processed pursuant to art. 6 para 1 letter c) Regulation (EU) 2016/679 dated 27 April 2016 in connection with art. 220-221 and art. 232-240 of the Higher Education and Science Act dated 20 July 2018, for the purposes of the procedure for the conferment of the post-doctoral degree of doctor habilitated and in order to exercise the rights and obligations as well as the right to appeal in this procedure.

For detailed information on processing personal data in the procedure see www.rdn.gov.pl/klauzula-informacyjna-rodo.html

…………………………...
(Applicant's signature)